THE UNIVERSITY OF YAOUNDÉ I
FACULTY OF SCIENCE
DEPARTMENT OF INORGANIC CHEMISTRY

UNIVERSITÉ DE YAOUNDÉ I
FACULTÉ DES SCIENCES
DÉPARTEMENT DE CHIMIE INORGANIQUE

POSTGRADUATE SCHOOL OF SCIENCE, TECHNOLOGY AND GEOSCIENCE
*CENTRE DE RECHERCHE ET DE FORMATION DOCTORALE EN SCIENCES, TECHNOLOGIE ET GÉOSCIENCES*

RESEARCH AND POSTGRADUATE TRAINING UNIT IN CHEMISTRY AND ITS APPLICATIONS
*UNITÉ DE RECHERCHE ET DE FORMATION DOCTORALE EN CHIMIE ET APPLICATIONS*

LABORATORY OF APPLIED INORGANIC CHEMISTRY
*LABORATOIRE DE CHIMIE INORGANIQUE APPLIQUÉE*

# Manganese(II), Zinc(II) and Cadmium(II) Complexes of 2-Aminopyridine and N-Phenylanthranilic Acid: Synthesis, Structural Investigation and Biological Screening

**Thesis presented and defended publicly on the 14th December 2022 by:**

**MBANI Armel Landry (Matricule: 09T0793)**
*M.Sc Inorganic Chemistry, UYI*

**For the award of a Doctorate/PhD degree in Inorganic Chemistry**
**Option: Coordination Chemistry**



**In front of the following members of the Jury:**

**President:** **KETCHA Joseph MBADCAM**, *Professor, The University of Yaoundé I*

**Supervisors:** **AGWARA Moise ONDOH**, *Professor, The University of Yaoundé I*

**PABOUDAM GBAMBIE AWAWOU**, *Associate Professor, The University of Yaoundé I*

**Members:** **NDIFON Peter TEKE**, *Professor, The University of Yaoundé I*

**NJIOMOU DJANGANG Chantale**, *Associate Professor, The University of Yaoundé I*

**CONDE ASSENG Mariam**, *Associate Professor, The University of Douala*

**MBOUOMBOUO NDASSA Ibrahim**, *Associate Professor, The University of Yaoundé I*

**Year 2022**

THE UNIVERSITY OF YAOUNDÉ I
FACULTY OF SCIENCE
DEPARTMENT OF INORGANIC CHEMISTRY

POSTGRADUATE SCHOOL OF SCIENCE, TECHNOLOGY AND GEOSCIENCE

RESEARCH AND POSTGRADUATE TRAINING UNIT IN CHEMISTRY AND ITS APPLICATIONS

UNIVERSITÉ DE YAOUNDÉ I
FACULTÉ DES SCIENCES
DÉPARTEMENT DE CHIMIE INORGANIQUE

CENTRE DE RECHERCHE ET DE FORMATION DOCTORALE EN SCIENCES, TECHNOLOGIE ET GÉOSCIENCES

UNITÉ DE RECHERCHE ET DE FORMATION DOCTORALE EN CHIMIE ET APPLICATIONS

LABORATORY OF APPLIED INORGANIC CHEMISTRY
*LABORATOIRE DE CHIMIE INORGANIQUE APPLIQUÉE*

# ATTESTATION OF CORRECTION

We, the undersigned, attest that this thesis defended publicly on the 14th December 2022 in the Pedagogic Block; Multimedia hall of the Faculty of Science, the University of Yaoundé I, by **MBANI Armel Landry** (Matricule: **09T0793**) entitled: "***Manganese(II), Zinc(II) and Cadmium(II) Complexes of 2-Aminopyridine and N-Phenylanthranilic Acid: Synthesis, Structural Investigation and Biological Screening***", for the award of a Doctorate/PhD in Inorganic Chemistry, has been corrected in conformity with the recommendations of the defence Jury.

In this testimony whereof, this attestation is issued.

Yaoundé, 23 JAN 2023

| The President | The Supervisors | The Examiner |
|---|---|---|
| KETCHA J.M. | Agwara Moïse Ondoh, PhD<br>Professor | Pelex T. Ndifon, PhD<br>Professeur |
| | PAGOUBAM GBANDIE ANAWOK, PhD<br>Maître de Conférences | |

**THE UNIVERSITY OF YAOUNDÉ I**
**FACULTY OF SCIENCE**
**DEPARTMENT OF INORGANIC CHEMISTRY**

**UNIVERSITÉ DE YAOUNDÉ I**
**FACULTÉ DES SCIENCES**
**DÉPARTEMENT DE CHIMIE INORGANIQUE**

**POSTGRADUATE SCHOOL OF SCIENCE, TECHNOLOGY AND GEOSCIENCE**
***CENTRE DE RECHERCHE ET DE FORMATION DOCTORALE EN SCIENCES, TECHNOLOGIE ET GÉOSCIENCES***

**RESEARCH AND POSTGRADUATE TRAINING UNIT IN CHEMISTRY AND ITS APPLICATIONS**
***UNITÉ DE RECHERCHE ET DE FORMATION DOCTORALE EN CHIMIE ET APPLICATIONS***

**LABORATORY OF APPLIED INORGANIC CHEMISTRY**
***LABORATOIRE DE CHIMIE INORGANIQUE APPLIQUÉE***

# Manganese(II), Zinc(II) and Cadmium(II) Complexes of 2-Aminopyridine and N-Phenylanthranilic Acid: Synthesis, Structural Investigation and Biological Screening

Thesis presented and defended publicly on the 14th December 2022 by:

**MBANI Armel Landry (Matricule: 09T0793)**
*M.Sc Inorganic Chemistry, UYI*

**For the award of a Doctorate/PhD degree in Inorganic Chemistry**
**Option: Coordination Chemistry**

In front of the following members of the Jury:

**President:** KETCHA Joseph MBADCAM, *Professor, The University of Yaoundé I*

**Supervisors:** AGWARA Moise ONDOH, *Professor, The University of Yaoundé I*
PABOUDAM GBAMBIE AWAWOU, *Associate Professor, The University of Yaoundé I*

**Members:** NDIFON Peter TEKE, *Professor, The University of Yaoundé I*
NJIOMOU DJANGANG Chantale, *Associate Professor, The University of Yaoundé I*
CONDE ASSENG Mariam, *Associate Professor, The University of Douala*
MBOUOMBOUO NDASSA Ibrahim, *Associate Professor, The University of Yaoundé I*

**Year 2022**

# Dedications

*To my lovely late Mother* MEKONGO Marie Jeanne,

*To my late Father* OPEPAM ABEGA Anaclet,

*To my late sister and brothers* MENDOUGA Sylvie, KOA Bruce, MEKONGO Jules Eric, and ZANGA Jean Paul.

**ACKNOWLEDGEMENTS**

To the Almighty GOD be the Glory!

I will like to express my warmest thanks and gratitude to my Supervisors, **Pr. AGWARA Moise ONDOH** and **Pr. PABOUDAM AWAWOU** for having accepted to supervise this work and for their guidance, suggestions, patience and all their encouragements.

I am grateful to **Pr. NDIFON Peter TEKE**, head of Coordination Chemistry Laboratory for the use of the laboratory and **Pr. Chantal STIEBER**, from California State Polytechnic University-Pomona, United States of America, for providing her expertise for the completion of this work.

I also thank **Dr. Vincent de Paul NZIKO** from the United States of America, for the technical support he brought during the course of this work.

I am grateful to **Dr. Divine YUFANYI** and **Dr. AMAH Colette** for their guidance and support during the course of this work.

I am grateful to all the lecturers of the Department of Inorganic Chemistry of the University of Yaoundé I, for the lectures and training.

My sincere gratitude goes to **Pr. Fabien NKOT** for his multiform assistance.

Special thanks to my brothers and sisters, **Marquise ASSOMO, Nicaise AMOUGOU, Carole ATENA, Merveille MEKONGO,** for their financial support and love.

To all coordination chemistry students, I thank you for the useful contributions.

## TABLE OF CONTENTS

**Page**

## LIST OF FIGURES

## LIST OF TABLES

## ABBREVIATIONS

| | |
|---|---|
| **2-Apy** | 2-aminopyridine |
| **cfu** | Colony Forming Unit |
| **dca** | Dicyanamide ion |
| **DMSO** | Dimethylsulphoxide |
| **MBC** | Minimum Bactericidal Concentration |
| **MFC** | Minimum Fungicidal Concentration |
| **MIC** | Minimum Inhibitory Concentration |
| **NCI** | Non-covalent interaction |
| **NPA** | N-phenylanthranilic acid |
| **NSAID** | Non-Steroidal Anti-inflammatory Drug |
| **SCC** | Supramolecular Coordination Complex |
| **$SCN^-$** | Thiocyanate ion |

## ABSTRACT

One of the objectives in coordination chemistry is the synthesis of molecules of various topologies that can exhibit interesting properties in several fields. Thus, three new supramolecular coordination compounds: $[Mn(2\text{-}Apy)_2(dca)_2]$ (*bis(2-aminopyridine)bis($\mu_{1,5}$-dicyanamido)manganese(II)*), $[Zn_3(H_2O)_2(NPA)_6]$ (*hexakis($\mu_2$-2-anilinobenzoato)diaquatrizinc(II)*) and $[Cd(2\text{-}Apy)_2(dca)_2]$ (*bis(2-aminopyridine)bis($\mu_{1,5}$-dicyanamido)cadmium(II)*) were synthesised in a water-ethanol mixture (1:5) and characterised by physico-chemical methods.

The complexes obtained have different melting temperatures ranging from 162 to > 300 °C, temperatures different from those of the precursors used. This indicates that new compounds have been obtained.

The results of elemental analysis show that the elemental contents present in the complexes are very close to the theoretical values, confirming the expected formulas of the complexes and purity.

The IR spectra of the ligands and the complexes indicate good cohesion: the functional groups present on the spectra of the ligands are also present on those of the complexes, thus indicating that the ligands have been coordinated, notably the metal-nitrogen and metal-oxygen bonds.

The X-ray diffractometry shows that the complexes of $[Mn(2\text{-}Apy)_2(dca)_2]$ and $[Cd(2\text{-}Apy)_2(dca)_2]$ are in a 1-D polymeric chain structure which crystallise in the monoclinic system with space group Cc. The complex of $[Zn_3(H_2O)_2(NPA)_6]$ is a 3D trinuclear structure which crystallises in a triclinic crystal system with space group $P\bar{1}$. The crystal structures obtained confirm the results of the elemental analysis, conductance measurements, and IR spectroscopy.

Thermal analyses show that the complexes decompose in various steps in the temperature range of 50 – 650 °C with the loss of various fractions.

The Hirsfeld surface analysis shows that C–H···π, H···H, and N···H/H···N intermolecular interactions for $[Mn(2\text{-}Apy)_2(dca)_2]$ and $[Cd(2\text{-}Apy)_2(dca)_2]$ constitute 82.0 % and 84.1 % respectively for the packing arrangement of the supramolecular crystal structure, while for $[Zn_3(H_2O)_2(NPA)_6]$ C–H···π, H···H, and H···O/O···H interactions, it constitutes 96.4 %.

DFT calculations show that $[Zn_3(H_2O)_2(NPA)_6]$ possesses the lowest electronegativity value and that it is the best electron acceptor on one hand, and on the other hand, $[Cd(2\text{-}Apy)_2(dca)_2]$ has been found to have the highest chemical reactivity amongst all due to its highest softness value.

*In vitro* antimicrobial analyses show that globally, there is an enhanced biological activity of the complexes synthesised as compared to the ligands, which would mean that the coordination would increase the biological potency of the ligands. Both $[Zn_3(H_2O)_2(NPA)_6]$ and $[Cd(2\text{-}Apy)_2(dca)_2]$

complexes have shown activities against all microbial strains. $[Mn(2\text{-}Apy)_2(dca)_2]$ shown no activity against the gram-negative bacteria *S. typhi.*

Docking studies show that $[Zn_3(H_2O)_2(NPA)_6]$ has potential for binding to the main protein in SARS-CoV-2 in a different location from Chloroquine, but with a higher binding strength. Which would indicate that it would be a potential candidate for the inhibition of SARS-CoV-2.

**Keywords**: *N-phenylantranilic acid, 2-aminopyridine, dicyanamide, coordination polymer, crystal structure, DFT, Hirshfeld surface analysis, biological test.*

## RÉSUMÉ

L'un des objectifs en chimie de coordination est la synthèse des molécules de topologies diverses pouvant exhiber des propriétés intéressantes dans plusieurs domaines. Ainsi, trois nouveaux composés de coordination supramoléculaire : $[Mn(2\text{-}Apy)_2(dca)_2]$ (*bis(2-aminopyridine)bis($\mu_{1,5}$-dicyanamido)manganèse(II)*), $[Zn_3(H_2O)_2(NPA)_6]$ (*hexakis($\mu_2$-2- anilinobenzoato)diaquatrizinc(II)*) et $[Cd(2\text{-}Apy)_2(dca)_2]$ (*bis(2-aminopyridine)bis($\mu_{1,5}$-dicyanamido)cadmium(II)*) ont été synthétisés dans un mélange eau-éthanol (1:5) et caractérisés par les méthodes physico-chimiques.

Les complexes obtenus ont des températures de fusion différentes allant de 162 à > 300 °C, températures différentes de celles des précurseurs utilisés. Ce qui indique l'obtention de nouveaux composés.

Les résultats d'analyse élémentaire montrent que les pourcentages des éléments présents dans les complexes sont très proches des valeurs théoriques, confirmant les formules attendues des complexes et leurs puretés.

Les spectres IR des ligands et des complexes indiquent qu'il y a formation de nouvelles entités chimiques : les groupes fonctionnels présents sur les spectres des ligands sont également présents sur ceux des complexes, indiquant ainsi que les ligands ont été coordinés.

La diffractométrie des rayons X montre que les complexes de $[Mn(2\text{-}Apy)_2(dca)_2]$ et $[Cd(2\text{-}Apy)_2(dca)_2]$ sont dans une structure de chaîne polymérique 1-D qui cristallise dans le système monoclinique avec le groupe d'espace Cc. Le complexe $[Zn_3(H_2O)_2(NPA)_6]$ a une structure trinucléaire 3D qui cristallise dans un système cristallin triclinique de groupe d'espace $P\bar{1}$.

Les analyses thermiques ont permis de montrer que les complexes se décomposent en plusieurs étapes dans la gamme de température de 50 à 650 °C avec perte de diverses fractions.

L'analyse de surface de Hirsfeld montre que les interactions intermoléculaires C–H···π, H···H et N···H/H···N pour $[Mn(2\text{-}Apy)_2(dca)_2]$ et $[Cd(2\text{-}Apy)_2(dca)_2]$ constituent respectivement 82,0 % et 84,1 % de l'agencement de la structure cristalline supramoléculaire, tandis que pour $[Zn_3(H_2O)_2(NPA)_6]$, les interactions C–H···π, H···H et H···O/O···H contribuent à hauteur de 96,4 % de la structure cristalline.

Les calculs de Théorie de la Fonctionnelle de la Densité (DFT) montrent que $[Zn_3(H_2O)_2(NPA)_6]$ possède la plus faible valeur d'électronégativité et qu'il est le meilleur accepteur d'électrons d'une part. D'autre part, le complexe $[Cd(2\text{-}Apy)_2(dca)_2]$ a la réactivité chimique la plus élevée parmi toutes.

Les analyses antimicrobiennes *in vitro* montrent globalement que l'activité biologique des complexes synthétisés est accrue comparé à celle des ligands, ce qui signifierait que l'association des ligands au fragment de sel métallique induit le pouvoir biologique appréciable sur la souche bactérienne et

fongique. Les complexes $[Zn_3(H_2O)_2(NPA)_6]$ et $[Cd(2\text{-}Apy)_2(dca)_2]$ sont actifs sur toutes les bactéries testées. Le complexe $[Mn(2\text{-}Apy)_2(dca)_2]$ n'a montré aucune activité contre la bactérie gram-négative *S. typhi.*

Des études d'amarrage moléculaire montrent que le complexe $[Zn_3(H_2O)_2(NPA)_6]$ a la capacité de se lier à la protéine principale du SRAS-CoV-2 à un endroit différent de la chloroquine, mais avec une force de liaison plus élevée. Ce qui indiquerait qu'il serait un candidat potentiel pour l'inhibition du SRAS-CoV-2.

**Mots-clés** : *Acide N-phénylantranilique, 2-aminopyridine, dicyanamide, polymère de coordination, structure cristalline, DFT, analyse de surface Hirshfeld, test biologique.*

# GENERAL INTRODUCTION

## 1. Background

The development of metal-organic framework hybrid materials, resulting to supramolecular coordination complexes, has become one of the most interesting fields in modern chemistry thanks to the advent of modern coordination chemistry. [1,2] The discovery of modern coordination chemistry is undisputedly owed to the 1913 Nobel prize winner, Alfred Werner, after his work on stereochemistry, which proved conclusively that metal complexes can be chiral. [3] In its simplest definition, coordination chemistry is the study of compounds that have a central atom (often metallic) surrounded by molecules or anions, known as ligands. On the other hand, the concept of supramolecular chemistry was first introduced by Jean-Marie Lehn in 1987. He defined it as "*chemistry beyond the molecule*". More specifically, supramolecular chemistry is the chemistry of the intermolecular bond, covering the structures and functions of the entities formed by association of two or more chemical species [4]. Here, the components self-assemble to form supramolecular networks. Whitesides defined self-assembly as "the spontaneous association of molecules under equilibrium conditions into stable, structurally well-defined aggregates joined by non-covalent bonds". [5]

So far, the field of supramolecular chemistry has witnessed significant advances in recent decades, moving from the synthesis of discrete supramolecules such as catenanes or rotaxanes, to dynamic self-assembled materials held together by non-covalent bonds. [6] Therefore, molecular self-assembly has been established as a powerful tool which bridge the gap between the nanoscopic and mesoscopic scale by careful control over non-covalent interactions, as some characteristics of the complexes are based on the non-covalent interactions that determine their networks. [5,7,8]

As reported for the first time three decades ago, supramolecular polymers have been primarily constructed from purely organic building blocks. The inclusion of metal centres in theses dynamic systems have induced new potential properties with various applications. [6]

Nowadays, supramolecular coordination compounds have given rise to a plethora of applications in various domains due to supramolecular networks which can be synthetically controlled and modified accordingly. This is owed to various physicochemical factors such as; steric hindrance, electron density, and complex geometry regarding the coordination relationship of the coordination compounds, which therefore condition the technological process. [9] These applications represent a long and impressive list of achievements. For instance, applications range from catalysis, medicine, molecular electronics, magnetism, hydrometallurgy and extraction, gas storage, non-linear optics, sensors, environmental remediation and energy storage. [1,10–13]

The most common approach in building supramolecular networks is the use of metal centres as structural building blocks to a rational assembly of molecular components. Holliday and Chad have listed three emerging synthetic strategies of supramolecular networks. These include: the symmetry interaction, directional-bonding, and weak-link synthetic approaches. [1] Each strategy has advantages as well as limitations.

Accurate prediction and control of the 3-D structure of molecular crystals and coordination polymers however remains difficult in any case, owing to the weak metal–ligand interactions found in coordination complexes. This weak bond often translates into many reaction pathways that are not substantially different from an energetic point of view, and therefore, results in poor selectivity. [1]

Despite these shortcomings, the subject of supramolecular coordination compounds continues to develop and grow rapidly. In the last 10 years however, and despite the exponential growth of the number of papers related to the synthesis of supramolecular coordination compounds, just a limited number of paper have reported on their biological/biomedical applications. [2]

Moreover, when publications on novel metal-based antimicrobial agents are reported, the research does not typically extend beyond their synthesis, their Minimum Inhibitory Concentrations and Minimum Bactericidal Concentrations analyses, and their haemolysis assay evaluation. [14]

At times, when done, to afford the synthesis of supramolecular coordination complexes with programmed biological properties, costly synthetic routes, expensive or less accessible ligands, as well as toxic metals are usually employed.

## 2. Problem statement

The obtaining and the structural investigation of supramolecular compounds remain a major challenge for chemists. The framework structure of supramolecular coordination polymers is primarily dependent upon the metal centre and the functionality of the ligands. [6] Moreover, as discussed above, just a limited number of papers are interested in studying the biological/biomedical applications of supramolecular compounds. [2]

Multidentate ligands such as carboxylates and N-heterocyclic ligands are widely used in the rational design and controlled synthesis of functional materials. [13]

The research on the metal carboxylates has always been intriguing in that they play important roles not only in synthetic chemistry with the essence of labile coordination modes of carboxylate group, such as architecture of open and porous framework but also in biological activities and physiological

effects. [12,15] A versatile carboxylate anions can adopt a wide range of bonding modes, including monodentate, symmetric and asymmetric chelating, and bidentate and monodentate bridging. [12] N-Phenylanthranilic acid is a β-amino acid chelating ligand, with potential for coordination through both the N atom of the amino group (N) and the O atoms of the carboxyl group ($-COO^-$). [16] However, little attention has been focused on the synthesis of its coordination complexes with first row transition metals. [17,18]

Several heterocyclic organic ligands, such as pyridine and derivatives, have been used in the construction of coordination polymers with diverse structures and numerous applications. [19,20] The rigid pyridine-based ligands are good N-donor ligands to metal ions through the pyridine N-atom, while the substituent groups are most often involved in non-covalent interactions. This confers to 2-Aminopyridine the property of being a good supramolecular synthon. [21]

Thus, with the evidence that just few 3d metal complexes of N-Phenylanthranilic acid are found in the literature, that 2-Aminopyridine is a good supramolecular synthon which can lead to the formation of interesting supramolecular networks, and that just very few supramolecular coordination complexes are being studied for their biological/biomedical activities, the present thesis proposes to expand the family of metallo-supramolecular compounds with the aforementioned ligands by synthesizing and characterizing them, and studying their biological properties.

## 3. The research question

By synthesising complexes of N-Phenylanthranilic acid and 2-Aminopyridine with Mn, Zn and Cd metal centres, is it possible to obtain supramolecular coordination complexes with improved biological properties against resistant microbial strains compared to the individual components?

## 4. Aim and objectives of the work

The aim of this work is therefore to synthesise N-Phenylanthranilic acid and 2-Aminopyridine coordination functional networks with Mn, Zn, and Cd transition metals.

The specific objectives of this work are to:

- Synthesise metal complexes of Mn(II), Zn(II), and Cd(II) with 2-aminopyridine, N-phenylanthranilic acid ligands, with dicyanamide and thiocyanate ions co-ligands.
- Elucidate the structures of the synthesised complexes using physico-chemical analyses such as melting point measurements, elemental analysis, conductivity measurement, IR spectroscopies, thermal studies, single crystal X-ray diffractometry.

- Investigate the Hirsfeld surface analysis for the intermolecular interactions, as well as DFT to calculate the electronic structure of the molecules.
- Conduct *in vitro* biological essays against selected microorganisms.
- Carry out molecular docking to predict the predominant binding modes of the molecules toward selected pathogens.

This thesis work is divided into three chapters and a conclusion. Chapter I covers the literature review, which provides scholarly research on the work. Chapter II is focused on experimental methods carried on in the laboratory. Chapter III deals with the presentation of the results obtained and with their discussion. A conclusion reiterates the importance of the main idea and summarises results obtained.

# Chapter I: LITERATURE REVIEW

## 1.1. N,O-donor and N-donor ligands in coordination chemistry

Nowadays, the design and synthesis of metal complexes with desired properties from simple, relatively cheap and available ligands is a major challenge for chemists. In this respect, Nitrogen-containing heterocyclic compounds have been found to be the key structural cores of various bioactive natural products, medicinally important compounds, and organic materials and therefore, considered to be of great biological and chemical significance. [22]

Coordination compounds containing amino acids have attracted much attention as a result of their biological properties which include antimicrobial, anti-inflammatory and anticancer. [23–25] For the latter property, it has been shown that drugs containing amino acids are less likely to suffer drug resistance for tumour cells as these cells require them in order to actively reproduce. [24] Moreover, it is suggested that N,O-donor ligands such as amino acids might inhibit enzyme production. This arises because the enzymes which require these groups for their activity appear to be especially more susceptible to deactivation by the metal ion upon chelation. [25] Such N,O-donor ligands include N-phenylanthranilic acid, which is the N-phenyl derivative of anthranilic acid.

Aminopyridines constitute an important class of compounds able to elicit a wide range of biological responses in a number of different organisms, with Sulfapyridine being one of the first effective antibiotics. [26] 2-Aminopyridine, an N-donor ligand, is among these compounds and its medicinal and pharmacological properties have been demonstrated. [27]

## 1.2. The chemistry of N-Phenylanthranilic acid and 2-Aminopyridine ligands

### 1.2.1. N-Phenylanthranilic acid ligand (NPA)

It is a β-amino acid chelating ligand, on which few complexes have been synthesised, especially with 3d transition metals. [17] The structure and the coordination mode of the ligand are highlighted below.

#### 1.2.1.1. Structure of N-Phenylanthranilic acid

NPA is composed of two phenyl moieties which are linked by an imino bridge (-NH-) (figure 1).

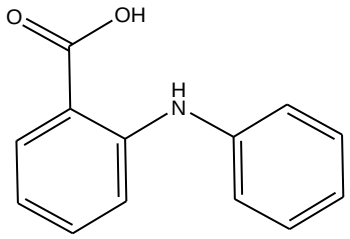


Figure 1: Structure of N-phenylanthranilic acid.

The two phenyl arms can rotate freely around the imino (–NH–) groups according to a change in the coordination environment in order to minimize steric hindrance and therefore lead to interesting structures with versatile motifs. Moreover, the N,O-donor atoms of NPA can chelate to a central metal to form a 6-membered ring which may bring-up an extra stability.

### 1.2.1.2. Coordination modes of N-Phenylanthranilic acid

NPA is a multidentate moiety, which can bind either through one carboxylate oxygen atom [12,28] or through both carboxylate oxygen atoms. [13,29] Moreover, intra-molecular hydrogen bond formation has been observed in the complex $[Mn(NPA)_2(Phen)_2]$ (where Phen = 1,10-phenanthroline) between the uncoordinated nitrogen of amino group and one of the coordinated oxygen atoms of carboxylic group. [28] Otherwise, NPA has been reported in the literature where it formed chelation through both the nitrogen of amino group (-NH) and the carboxylic group (-COO-). [16,30] This variety of coordination modes of NPA leads undoubtedly to the formation of metal complexes with versatile structures as shown in Figure 2 below.

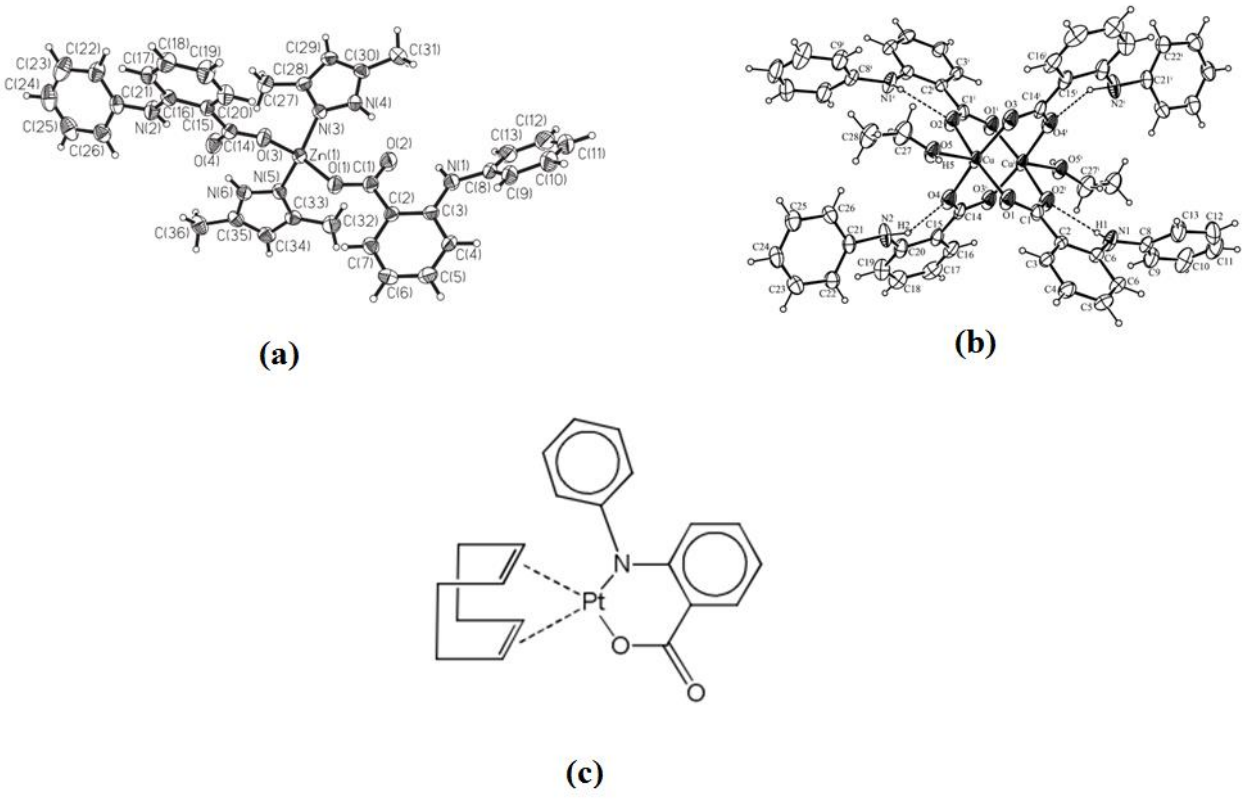


Figure 2: Coordination modes of NPA as a (a) monodentate O'–donor ligand, [12] (b) bidentate O,O'– donor ligand, [17] and (c) bidentate N,O'–donor ligand. [30]

### 1.2.2. 2-Aminopyridine ligand (2-Apy)

It is an organic compound with the formula $H_2NC_5H_4N$. It is obtained from the reaction between sodium amide and pyridine. 2-aminopyridine is one of the three isomers of aminopyridines. The other ones are 3-aminopyridine and 4-aminopyridine.

#### 1.2.2.1. Structure of 2-Aminopyridine

2-aminopyridine is made up of one pyridine moiety on which an amine group is attached at the β-position. This is shown in the Figure 3 below.

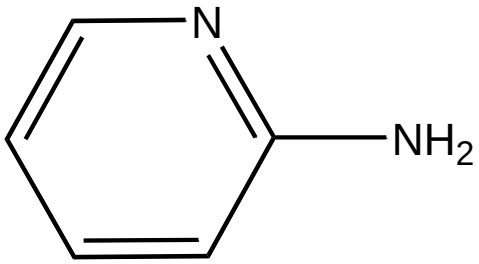


Figure 3: Structure of 2-aminopyridine.

The compounds inherently exist as a mixture of tautomeric amino and imino isomers with the predominance of the amino form over the imino form. The predominance is in the ratio 1000:1. [31]

#### 1.2.2.2. Coordination modes of 2-Aminopyridine

The structure of 2-Apy ligand favours the variety of its mode of coordination. The most commonly encountered coordination mode of 2-Apy is the monodentate coordination of the ligand through its pyridine nitrogen atom. [32–35] The less common mode of coordination of the ligand is through the exocyclic amino N-atom. [36] However, 2-Apy can also acts either as a bridging ligand or a chelating ligand, as both the exocyclic amino N-atom and the pyridine nitrogen atom coordinate to a central metal. [37,38] Furthermore, the chelation ability of 2-Apy has been reported in the literature in which the N-atom of the amino group is either protonated or not. [38]

These coordination modes are represented in Figure 4 below.

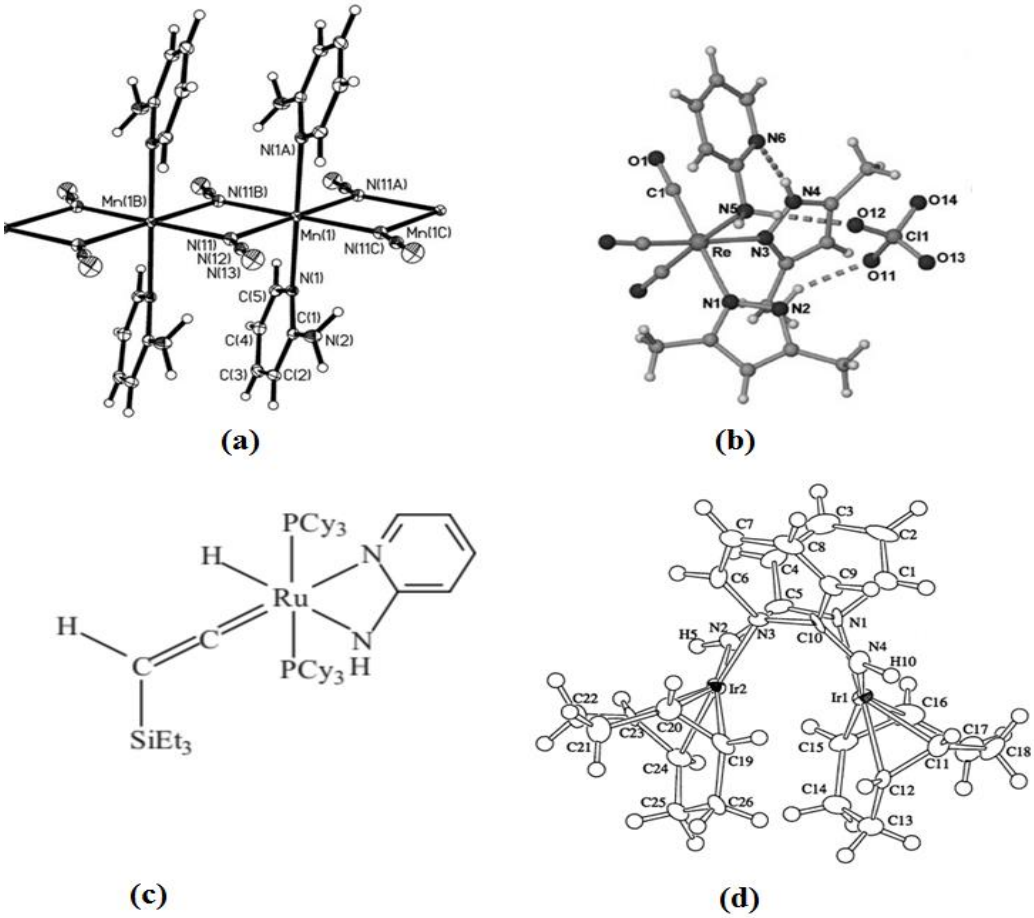


Figure 4: Coordination modes of 2-Apy as a (a) monodentate $N_{py}$-donor ligand, [35] (b) monodentate $N_{NH2}$– donor ligand, [36] (c) chelating ligand, [38] and (d) bridging ligand. [37]

### 1.3. Survey of metal complexes of N-Phenylanthranilic acid and 2-Aminopyridine

According to Batten *et al.* [39] the definition of dimensionality of a coordination compound only depends on the directionality of coordination bond. For instance, a structure linked by coordination bonds in one direction and by hydrogen bonds in two other directions is a 1D coordination polymer. This definition properly includes ligands with bridging features.

In this survey, the definition of the dimensionality is based on all the bonding modes (hydrogen bonds, π – bonds, coordination bond, etc.) associated with a coordination compound.

The structures of both NPA and 2-Apy can favour the formation of a variety of chemical links such as: metal···π bonds, π···π bonds, C–H···π bond, and hydrogen bonding. Therefore, due to their structures, these compounds can form interesting 1D, 2D, and 3D edifices.

### 1.3.1. Metal complexes of N- Phenylanthranilic acid

#### 1.3.1.1. One-dimensional coordination polymer

The mononuclear complex of $Zn(Hdmpz)_2(NPA)_2$ (with Hdmpz = 3,5-dimethylpyrazole) crystallizes in the triclinic space group P1 and exhibits a 1D chain structure (Figure 6). [12] In this complex, each zinc ion is tetrahedrally coordinated by two oxygen atoms of two monodentate NPA ligands and by two nitrogen atoms, belonging to two monodentate pyrazole ligands. This forms a $ZnN_2O_2$ binding set as shown in Figure 5. The $ZnN_2O_2$ unit possesses coordination distances and angles respectively in the ranges of 1.920(3)–1.998(4) Å and 104.33(14)–114.71(15). Intramolecular hydrogen bonds arise in the complex from the non-bonded oxygen atoms of NPA and the N-H moiety of pyrazole (N(6)–H(6) O(4), and N(4)– H(4) O(2)).

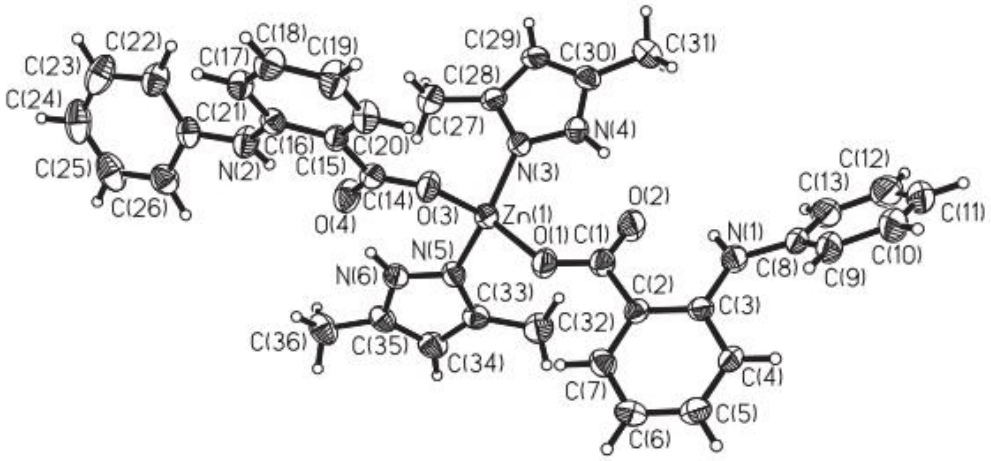


Figure 5: Molecular structure of complex $Zn(Hmpdz)_2(NPA)_2$. [12]

The 1D chain structure arises from the combination of mononuclear units via the CH···π association between the phenyl CH of the anion and the phenyl ring of adjacent mononuclear moiety with a C–Cg distance of 3.732 Å (Figure 5). This forms a dinuclear aggregate with the Zn–Zn distance calculated to be 8.982 Å, and there is an inversion centre at the middle of the adjacent Zn ions.

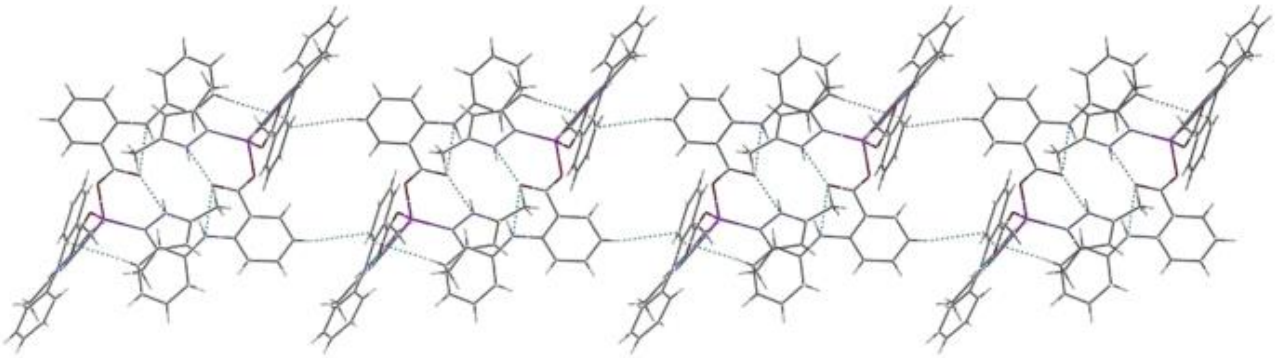

Figure 6 : The 1D chain structure of $Zn(Hmpdz)_2(NPA)_2$. [12]

### 1.3.1.2. Two-dimensional structures

In the compound $[Mn(NPA)_2(Phen)_2]$, the most meaningful feature is the two-dimensional layer molecular structure formed by connecting the wave-like 1D chain in a cross-linker fashion arrangement through the π···π interaction. [13] As it can be observed from Figure 7, the 2D motif is owed to the fact that, firstly, two kinds of face-to-face π···π interactions (Cg(7) → Cg(7), 3.540 Å; Cg(5) → Cg(5), 3.796 Å between planes of adjacent 1,10-phenanthroline groups connect the asymmetric units into a 1D zig–zag chain. Then, the other offset face-to-face π···π interactions (Cg(6) → Cg(12)) between the pyridine rings of 1,10-phenanthroline and phenyl rings from NPA with calculated distance being 3.895 Å and calculated dihedral angle of 22.39° connect the 1D chains along the cross direction into an infinite two-dimensional layer structure.

In the asymmetric unit of the complex, the central $Mn^{II}$ ion is coordinated by two oxygen atoms from two NPA ligands in monodentate mode, four nitrogen atoms from two 1,10-phenanthroline in chelating model, thereby forming a distorted octahedron coordination geometry. All the ligands around the $Mn^{II}$ centres are arranged in a cis-configuration.

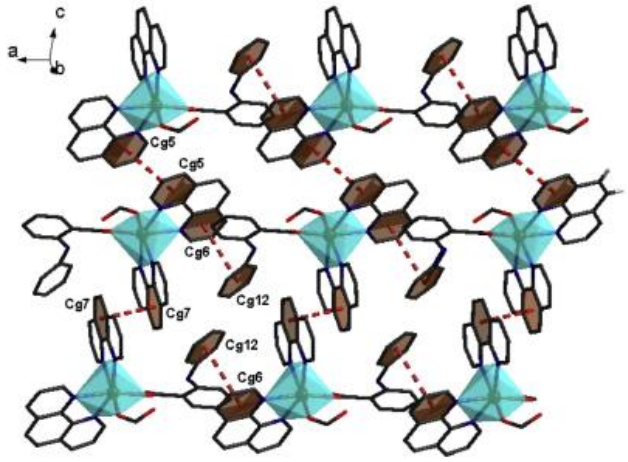


Figure 7: 2D structure of $[Mn(NPA)_2(Phen)_2]$. [13]

On the other hand, Tan *et al.* [13] also reported a 2D net structure of $[Cd_{1.5}(NPA)_3(2,2'\text{-bipy})]_n$ made from a trinuclear unit (Figure 8(a)). The complex exhibits a 1D ribbon chain structure which displays a peculiar trinuclear center-symmetrical unit with Cd···Cd inter-distance of 3.4872 Å, which is built from connecting $Cd^{II}$ ions via the O-atoms from different NPA ligands. In this complex, and according to the coordination mode, NPA provides two kinds of carboxylic groups: the carboxylic group adopting a bi-monodentate coordination modes connecting to different $Cd^{II}$ ions, and the one with a tridentate mode of coordination linking two of the three $Cd^{II}$ ions. The 2D net structure (Figure 8(b)) is built, firstly, from the basic trinuclear units interlinked to form a 1D chain through strong intermolecular π···π interactions between parallel phenyl rings as well as C–H···π interactions between adjacent phenyl rings. Secondly, a series of interactions between neighbouring C–H···π interactions connected to a centroid in chelating model like a pliers, then, another interaction along the cross direction linking the 1D ribbon chain generate a 2D layer structure (Figure 8(b)).

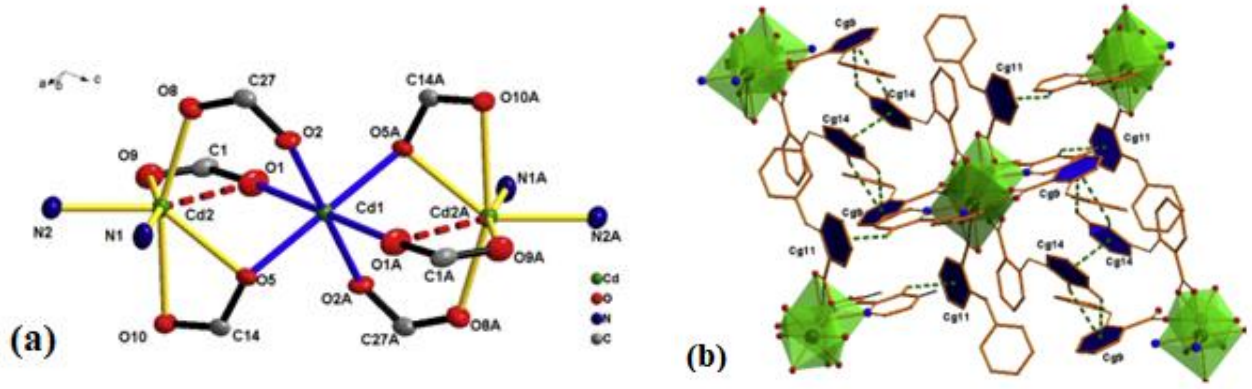


Figure 8: (a) Asymmetric trinuclear unit and (b) 2D net structure of $[Cd_{1.5}(NPA)_3(2,2'\text{-bipy})]_n$. [13]

### 1.3.1.3. Three-dimensional frameworks

The complex tetra-l-[2-(phenylamino)benzoato](O,O')-bis[(ethanol)copper(II)] [17] forms a three-dimensional, supramolecular network. Here, the crystal unit of the complex is a dinuclear species with $Cu^{II}$ ions separated by 2.591 Å. These ions are bridged by the carboxylate groups of four N-phenylanthranilate ligands. Each $Cu^{II}$ atom is in a slightly distorted square pyramidal environment, coordinated equatorially by four N-phenylanthranilate O-atoms with varied distances (1.954 – 1.981 Å) and apically to the O-atoms of ethanol with the same Cu-O distance of 2.131 Å. In this complex, all ligands around $Cu^{II}$ centres are disposed in trans configuration. The three-dimensional motif is made of a combination of intermolecular interactions between the synthons (Figure 9).

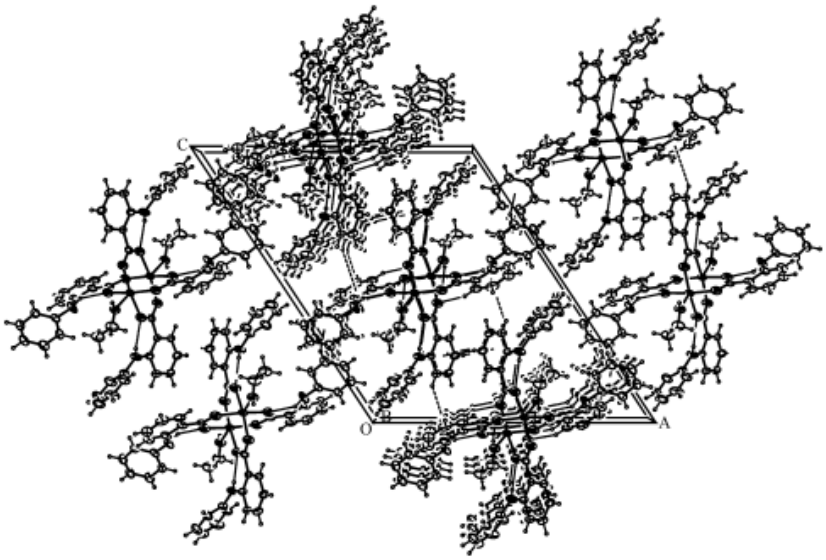

Figure 9: Three-dimensional $Cu^{2+}$ complex of NPA. [17]

Similarly, the mononuclear ternary complex $[Zn_4(NPA)_8(2,2'\text{-bipy})_4]$ in which the asymmetric unit exhibits four discrete similar molecular units (Figure 10(a)) with each containing one $Zn^{II}$ core, two NPA groups and one 2,2'-bipyridine molecule, assembles in a three-dimensional structure (Figure 10 (b)). [17] In each unit, each NPA ligand acts as bidentate ligand chelating the $Zn^{II}$ ions through the O,O-mode to form a four-membered ring. As well, two nitrogen atoms from 2,2'-bipyridine coordinate by chelating mode to form a six coordinate bonds to the central $Zn^{II}$ ion. The coordination geometry around this central atom is a distorted octahedral structure. The abundant non-covalent interaction present in the compound contributes in assembling the compound in three-dimensional structure.

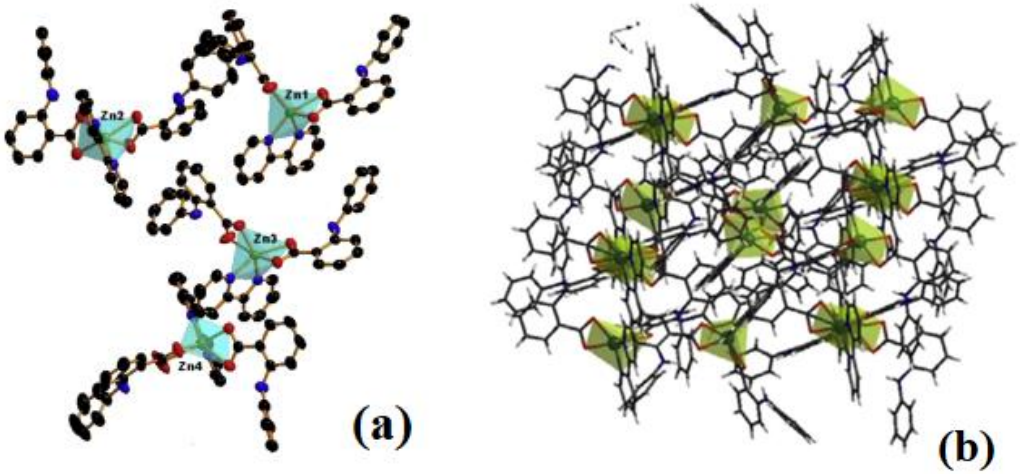


Figure 10: (a) asymmetric unit of four detached similar units and (b) stacking diagram of $[Zn(NPA)_2(2,2'\text{-bipy})]$. [17]

NPA therefore forms interesting 1D, 2D and 3D edifices. The 3D edifices are mostly built from 1D and 2D motifs from which intermolecular and intramolecular bonds play a key role. The non-covalent interactions associated with these compounds can lead to compounds with varied applications.

### 1.3.2. Metal complexes of 2-Aminopyridine

2-Apy can act both as a terminal and bridging ligand, depending on the environment in which it is found to form coordination polymers with 1D, 2D, and 3D structures. When these polymers form, there is always association with other ligands.

#### 1.3.2.1. One-dimensional coordination polymers

The compound $[(C_7H_5O_2)_2(C_5H_6N_2)_2Ni]$ (Figure 11) exhibits a 1D chain structure [40] in which $Ni^{2+}$ is six coordinated by four O atoms from benzoate ions and two pyridine N atoms from 2-Apy exhibiting a distorted octahedral configuration of the $Ni^{2+}$ atom. The angle between the atoms O1–Ni1–O2 is [62.02(4)°] and is different from the angle between O3–Ni1–O4 [61.79(4)°] Figure 11. This difference has been reported to be usual in comparison to similar $Ni^{2+}$ complex with carboxylates. [40] Moreover, Ni–O and Ni–N bond distances vary from different atoms. In this respect, Ni–O distances range from 2.0716(12) to 2.1750(12) Å, while the Ni1–N3 and Ni1–N1 bond lengths are respectively 2.0569(14) and 2.0647(15) Å. The 1D chain (Figure 12) is built along the [110] from the connection of N–H···O hydrogen bonds arising from all the O atoms and the primary uncoordinated N atoms.

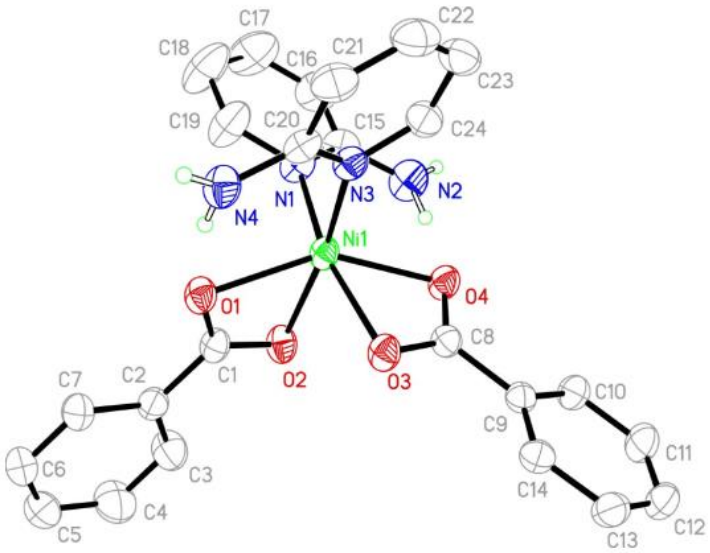


Figure 11: Structural unit of $[(C_7H_5O_2)_2(C_5H_6N_2)_2Ni]$. [40]

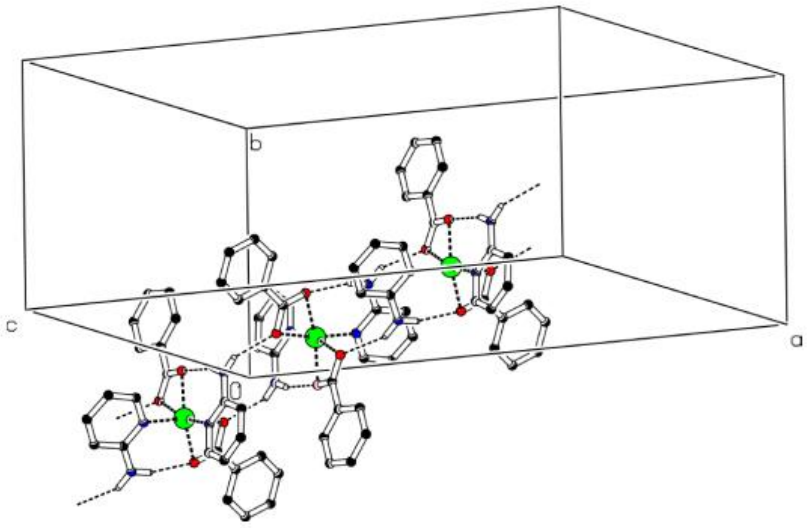


Figure 12: One-dimensional polymer of $[(C_7H_5O_2)_2(C_5H_6N_2)_2Ni]$. [40]

Another example of 1D complex is formed by $[Co(2\text{-ampy})_2(dca)_2]$ reported by Amah *et al.* [33] and shown in Figure 14 below. The 1D polymeric chain structure of the complex is made up of Co, which adopts a slightly distorted octahedral environment. Here, Co is covalently bonded to two pyridine N-atoms (Co-N1 2.193(3) Å) arranged axially and four nitrile N-atoms (Co1-N3 2.126(2) Å) and Co1-N5 2.128(2) Å from four dca anions in equatorial positions (Figure 14).

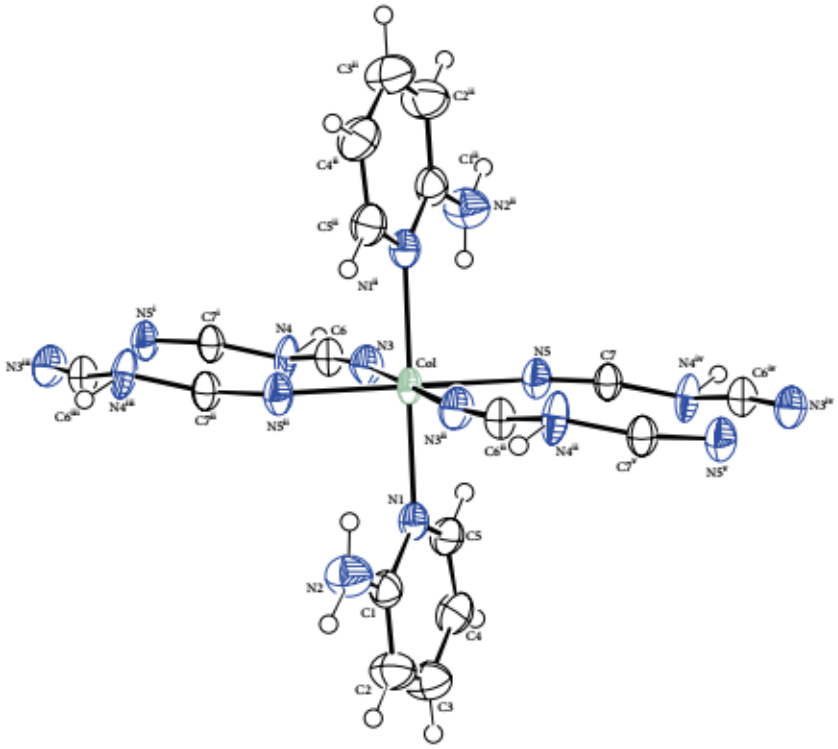

Figure 13: Structural unit of $[Co(2\text{-ampy})_2(dca)_2]$ complex. [33]

The 1D chain arises as a result of the linkage of one Co to two others through two 1,5-$\mu_2$-dca bridging ligands (Figure 13). In this complex, 2-Apy does not participate in the formation of the polymeric chain, but favours H-bonds formation between the exocyclic amino group and dca N atoms.

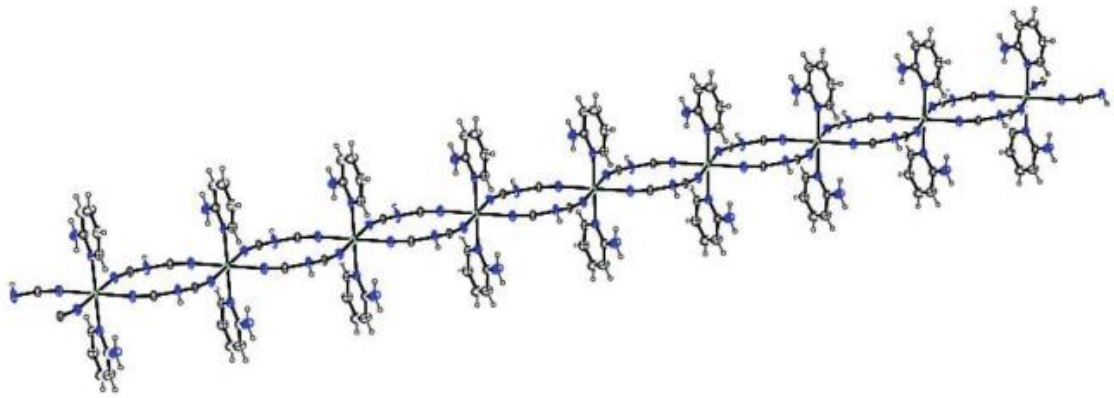

Figure 14: View of 1D polymeric chain of $[Co(2\text{-ampy})_2(dca)_2]$ complex. [33]

### 1.3.2.2.Two-dimensional structures

In the compound $[Co(O_2CCH_3)_2(2\text{-apy})_2]$, the most meaningful feature is the two-dimensional layer molecular structure [32] formed from hydrogen bonds assisted by $\pi\cdots\pi$ interactions between the aromatic rings as shown in Figure 15 below.

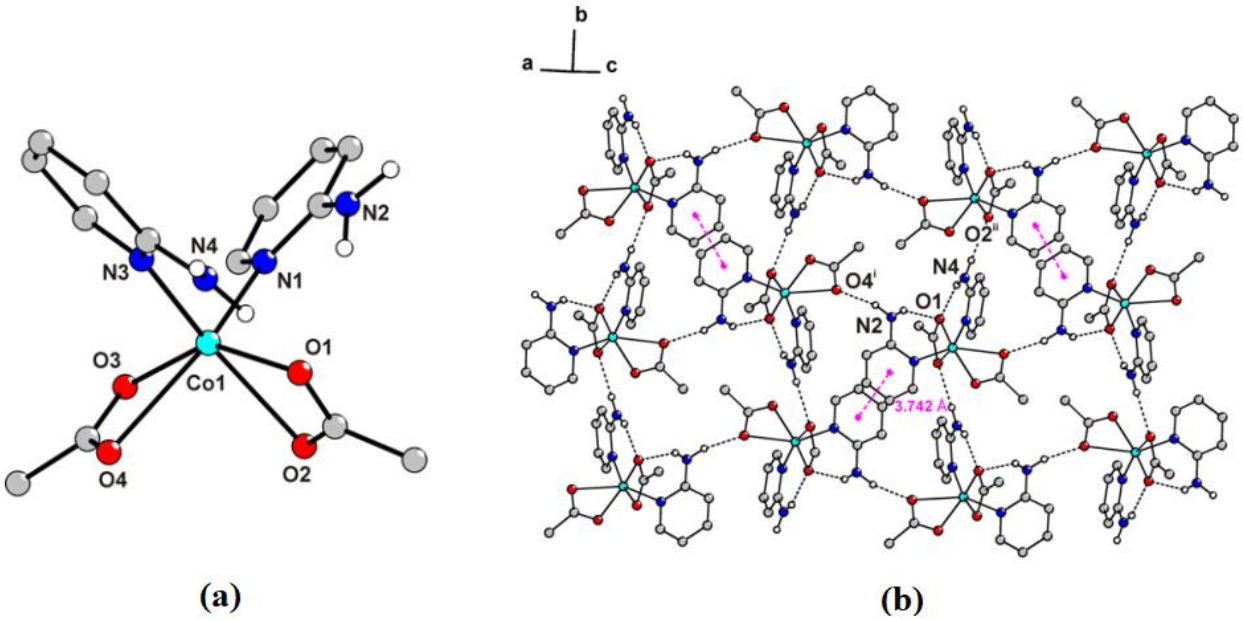


Figure 15: (a) Molecular structure of $[Co(O_2CCH_3)_2(2\text{-apy})_2]$ and (b) Paccking diagram of $[Co(O_2CCH_3)_2(2\text{-apy})_2]$. [32]

As it can be observed in Figure 15(b), the π···π interactions are in a face-to-face manner with a distance among ring centroids equal to 3.742 Å. Moreover, the complex displays both intramolecular and intermolecular H-bonding. It is the latter who takes part in the edification of the 2D structure, for instance, through N4 – H3N···O2 and N2–H1N···O4.

In the asymmetric unit of the complex (Figure 15(b)), the central $Co^{2+}$ ion is coordinated by two bidentate acetate ligands and by two pyridine N of 2-aminopyridine molecules. The geometry around $Co^{2+}$ is a distorted cis-octahedral, with Co–O bonds of Co1···O2 (2.378 Å) and Co1···O4 (2.502 Å) longer than the other two Co1···O1 (2.042 Å) and Co1···O3 (2.001 Å). This difference is attributed to the presence of intermolecular hydrogen bonds.

Another 2D molecule, $(C_5N_2H_7)_5H[P_2Mo_5O_{23}]$, has been reported by Gong *et al.* [21] (Figure 16). The complex consists of one polyoxometalate ($[P_2Mo_5O_{23}]^{6-}$) entity and five 2-Apy molecules. Phosphorous atom has terminal O atoms which can form H-bonds with the N atoms of 2-Apy. Furthermore, both the terminal and bridging O atoms of molybdenum atom can participate in the formation of H-bond with N and C atoms of 2-Apy. Almost all the aromatic rings of 2-Apy are perpendicular to the *bc* plane. Moreover, the orderly arrayed 2-Apy cations are just like ribbons to bridge different $[P_2Mo_5O_{23}]^{6-}$, which leave equal cavities for it to just fit-in (Figure 16(a)).

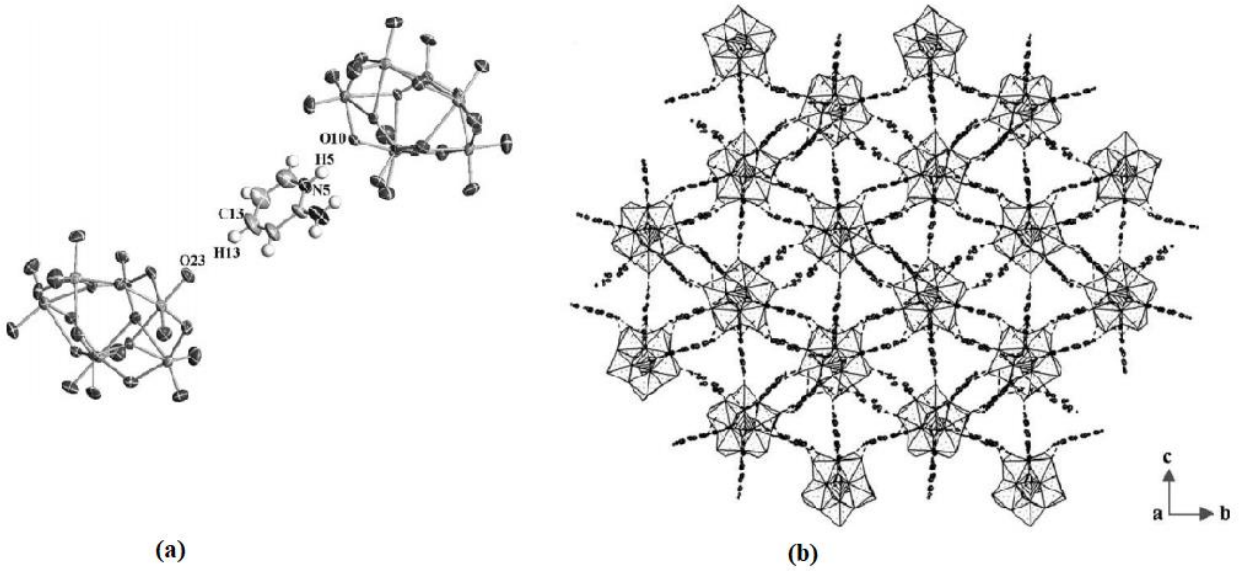


Figure 16: (a) View of 2-aminopyridine just fitting into the distance between two $[P_2Mo_5O_{23}]^{6-}$ and (b) Crystal packing of $(C_5N_2H_7)_5H[P_2Mo_5O_{23}]$. [21]

2-Apy therefore acts as a bridging ligand to form the 2D empty channel through the H-bond arising from C–H···O and N–H···O hydrogen bonds respectively from C(13) with O(23) and N(5) with O(10) (Figure 16(b)).

### 1.3.2.3. Three-dimensional frameworks

Complexes with 3D motif in which 2-aminopyridine is involved were also reported in the literature. For instance, the complex $\{(C_5H_7N_2)_6[Cu(C_3H_2O_4)_2(H_2O)_2][Cu(C_3H_2O_4)_2](PF_6)_2\}n$ reported by Mitra *et al.* [41] arise as a result of two crystallographically independent copper malonate units; $[Cu(1)(C_3H_2O_4)_2(H_2O)_2]$, and $[Cu(2)(C_3H_2O4)_2]$ whose copper atoms each lie on inversion centres. The ORTEP diagram of the complex is shown in Figure 17(a). It consists of six protonated 2-Apy moieties and two hexafluoridophosphate anion. The 3D motif (Figure 17(d)) arises due to the combinations of 1D and 2D frameworks.

The 1D polymeric chain forms because of the interlink between two different copper malonate units through carboxylate bridges [Cu(2)–O3] which is further strengthened by the O5–H4B···O8 hydrogen bond (Figure 17(b)). These 1D polymeric chains interlink between them to result to a 2D chain formation through the O5–H4A···O7 hydrogen bonds (Figure 17(c)).

2-Apy plays a key role in the formation of the 3D motif, in that the aminopyridinium cations ($C_5H_7N_2^+$) are attached above and below the hydrogen bonded 2D sheet constructed by the two different copper(II) malonate moieties. This arises because the diaquabis(malonato)copper(II) unit and the bis(malonato)copper(II) unit respectively recognize four and two $C_5H_7N_2^+$ cations through doubly coordinated carboxylate ends, leading to a $R_2^2(8)$ hydrogen bonding motifs. Hence, the aminopyridinium cations are locked side by side along the crystallographic *c*-axis by a series of hydrogen bonds formed between aminopyridinium cations and hexafluorophosphate anions to generate the 3D assembly.

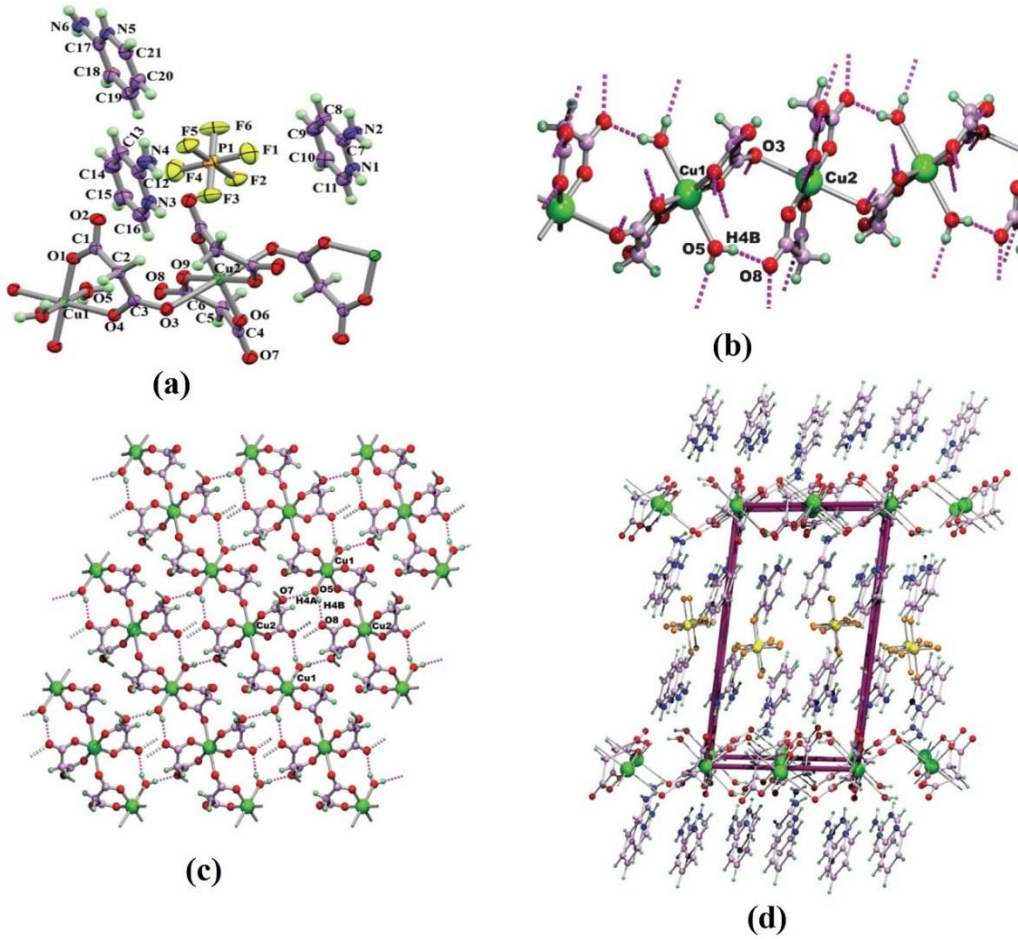


Figure 17: (a) ORTEP diagram of the 2-Apy complex, (b) Hydrogen bonded 1D polymeric chain of copper malonate units, (c) Formation of 2D sheet, and (d) 3D packing arrangement of the complex [41]

### 1.4.Non-covalent interactions in N-Phenylanthranilic acid and 2-Aminopyridine metal complexes

It is known that non-covalent interactions (NCI) play undoubted role in chemistry, physics and in bio disciplines. For the latter, they are responsible for the spatial arrangement of proteins and their properties, as well, they are responsible for their secondary coordination sphere. [42,43] In chemistry, while covalent bonds determine the spatial disposition of atoms inside a molecule, NCIs can control or organize the conformation, aggregation, tertiary and quaternary structures of the molecule, its stabilization and confer peculiar properties. [44] Thus, these interactions are of great contribution for both the chemical and biochemical systems.

Coordination compounds containing NPA and 2-Apy are structurally favoured to form NCIs such as H-bonding, pi-pi bonds, metal-pi interaction, etc. Amongst these NCI, emphasis will be laid on the most common ones: hydrogen and pi-pi bonding.

### 1.4.1. Hydrogen bonding

The concept of hydrogen bonding was first introduced almost 100 years ago. [45] According to Arunan *et al.* in their IUPAC Technical Report, Latimer and Rodebush were the first to introduce the term "Hydrogen bond" in 1920. [46] They further indicated that other scientists used different words to describe the same phenomenon. For instance, Werner described it as *Nebenvalenz (*German for secondary or weak valence) and Pfieffer described it as *Innere Komplexsalzbildung* ("internal complex salt-bridge" for describing the intramolecular hydrogen bond in 1-hydroxyanthraquinone). The concept of hydrogen bonding is not universally unanimous as there is no universal definition for hydrogen bonding. Arunan *et al.* defined hydrogen bonding as "*an attractive interaction between a hydrogen atom from a molecule or a molecular fragment X–H in which X is more electronegative than H, and an atom or a group of atoms in the same or a different molecule, in which there is evidence of bond formation".* [47] Classically, for both the donor and acceptor species, it was considered at first that only the most electronegative atoms N, O and F could be involved in hydrogen bonding. Aranun *et al.* in their paper quoted Rao and Jakkarto who have realised that X may be any element having electronegativity greater than that of H (i.e. F, N, O, C, P, S, Cl, Se, Br, and I) and Y could be any of these elements and π-electrons. The authors further cited Crabtree *et al.* to have extended the list of these species to another H atom itself as in metal hydride. [46]

It is therefore obvious that hydrogen bond can form a wide range of bonding with respect to the strength. The strengths of the bonds were being defined by Jeffrey to either be normal or moderate hydrogen bonds which are those that resemble bonds between water molecules or carbohydrates (associated energies in the range of4–15 kcal·mol$^{-1}$) or those above and below this range which could be called, respectively, strong and weak, with not clear cut off limits between them. [47] Therefore, the peculiarity of H-bonding is its ability to a have a continuum of strength. As such, some of the hydrogen bonds appear to be so strong that they resemble covalent bonds, and some others are so weak that they can hardly be distinguished from van der Waals interactions. [47]

Apart from the classical hydrogen bonding which appears between the classical examples of water molecules, neo-hydrogen bonding types have recently appeared in the literature. They include resonance-assisted hydrogen bonding, polarization-assisted hydrogen bonding, and charge-assisted hydrogen bonding. [45,47]

Resonance-assisted hydrogen bonding (RAHB) is an intermolecular H-bonding strengthened by a conjugated π-system, usually in 6-, 8- or 10-membered rings.

The polarized-assisted hydrogen bonding is a H-bonding strengthened by σ-bond cooperativity.

In the charge-assisted hydrogen bonding (CAHB), the strength is enhanced by ionic charges which provide less directional electrostatic interactions between complex molecules, unique coordination geometries and can regulate the properties of those materials. In most cases, due to the additional electrostatic interactions involved, CAHB is stronger in comparison to regular hydrogen bonds.

A variety of H-bonding has been reported in the literature for NPA-based metal complexes. For example, the complex $[Cu_2(C_6H_5NHC_6H_4COO)_4(CH_3CH_2OH)_2]$ displays three types of H-bonding. [17] They include the intramolecular hydrogen bonding N–H···H, the C–H···π, and the O–H···H hydrogen bonding. The last two types of H-bonding contribute respectively to the formation of three-dimensional supramolecular structure along the *a*- and *c*-axis, and the formation of infinite polymeric chain along the *b*-axis (Figure 8).

In 2-Apy containing complexes, it has been found that 2-Apy sometimes acts as a bridging ligand through H-bonding. For instance, in the complex $(C_5N_2H_7)_6(H_2O)_2[V_{10}O_{28}]$ reported by Gong *et al.*, [21] the nitrogen atom of one 2-aminopyridine can form H-bonds with two oxygen atoms from two $[V_{10}O_{28}]^{6-}$ at the same time. On the other side, the carbon atoms of 2-aminopyridine also can form H-bonds with the oxygen atom of $[V_{10}O_{28}]^{6-}$.

### 1.4.2. π – interactions

This is one of the most common NCIs in complexes containing NPA due to its benzene rings. It may occur within the complex as intramolecular non-covalent interaction, between adjacent molecules or atoms as intermolecular interaction, or occurring both as intermolecular and intramolecular interaction within the same molecule. [44]

Hunter and Sanders [48] proposed a model which considers the σ–framework and the π–system separately and assumed that the overall π–π interactions are the result of π–σ attractions that overcome the π–π repulsions. The electrostatics of the model can be visualized by describing the aromatic ring as two regions of negatively charged π-electron density surrounded by a positively charged σ-framework. Generally, three stacking patterns for phenyl–phenyl π–π stacking interactions can be considered: face-to-face (sandwich), edge-to-face (T-shaped), and offset face-to-face (parallel-displaced) (*see* scheme I, appendix I).

C–H···π interactions has been reported in the complex $Zn(Hdmpz)_2(NPA)_2$ (with Hdmpz = 3,5-dimethylpyrazole) and is responsible for the 1D chain structure. [12] in the complex $[Mn(NPA)_2(Phen)_2]$, the most prominent face-to-face π – π interactions arise between two adjacent pyridine rings of the

ligands. [49] Some complexes can exhibit both C–H···π and π – π interactions. It is the case with $[Cd_{1.5}(NPA)_3(2,2'\text{-bipy})]_n$ and are responsible respectively for its 1D and 2D motifs. [49]

Furthermore, the literature has cited some molecules with intermolecular π···π stacking features which confer to them catalytic, magnetic, and photoluminescent properties. [47]

Mitra *et al.* [41] in their article has identified the classical π···π stacking, as well as the π ··· anion stacking in the molecule $\{(C_5H_7N_2)_6[Cu(C_3H_2O_4)_2(H_2O)_2][Cu(C_3H_2O_4)_2](PF_6)_2\}n$. They however came out with a tentative definition of a novel class of π - interaction in the same molecule ; they named it as salt-bridge···π interaction. Here, the aromatic ring must be in the middle of both cation···π interaction and anion···π interaction.

Many other complexes of 2-Apy with π···π stacking have also been reported in the literature. [35,50]

### 1.5. Applications of the ligands

Both NPA and 2-Apy have been shown to possess useful biological and non-biological properties either in their uncombined form, or when complexed with metallic ions. Therefore, some relevant applications have been found in the biological domain.

#### 1.5.1. Applications of N-phenylanthranilic acid

NPAs are among the Non-Steroidal Anti-Inflammatory Drugs (NSAID) class. This class of compounds have shown promising prophylactic treatment against a variety of cancer, generally through two mechanisms: restoration of normal apoptosis and reduction of cancer cell proliferation. [51,52] A study conducted by Endo *et al.* showed that N-phenylanthranilic acid derivatives (flufenamic acid, mefenamic acid and meclofenamic acid) selectively inhibited a human aldose reductase-like protein, AKR1B10, which is a tumor marker of several types of cancer. [53]

NPA derivatives have shown potent antimicrobial activities against gram positive, gram negative and fungi. For example, binary and ternary mixed complexes of NPA and 1,10-phenanthroline with Sm(III), Eu(III) and Gd(III) ions were synthesised and tested against two gram-negative (*Escherichia coli* and *Pseudomonas aeruginosa*) and one gram-positive (*Staphylococcus aureus*) bacterial strains, with marked activities. [54]

Moreover, NPA is used as a prominent biomarker in the study of some pathologies in animals. For instance, it was used in assessing renal function through the development of Renal Papillary Necrosis. [55,56] In another study, it was used as a urinary biomarker where it induced nephrotoxic injury and served as renal injury indicator. [57]

Few non-biological applications of NPA have been found in the literature. For instance, rhodium complex of NPA has been shown to be the one of the most active hydrogenation catalysts for aromatic hydrocarbons. [58]

In waste water treatment plants, NPA has been used as a complexing agent for the highly sensitive and selective determination of uranium(VI) by adsorptive cathodic stripping voltammetry. [59] Acceptable recoveries of 96–105% for waste water and 98% for tap water samples shows that the method can be used for the determination of uranium(VI) in various water samples. Moreover, NPA is used as indicator in titrations for Fe(II), Ce(IV) and vanadate. [60]

### 1.5.2. Applications of 2-aminopyridine

2-Apy offers a wide range of therapeutic applications. A number of drugs containing a residue of 2-Apy are already offered on the market, such as Piroxicam, Tenoxicam, Sulfasalazine with anti-inflammatory properties, Delavirdine, as anti-HIV drug, Sulfapyridine, as antibacterial and Tripelenamine as antihistaminic drug. [27]

## 1.6. Review of the co-ligands

The co-ligands used in this work are short bridging inorganic pseudohalides. Pseudohalides are polyatomic analogue of halogens. [61] They have a great ability of connecting transition metals in solid state. These compounds are generally rigid with somewhat defined directionality and bear many potential binding modes. [39] This class of compounds can therefore form a range of structural diversity in coordination compounds containing them. The pseudohalides of interest include dicyanamide and thiocyanate amongst others.

### 1.6.1. Dicyanamide

Dicyanamide (dca) is a polynitrile, short ligand which is very effective in forming coordination polymers with transition metals as they show a large range of coordination binding mode. [39] Dca anion can act as either a terminal ligand or bridging ligand but has a variety of coordination mode through which it can bind in the nitrile nitrogen atom, in the amide nitrogen atom (Figure 18), or in both. [62] In this way, it can act as either a 2-connecting ligand (through μ-1,5 or μ-1,3), a 3-connecting ligand(through μ-1,3,5), or as a more complicated 4-connecting ligand (through μ-1,1,3,5). [39]

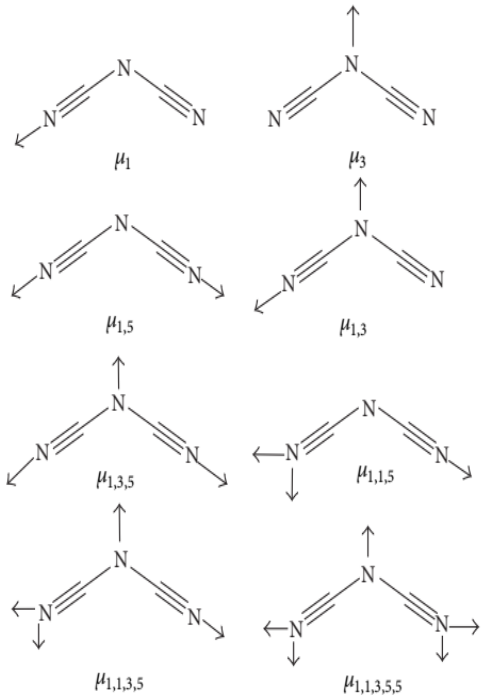


Figure 18: Coordination modes of dca.

This pseudohalide therefore can form interesting extended architecture owing to its extreme coordination versatility. Literature has reported numerous dca ligand in magnetic coordination polymers. For instance, the magnetic properties of dca, used as co-ligand, was investigated in many complexes and have shown to possess weak antiferromagnetic interaction through the ligand. [63,64] On the other hand, it was proven that in the complexes **[**$Fe_2(dca)_4(bpym)$**].**$H_2O$ and $[Fe_2(dca)_4(bpym)(H_2O)_2]$, the magnetic exchange in dca is negligible as compared to the bpym ligand (where bpym =2,2-bipyrimidine). [64] In the first complex, all four dca anions acts as bridging ligands in the axial and equatorial positions. In the second complex, only two of the four dca ligands adopt the bridging co-ordination mode, the other two acting as unidentate ligands.

### 1.6.2. Thiocyanate

With the chemical formula SCN, the thiocyanate ligand is potentially ambidentate with the possibility of forming a coordinate bond either through the N- or through S-atom. Different coordination modes of thiocyanate have been referenced in the literature (Figure 19). [65]

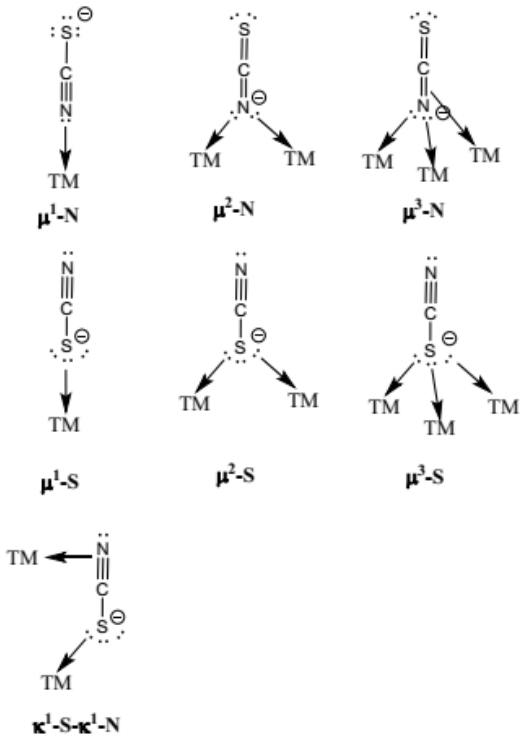


Figure 19: Coordination modes of $SCN^-$.

The coordination mode formed mainly depends on the nature of the metal. However, this preference may be modified by the presence of other ligands or whether the complex is in solid state or in solution. [66] For instance, the binuclear complex $[Cu_2L_1(SCN)_3(ClO_4)]$ containing a tetradentate-Schiff base macrocycle ($C_{26}H_{34}N_6O_4$= $L_1$) with SCN has been synthesised. The SCN has been found to form both the Cu-NCS-Cu bridging mode through its N and S atoms, and the monocoordinated Cu-NCS mode through the N atom. [67] Chunga *et al.* have synthesised a mononuclear complex [Cu(Hdpa)(Acac)(NCS)] from 2,2-dipyridylamine (abbreviated as Hdpa) ligand with SCN. [68] In this complex, the SCN only binds through its N atom on the central metal. Another example of the versatility of SCN binding mode is its double end-to-end coordination mode in the binuclear complex $[Cu_2(L)_2(\mu_{1,3}\text{-}NCS)_2]\cdot DMF\cdot H_2O$ through the $Cu^{2+}$ion which is built from the tridentate $N_2O$ Schiff base L (L = [1((2-(ethylamino)ethylimino)methyl)naphthalen-2-ol]). [69]

In mammals, SCN is ubiquitously found in extracellular fluids such as saliva, tears, milk, etc. and in a wide range of concentrations varying from 0.1 μM to > 2 mM depending on physiologic and environmental contexts and enters the human body from the diet (such as cruciferous vegetables) or is synthesized from cyanide by sulphur transferase enzymes including mitochondrial rhodanese and cytosolic mercapto pyruvate sulphur transferase. [70,71] It has been found to possess beneficial bivalent biological effects with respect to human health. Studies conducted by Chandler and Day have underscored its defence function as well as its antioxidant property. [70,71] For the former study, it has

been shown that in an inflammatory milieu, SCN inhibits the metabolism of pathogens, thereby being rapidly oxidised to HOSCN (Hypothiocyanous acid) which in turn inhibits the metabolism of bacteria, viruses and fungi by targeting strongly acidic thiols. This mechanism is entirely a different mode of action as compared to approved antibiotics. For the latter, SCN's antioxidant capacity comes from its ability to scavenge cytotoxic oxidizing agents, such as HOCl (Hypochlorous acid) and RNHCl, spares host tissue while generating more of the host defence factor HOSCN in turn.

Coordination complexes containing SCN have been synthesised and investigated for their antibacterial [72,73] and antifungal [73] showing significant biological activity. Human *et al.* have explored the induction of cell death with various phosphine silver(I) thiocyanate complexes. [74] They concluded that these complexes significantly induced malignant cell death with antiproliferative activities higher than that of cisplatin, considered as the reference anticancer agent, towards the SNO-oesophageal cancer cells.

### 1.7. Survey of transition metals used in this work

The first-row transition metals are reputed to be non-toxic and many of them constitute a group of metals called essential elements, necessary for the proper functioning of organisms. Therefore, this survey is focused on their biological roles, their involvement as antimicrobial, antiviral and anticancer agents, amongst others. These metals include Manganese, Zinc, and Cadmium.

#### 1.7.1. Manganese

Manganese can exist in a wide variety of oxidation states, ranging from -3 to +7 [75]. However, only Mn(II), Mn(III), and Mn(IV) need to be considered in the aqueous environment of a cell. [75,76] Mn is a micronutrient required for normal immunity system, regulation of blood sugar and cellular energy, reproduction, digestion, and for the defence mechanisms against free radicals. [77] Free radicals can be eliminated either through enzymatic detoxification or non-enzymatic detoxification. [78] Manganese is required for the proper function of several metalloenzymes such as arginase, glutamine synthetase, phosphoenolpyruvate decarboxylase, and manganese superoxide dismutase. [76,77]

In humans, tissues maintain a stable level of Mn via a tight homeostatic control of both absorption and excretion. Hence, excess uptake or deficiency is related to well-known diseases, disorders or syndromes that occur in organisms. [75]

Excessive uptake of Mn tends to accumulate in the liver, pancreas, bone, kidney and brain. Among these tissues, the brain is the privileged target of Mn toxicity although it is not the tissue with the highest Mn concentration. [79] Hepatic cirrhosis, polycythemia, hypermanganesemia, dystonia and Parkinsonism-like symptoms have been reported in patients with manganese poisoning. [79]

Molecular mechanisms of Mn toxicity include oxidative stress, mitochondrial dysfunction, protein misfolding, endoplasmic reticulum (ER) stress, autophagy dysregulation, apoptosis, and disruption of other metal homeostasis. [79]

Manganese deficiency in humans results either from failure to absorb the metal or from failure in adequate dietary intake of the metal. For the former case, failure to absorb Mn may arise because both manganese and iron compete for sites of absorption in the gut. On the other hand, excessive intake of magnesium may interfere with manganese absorption. [80]

Diseases such as amylotrophic lateral sclerosis, acromegaly transient dermatitis, hypercholesterolaemia, development of osteoporosis in women, and epilepsy are believed to be associated with this deficiency. [77,80] The associated symptoms include ataxia, fainting, hearing loss, weakness in tendons and ligaments and, possibly, type 2 diabetes mellitus. The diabetes arises because the low levels of manganese reduce insulin production and impair glucose metabolism.

Several manganese complexes with pharmacological activities have been referred in the literature. For instance, Mn(II) based complexes have been synthesised and screened for their anticancer properties. One such molecule includes Mn(II) arginine dithiocarbamate complex revealed a moderate cytotoxicity against the breast cancer cell line MCF-7. [81] Another example is manganese complex with mefenamic acid, a derivative of NPA, in the investigation of its anticancer property. The complex revealed activity in human breast cancer cells, acting as an estrogen receptor alpha antagonist, and as a down-regulator for DEK proto-oncogene, a novel estrogen receptor α target gene whose expression promotes estrogen-induced proliferation. [82] Zhang and co-workers synthesized three transition metal complexes, one of which was a Mn(II). [83] This complex revealed antiproliferative activity, showing strong inhibition ratio against human hepatoma cells and moderate inhibition ratio against human gastric cancer cells *in vitro*.

Manganese complexes derived from 2-acetylpyridine-N(4)-R-thiosemicarbazones have showed potential anti-Mycobacterium tuberculosis activity. These compounds have shown low cytotoxicity against eukaryotic cells and selectivity index values comparable or even better than some commercial drugs in use for tuberculosis treatment. [84] Another complex containing Manganese(II) with 1,10-phenanthroline and dicarboxylate ligands also inhibited the viability of *M. tuberculosis* strains with high selectivity and low toxicity, therefore a promising new drug for the treatment of *Mycobacterium tuberculosis.* [85]

### 1.7.2. Zinc

Presents in all organs, tissues, fluids in the organism, zinc is a prominent metal in biological systems where it carries its activities as a divalent cation primarily when bound to enzymes or protein. Moreover, it is found to be the only metal which appears in all enzyme classes. [86,87] Its main function is the total control of proper conformational state of many constituents of the organism and components of biochemical processes such as immune function, wound healing, protein synthesis, DNA synthesis and cell division. [86,88,89] This is owed by two of its main properties; its virtually nontoxic nature on one hand, and on the other, its physical and chemical properties. [87]

The virtually nontoxic nature of zinc arises from the fact that, the haemostatic mechanism that regulates its absorption, distribution, and excretion is so effective that, under most conditions, they protect the organism from deficiency of the metal and almost always from its excess.

The physical and chemical features characterising zinc include its stable association with macromolecules and its coordination flexibility which favours its high adaptability to meeting the needs of proteins and enzymes that carry out diverse biological functions. For zinc cation is redox-inert and therefore renders it stable in biological milieu. It is also found to be amphoteric at pH values nearer to neutrality as it exists both as aquo- and hydroxo-metal complex. It can also assume multiple coordination geometries varying from two to eight with respect to the ligands to which it is bound, allowing them to alter its intrinsic reactivity accordingly.

These features provide zinc with important biological roles in organism. For example, the antioxidant and anti-inflammatory properties, the development of Alzheimer's disease and the proper functioning of the immune system are closely linked to the concentration of zinc ions in the organism.

Zinc has potent antioxidant activity, primarily as a component of superoxide dismutase which catalyses the dismutation of superoxide anion radicals to hydrogen peroxide and thus preventing the generation of other toxic free radicals and their derivatives. [89,90] On the other hand, the normal level of zinc ensures the anti-inflammatory role, especially the maintaining of homeostasis of epithelial tissues which are the front edge to combat infections. [88] Therefore, changes in metabolism caused by zinc may render the epithelial barrier vulnerable thereby opening the way to pulmonary diseases, asthma and other inflammatory processes in respiratory routes.

With the highest concentration of zinc in the brain tissue as compared to other tissues, the disruption of zinc binding in the brain is believed to promote Alzheimer's disease. [88] This may be associated with the accumulation of incorrectly folded proteins in brain tissues.

It is known that the immune system is particularly sensitive to zinc level in the body because it is a stimulator of many elements involved in the immune system, responsible for the search and destruction of pathogens and cancer cells without damaging of healthy cells. [91] This is true as zinc deficiency results to increased susceptibility to infection and weakening of the body's defence. [92] For instance, the cancer of the lungs, breast, head, and neck observed in many patients have been associated with decreased level of zinc in the blood despite its multifunction role in defending against the initiation and promotion of tumours. Therefore, if zinc depletion precedes the transformation of cells from normal to cancerous type, [91] its excess is not without consequence as it can be dangerous due to its immunosuppressive effect, which tends to inhibit important immune system elements, thereby rendering the system vulnerable to pathogens. [90]

Apart from these prominent and varied inherent biological roles, zinc-based complexes have been widely developed because of their interesting biological activities against pathogens as well as tumour cells.

If the role of zinc in organism is clearly defined, this has not prevented the development of pathogens and other drug resistant agents. The development of metal-based drugs as alternative with specific properties against microorganism or cancer have been noticed. Thus, the last decades have been marked with the development of novel metal complexes possessing antimicrobial as well as anticancer properties, among which zinc occupies a prime place. [77]

Complexes containing zinc and NPA have been synthesized and reported in the literature. For instance, ternary zinc complex $[Zn(NPA)_2(2,2'\text{-bipy})]$ (with 2,2'-bipy = 2,2'-bipyridine) has been synthesized in which zinc adopts a distorted octahedral structure (Figure 10). [49] Another ternary zinc complex $[Zn(Hdmpz)_2(NPA)_2]$ (with Hdmpz = 3,5-dimethylpyrazole) has been synthesized and zinc is tetrahedrally coordinated by two oxygen atoms from two monodentate NPA ligands and by two nitrogen atoms, belonging to two monodentate pyrazole ligands. [93]

### 1.7.3. Cadmium

The chemistry of Cd is similar to that of Zn and shows versatile coordination abilities, giving $Cd^{2+}$ structures ranging from simple complexes to 1D, 2D, and 3D polymeric architectures. [94] However, contrary to Zn, Cd can exist in +1 and +2 oxidation states even though its +2 states is the more common. [94]

Cadmium is not among the essential metals needed for the vital biochemical and physiological functions, and all its compounds are considered to be highly toxic to humans. [95] Human are exposed

to cadmium by inhalation and ingestion through contaminated food and water. [96,97] Therefore, Cd acts as a mitogen, favours cancer in a number of tissues, stimulates cell proliferation, inhibit DNA repair and inhibit apoptosis. [97] The liver and kidneys are tissues with extreme sensitivity to cadmium's toxic effects. [94,97] This may be attributed to the ability of these tissues to synthesize metallothioneins (MT), which are Cd-inducible proteins that protect the cell by tightly binding the toxic cadmium ions.

Despite the toxic of Cd compounds to humans, a number of coordination complexes with interesting biological properties have been synthesised. For instance, Saghatforoush *et al.* synthesised a Cd(II) complex with a tridentate ligand, 4'-Chloro-2,2':6',2''-Terpyridine, which showed good activity against all tested bacteria. [98] Other examples of Cd(II) complexes with good biological activities are cited in the literature. [99,100] The higher activity of these complexes has been suggested to be on the basis of chelation theory. Furthermore, a cadmium dicyanoargentate(I)-based complex with a tetradentate ligand [N, N-bis (2-hydroxyethyl)-ethylenediamine; *N-bishydeten*] has exhibited significant antibacterial and anticancer effects respectively towards bacterial strains and three tumor cells. [101]

## 1.8. The biology of selected pathogens

The present study focuses on the biological evaluation of some pathogens which have the merits to be evaluated. The emphasis is laid on these because of the serious public health they cause worldwide. *Staphylococcus aureus, Salmonella typhi, Candida albicans,* cancer, and Coronavirus 19 are pathogens of interest.

### 1.8.1. *Staphylococcus aureus*

*Staphylococcus aureus* is a gram-positive cocci, 0.5 – 1.5 μm in diameter, that colonises the nasal mucosa and skin of healthy individuals. [102,103] It is both commensal and a human pathogen, with approximately 30% of human population colonised by it. [104] In the pathogenic form, it is the leading cause of bacteraemia and can cause infective endocarditis as well as osteoarticular, skin and soft tissue, pleuropulmonary, and device-related infections. [103–105] It accounts for more than 10% of nosocomial infections and about 20% of food-borne disease outbreaks. [103]

The high resistance rate due to methicillin-resistant *S. aureus* (MRSA) make it difficult to be treated and results in higher morbidity and mortality than methicillin-susceptible *S. aureus* (MSSA). According to the U.S. Centers for Disease Control and Prevention (CDC) report, in 2012 the number of severe MRSA infections was 75,000 of which 9,700 resulted in death, that is about 13% death rate. [105]

A study conducted by Schaumburg *et al.* [106] has shown that there is a wide diversity among *S. aureus* lineages colonizing and infecting the African population, in part with different genetic backgrounds, with one MRSA clone seeming to be a typical African clone. Furthermore, the authors found that ST5-MSSA and ST15-MSSA (with ST = sequence type) are highly prevalent in West Africa, including Cameroon. In an attempt to determine the prevalence and antibiotic susceptibility patterns of MRSA in eight large hospitals (>500 beds) in Africa and Malta, Kesah *et al.* [107] estimated the rate of MRSA in Cameroon at 21 – 30%, with more than 60% of the isolates exhibiting resistance to at least three antibiotics.

It has been shown that virulence of *S. aureus* is an inherent characteristic of each of its strain. On the other hand, the degree of drug resistance is dependent on medical activities such as; prescribing habits, hospitalization periods, and hospital environment. In addition, drug-resistant strains appear mainly due to changes in the bacteria environment. [105]

The analysis of bacterial pathogenesis identifies several important mechanisms: adherence to host sites, penetration of anatomic barriers, disruption or avoidance of the host humoral defences, avoidance or inactivation of phagocytic cells, and production of other toxins. [103]

According to the literature, *S. aureus* has a unique ability to rapidly acquire antibiotic resistance to virtually any antimicrobial molecules that has been developed. [108] This is done through horizontal gene transfer, as well as through chromosomal mutation.

The mechanism of drug resistance is attributed to the formation of bacterial biofilms. Here, the virulence factor of *S. aureus* called coagulase, binds to host prothrombin and forms active staphylothrombin complexes, which converts soluble monomeric fibrinogen into selfpolymerizing insoluble fibrin thereby activating a coagulation cascade. [102] By so doing, *S. aureus* is relatively protected from antimicrobial agents and the host immune response. [103,104]

Penicillin was introduced in the early 1940s to treat *S. aureus* infections, which effectively decreased mortality and morbidity. However, in the late 1940s, resistance to this compound was witnessed. [109] Nowadays, modern treatment of *S. aureus* is based on whether which of the MRSA or MSSA has to be treated. Therefore, methicillin-sensitive β-lactamase-producing strains can be treated with oxacillin, cloxacillin, and nafcillin; however, for the treatment of methicillin-resistant strains, vancomycin, teicoplanin and mupirocin are employed. [110]

Many coordination compounds have been synthesised and tested for their activities against *S. aureus* strains with interesting results. Some of these include Gold(III) dithiocarbamate, [111] Cu(II) complex

containing 2-Apy and 2,6-pyridinedicarboxylic acid ligands, [50] binary and ternary compounds of Sm(III), Eu(III), and Gd(III) with NPA and 1,10-phenanthroline. [54]

### 1.8.2. *Salmonella typhi*

The genus *Salmonella* contains only two species; *Salmonella bongori* and *Salmonella enterica* according to the contemporary classification. [112] *Salmonella enterica* serovar typhi are responsible for enteric fever in some parts of developing world, with estimated cause of approximately 22 million cases of disease and 200,000 deaths each year, primarily in regions where sanitation is poor and clean water is inaccessible. [112] In sub-Saharan Africa, nontyphoidal salmonellosis (NTS) cases frequently complicated by bacteremia (comprising as much as 50 % of cases of bacteremia), now seem to be more numerous than cases of enteric fever. [112] This incidence has arisen with predisposing infections to HIV and *Plasmodium falciparum.*

In a study conducted in Bui division, North-West Region in Cameroon, 30,1 % of recruited patient were diagnosed with *S. typhi*, of which 92 % had a higher level of education. [113] The prevalence of *Salmonella typhi* (94.2 %) was higher than Salmonella paratyphi (5.8 %).

In cases where there was a dramatic decline in the overall incidence of typhoid fever in many countries, economic growth and improved sanitation conditions have been identified as to be the main causative factors responsible for the decline of such incidence. [112]

Medicinal plants have been described in the literature as a credible alternative and as having potent antibacterial activity against *S. Typhi.* Among these, *Cymbogogon citratus*, *Carica papaya* and *Zea mays* silk have been reported with the lowest MIC of 0.02–0.06 μg/ml against *S.* Typhi. [114] They offer the advantage of being more affordable than the conventional drug.

Conventionally, the following classes of antibiotics are mainly used for *S. typhi* treatment: β-lactams, chloramphenicol, sulfonamides, quinolones, cephalosporins, and macrolides. [114] But still, drug resistance is reported in the literature against these antibiotic agents.

Therefore, despite multiple mechanisms put into place to tackle this pathology, resistance due to *S. typhi* is more worrying than ever. As such, report from antimicrobial resistance due to *S. typhi* is that it varies much from one region of the world to the other. For instance, countries in Asia and Africa have witnessed antimicrobial resistance (AMR) among *Salmonella Typhi* isolates. [115] Moreover, multidrug resistant (MDR) *Salmonella Typhi* remains prevalent in Asia, with resistance developing to an increasing number of antimicrobial classes such that XDR *Salmonella Typhi* becoming a major threat. MDR *Salmonella Typhi* is a growing problem in Africa.

Coordination compounds which have shown relatively good properties against *S. typhi* have been reported in the literature. [33,116]

### 1.8.3. *Candida albicans*

*Candida* species are part of the normal flora of the genital tract. Reports indicate that the yeasts is found in about 20 – 30% of healthy asymptomatic non-pregnant women globally. [117] Recent global estimates have suggested that roughly 700,000 - 750,000 cases of invasive candidiasis occur annually [118,119]. Mortality attributed to Candidemia is around 15–35 % for adults and 10–15 % for neonates. [120]

Epidemiological surveys worldwide have indicated that distribution of *Candida* species responsible for vulvovaginal candidiasis, which is the second most common vaginal infection in reproductive age women, varies widely among countries, regions and also the study population, and women with vaginal candidiasis are more susceptible to HIV. [117,118] Another study suggests that *Candida albicans* virulence may increase in HIV-infected subject. [121] A study conducted in Yaoundé, by Kechia *et al.* [122] showed that about 36 % of diagnosed pregnant women suffered from vulvovaginal candidiasis with about 30 % of them having no clinical sign. The isolates indicated that *C. albicans* was the most common yeast, at around 86 % of the candidiasis.

Apart from causing vaginal infections in woman, *C. albicans* is known to be the common species in the genitourinary tract of healthy people, where it can be responsible for mouth and mucocutaneous infections. [123]

Currently, there are three major drug classes for the clinical treatment of candidiasis which comprise: the polyenes, azoles, and echinocandins. [119] In addition to these major drugs, flucytosine, which is a pyrimidine analogue, has specific roles as an adjunct in the treatment of central nervous system candidiasis and *Candida* endocarditis. [119]

Drug resistance due to candidiasis has been reported in literature. However, antifungal resistance has been found to be less common in *C. albicans*, but has been reported with long-term antifungal use and with recurrent infections, such as those with chronic mucocutaneous candidiasis or recurrent oropharyngeal candidiasis in patients with uncontrolled HIV infection. [124] Despite this, resistance to the most widely used drug, the azoles, is increasing, especially in patients, such as those with HIV, who are given azoles prophylactically. [125]

Three types of antifungal resistance has been described in the literature, namely: primary or intrinsic, exhibited before antifungal exposure; secondary or acquired, which develops following exposure to an antifungal agent; and clinical resistance. [126] The mechanism through which drug resistance occur has

been described. This appears through several independent, and potentially synergistic mechanisms, which include altered activity or regulation of drug efflux transporters; new point mutations; homozygosis of existing mutations or increased copy number of genes encoding the drug targets; alterations in regulatory factors that regulate the drug efflux pumps or targeted biochemical pathways, as well as chromosomal rearrangements or amplifications. [125]

Till date, there is no metallodrugs involved in the clinical treatment of *C. albicans.* However, despite the non-availability of metallodrugs in the treatment of *C. albicans*, a number of experimental studies involving coordination compounds have reported good activities against *C. albicans.* For instance, 2-aminopyridine containing complexes have shown good activities against the bacteria. [33,50] Moreover, $TiO_2$ nanoparticles has been useful in the disinfection of water contaminated with *E. coli* through changes in the morphology of the bacterial cell. [116]

### 1.8.4. Cancer

Cancer is the leading cause of death globally with 7.6 million deaths worldwide yearly, from which 63 % are reported to be from developing countries, and 12.7 million new cases per year being reported worldwide. [127] A study conducted by Enow *et al.* [128] reveals that about 15.000 new cases of cancer are diagnosed annually in Cameroon, with a prevalence of about 25.000 throughout the country. Therefore, cancer is being increasingly recognized as a public health problem in Cameroon. Moreover, this study reveals that breast cancer is the most diagnosed one among Yaoundé inhabitants and there are about 10.000 total death of cancer annually.

From the biological point of view, cancer is a multigenic and multicellular disease that can arise from all cell types and organs with a multi-factorial etiology. [129] Hanahan and Weinberg [130] have identified six cancer cell phenotypes or hallmarks of cancer. They are: cells with unlimited proliferative potential, environmental independence for growth, evasion of apoptosis, angiogenesis, invasion and metastasis to different parts of body. The metastasis, if it occurs, results in the death of the individual.

Microorganisms have been reported as part of the causative agents of cancer. This causative link was identified as early as the 16$^{th}$ century, however it was not until the late 20$^{th}$ century that reproducible, peer-reviewed work definitively identified a bacterial cause of malignancy. [131] With regard specifically to bacteria, they have been linked to cancer by two mechanisms: induction of chronic inflammation and production of carcinogenic bacterial metabolites. [132]

Microorganisms are estimated to account for about 20 % of all fatal cancers in humans, and can be indigenous or exogenous. The following three types of agents are the most known microbe-related

cancer cases in humans: human papilloma viruses (HPV; causing anogenital cancers), *Helicobacter pylori* (causing gastric cancers), and hepatitis B and C viruses (causing hepatic cancers). [133]

Despite the fact that cancer is among the leading cause of death globally, its therapy has witness significant progress in the last decades, with two thirds of cancers experiencing healing. The age when surgery and radiotherapy were the only effective way to fight tumour growth has ended giving rise novel treatment approaches such as: chemotherapy, and endocrine therapy. Some up-coming therapies include: new antibodies, small molecules, antiangiogenics and viral therapy. [134]

Among the metallodrugs, *cis*-platin has been a popular therapeutic drug against several solid neoplasms, including (but not limited to) head and neck, ovarian and lung cancers. However, cancer cells have become resistant to *cis*-platin resulting to relapse or therapeutic failure. As such, in cancer chemotherapy using *cis*-platin, drug resistance occurs because of the decreased intercellular accumulation, which cannot form adduct with DNA. [135] More generally, at least four distinct classes of mechanisms by which cancer cells become resistant have been identified for *cis*-platin based chemotherapy. [136] These include: pre-target, on-target, post-target and off-target resistances.

Beside *cis*-platin, coordination complexes with different mechanism of action such as Pt(IV) and Ru(III) have entered clinical trials for cancer therapy. The mechanism is based on the redox properties of both the metal and ligands which offer unusual routes for anticancer therapy. Here, the metal complexes can introduce artificial reductive and oxidative stress into cancer cells, including behaviour as photoactivatable agents and catalysts. [137] Moreover, gold, iron, and titanium have been reported to have interesting properties against some cancer cells. [135]

### 1.8.5. Coronavirus disease 19 (SARS-CoV-2)

The Coronavirus disease 19 (Covid-19) was first identified in Wuhan province in China, in patients with severe respiratory diseases. The causative agent was a novel coronavirus scientifically named severe acute respiratory syndrome coronavirus 2 (SARS-CoV-2) and causes severe diseases to elderly adults and patients with existing health conditions. [138] By march 2020, it became a worldwide pandemic.

Covid-19 is a zoonotic disease and has been evidenced to originate from bats. [139] Beside covid-19, Bats are host to many other coronaviruses. [138] Its genome has been reported to be over 80% identical to the previous human coronavirus (SARS-CoV-1) [139] whose outbreak emerged in China in 2003. However, SAR-CoV has a higher pathogenicity and lead to higher mortality rate, SAR-COV-2 infection appears to be much more contagious. [140]

For illustration, the mortality rate of Covid-19 lies between 4.5 – 5.5 % and had spread to 99.8% of the global population by April 2020, as compared to SARS-CoV whose mortality rate is between 9.6 – 21% and was limited to just 29 countries. [141]

Covid-19 infection is characterised by a wider clinical spectrum, including asymptomatic infection, mild upper respiratory tract illness, severe viral pneumonia with respiratory failure and possibly death. [140–142]

Since the outbreak of Covid-19, there has been tentative treatment of the disease by the adoption of many therapeutic approaches. These either involve the targeting action on the human immune system or human cells, or the targeting action on the virus itself. [143] For the latter approach, antiviral compounds have been extensively used, of which the most popular are remdesivir, chloroquine, and azithromycin. [138,139,141,143] They are mostly used as combinatorial drugs as: remdesivir–chloroquine or chloroquine–azithromycin.

Till date, a tremendous amount of research is in progress to develop a vaccine against Covid-19. In this respect, some pharmaceutical firms have declared to have successfully found vaccines with good efficiency.

# Chapter II: EXPERIMENTAL METHODS

## 2.1. Reagents and materials

### 2.1.1. Reagents

The following reagents and solvent were used as purchased, without further purification.

Metal salts:

- Manganese(II) chloride tetrahydrate (98 %), $MnCl_2.4H_2O$ (REIDEEL-DE HAEN AG).
- Zinc(II)chloride anhydrous (99 %), $ZnCl_2$ (LABOSI).
- Cadmium(II) chloride tetrahydrate (99 %), $CdCl_2 \cdot 4H_2O$ (REIDEEL-DE HAEN AG)

Ligands

- N-phenylanthranilic acid (98 %), $C_{13}H_{11}N$ (REIDEEL-DE HAEN AG).
- 2-aminopyridine (99 %), Acros organics
- Sodium dicyanamide, $Na(N(CN)_2)$ (95 %), (REIDEEL-DE HAEN AG).
- Ammonium thiocyanate (98 %), $NH_4SCN$ (REIDEEL-DE HAEN AG).

Other reagents

- Triethylamine

Solvents:

- Ethanol (95%) further distilled.
- Distilled water.

### 2.1.2. Materials

- Beakers, shlenk flask, conical flasks, graduated cylinders, evaporation column, volumetric flasks, pipettes, burette, funnel, stand.

## 2.2. Synthesis of the complexes

The synthesis of the complexes was done using a readily available N– phenylanthranilic acid, 2-aminopyridine and one of the co-ligands.

### 2.2.1. Synthesis of $[Mn(2\text{-}Apy)_2(dca)_2]$ complex

To an ethanolic solution (10 mL) of $MnCl_2 \cdot 4H_2O$ (0.1979 g; 1 mmol) at room temperature, was added dropwise a 10 mL ethanol/water (1:1) solution of sodium dicyanamide, $NaC_2N_3$ (0.16 g; 2 mmol). The

colourless mixture was stirred for 30 min after which an ethanolic solution (10 mL) of 2-aminopyridine (0.377 g; 4 mmol) was added drop wise into the stirred solution. The resulting mixture was further refluxed for 2h. The white precipitate formed was filtered, washed with ethanol/distilled water (1:1); air dried and weighed. The filtrate was allowed to evaporate slowly at room temperature from which colourless crystals, suitable for single crystal X-ray diffraction, were obtained within a few days. The equation representing the synthesis of the Mn(II) complex is shown below.

$$MnCl_2.4H_2O + 2Na(N(CN)_2 \xrightarrow{\text{Stirring for 30 min}} \xrightarrow[EtOH]{4C_5H_6N_2} [Mn(N(CN)_2)_2(C_5H_6N_2)_2] + 2NaCl + 2C_5H_6N_2 + 4H_2O \ldots\ldots (1)$$

### 2.2.2. Synthesis of $[Zn_3(H_2O)_2(NPA)_6]$ complex

$ZnCl_2$ (0.272 g, 0.002 mol) and $NH_4SCN$ (0.144 g, 0.002 mol) were respectively dissolved in about 10 mL water-ethanol solution (1:5) and put in a 100 mL Erlenmeyer with stirring at room temperature for about 30 minutes. To this solution was added a 20 mL ethanolic solution of *N*-phenylanthranilic acid (0.426 g, 0.002 mol). The pH of the resulting solution was adjusted to about 6 using 10 % $Et_3N$ solution and further stirred for 24 hours. A transparent crystalline complex was obtained from the solution by slow evaporation for several days, producing crystals suitable for X-ray analysis. The equation representing the synthesis of the Zn(II) complex is shown below.

$$3ZnCl_2 + NH_4SCN \xrightarrow{\text{Stirring for 30 min}} \xrightarrow[H_2O\,/\,EtOH,\ pH \sim 6]{6C_{13}H_{11}NO_2} [Zn_3(H_2O)_2(NH_4SCN)_6] + NH_4SCN \ldots\ldots\ldots\ldots (2)$$

### 2.2.3. Synthesis of $[Cd(2\text{-}Apy)_2(dca)_2]$ complex

A similar procedure to that for $[Mn(2\text{-}Apy)_2(dca)_2]$ was followed to prepare $[Cd(2\text{-}Apy)_2(dca)_2]$, except that $MnCl_2{\cdot}4H_2O$ was replaced by $CdCl_2{\cdot}4H_2O$ (0.1834 g; 1 mmol). The white precipitate formed was filtered, washed with ethanol/distilled water (1:1), air dried and weighed. The filtrate was allowed to evaporate slowly at room temperature from which and colorless crystals, suitable for single crystal X-ray diffraction, were obtained within a few days. The equation representing the synthesis of the Cd(II) complex is shown below.

$$CdCl_2.4H_2O + 2Na(N(CN)_2 \xrightarrow{\text{Stirring for 30 min}} \xrightarrow[EtOH]{4C_5H_6N_2} [Cd(N(CN)_2)_2(C_5H_6N_2)_2] + 2NaCl + 4H_2O + 2C_5H_6N_2 \ldots\ldots (3)$$

## 2.3. Physico-chemical analyses of the complexes

### 2.3.1. The melting point

The melting temperatures of the complexes were determined using an SMP11 melting point measurement instrument, with the melting points ranging from 50 to 300 °C in the Laboratory of Applied Inorganic Chemistry of the University of Yaoundé I. Small amounts of compounds were placed in capillary and inserted in the apparatus, and the melting temperature measured. The melting point instrument was calibrated using five reference substances (vanillin, acetanilide, finely crushed urea, sulphonamide, and caffeine).

### 2.3.2. Microanalysis

This analysis is usually carried out to determine the percentage weight of each element present in a compound.

Elemental analyses for C, H, N, and S were carried out using a Euro Vector CHNS-O element analyzer (Euro EA 3000) or a vario MICRO Cube (Co. Elementar Analysensysteme): (HEKAtech GmbH, Friedrich-List-Allee 26, 41844 Wegberg, Germany). Company: HEKAtech GmbH, Friedrich-List-Allee 26, 41844 Wegberg, Germany on a Flash 2000 Thermo Scientific analyzer, the University of Liepzig, Germany. The instrument was calibrated using sulphanamide.

### 2.3.3. Measurement of conductivity

Conductance measurements are carried in order to determine the ionic or the molecular nature of the complexes.

Conductivity measurements were determined in DMSO as solvent using a TACUSSEL electronic conductimeter, type CD 810 and a TACUSSEL type TF 100 electrode. The conductimeter was first calibrated with a $1x10^{-3}$ M KCl solution. This was done in in the Laboratory of Applied Inorganic Chemistry of the University of Yaoundé I. The instrument was calibrated using potassium iodide solution.

### 2.3.4. Infrared spectroscopy

This analysis determines the various functional groups present in a given compound.

The IR analyses were done at the Applied Physical and Analytical Chemistry Laboratory from the University of Yaoundé I. The IR Spectra were recorded on a spectrophotometer of mark ALPHA P from the BRUCKER firm. The instrument was calibrated using polystyrene as a calibration standard.

### 2.3.5. Single crystal X-ray crystal structure determination

Max von Laue, in 1912, discovered that crystalline substances act as three-dimensional diffraction gratings for X-ray wavelengths similar to the spacing of planes in a crystal lattice. X-ray diffraction is now a common technique for the study of crystal structures and atomic spacing.

X-ray diffraction is based on constructive interference of monochromatic X-rays and a crystalline sample. These X-rays are generated by a cathode ray tube, filtered to produce monochromatic radiation, collimated to concentrate, and directed toward the sample. The interaction of the incident rays with the sample produces constructive interference (and a diffracted ray) when conditions satisfy Bragg's equation ($n\lambda=2d\sin\theta$). This equation relates the wavelength of electromagnetic radiation to the diffraction angle and the lattice spacing in a crystalline sample. These diffracted X-rays are then detected, processed and counted. By changing the geometry of the incident rays, the orientation of the centered crystal and the detector, all possible diffraction directions of the lattice should be attained.

#### 2.3.5.1 Single crystal for $[Mn(2\text{-}Apy)_2(dca)_2]$ complex

X-ray data were collected using a Bruker *APEX*-II CCD diffractometer, $\lambda$(Mo-*K*α) = 0.71073 Å, *T*=100 K. Data reduction was performed with CrysAlis Pro including the program SCALE3 ABSPACK for empirical absorption correction. The structure was solved by dual space methods with SHELXT-20xy. Structure refinement was done with SHELXL-2018 by using full-matrix least-square routines against $F^2$. Hydrogen atoms and NH were located on difference Fourier maps calculated at the final stage of the structure refinement. This was done in Leipzig, Germany.

#### 2.3.5.2 Single crystal for $[Zn_3(H_2O)_2(NPA)_6]$ complex

$[Zn_3(H_2O)_2(NPA)_6]$ was mounted on a Bruker Kappa Venture D8 instrument on a Kapton sample holder that was then placed in a liquid nitrogen stream to cool the sample down to 100 K. The sample was run with a molybdenum micro source (Mo-Kα, λ= 0.71073 Å) using a Photon II detector. The unit cell was determined prior to full data collection, and data were integrated using the Bruker SAINT program using SADABS for absorption correction. Structural refinement was conducted using APEX3 and Olex2 software that interfaced with the ShelXL, PC suite. All non-hydrogen atoms were refined using anisotropic thermal parameters. Hydrogen atoms were placed at ideal positions excluding the hydrogen atoms on the solvent water molecules which were manually placed at q-peaks. This was done in California State University, Pomona, USA.

### 2.3.5.3 Single crystal for [Cd(2-Apy)$_2$(dca)$_2$] complex

Here, X-ray data were collected with a GEMINI CCD diffractometer (Rigaku Inc.), $\lambda$(Mo-$K\alpha$) = 0.71073 Å, $T$=130(2) K, ω-scan rotation. Data reduction was performed with CrysAlis Pro including the program SCALE3 ABSPACK for empirical absorption correction. All structures were solved by dual space methods with SHELXT-20xy. Structure refinement was done with SHELXL-2018 by using full-matrix least-square routines against $F^2$. Hydrogen atoms and NH were located on difference Fourier maps calculated at the final stage of the structure refinement. The remaining hydrogen atoms were calculated on idealized positions using the riding model. This was done in Leipzig, Germany.

### 2.3.6. Thermal analyses

Thermogravimetry (TG) studies the change (gain or loss) of a sample mass as a function of temperature and/or time. The measurements of these changes are made using a thermobalance in which the tests are accomplished according to a programmed heating rate in a suitable enclosed system with a controlled atmosphere. It has been used to determine the physical and chemical properties of polymers, crystalline and geological materials. It plays an important role both in qualitative and quantitative analyses. Qualitative studies of thermal behaviour are used to identify and characterise materials. Quantitative analyses are being made from changes in weight and enthalpy as the material is being heated. Therefore, TGA is used to investigate the thermal stability and composition of a compound. Temperature here varies from 25 to 600 °C in nitrogen gas, with a flow rate of 50 mL/minute, and linear heating rate of 10 °C/minute. In TGA, the weight of a sample is recorded continuously as temperature is increased. A sample is placed in the dish that is sitting inside a furnace on a quartz beam which is attached to the automatic recording balance. Any change in the weight of the sample causes a deflection of the beam which is sensed by photodiodes. When the beam is restored to the original position, the balance detects the current which is sent from the photodiodes. The current here is proportional to the weight of the sample.

Part of TGA/DTA of the samples were recorded on a TGA/DSC 1 METELEDO (STAR system) instrument with a heating rate of 10 °C/min at the University of Brussels, in Belgium. The other part was carried on at the University of Yaoundé I.

### 2.3.7. The Hirshfeld surfaces

To understand the different interactions and contacts in the crystal, it is necessary to represent the Hirshfeld surface (HS). The Hirshfeld surface has recently been shown to be a very efficient method for characterizing intra- and intermolecular interactions.

HS analysis can be employed to visualize and quantify various non-covalent interactions that stabilize the crystal packing. Some properties can be represented on a Hirshfeld surface such as:

- ✓ The $d_{norm}$ property is a symmetric function of distances to the surface between nuclei inside and outside the Hirshfeld surface ($d_i$ and $d_e$, respectively), relative to their respective van der Waals radii. The $d_{norm}$ values are negative or positive depending on whether the intermolecular contact is shorter or longer than the sum of the van der Waals radii. [144,145]
- ✓ The term $d_i$ is the distance from the Hirshfeld surface to the nearest atomic nucleus **inside** the surface.
- ✓ The term $d_e$ corresponds to the distance between the Hirshfeld surface and the nearest atomic nucleus **outside** this surface.
- ✓ A colour scheme is applied such that where the contact is shorter than the van der Waals separation the point is coloured red, white is used for contacts around the van der Waals separation and blue is for longer contacts.

The HS analyses and their associated 2D fingerprint plots [144] were carried out employing the *CrystalExplorer* 17.5 program. The HS analyses were carried out in the Laboratory of Applied Inorganic Chemistry of the University of Yaoundé I.

### 2.3.8. Frontier Molecular orbital theory

A theoretical quantum-chemical method widely used today is the density functional theory (DFT). DFT method combines accuracy with computational speed and ease of use. This is particularly true for hybrid DFT methods, which consistently have been shown to be highly reliable. Of all hybrid DFT methods, the B3LYP functional is the most widely used and yields accurate results for many systems containing transition metal atoms. For the present study, the energy levels for all the compounds were computed using the DFT-B3LYP/3-21G method with Gaussian 09 software. This analysis was carried out in the Laboratory of Applied Inorganic Chemistry of the University of Yaoundé I.

## 2.4. Biological applications

The biological application involves the antimicrobial studies of the ligand, the co-ligands and its complexes on different microbial strains. Further, a computational docking is run to explore the possible interaction occurring between the complexes and the breast cancer mutant and SARS-CoV-2 proteins.

### 2.4.1. Antimicrobial tests

The antimicrobial tests were carried out in the Microbiology Laboratory of the University of Yaoundé I, Cameroon. The products tested are metal (II) complexes of 2-Apy with dca coligand (Mn and Cd) and NPA (Zn) synthesised and characterised as new products.

The screening of antimicrobial activity of the ligand, metal salts and metal complexes was performed using the disk diffusion method in solid medium from paper disks.

**Goal**: this test was performed to screen and select the best active products according to their inhibition zone diameter, prior to running the minimum inhibitory concentration (MIC).

**Material**: the antibiotics used are Chloramphenicol for bacteria (*Staphylococcus aureus* and *Salmonella Typhi*) and gentamicin for fungi (*Candida albicans*) from Sigma-Aldrich, St Quentin Fallavier, France. *Staphylococcus aureus* ATCC23565 and two isolates *Salmonella Typhi* and *Candida albicans* from the University of Bologna (Italy) and stored at 4 °C in the Microbiology laboratory of the University of Yaoundé 1.

**Preparation of inocula**

A revivification of the strains stored in the fridge was done beforehand, then an evaluation of the microbial load was carried out to get an idea of the microbial concentration of each strain after 24 hours. Then a culture of each strain was inoculated in nutrient broth. and incubated at 37 °C for *Staphylococcus aureus* and *Salmonella Typhi* and at room temperature (25 °C ± 2) for *Candidate albicans* for 24 hours.

**Preparation of discs impregnated with antimicrobial substances**

40 mg / mL solutions were prepared by dissolving masses of the compounds in 10 % DMSO solution. In the case of antibiotics, solutions of 30 µg / mL were made by dissolving the latter in sterile distilled water. Then 20 µL of each antimicrobial substance was deposited on discs 6 mm in diameter and then left at room temperature for 3 hours so that the discs incorporated the antimicrobial substances well.

**Evaluation of antimicrobial activity**

Decimal dilutions were made and then 200 µL of the dilution containing $10^6$ cfu / mL were taken and seeded at the surface by spreading on the Brain Heart Bouillon (BHI) agar. The petri dishes were left to dry at room temperature for 30 min, then the discs impregnated with antimicrobial substances were placed on the surface of the latter and incubated at 37 °C for *Staphylococcus aureus* and *Salmonella*

*Typhi* and at room temperature for *Candida albicans* this for 24h. then, the inhibition halos were measured using a calliper.

**Culture medium composition:**

Heart-brain infusion 8 g/L; animal peptide digestion 5 g/L; pancreatic digestion of casein 16 g/L; sodium chloride 5 g/L; glucose 2 g/L; dissodium hydrogen phosphate 2.5 g/L; agar 15 g/L.

**Minimum Inhibitory Concentrations and Minimum Bactericidal/Fungicidal Concentration**

The minimum inhibitory concentrations (MIC) of the various compounds were determined by the macrodilution method. The latter is based on bringing a standardized bacterial inoculum ($10^6$ cfu/mL) into contact with decreasing concentrations of compounds (20 to 0.15 mg/L) according to a geometric progression of ratio 2. After incubation at 37 °C for 24 hours, the minimum inhibitory concentration is indicated by the lowest compound concentration where there is no visual growth in the broth. 2,3,5-triphenyltetrazolium chloride (TTC) was used to reveal microbial growth. Indeed, this chemical compound highlights the production of succinate dehydrogenase which forms with it an insoluble complex of red color whose intensity depends on the quantity of enzymes present in the reaction medium. The minimum bactericidal concentration (MBC) or the minimum fungicidal concentration (MFC) is also determined on the basis of the smallest concentration which did not generate growth on agar.

### 2.4.2. Molecular docking studies

Molecular docking is a computational technique used to predict the possible structure and interactions of a biomolecular complex. During the drug design process, computer simulation is used for the identification and study of interactions between ligands and receptors, such as binding affinities, binding orientations and binding sites. The method relies on the estimation of free energy of the complex. The complex with lower free energy is the one that probably will be formed in nature. Moreover, drug-receptor interactions can cause structural and conformational changes on the receptor molecule, which are associated to enthalpy and entropy contributions to the binding free energy and can be theoretically estimated from structures generated during simulation.

Molecular docking analysis was performed to predict the binding sites for the complexes to different pathogenic proteins using an Intel Pentium duo core, 2.20 GHz based machine running MS Windows XP SP1 as operating system and Autodock Vina software (Scripps Research Institute, La Jolla, California, USA). [146]

The Autodock program predicts the optimal free energy of association and the best conformation for the complexes to the protein. The program calculates binding free energies of all possible ligand/receptor conformations based on dispersion/repulsion forces, hydrogen bonding, electrostatics, desolvation and torsional entropy, and incorporating intramolecular energies into the predicted free energy of binding. To evaluate rapidly the energy of each ligand-receptor interaction, Autodock program uses a grid-based method: interaction energies between the ligand and the receptor binding site are calculated for each atom of the ligand and used to create a grid, in which free energy of binding is correlated to a specific ligand conformation and spatial coordinates. This method allows flexibility only of the ligand, but only torsional variations are explored.

The molecular docking studies were performed by using Autodock Vina software. [146] The coordinates of complexes were taken from their respective crystal structure as a CIF file and was converted to the PDB format using Mercury software (http://www.ccdc.cam.ac.uk/). The crystal structures of the different proteins were downloaded from the protein data bank (http://www.rcsb.org./pdb). All calculations were carried out on an Intel Pentium duo core, 2.20 GHz based machine running MS Windows XP SP1 as operating system. Visualization of the docked pose has been done by Discovery Studio software.

Molecular docking was carried out using the following steps:

1. The protein was retrieved from the protein database;
2. Both the protein and the ligands (complexes) were prepared and saved in a .pdbqt file;
3. The docking site of the protein was selected accordingly using appropriate online programme simultaneously with Discovery studio software;
4. The protein-ligand docking was carried out using docking tool.

# Chapter III: RESULTS AND DISCUSSION

## 3.1. Synthesis of the complexes

Different synthetic methods were used to obtain the pure complexes, $[Mn(2\text{-}Apy)_2(dca)_2]$ (*bis(2-aminopyridine)bis($\mu_{1,5}$-dicyanamido)manganese(II)*) and $[Cd(2\text{-}Apy)_2(dca)_2]$ (*bis(2-aminopyridine)bis($\mu_{1,5}$-dicyanamido)cadmium(II)*) complexes were synthesised by refluxing at 75 – 80 °C for three hours in ethanol/water solvent, while $[Zn_3(H_2O)_2(NPA)_6]$ complex (*hexakis($\mu_2$-2-anilinobenzoato)diaquatrizinc(II)*) was synthesised at room temperature in ethanol solvent.

## 3.2. Physical properties of the complexes

The complexes are all air-stable solids with melting temperatures varying from 162 °C to more than 300 °C, meaning that the compound did not melt at the limit of the apparatus. The sharp melting points for Zn(II) and Cd(II) complexes is an indication of their purity. They percentage yields range from 26% to 84%. The low percentage yield observed for $[Cd(2\text{-}Apy)_2(dca)_2]$ may be due to incomplete crystallisation of the compound in the solvent.

The complexes are colourless except $[Cd(2\text{-}Apy)_2(dca)_2]$ complex which is white-transparent and are all stable at room temperature. These colours are quite different from the starting materials indicating that new substances are formed during reaction. The metal salts from which they are synthesised are hygroscopic.

The physical properties of the synthesised complexes are presented in Table I.

**Table I: Physical properties of the complexes**

| Complex | Colour | Physical form | % yield | Molar mass (g/mol) | M. pt/ decomposition temperature |
|---|---|---|---|---|---|
| $[Mn(2\text{-}Apy)_2(dca)_2]$ $C_{14}H_{12}MnN_{10}$ | Colourless | Crystal | 84 % | 375.28 | > 300±2 °C |
| $[Zn_3(H_2O)_2(NPA)_6]$ $C_{78}H_{64}N_6O_{14}Zn_3$ | Colourless | Crystal | 54 % | 1505.46 | 220±2 °C |
| $[Cd(2\text{-}Apy)_2(dca)_2]$ $C_{14}H_{12}CdN_{10}$ | White transparent | Crystal | 26 % | 432.74 | 162±2 °C |

## 3.3. Elemental analysis

Analytical data for CHNS of the complexes is presented in Table II. The values obtained are close to the calculated ones. Therefore, the analysis confirms the expected formulae for the different

complexes. Moreover, the results indicate that for all the complexes, one equivalent metal salt reacts with two equivalents of the ligand.

**Table II: Elemental analysis of the complexes**

| Complex | % C | | % H | | % N | |
|---|---|---|---|---|---|---|
| | Found | Calc. | Found | Calc. | Found | Calc. |
| $[Mn(2\text{-}Apy)_2(dca)_2]$ | 44.23 | *44.81* | 3.06 | *3.22* | 37.33 | *37.54* |
| $[Zn_3(H_2O)_2(NPA)_6]$ | 62.04 | *62.23* | 3.83 | *4.28* | 5.67 | *5.58* |
| $[Cd(2\text{-}Apy)_2(dca)_2]$ | 38.32 | *38.86* | 2.46 | *2.68* | 31.27 | *31.92* |

### 3.4. Molar conductance

Table III presents the molar conductivities of the complexes. The concentrations of the complexes were all fixed at around $10^{-3}$ mol/L in DMSO. Conductance values of the complexes were obtained in the range 20 to 73 $\Omega^{-1}cm^{-2}mol^{-1}$. The molar conductance values were compared with values in literature in order to determine the type of electrolyte and also the number of ions present in solution for each complex. The results suggest that all of the complexes were non-electrolyte (molecular in nature). The results are summarised in Table III.

**Table III: Molar conductance of the complexes**

| Complex | Conductivity ($\boldsymbol{\Omega^{-1}cm^{-1} \times 10^{-6}}$) | Molar conductance ($\Omega^{-1}cm^{-2}mol^{-1}$) | N° of ions | Nature |
|---|---|---|---|---|
| $[Mn(2\text{-}Apy)_2(dca)_2]$ | 0.146 | 73 | 0 | Molecular |
| $[Zn_3(H_2O)_2(NPA)_6]$ | 0.04 | 20 | 0 | Molecular |
| $[Cd(2\text{-}Apy)_2(dca)_2]$ | 0.094 | 47 | 0 | Molecular |

### 3.5. Infrared Spectroscopy

IR spectroscopy have proven to be a suitable technique to give enough information for successful elucidation of the nature of ligand bonding to a metal ion even in the case of absence of a powerful technique such as single crystal X-ray crystallography. The measured relevant IR band frequencies of both the ligands and the complexes are shown in Figure 20, 21 and 22, and are summarised in Table IV.

### 3.5.1. IR spectra of the [Mn(2-Apy)$_2$(dca)$_2$] crystal complex

The IR spectrum of the Mn(II) complex clearly shows the existence of 2-Apy and dicyanamide moieties in the compound as seen on Figure 20 below.

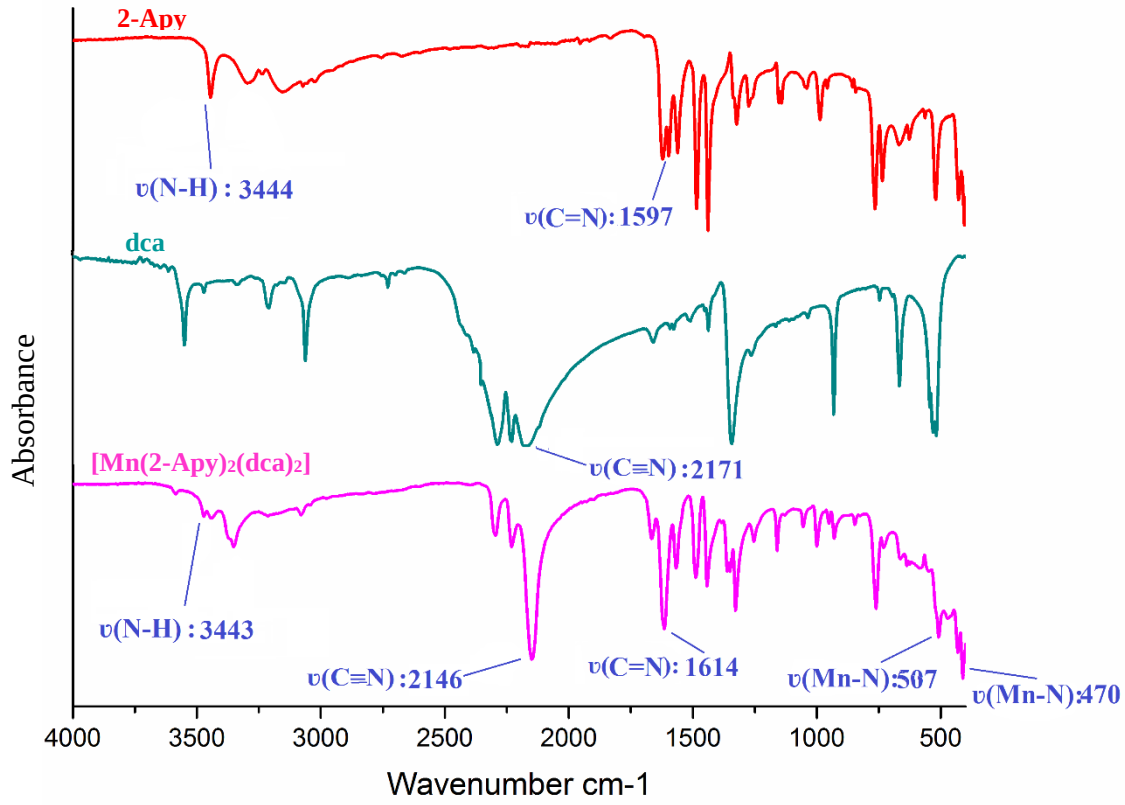


Figure 20: IR spectra of [Mn(2-Apy)$_2$(dca)$_2$] complex, NPA and 2-Apy.

Characteristic medium to strong IR absorption bands, shown on figure 20, for dca include $\upsilon_{as}$(C≡N) + $\upsilon_s$(C≡N) at 2286 cm$^{-1}$, $\upsilon_{as}$(C≡N) at 2228 cm$^{-1}$ and $\upsilon_s$(C≡N) at 2171 cm$^{-1}$. These bands are shifted to higher wavenumbers 2297, 2232 and 2146 cm$^{-1}$. These shifts can be attributed to the bridging coordination mode of the ligand. [35,63,147] Absorption bands for dca at 1344 cm$^{-1}$ for $\upsilon_{as}$(N–C), 930 cm$^{-1}$ for $\upsilon$s(N–C), 664 cm$^{-1}$ for $\delta$(CNC), 543 cm$^{-1}$ for $\delta$(NCN), and 529 cm$^{-1}$ for $\delta$(NCN) could not be assigned in the complex because they are masked by vibrational bands of the 2-Apy ligand as previously reported. [35,147] The medium to strong absorption bands of 2-Apy at 3447 and 3353 cm$^{-1}$ are attributed to $\nu_s$(NH$_2$) and $\nu_{as}$(NH$_2$) vibrations of the NH$_2$ group, respectively. The characteristic υC=N stretching modes of the pyridine ring shifted from 1595 to 1614 cm$^{-1}$ in the spectra of [Mn(2-Apy)$_2$(dca)$_2$], indicating its participation in bonding. [33]

### 3.5.2. IR spectra of the [Zn3(H2O)2(NPA)6] crystal complex

The IR spectrum of $[Zn_3(NPA)_6(H_2O)_2]$ complex, as well as those of SCN and NPA ligands are shown in Figure 21.

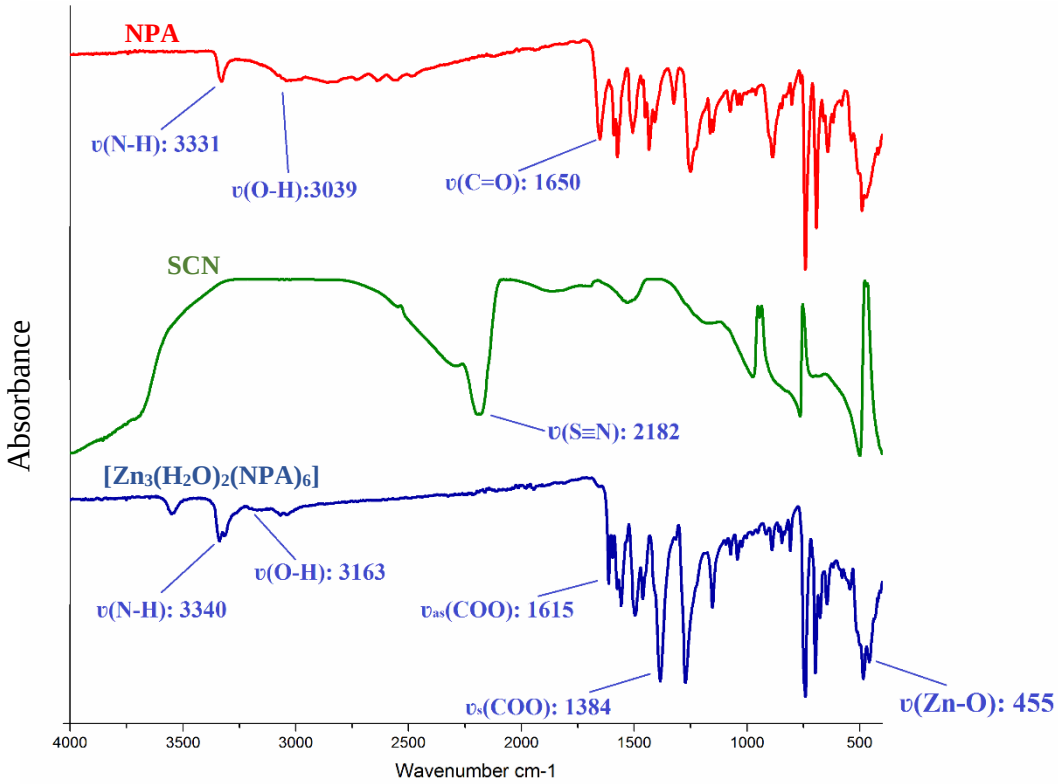


Figure 21: IR spectra of $[Zn_3(H_2O)_2(NPA)_6]$ complex, NPA and 2-Apy.

In Figure 21, the band observed at 3340 $cm^{-1}$ is due to the uncoordinated N–H bond in the complex. The O–H band of the free NPA ligand observed at around 3038 $cm^{-1}$ disappears in the spectrum of the complex indicating the involvement of the oxygen of carboxylic group in complexation. However, there is appearance of a band at the region of 3163 $cm^{-1}$ in the complex assignable to hydroxyl groups ν(OH) of water molecules indicating that the complex is hydrated. [54]

Moreover, significant changes are observed in the spectral region 1700 – 1300 $cm^{-1}$ of the complex. The spectrum of the free NPA shows strong band at 1650 $cm^{-1}$ which are from the stretching vibrations of the carbonyl group ν(C=O). This band disappears in the complex spectrum to give way to the appearance of two new bands at 1615 and 1384 $cm^{-1}$ respectively corresponding to asymmetric and symmetric stretching vibrations of the $COO^{-}$ group. Hence, an indication of participation of carboxylate group in metal ions coordination. The difference between the asymmetric and symmetric carboxylate vibrations ($\Delta = \nu_{as}(COO^-) - \nu_s(COO^-)$) is often used to determine the coordination mode of the carboxylate group. In this case, $\Delta$ = 232 $cm^{-1}$ corresponding to a bidentate bridging coordination. [54,148] There is no peak around 2180 $cm^{-1}$ on the spectrum of the complex, which is an indication that

SCN ligand did not take part in coordination. A new band at 455 $cm^{-1}$ appears in the complex spectrum and is assignable to the Zn–O.

### 3.5.3. IR spectra of the [Cd(2-Apy)2(dca)2] crystal complex

The IR spectrum of Cd(II) complex is quite similar to that of Mn(II) complex as shown in Figure 22. This may suggest compounds with a same structural architecture.

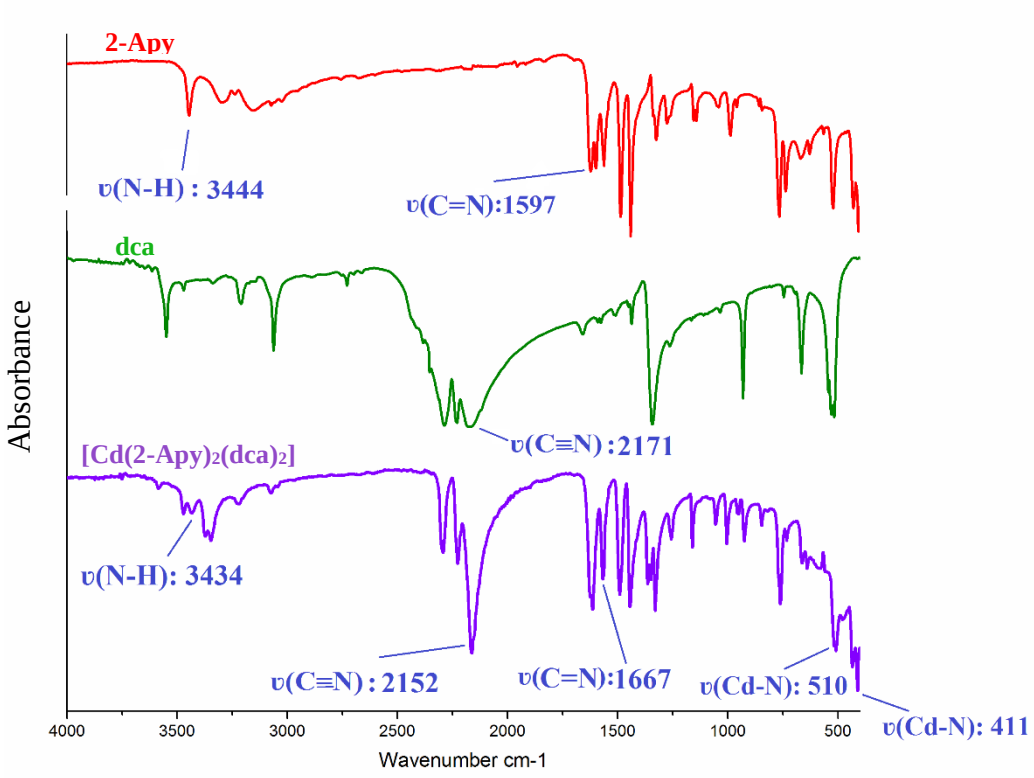


Figure 22: IR spectra of $[Cd(2\text{-}Apy)_2(dca)_2]$ complex, NPA and 2-Apy.

In the spectrum of the complex, characteristic medium to strong IR absorption bands for dca which include $\upsilon_{as}(C{\equiv}N) + \upsilon_s(C{\equiv}N)$ at 2286 $cm^{-1}$, $\upsilon_{as}(C{\equiv}N)$ at 2228 $cm^{-1}$ and $\upsilon_s(C{\equiv}N)$ at 2171 $cm^{-1}$ are shifted to higher wavenumbers 2293, 2226 and 2152 $cm^{-1}$. They are attributed to the bridging coordination mode of the ligand. [35,63,147] Once more, the vibrational bands of 2-Apy mask dca absorption bands between 1344 to 529 $cm^{-1}$. [35,147] The medium to strong absorption bands observed at 3471 and 3372 $cm^{-1}$ are attributed to are attributed to $\nu_s(NH_2)$ and $\nu_{as}(NH_2)$ vibrations of the $NH_2$ group of 2-Apy._As in Mn(II) complex, The characteristic υC=N stretching modes of the pyridine ring is shifted from 1595 to 1614 $cm^{-1}$ in the spectra, which is an indicating of its participation in bonding. [33]

**Table IV: Characteristic IR bands ($cm^{-1}$) of the ligands and their metal complexes**

| Compound | $\upsilon_{N-H}$ | $\upsilon_{O-H}$ | $\upsilon_{C\equiv N}$ | $\upsilon_{C=N}$ | $\upsilon_{C=O}$ | $\upsilon_{C-N}$ | $\upsilon_{as(COO-)}$ | $\upsilon_{s(COO-)}$ | $\upsilon_{M-N}$ | $\upsilon_{M-O}$ |
|---|---|---|---|---|---|---|---|---|---|---|
| 2-Apy | 3300*m* | | | 1598*s* | | 1140*s* | | | | |
| NPA | 3334*m* | | | | 1650vs | | | | | |
| dca | | | 2171*vs* | | | 1338*s* | | | | |
| SCN | | | 2181*vs* | | | | | | | |
| $[Mn(2\text{-}Apy)_2(dca)_2]$ | | | 2146*vs* | 1614 | | | | | 470/507*m* | |
| $[Zn_3(H_2O)_2(NPA)_6]$ | 3340*m* | 3163*br* | | | | | 1615*s* | 1384*vs* | | 455*m* |
| $[Cd(2\text{-}Apy)_2(dca)_2]$ | 3434*m* | | 2152*vs* | 1667 | | | | | 411/510*m* | |

*br* = broad; *m* = medium; *s* = strong; *vs* = very strong

## 3.6. X-ray crystal structure determination

### 3.6.1. Single crystal X-ray diffraction of [Mn(2-Apy)$_2$(dca)$_2$] complex

The ORTEP drawing of the symmetric unit compound is shown in Figure 23, together with the atom numbering scheme used in the corresponding tables. The crystallographic data for the compound is presented in Table V, the H-bond in Table VII, while selected bond parameters are given in Table VIII.

[Mn(2-Apy)$_2$(dca)$_2$] crystallizes in a monoclinic crystal system with a Cc space group. The asymmetric units of [Mn(2-Apy)$_2$(dca)$_2$] contains one Mn atom, two bridging bidentate $\mu_{1,5}$-dca anions, coordinating through the nitrile nitrogen, and two monodentate 2-Apy ligands, through its ring N-atoms ($\kappa^1$N). Mn atom is coordinated to four equatorial $\mu_{1,5}$-bridging dca ligands and two monodentate 2-Apy ligands in axial positions. The coordination environment around the metal centre represents an MN$_6$-octahedron.

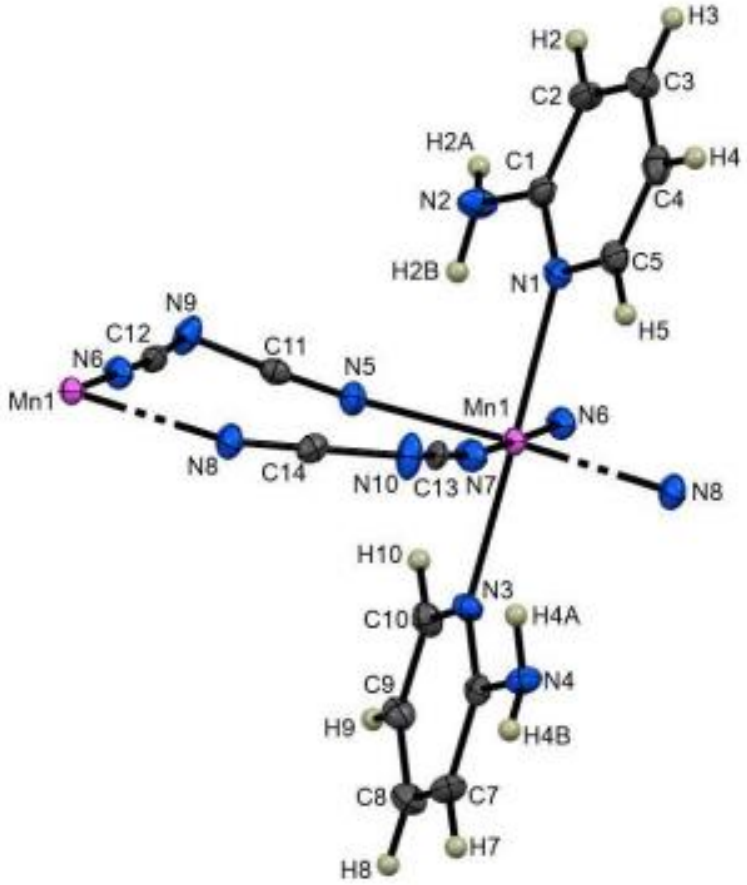


Figure 23: Molecular structure and atom-labelling scheme for [Mn(2-Apy)$_2$(dca)$_2$] with ellipsoids drawn 50% probability level.[149]

The octahedra in the complex is distorted, with four short M-$N_{dca}$ bonds in the range 2.211(3) – 2.231(3) Å, in addition to two long M-$N_{py}$ bonds in the ranges 2.302(3) – 2.303(3) Å which are consistent with obtained values for a comparable reported structure [35]. The N-M-N bond angles are in the range 86.73(10) - 93.58(10)º and are comparable to similar compounds previously reported [33,150]. The N(3)-Mn(1)-N(1) bond angle (177.46(14)º), deviate slightly from 180º. The terminal N atoms of four dicyanamide ligands form an approximate square plane, with N—M—N bite angles of 88.04(11)° and 89.34(12)°.

A summary of the crystal data and structure refinement for [Mn(2-Apy)$_2$(dca)$_2$] complex is shown in Table V below.

**Table V: Crystal data and structure refinement for [Mn(2-Apy)$_2$(dca)$_2$]**

| | |
|---|---|
| Empirical formula | $C_{14}H_{12}MnN_{10}$ |
| $M_r$ | 375.28 |
| Wavelength | |
| Crystal system, Space group | Monoclinic, *Cc* |
| Temperature (K) | 100 |
| *a, b, c* (Å) | 16.0680(5), 7.5050(3), 14.4658(4) |
| β (°) | 113.087(2) |
| V(Å$^3$) | 1604.72(9) |
| *Z* | 4 |
| Radiation type | Cu *Kα* |
| μ (mm$^{-1}$) | 6.88 |
| Crystal size (mm) | 0.29 × 0.15 × 0.03 |
| ***Data collection*** | |
| Diffractometer | Bruker APEX-II CCD diffractometer |
| Absorption correction | Multi-scan SADABS |
| $T_{max}$, $T_{min}$ | 0.541, 0.820 |
| No. of measured, independent and observed [$I > 2\sigma(I)$] reflections | 5357, 2593, 2442 |
| $R_{int}$ | 0.035 |
| $(\sin \theta/\lambda)_{max}$ (Å$^{-1}$) | 0.617 |
| ***Refinement*** | |
| $R[F^2 > 2\sigma(F^2)]$, $wR(F^2)$, *S* | 0.030, 0.064, 1.03 |
| No. of reflections | 2593 |
| No. of parameters | 243 |
| $\Delta\rho_{max}$, $\Delta\rho_{min}$ (e Å$^{-3}$) | 0.31- 0.29 |

The metal centers in [Mn(2-Apy)$_2$(dca)$_2$] are arranged in linear chains along (010) (Figure 24(a)) with [Mn1···Mn1] intra-chain separations, through the bridging dicyanamido anions of 7.505 Å (Figure 24(b)), whereas the shortest [Mn1···Mn1] inter-chain distance is 7.405 Å. While the intra-chain

separations are similar, the inter-chain distances are slightly longer than those reported in Table VI, for other catena-$M(dca)_2L_2$ structures. [150,151]

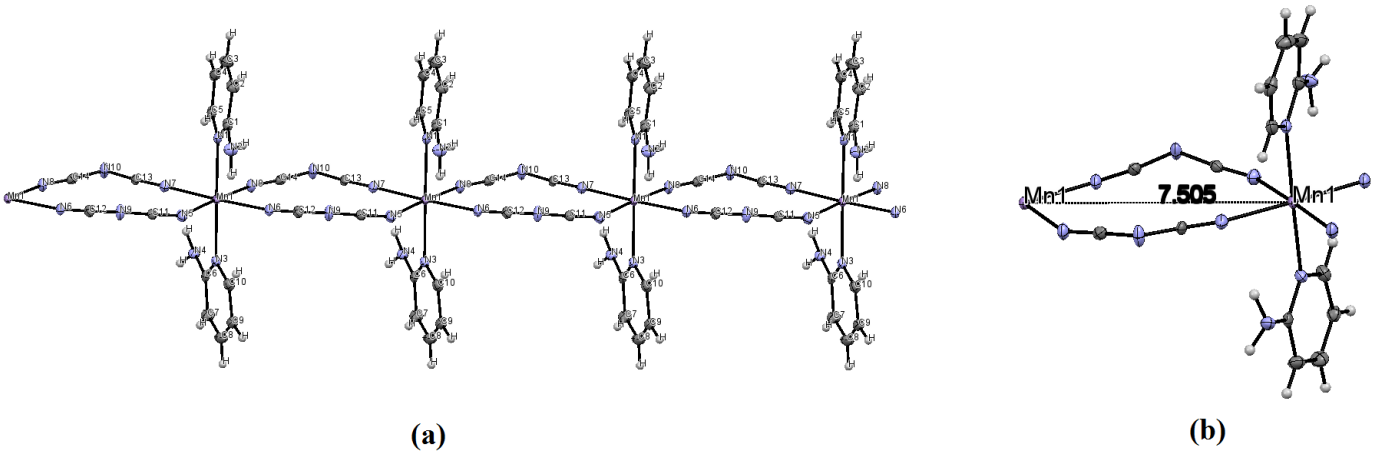


Figure 24: (a) 1D polymeric chain of $[Mn(2\text{-}Apy)_2(dca)_2]$ along the *c*-axis (b) Mn···Mn intra-chain separation in Å.[149]

**Table VI: Comparative data on $M–N_{py}$, $M\text{-}Nd_{ca}$ bond lengths and $N_{dca}–M–Nd_{ca}$, $N_{py}–M–N_{dca}$ bond angles of some $[M(dca)_2(L)_2]_n$.**

| Complex | $M–N_{py}$ (Å) | $M–N_{dca}$ (Å) | | $N_{dca}–M–N_{dca}$ (°) | | $N_{py}–M–N_{dca}$ (°) | | Ref |
|---|---|---|---|---|---|---|---|---|
| $[Mn(dca)_2(pydz)_2]_n$ | 2.2870(13) | 2.2009(13) | 2.2150(13) | 88.09(5) | 180 | 87.96(5) | 91.14(5) | 151 |
| $[Fe(dca)_2(pydz)_2]_n$ | 2.221(4) | 2.153(3) | 2.153(3) | 87.94(14) | 180 | 88.89(10) | 91.11(10) | 151 |
| $[Co(dca)_2(4\text{-}OMP)_2]_n$ | 2.126(4) | 2.116(4) | 2.124(5) | 90.34(17) | 180 | 91.16(17) | 90.47(17) | 152 |
| $[Cd(dca)_2(4\text{-}OMP)_2]_n$ | 2.302(3) | 2.340(4) | 2.354(3) | 93.24(11) | 180 | 90.66(12) | 91.38(12) | 152 |

In the symmetric unit of the compound, the two planes C1C2C3C4C5N1 and C6C7C8C9C10N3 are not coplanar as their torsional angle is found to be 9.58°. This may be most probably due to the hydrogen bonding requirement. Moreover, the N-atoms of both amino groups of 2-Apy does not take part in coordination. They however constitute, together with dca, sources of intermolecular and intramolecular hydrogen bonding as shown in Figure 25.

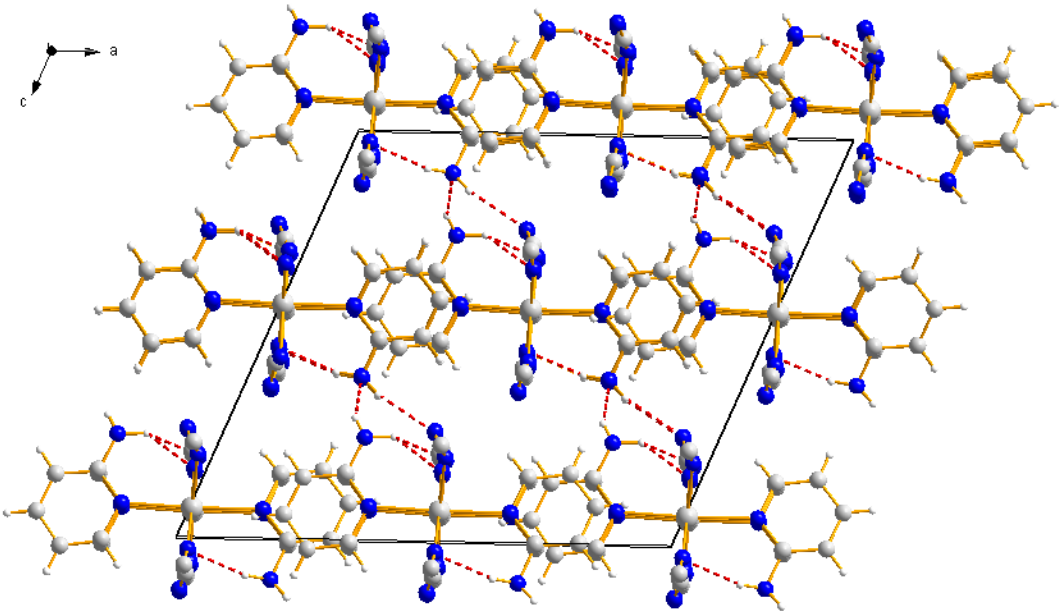


Figure 25: Hydrogen bonding occurring in $[Mn(2\text{-}Apy)_2(dca)_2]$ compound along the *b*-axis.

It is expected that each C≡N group constitutes a source of π–acceptor for H-bond. Many authors have demonstrated that the basicity of nitrogen seems to be much greater than that of the CN π-electrons, therefore C≡N terminal with π-electrons as a proton acceptor is most likely not plausible. [153,154]

From Figure 25, it can be observed that there are two kinds of hydrogen bonds; the conventional and the bifurcated hydrogen bonds types. As shown in Figure 26, both are of N-H···N types, with N-acceptor originating from the C≡N functional groups of dca.

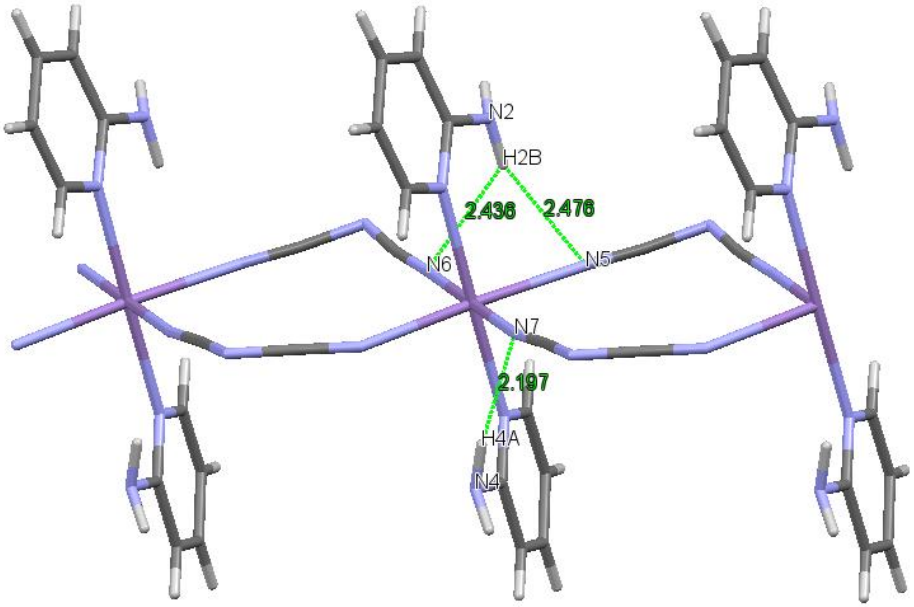


Figure 26: Intramolecular H-bonding (N-H···N) in $[Mn(2\text{-}Apy)_2(dca)_2]$.

The bifurcated hydrogen bond forms for N2-H2B···N6 (130.12°) and N2-H2B···N5 (130.78°), with respective distances of 2.436(4) Å and 2.476(4) Å. Here, N2 atom from the free amino group acts as a donor atom for both N5 and N6 atoms. On the other hand, the conventional hydrogen bond extends to the atoms N4-H4A···N7 (167.77°) and measures 2.197 Å, suggesting its stronger nature than the bifurcated H-bonds. These intramolecular bonds stabilise the 1D chain.

Apart from these intramolecular H-bonding, intermolecular H-bonding are also present in the complex and are built along the *b*-axis from the connections between neighbouring parallel molecules as shown in Figure 27.

It is worth noted that intermolecular interactions along the *b*-axis are built from the connection of N2–H2A···N4 hydrogen bonds arising from neighbouring parallel molecules. These intermolecular hold adjacent chains together and therefore lead to the formation of a layered structures.

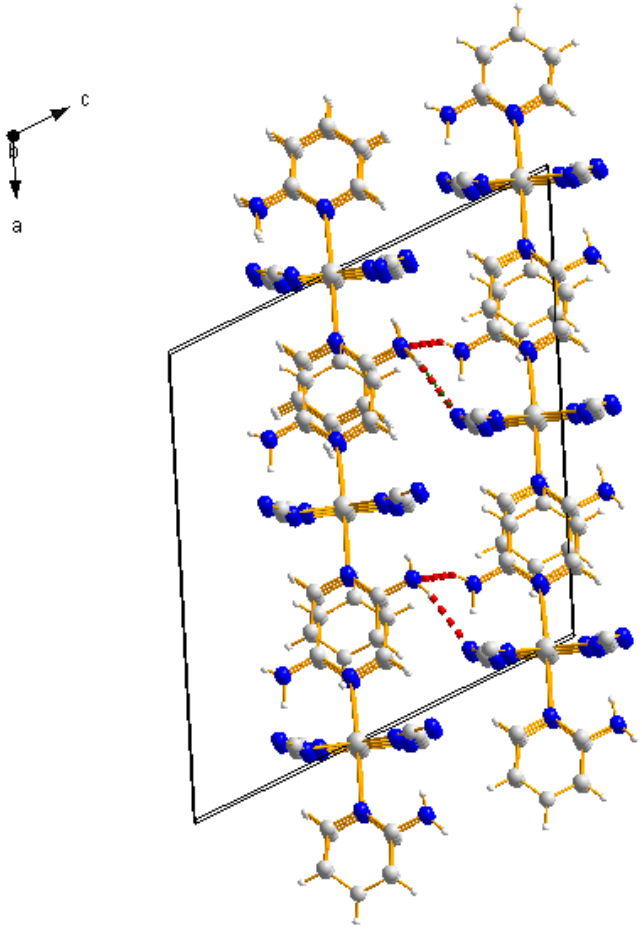


Figure 27: Intermolecular H-bonding shown in red along the *b*-axis (intramolecular H-bond have been removed for clarity).

There are essentially two intermolecular hydrogen bonds. The first one arises along N4-H4B···N9 (160.76°), with a H4B···N9 distance of 2.352 Å. The second one lies along N2-H2A···N4 (143.00°), with a H2A···N4 distance equal to 2.492 Å as shown in the figure below.

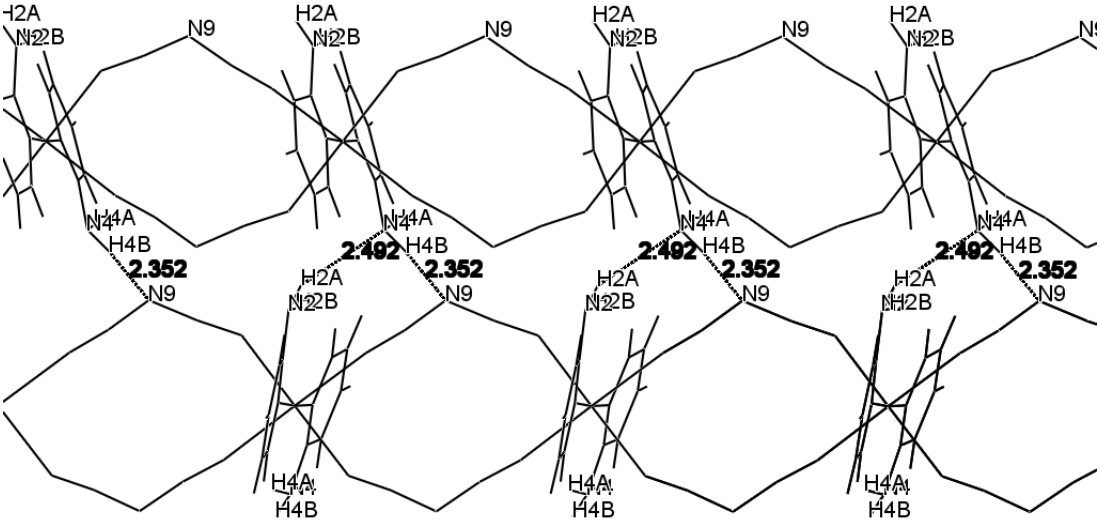


Figure 28: Intermolecular hydrogen bonds between adjacent molecules along the *a*-axis.

Therefore, for the intermolecular hydrogen bonding in $[Mn(2\text{-}Apy)_2(dca)_2]$, N4 acts both as a donor and an acceptor atom. The table below shows hydrogen bonds lengths and their respective angles in $[Mn(2\text{-}Apy)_2(dca)_2]$ complex.

**Table VII: Hydrogen Bonds (Å and °) for $[Mn(2\text{-}Apy)_2(dca)_2]$**

| D–H···A | Nature | d(D–H) | d(H···A) | d(D–A) | $\theta$(DHA) |
|---|---|---|---|---|---|
| N2–H2B···N6#1 | intramolecular | 0.96(4) | 2.43(4) | 3.138(4) | 130.12(3) |
| N2–H2B···N5 | intramolecular | 0.96(4) | 2.48(4) | 3.183(4) | 130.78(3) |
| N4–H4A···N7 | intramolecular | 0.89(5) | 2.20(5) | 3.081(4) | 167.77(4) |
| N2–H2A···N4#2 | intermolecular | 0.80(4) | 2.49(4) | 3.164(4) | 143.00(3) |
| N4–H4B···N9#3 | intermolecular | 0.90(4) | 2.36(4) | 3.217(4) | 161.76(3) |

*Symmetry transformation used to generate equivalent atoms:* #1: x, 1+y, z #2: -1/2+x, 3/2-y, -1/2+z #3: 1/2+x, 1/2-y, 1/2+z

However, hydrogen bonding is not the only NCI present in the molecule. π···π interactions are also present. These interactions arise between parallel aromatic rings as shown in Figure 29(a) below.

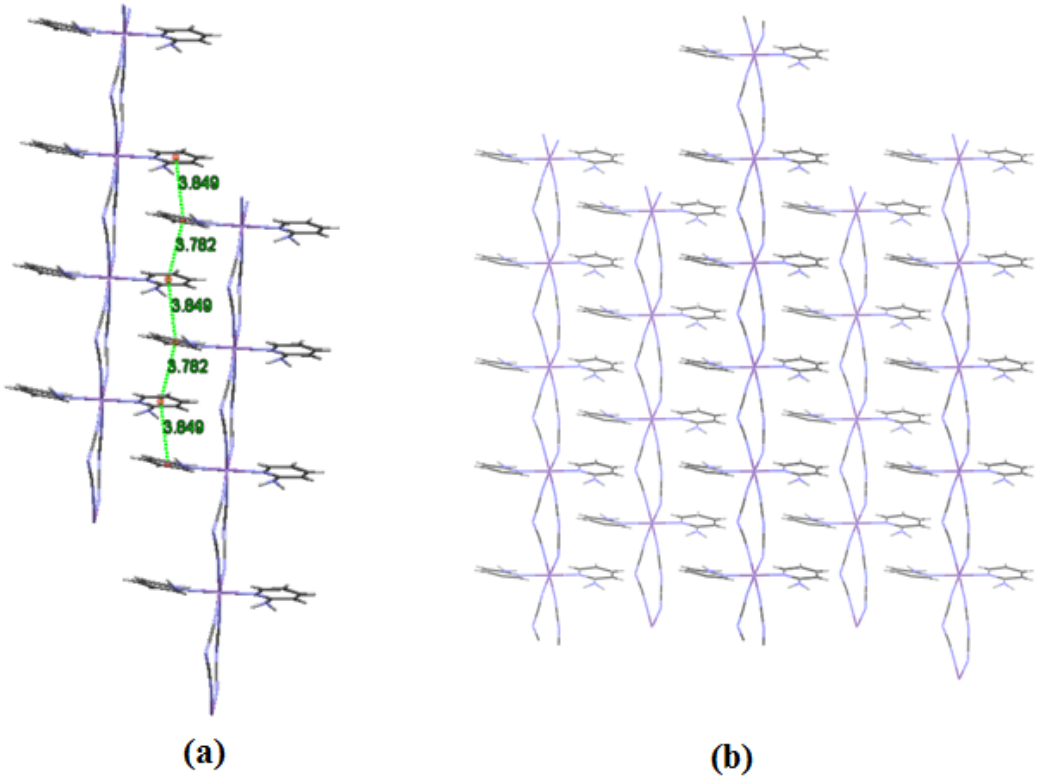


Figure 29: (a) π–π interaction along the c-axis (b) stacking diagram due to pi-pi interactions in $[Mn(2\text{-}Apy)_2(dca)_2]$.

The distances between parallel stacking centroids are not identical, as there is a regular repetitive distance alteration of 3.840 Å and 3.782 Å along the *c*-axis. The shorter distance being observed when the measurement is made from centroid C6C7C8C9C10N3 to C1C2C3C4C5N1.

Therefore, $[Mn(2\text{-}Apy)_2(dca)_2]$ complex extends to form an infinite polymeric chain along the *b*-axis through H-bonds, while the π stacking is the primary contact connecting adjacent pyridine aromatic rings along the *c*-axis. The abundant non-covalent interaction present in the compound therefore contributes in assembling of the compound in a three-dimensional structure as shown in **Erreur ! Source du renvoi introuvable.** below.

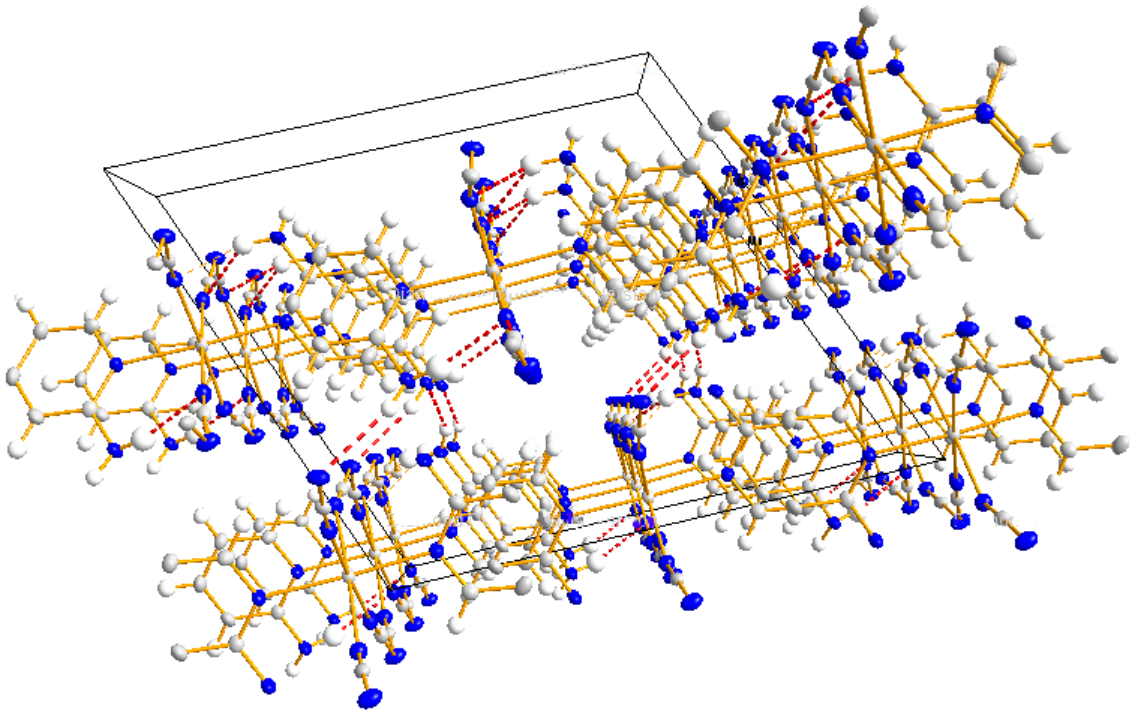

Figure 30: ORTEP stacking diagram of $[Mn(2\text{-}Apy)_2(dca)_2]$ complex.

**Table VIII: Selected bond lengths and angle for $[Mn(2\text{-}Apy)_2(dca)_2]$**

| Atoms 1,2 | d 1,2 [Å] | Atoms 1,2,3 | Atoms 1,2,3 [°] |
|---|---|---|---|
| C1 – N1 | 1.348(5) | N1 – C1 – N2 | 118.2(3) |
| C1 – N2 | 1.370(4) | C3 – C2 – C1 | 119.1(3) |
| C2 – C3 | 1.367(5) | C1 – C2 – H2 | 120.400 |
| C2 – H2 | 0.9500 | C2 – C3 – C4 | 119.7(3) |
| C3 – C4 | 1.394(5) | C4 – C3 – H3 | 120.100 |
| C3 – H3 | 0.9500 | C5 – C4 – H4 | 121.100 |
| C4 – C5 | 1.371(5) | N1 – C5 – C4 | 124.1(3) |
| C4 – H4 | 0.9500 | C4 – C5 – H5 | 118.000 |
| C5 – N1 | 1.354(5) | N3 – C6 – C7 | 121.8(3) |
| C5 – H5 | 0.9500 | N4 – C6 – C7 | 119.2(3) |
| C6 – N4 | 1.370(4) | C8 – C7 – C6 | 119.0(3) |
| C6 – C7 | 1.419(5) | C7 – C8 – C9 | 119.7(3) |
| C7 – C8 | 1.363(5) | C9 – C8 – H8 | 120.100 |
| C8 – H8 | 0.9500 | C10 – C9 – C8 | 118.1(3) |
| C9 – C10 | 1.381(4) | C8 – C9 – H9 | 120.900 |
| C10 – H10 | 0.9500 | N3 – C10 –H10 | 118.300 |
| C11 – N5 | 1.162(4) | N8 – Mn1 – N7 | 90.95(10) |
| C12 – N9 | 1.299(4) | N8 – Mn1 – N6#1 | 88.04(11) |
| C13 – N7 | 1.155(4) | N5 – Mn1 – N6#1 | 91.75(10) |
| C14 – N8 | 1.156(4) | N7 – Mn1 – N6#1 | 177.96(11) |
| Mn1 – N8#1 | 2.211(3) | N5 – Mn1 – N3 | 86.73(10) |
| Mn1 – N5 | 2.226(3) | N8 – Mn1 – N1 | 90.99(10) |
| Mn1 – N6#1 | 2.231(3) | N3 – Mn1 – N1 | 177.46(14) |
| Mn1 – N3 | 2.302(3) | C1 – N2 – H2A | 123.(3) |
| Mn1 – N1 | 2.303(3) | C6 – N3 – C10 | 118.0(3) |

| | | | |
|---|---|---|---|
| N2 – H2B | 0.96(4) | C12 – N6 – Mn1#2 | 171.5(2) |
| N4 – H4B | 0.90(4) | C13 – N7 – Mn1 | 170.6(3) |
| N6 – Mn1#2 | 2.231(3) | C14 – N8 – Mn1#2 | 145.9(2) |
| N8 – Mn1#2 | 2.211(3) | C13 – N10 – C14 | 120.1(3) |

*Symmetry transformation used to generate equivalent atoms:* #1 x, 1+y, z #2 x, -1+y, z

### 3.6.2. Single crystal X-ray diffraction of $[Zn_3(H_2O)_2(NPA)_6]$ complex

As shown in Figure 31 and Table IX, the crystallographic analysis reveals that $[Zn_3(H_2O)_2(NPA)_6]$ crystallizes in a triclinic crystal system with a $P\bar{1}$ space group and no solvent molecules are found to be trapped in the structure. The structure is centrosymmetric, with Zn2 atom located in the inversion centre. The asymmetric unit contains two Zn centres (Zn1 and Zn2), about which three NPA ligands and one $H_2O$ ligand are coordinated. The full molecule fills the unit cell which contains three Zn atoms, six coordinated NPA ligands, and two coordinated terminal $H_2O$ ligands.

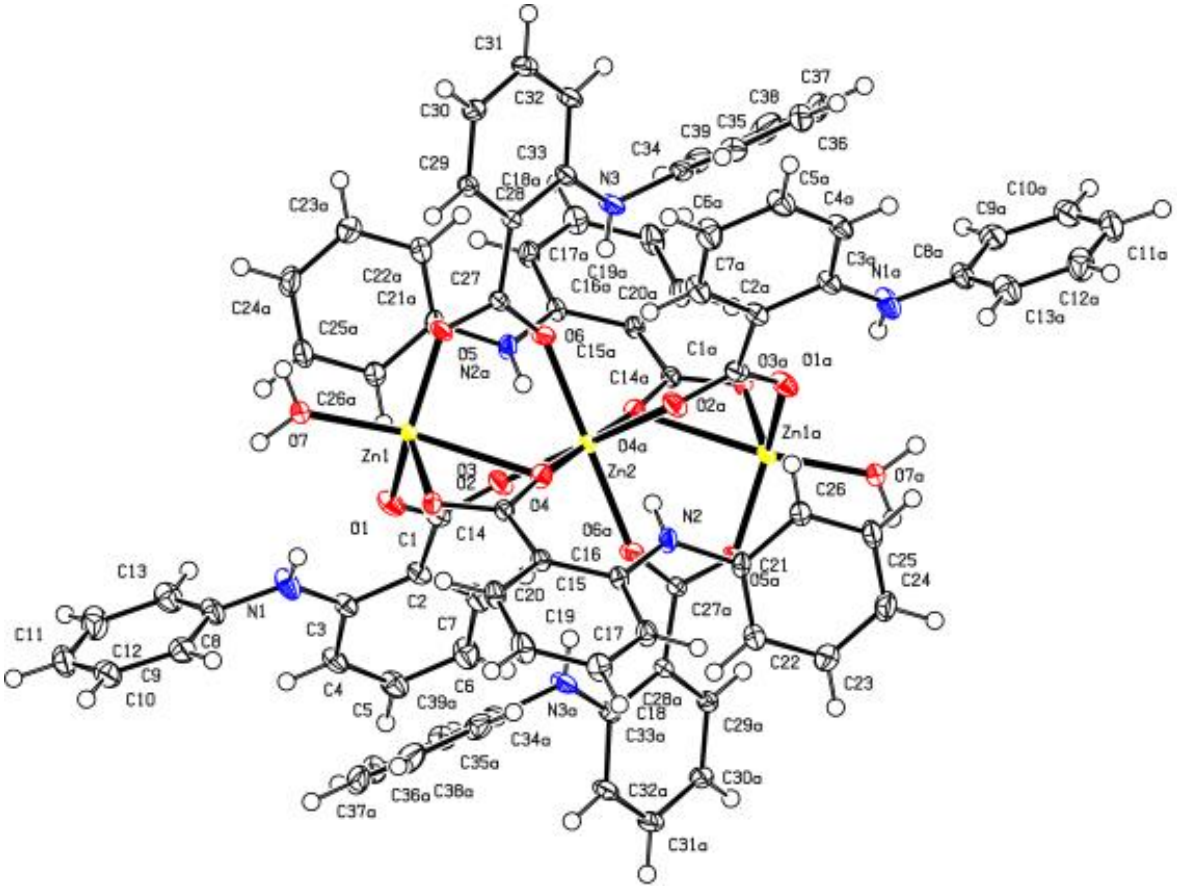


Figure 31: View of $[Zn_3(H_2O)_2(NPA)_6]$, drawn with 50% probability displacement ellipsoids. [Symmetry code: (a) -x + 1, -y + 1, -z + 1.]. [155]

**Table IX : Crystal data and structure refinement for $[Zn_3(H_2O)_2(NPA)_6]$**

| Chemical formula | $C_{78}\ H_{64}\ N_6\ O_{14}\ Zn_3$ |
|---|---|
| *M*r | 1505.46 |
| Crystal system, space group | Triclinic, $P\bar{1}$ |
| Temperature (K) | 100 |
| a, b, c (Å) | a = 11.0968(5); b = 12.8319(6); c = 13.3134(6) |
| α, β, γ (°) | α = 111.703(2); β = 108.028(2); γ = 93.125(2) |
| V ($Å^3$) | 1643.97(13) |
| Z | 1 |
| Radiation type | Mo *Kα* |
| μ (mm-1) | 1.16 |
| Crystal size (mm) | 0.3 × 0.1 × 0.03 |
| ***Data collection*** | |
| Diffractometer | Bruker Kappa Venture D8 |
| Absorption correction | Multi-scan |
| $T_{min}$, $T_{max}$ | 0.664, 0.748 |
| No. of measured, independent and observed [I > 2σ(I)] reflections | 86106, 10025, 8556 |
| $R_{int}$ | 0.044 |
| (sin θ/λ)max (Å-1) | 0.714 |
| ***Refinement*** | |
| $R[F^2 > 2\sigma(F^2)]$, $wR(F^2)$, *S* | 0.030, 0.078, 1.03 |
| No. of reflections | 10025 |
| No. of parameters | 477 |
| $\Delta\rho_{max}$, $\Delta\rho_{min}$ (e $Å^{-3}$) | 0.65, -0.84 |

The central $Zn^{2+}$ atom, Zn2, is hexacoordinated exclusively by O atoms from the carboxylate groups of the NPA ligands. This central zinc atom has an approximately octahedral molecular geometry, with bond angles ranging from 83.78° for O2-Zn2-O4' to 96.22° for O2-Zn2-O4 [symmetry code: (i) -x + 1, -y + 1, -z + 1]. The ligand bond lengths range from 2.0219(11) A˚ for Zn2–O2, to 2.0775(10) A˚ for Zn2–O6, to 2.1762(10) A˚ for Zn2–O4. The N atoms of the NPA ligands are not found to be involved in any coordination activity with the zinc centres, which is consistent with predictions from hard-soft acid base theory (HSAB). However, the hydrogen atoms on the nitrogen atoms are involved in intramolecular hydrogen bonding with the carboxylate O atoms of NPA, as shown in Figure 32. The hydrogen bond distances within the asymmetric unit were all around a similar length, with distances of 2.01(2) Å for O1···H1, 2.12(2) Å for O4···H2 and 2.04(2) Å for O6···H3.

Intramolecular hydrogen bonding between the two symmetry-generated halves of the molecule was found between H2 and O2' with a distance of 2.28(3) Å (Figure 33). The same H-atom forms a bifurcated H-bond with O4 (H2···O4 = 2.116 Å).

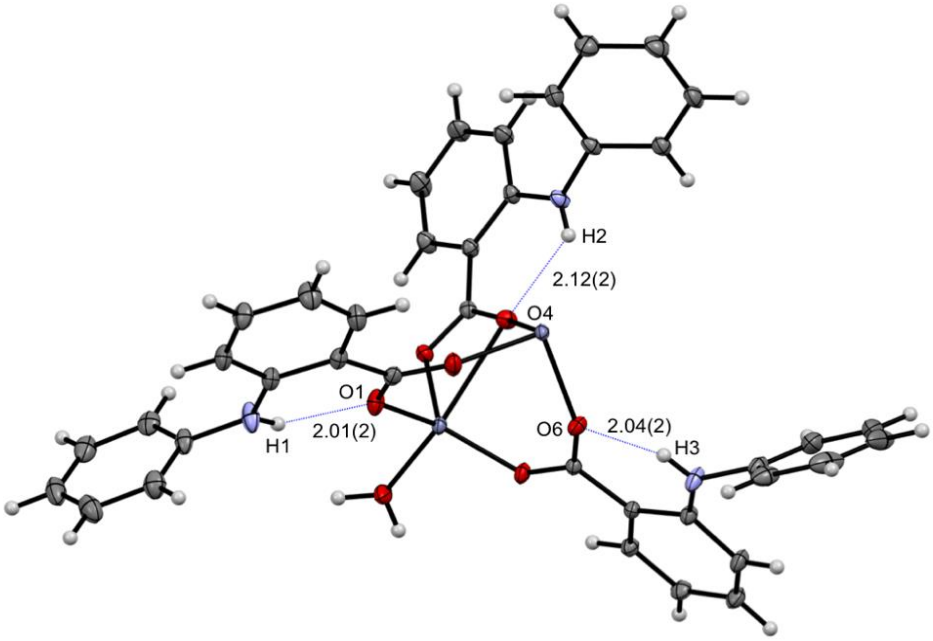


Figure 32: View of half the asymmetric unit of $[Zn_3(H_2O)_2(NPA)_6]$, drawn with 50% probability displacement ellipsoids, highlighting intramolecular hydrogen bonding. Distances are in Å. [155]

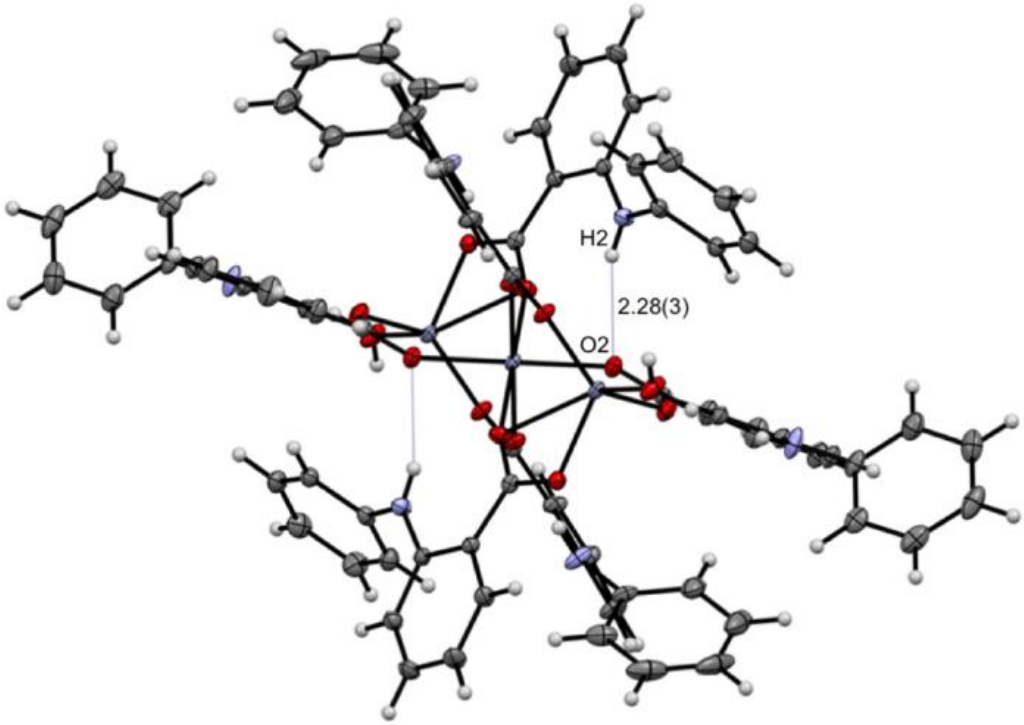


Figure 33: View of half the asymmetric unit of $[Zn_3(H_2O)_2(NPA)_6]$, drawn with 50% probability displacement ellipsoids, highlighting the intramolecular hydrogen bonding. Distances are in Å. [155]

The two water ligands are located axially along the complex. Each water ligand is involved in intermolecular hydrogen bonding from a H atom to a carboxylate O atom of the next unit cell, with a distance of 1.80 (3) Å for H7A···O3. As a result, each complex donates and accepts a hydrogen bond at each end, for a total of four intermolecular hydrogen bonds per molecule. Owing to symmetry-generated elements, it can be seen that all four hydrogen bonds arise from one unique bond (Figure 35). These intermolecular hydrogen bonds are the main factor determining the arrangement of adjacent complexes. Due to the centrosymmetric nature of the complex and the axial hydrogen bonding, adjacent complexes attach end-on to form rigid straight chains, as shown in Figure 34. The angle each chain forms is precisely 180° such that the molecules stack perfectly when viewing a chain of complexes down the *c*-axis (Figure 35). All unique hydrogen bonds and their respective length are shown in Table IX.

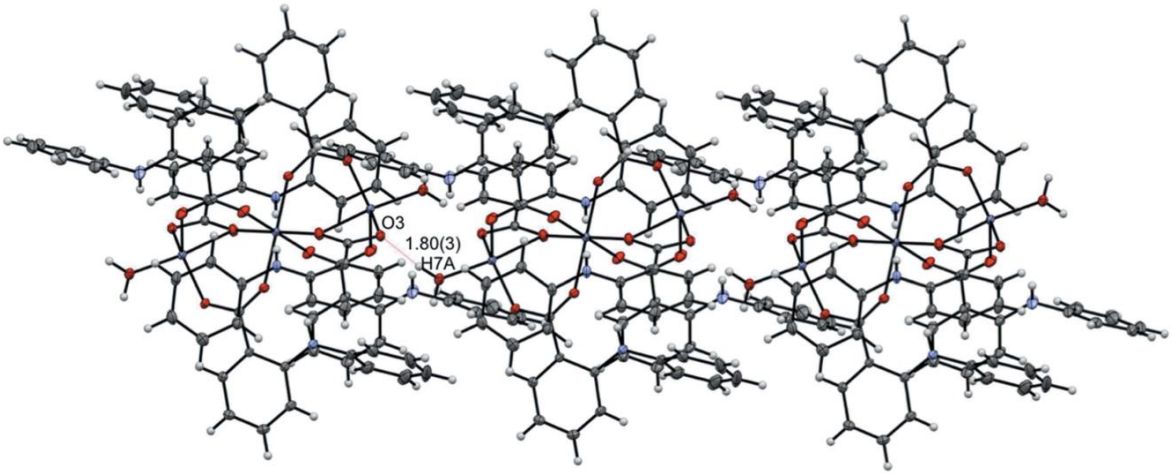


Figure 34: View three molecules of $[Zn_3(H_2O)_2(NPA)_6]$ with 50% probability displacement ellipsoids, highlighting intermolecular hydrogen bonding. Distances are in Å. [155]

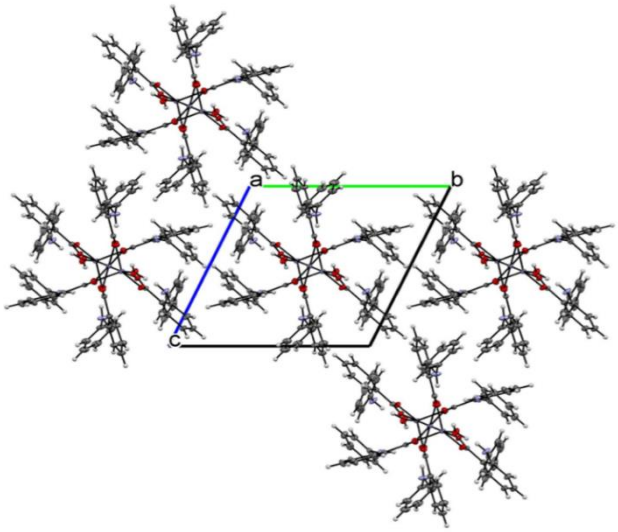


Figure 35: View of the macromolecular packing of $[Zn_3(H_2O)_2(NPA)_6]$ with 50% probability displacement ellipsoids, as viewed along the *c*-axis. [155]

**Table X: Selected hydrogen bond distances (Å) and angles (°) for $[Zn_3(H_2O)_2(NPA)_6]$**

| D–H···A | | d(D–H) | d(H···A) | d(D–A) | $\theta$(DHA) |
|---|---|---|---|---|---|
| N(1)-H(1)···O(1)#1 | intramolecular | 0.83(2) | 2.01(2) | 2.648(2) | 133.06(2) |
| N(2)-H(2)···O(2)#1 | intramolecular | 0.81(2) | 2.28(3) | 3.021(3) | 149.88(2) |
| N(2)-H(2)···O(4)#1 | intramolecular | 0.81(2) | 2.12(3) | 2.93(3) | 129.24(2) |
| N(3)-H(3)···O(6) | intramolecular | 0.80(2) | 2.04(2) | 2.687(2) | 137.56(2) |
| O(7)-H(7A)···O(3)#1 | intermolecular | 0.90(3) | 1.80(3) | 2.696(1) | 171.89(3) |

*Symmetry transformation used to generate equivalent atoms:* #1: x-1, 1-y, z-1

The exterior $Zn^{2+}$ centres (Zn1 and Zn1') are penta-coordinated with only O atoms coordinated to these centres. The Zn1–O bond lengths are generally shorter than the Zn2–O bond lengths, with Zn1–O1 at 1.9298(11) Å, Zn1–O3 at 1.9920(10) Å, and Zn1–O5 at 1.9063(10) Å. However, the notable outlier is that one of the O atoms coordinated to Zn1 comes from an $H_2O$ ligand, with Zn1–O7 at 2.0274(12) Å. Because the Zn1 and Zn1' centers are pentacoordinated, there are two modes which can be used to classify their geometry: square pyramidal or trigonal bipyramidal. This distinction is made mathematically by utilizing the Addison parameter. [156] In this analysis, a trigonal index ($\tau$) is assigned according to the equation $\tau = (ß - \alpha)/60$, where ß and α are the largest angles about the metal center. If the resulting value for $\tau$ is closer to 0, the centre is classified as having a square pyramidal geometry. Conversely, if $\tau$ lies closer to 1, the centre is classified as having a trigonal bipyramidal geometry. This analysis yielded the value $\tau = 0.5\overline{66}$, indicating that the molecular geometry of Zn1 and its symmetry-generated counterpart Zn1' are best described as trigonal bipyramidal in nature.

The zinc centres Zn1 and Zn2 are bridged by O4 which is one of the carboxylate oxygens of NPA with a Zn1-Zn2 distance of 3.4557 Å. Interestingly, all of the Zn-O bond lengths for both Zn1 and Zn2 are statistically unique. The Zn-O bond lengths, which vary from 1.2555(17) Å between O6-C27 to 2.538(1) Å between Zn1-O4, are displayed in Table XI. Additionally, most of the O-Zn-O bond angles are different, as can be seen in Table XII. These different lengths and angles are likely due to both the variety of ligands (both $H_2O$ and NPA) and the different binding modes of the oxygen atoms. Another factor may be the intramolecular hydrogen bonding between the nitrogen atoms and the carboxylate oxygen atoms of NPA, which may be inducing torsion.

**Table XI: Selected distances of the asymmetric unit (Å) for $[Zn_3(H_2O)_2(NPA)_6]$**

| Atoms 1,2 | d 1,2 [Å] | Atoms 1,2 | d 1,2 [Å] |
|---|---|---|---|
| Zn(1)-O(1) | 1.9298(11) | Zn(2)-O(6) | 2.078 |
| Zn(1)-O(3) | 1.9920(10) | Zn(1)-Zn(2) | 3.456 |
| Zn(1)-O(4) | 2.538(1) | O(1)-C(1) | 1.2742(19) |
| Zn(1)-O(5) | 1.9063(10) | O(2)-C(1) | 1.2559(18) |
| Zn(1)-O(7) | 2.0274(12) | O(3)-C(14) | 1.2866(17) |
| Zn(2)-O(2) | 2.0219(11) | O(4)-C(14) | 1.2572(17) |
| Zn(2)-O(2) | 2.0219(11) | O(5)-C(27) | 1.2788(17) |
| Zn(2)-O(4) | 2.1762(10) | O(6)-C(27) | 1.2555(17) |
| Zn(2)-O(4) | 2.1762(10) | C(1)-C(2) | 1.484(2) |
| Zn(2)-O(4) | 2.176 | C(27)-C(28) | 1.4893(19) |
| Zn(2)-O(6) | 2.0775(10) | C(14)-C(15) | 1.4752(19) |

**Table XII: Selected bond angles of the asymmetric unit (°) for $[Zn_3(H_2O)_2(NPA)_6]$**

| Atoms 1,2,3 | Atoms 1,2,3 [°] | Atoms 1,2,3 | Atoms 1,2,3 [°] |
|---|---|---|---|
| Zn(1)-O(4)-Zn(2) | 93.98 | O(2)-Zn(2)-O(2) | 180 |
| Zn(2)-O(4)-Zn(1) | 93.98 | O(4)-Zn(2)-O(4) | 180 |
| Zn(1)-O(1)-C(1) | 123.40(10) | O(6)-Zn(2)-O(6) | 180 |
| Zn(1)-O(3)-C(14) | 104.17(9) | O(2)-Zn(2)-O(4) | 96.22(4) |
| Zn(1)-O(4)-C(14) | 79.69(9) | O(2)-Zn(2)-O(4) | 83.78(4) |
| Zn(1)-O(5)-C(27) | 127.60(9) | O(2)-Zn(2)-O(4) | 96.22(4) |
| Zn(2)-O(2)-C(1) | 142.24(10) | O(2)-Zn(2)-O(4) | 83.78(4) |
| Zn(2)-O(4)-C(14) | 161.37(10) | O(2)-Zn(2)-O(4) | 83.78 |
| Zn(2)-O(6)-C(27) | 137.10(9) | O(2)-Zn(2)-O(6) | 93.86(4) |
| O(1)-Zn(1)-O(3) | 101.15(5) | O(2)-Zn(2)-O(6) | 86.14(4) |
| O(1)-Zn(1)-O(4) | 97.39(5) | O(2)-Zn(2)-O(6) | 86.14(4) |
| O(1)-Zn(1)-O(7) | 98.30(5) | O(2)-Zn(2)-O(6) | 93.85(4) |
| O(1)-Zn(1)-O(5) | 135.15(5) | O(2)-Zn(2)-O(6) | 93.85 |
| O(3)-Zn(1)-O(4) | 56.54(4) | O(4)-Zn(2)-O(6) | 87.99(4) |
| O(3)-Zn(1)-O(5) | 118.92(5) | O(4)-Zn(2)-O(6) | 92.00(4) |
| O(3)-Zn(1)-O(7) | 97.20(5) | O(4)-Zn(2)-O(6) | 88.00(4) |
| O(4)-Zn(1)-O(5) | 89.33(4) | O(4)-Zn(2)-O(6) | 92.00(4) |
| O(4)-Zn(1)-O(7) | 151.66(5) | O(4)-Zn(2)-O(6) | 87.99 |
| O(5)-Zn(1)-O(7) | 95.94(5) | O(1)-C(1)-O(2) | 123.47(14) |

For all three NPA ligands of the asymmetric unit, both of the carboxylate O atoms are involved in coordination to Zn. This indicates that the formal negative charge of the ligand is delocalized between both oxygen atoms instead of being localized on a single O atom. Each of the bond distances between C and O atoms of the carboxylate groups are statistically different, indicating that the resonance is not shared equally. In all cases, the longer carboxylate C–O bond lengths are found for O atoms that are coordinated to Zn1, while shorter carboxylate C–O bond lengths are found for O atoms that are coordinated to Zn2 (Figure 36). The longer carboxylate C–O bond lengths for C1–O1 at 1.2742(19)

Å, C14–O3 at 1.2866(17) Å, and C27–O5 at 1.2788(17) Å correlate with shorter Zn1–O bond lengths of Zn1–O1 at 1.9298(11) Å, Zn1–O3 at 1.9920(10) Å, and Zn1–O5 at 1.9063(10) Å respectively. By contrast, the shorter carboxylate C–O bond lengths for C1–O2 at 1.2559(18) Å, C14–O4 at 1.2572(17) Å, and C27–O6 at 1.2555(17) Å correlate with longer Zn2–O bond lengths of Zn2–O2 at 2.0219(11) Å, Zn2–O4 at 2.1762(10) Å, and Zn2–O6 at 2.0775(10) Å respectively. The longer Zn2–O bond lengths are likely due to increased steric hindrance around the central Zn2 atom and additional intramolecular hydrogen bonding of the O atoms (O2, O4, and O6) with a neighboring NPA ligand, causing additional torsion and strain (Figure 36).

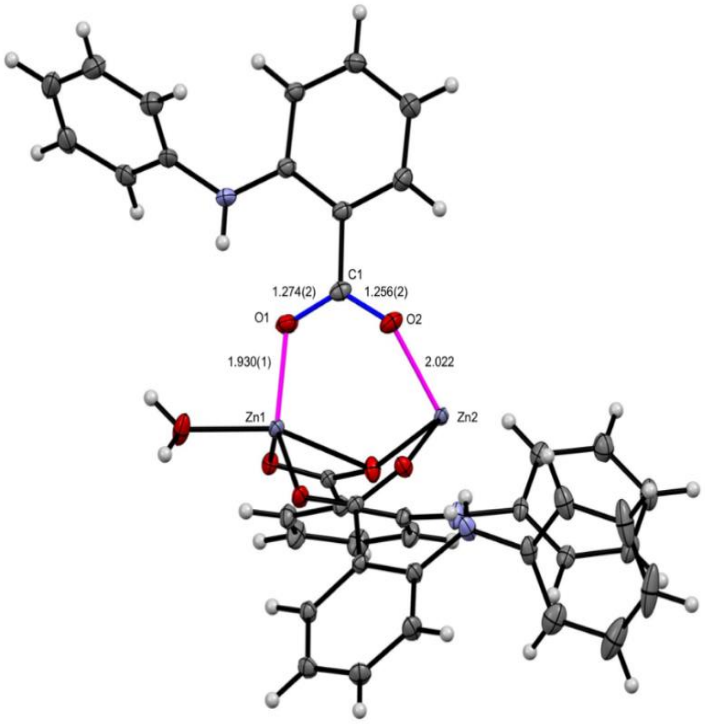


Figure 36: View of half the asymmetric unit of $[Zn_3(H_2O)_2(NPA)_6]$, drawn with 50% probability displacement ellipsoids, highlighting Zn–O and carboxylate bond distances (Å). [155]

Multiple chains of the complex are stacked side-by-side (Figure 37), with the arene groups of the NPA ligands of adjacent complexes in close proximity to one another. Perpendicular π stacking is observed between the centroid defined by C8-C13 and C31, with a distance of 3.619 Å and an angle of 83.4° (Figure 37). π stacking is the primary contact connecting adjacent chains of molecules along the *a* and *b* axes, while hydrogen bonding is the primary contact along the *c*-axis.

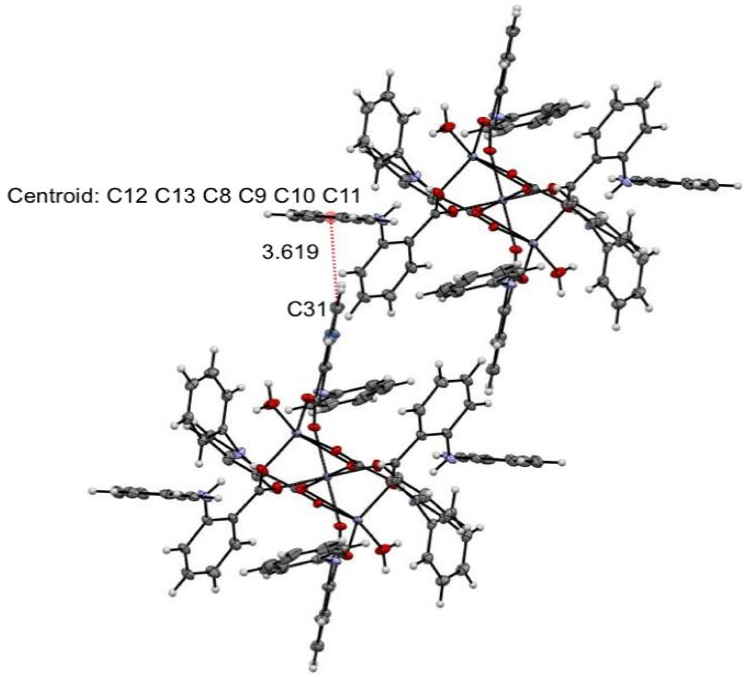


Figure 37: View of two molecules of $[Zn_3(H_2O)_2(NPA)_6]$, drawn with 50% probability displacement ellipsoids, highlighting perpendicular π stacking. The distances are in Å. [155]

Therefore, in the $[Zn_3(H_2O)_2(NPA)_6]$ complex, both hydrogen bonding and π stacking are the non-covalent interactions which organise the supramolecular conformation of the structure.

### 3.6.3. Single crystal X-ray diffraction of $[Cd(2\text{-}Apy)_2(dca)_2]$ complex

The ORTEP view of the crystal structure of $[Cd(2\text{-}Apy)_2(dca)_2]$ together with the numbering scheme used in the corresponding tables is shown in Figure 38. In $[Cd(2\text{-}Apy)_2(dca)_2]$ compound, as in the $[Mn(2\text{-}Apy)_2(dca)_2]$ complex above, Cd is found to be in coordination environment in a distorted $MN_6$-octahedron. The two long Cd–$N_{py}$ bonds are in the range 2.324(5) – 3.347(4) Å in the axial position, and the four short Cd–$N_{dca}$ bonds range from 2.326(2) – 3.351(2) Å in the equatorial one. Moreover, the bond angle between the two pyridine N-atoms N3–Cd1–N1 is 177.00° and deviate slightly from 180°. The other bond angles range from 85.64(99)° for N3–Cd–N1 to 93.66(88)° for N3–Cd1–N7, are consistent with similar compounds previously reported. [33,150] Therefore, $[Cd(2\text{-}Apy)_2(dca)_2]$ is found to be in a similar configuration as [Mn(2-Apy)2(dca)2] complex (Figure 38). The Cd–$N_{py}$ bond length values, although lower, are similar with those obtained in the literature for Cd(II) compounds containing 2-Apy. [157]

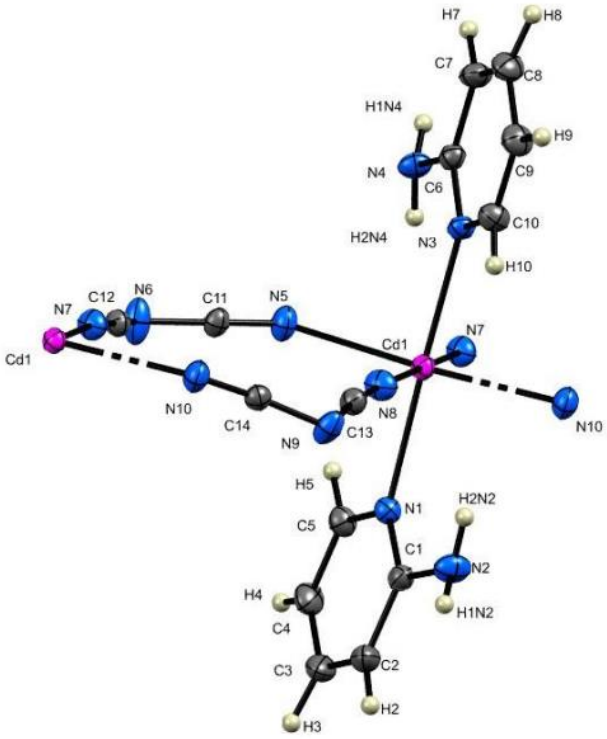


Figure 38: Molecular structure and atom-labelling scheme for $[Cd(2\text{-}Apy)_2(dca)_2]$ complex with its numbering scheme. [149]

As in Mn complex, the metal centers in $[Cd(2\text{-}Apy)_2(dca)_2]$ are also arranged in linear chains along the *c*-axis (Figure 39(a)) with [Cd1···Cd1] intra-chain separations, through the bridging dicyanamido anions of 7.609 Å (Figure 39(b)). The shortest [Cd1···Cd1] inter-chain distance is 7.442 Å. Both the inter-chain and intra-chain separations are therefore greater in Cd(II) complex. Again, while the intra-chain separations are similar, the inter-chain distances are also slightly longer than those reported in Table VI above for other catena-$M(dca)_2L_2$ structures [117, 118].

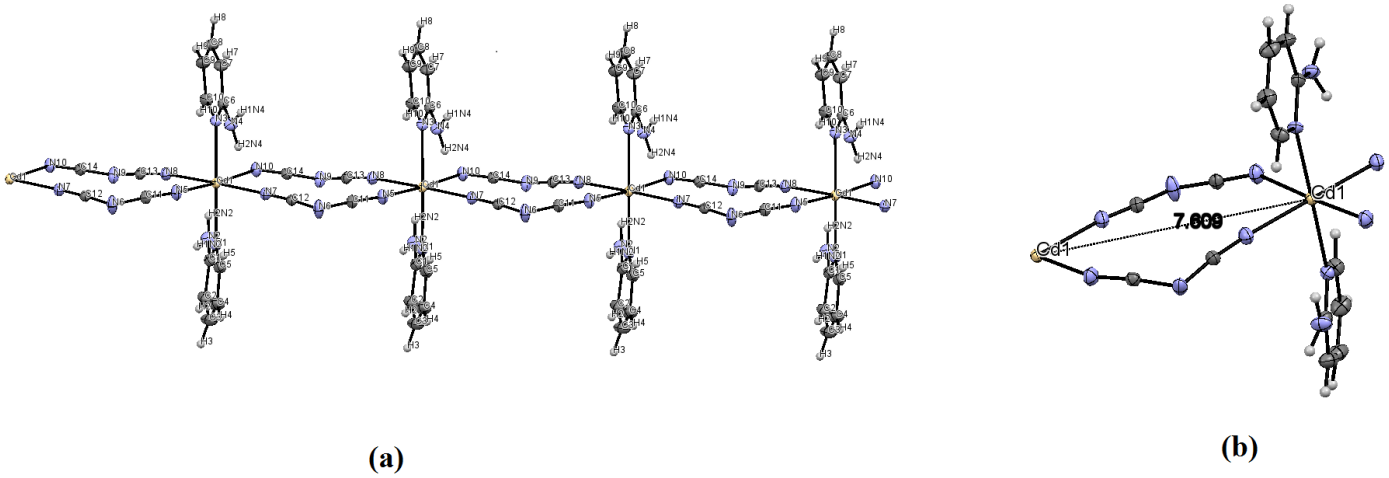


**(a)** **(b)**

Figure 39: (a) 1D polymeric chain of $[Cd(2\text{-}Apy)_2(dca)_2]$ along the c-axis (b) Cd···Cd intra-chain separation in Å. [149]

The two planes C1C2C3C4C5N1 and C6C7C8C9C10N3 have a torsional angle of -7.86°. Therefore, the two pyridine centroids are not coplanar, but their torsional angle is lower than that of Mn(II) compound above.

It can be expected that NCIs found in $[Mn(2\text{-}Apy)_2(dca)_2]$ are the same found in $[Cd(2\text{-}Apy)_2(dca)_2]$ due to their similar structural nature. A priori, this seems to be obvious, however the non-covalent interactions witness some differences. The hydrogen bonds in the compound are exclusively intermolecular in nature as shown in the Figure 40.

As in $[Mn(2\text{-}Apy)_2(dca)_2]$, hydrogen bonds arise along corresponding neighbouring N4–H1N4···N9 and N2–H1N2···N4 atoms. However, in $[Cd(2\text{-}Apy)_2(dca)_2]$, the H1–N4···N9 is 2.344 Å with a H-bond angle of 168.34°. The distance H1–N2···N4 equals 2.49 Å with a H-bond angle of 141.08°. Moreover, there is similarity between the two compounds, in which N4 acts as both a donor and an acceptor for hydrogen bonding.

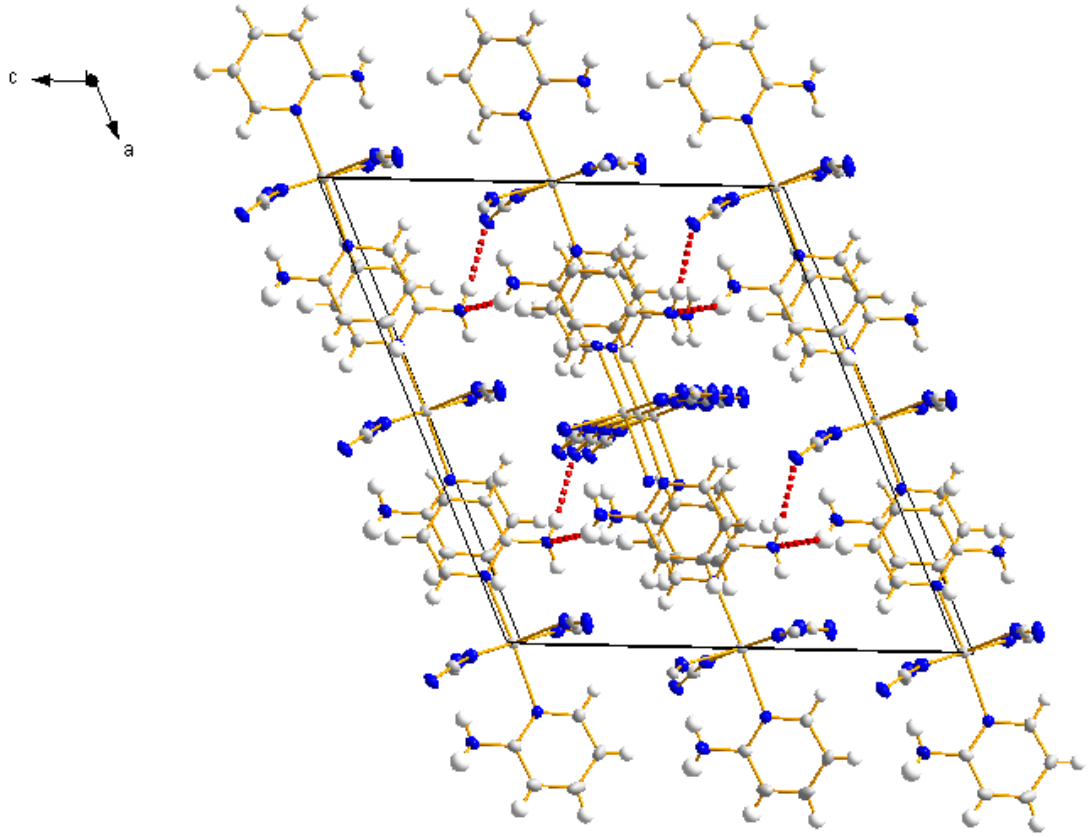


Figure 40: Intermolecular H-bond in in $[Cd(2\text{-}Apy)_2(dca)_2]$.

**Table XIII: Hydrogen Bonds (Å and °) for [Cd(2-Apy)$_2$(dca)$_2$]**

| D–H···A | d(D–H) | d(H···A) | d(D–A) | $\theta$(DHA) |
|---|---|---|---|---|
| N2–H1N2–N4#1 | 0.84(5) | 2.49(4) | 3.33(3) | 141.08(3) |
| N4–H1N4–N9#2 | 0.83(4) | 2.35(4) | 3.18(3) | 168. 34(3) |

*Symmetry transformation used to generate equivalent atoms:* #1: 1/2+x, 3/2-y, 1/2+z #2: -1/2+x, 3/2-y, -1/2+z

Apart from the intermolecular hydrogen bonding, π···π interactions also occur along the *c*-axis between adjacent pyridine rings centroids as shown on Figure 41.

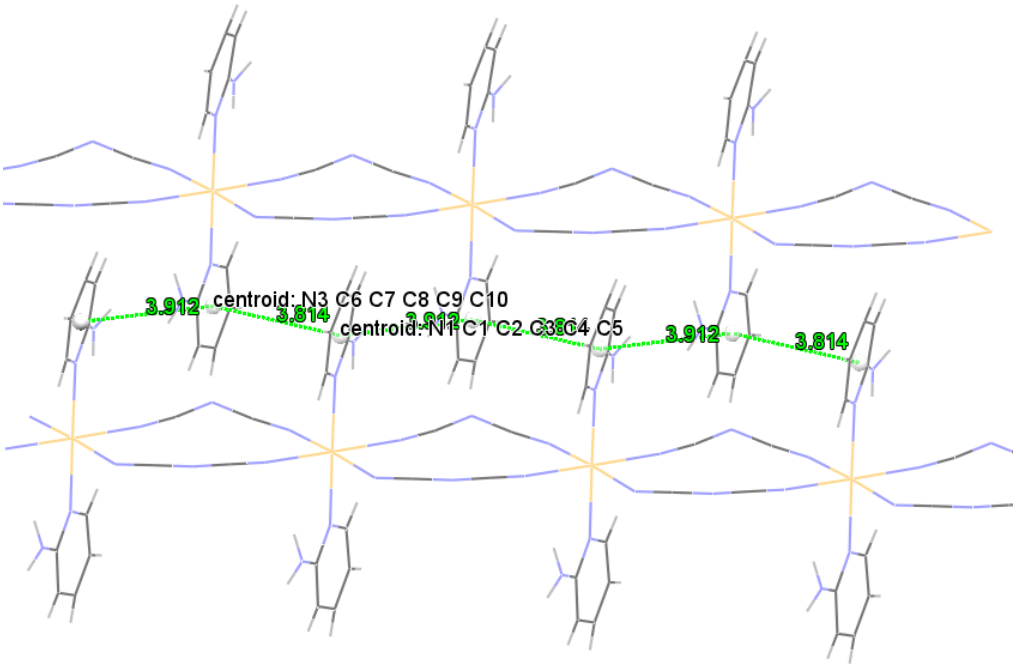


Figure 41: π-π interaction of [Cd(2-Apy)$_2$(dca)$_2$] along the *c*-axis.

As in [Mn(2-Apy)$_2$(dca)$_2$], it is observed that there is alternating π···π interaction distance of 3.814 and 3.912 Å between successive parallel centroids (Figure 41). This alteration distance is however greater than that observed in [Mn(2-Apy)$_2$(dca)$_2$] complex. The shorter distance (3.814 Å), as in [Mn(2-Apy)$_2$(dca)$_2$], is measured when we move between centroids along the *c*-axis from C6C7C8C9C10N3 to C1C2C3C4C5N1.

**Table XIV: Crystal data and structure refinement for $[Cd(2\text{-}Apy)_2(dca)_2]$**

| Empirical formula | $C_{14}H_{12}CdN_{10}$ |
|---|---|
| $M_r$ | 432.74 |
| Crystal system, Space group | Monoclinic, *Cc* |
| Temperature (K) | 130(2) |
| *a, b, c* (Å) | 16.1412(2), 7.6088(0), 14.5173(2) |
| β (°) | 113.371(2) |
| V(Å$^3$) | 1636.66(4) |
| *Z* | 4 |
| Radiation type | Mo *Kα* |
| μ (mm$^{-1}$) | 1.355 |
| Crystal size (mm) | 0.30 x 0.20 x 0.10 |
| ***Data collection*** | |
| Diffractometer | Xcalibur, Sapphire3, Gemini |
| Absorption correction | Multi-scan |
| $T_{max}$, $T_{min}$ | 0.969, 1.000 |
| No. of measured, independent and observed [$I > 2\sigma(I)$] reflections | 23787, 8221, 7995 |
| $R_{int}$ | 0.019 |
| $(\sin \theta/\lambda)_{max}$ (Å$^{-1}$) | 0.861 |
| ***Refinement*** | |
| $R[F^2 > 2\sigma(F^2)]$, $wR(F^2)$, *S* | 23787, 8221, 7995 |
| No. of reflections | 8221 |
| No. of parameters | 275 |
| $\Delta\rho_{max}$, $\Delta\rho_{min}$ (e Å$^{-3}$) | 2.29, - 0.31 |

**Table XV: Selected bond lengths and angle for $[Cd(2\text{-}Apy)_2(dca)_2]$**

| Atoms 1,2 | d 1,2 [Å] | Atoms 1,2,3 | Atoms 1,2,3 [°] |
|---|---|---|---|
| Cd1 – N3 | 2.324(5) | Cd1 – N3 – N5 | 90.874(99) |
| Cd1 – N8 | 2.3426(19) | Cd1 – N3–N10#1 | 85.635(99) |
| Cd1 – N7#1 | 2.348(2) | Cd1 – N8– N1 | 90.279(87) |
| N1 – C1 | 1.334(5) | Cd1 – N7–N10#1 | 90.745(77) |
| N1 – C5 | 1.354(5) | N1 – C1– C5 | 118.789(311) |
| N2 – C1 | 1.364(3) | N1 – C1 – C2 | 30.198(166) |
| N2 – H1N2 | 0.84(5) | N1 – C5 – H2N2 | 170.119(1025) |
| N3 – C10 | 1.352(5) | N3 – C6 – C10 | 117.172(292) |
| N4 – C6 | 1.371(3) | N3 – C6 – N4 | 31.213(139) |
| N6 – C12 | 1.291(3) | N3 – H10 – H2N4 | 166.041(1519) |
| N6 – C11 | 1.304(3) | N3 – Cd1 – N4 | 96.249(166) |
| N8 – C13 | 1.154(3) | N3 – N4 –H2N4 | 20.847(923) |
| N9 – C13 | 1.297(3) | N4 – H1N4 – H1N2#2 | 94.441(2851) |
| N10 – C14 | 1.157(3) | N4 – C6 – C7 | 30.500(123) |
| C1 – C2 | 1.408(3) | N4 – N3 – H1N2#2 | 108.714(927) |
| C2 – C3 | 1.372(6) | N5 – C11 – Cd1 | 139.265(187) |
| C2 – H2 | 0.92(4) | N5 – C11 – N6 | 3.711(138) |
| C3 – C4 | 1.384(6) | N5 – Cd1 – N6 | 142.583(112) |
| C3 – H3 | 0.97(4) | N6 – C12 – C11 | 121.124(225) |

| | | | |
|---|---|---|---|
| C4 – H4 | 0.88(4) | N6 – C11 – N5 | 3.286(122) |
| C6 – C7 | 1.405(3) | N7 – C12 – H2N4#3 | 106.126(981) |
| C7 – C8 | 1.365(5) | N7 – C12 – N6 | 3.419(137) |
| C8 – C9 | 1.406(5) | N8 – C13 – Cd1 | 171.626(202) |
| C8 – H8 | 0.93(4) | N8 – C13 – N9 | 3.597(136) |
| C9 – C10 | 1.372(3) | C1 – N1 – N2 | 118.788(251) |
| C9 – H9 | 1.00(4) | C2 – H2 – C3 | 118.076(2515) |
| C10 – H10 | 0.89(3) | C9 – H9 – C10 | 120.133(2141) |

*Symmetry transformation used to generate equivalent atoms: #1: x, 1+y, z; #2: -1/2+x, 3/2-y, -1/2+z; #3: x, -1+y, z*

### 3.7. Thermal analyses

The thermal behaviour of the complexes was studied using the combined analysis techniques, TGA/DTG under nitrogen atmosphere. All the compounds undergo decomposition with the release of gaseous species. Decomposition steps vary from one compound to the other. Figure 42, 44, and 46 show various thermal behaviour of the complexes.

#### 3.7.1. TGA/DTG thermogram of $[Mn(2\text{-}Apy)_2(dca)_2]$

The thermogram of $[Mn(2\text{-}Apy)_2(dca)_2]$ (Figure 42) shows two decomposition steps that are accompanied by endothermic events in the DTG curve.

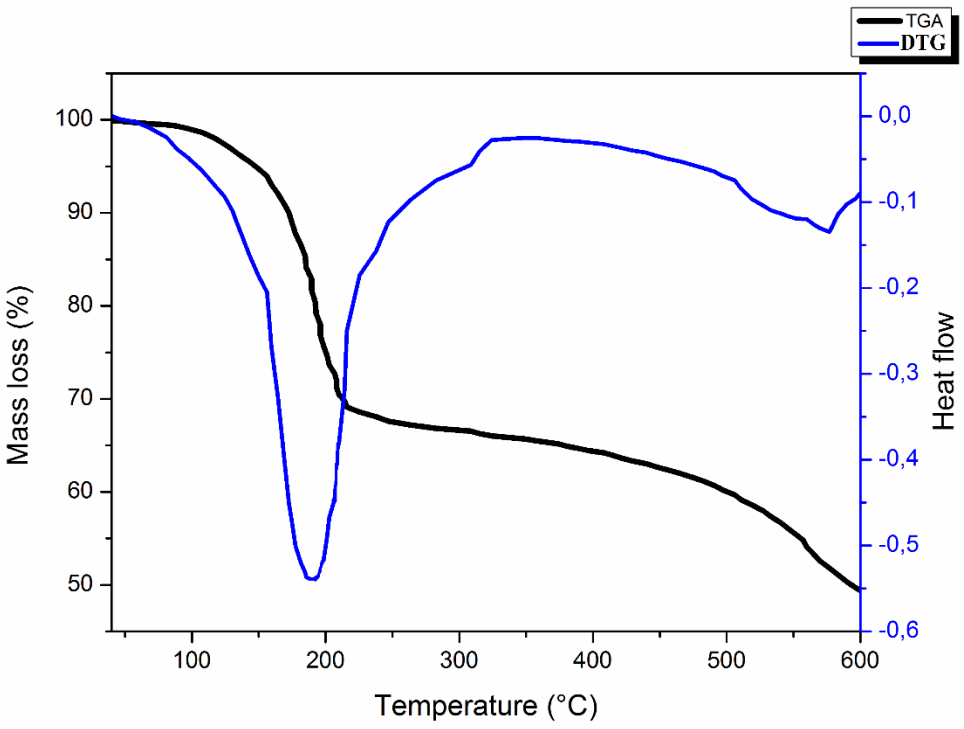


Figure 42: TGA/DTG thermograms of $[Mn(2\text{-}Apy)_2(dca)_2]$.

The first and major decomposition step takes place with a mass loss of 33.11 %, and occurs at the temperature range of 130 – 250 °C. This can be attributed to the loss of one molecule of 2-Apy followed by HCN and $H_2$ from the second 2-Apy ligand (Calc. 32.77 %). The second major decomposition step which occurs at the temperature range 500–600 ˚C (Δm = 17.87 %) and is attributed to loss of the remaining 2-Apy ligand (calc. 17.32 %). A stable mass is reached at around 600 °C, with a residual mass of 49.02 % attributed to the deposition of $Mn(dca)_2$ (Calc. 49.91 %). This decomposition pattern is similar to that of the coordination polymer *catena*-[(bis($\mu_2$-dicyanamido-N,N')-bis(pyridazine-N)-manganese(II)] found in the literature. [151] The decomposition scheme proposed is shown in the following figure.

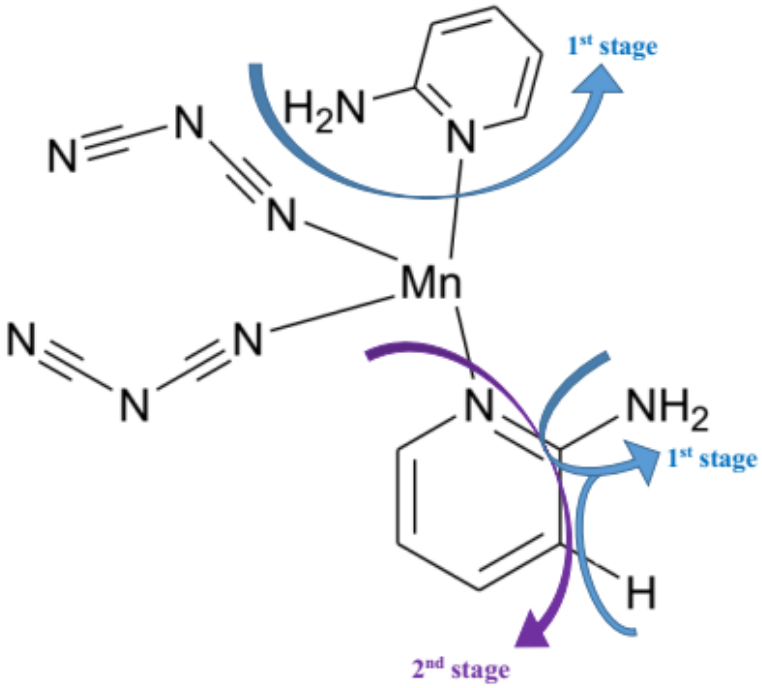


Figure 43: Proposed scheme of thermal degradation of $[Mn(2\text{-}Apy)_2(dca)_2]$.

### 3.7.2. TGA/DTG thermogram of $[Zn_3(H_2O)_2(NPA)_6]$

The TGA thermogram of $[Zn_3(NPA)_6(H_2O)_2]$ shows a mass loss in four steps. $[Zn_3(H_2O)_2(NPA)_6]$ complex is stable up to 140 °C and shows no weigh loss below this temperature. However, the mass loss occurs between the temperature range 200 – 590 °C as shown in the Figure **44**.

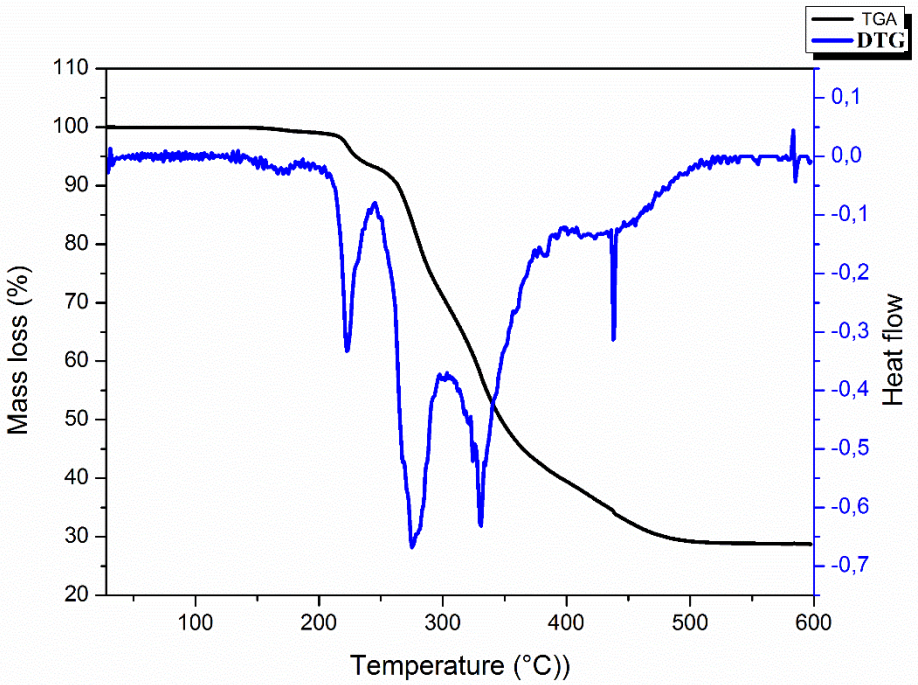


Figure 44: TGA/DTG thermograms of $[Zn_3(H_2O)_2(NPA)_6]$.

The weight loss (6.49 %) in the first step (200 – 245 °C) probably corresponds to the loss of $C_5H_5$ and HCN fragments and $H_2O$ molecule (calculated 6.11 %). In the second step, there is a percentage loss of 21.94 % occurring at temperature range 245 – 300 °C, probably corresponding to the loss of one $C_{13}H_{11}NO_2$ fragment (from NPA ligand), one $C_7H_3O$ fragment (from the first NPA ligand), and one $H_2O$ molecule (calculated 22.18 %). The third step, which occurs at the temperature range 304 – 378 °C, shows a mass loss of about 32.55 %. This may be due to probable loss of a fragment of $C_{13}H_{11}NO$, a fragment of $C_{13}H_{11}NO_2$ (from two NPA ligands) and one $C_6H_4N$ fragment (calculated 33.21 %). The last step of decomposition corresponds to a mass loss of 14.15 % which occurs at temperature range 387 – 498 °C. This may be due to the loss of one $C_{13}H_{11}NO_2$ fragment from NPA ligand (calculated 13.8 %). A stable mass is reached at 579 °C with a residual mass of 24.87 %, which is probably due to 3ZnO deposition and the loss of $C_7H_5O$ fragment (calculated 24.70 %).

Figure 45 proposes the decomposition scheme for $[Zn_3(H_2O)_2(NPA)_6]$ complex.

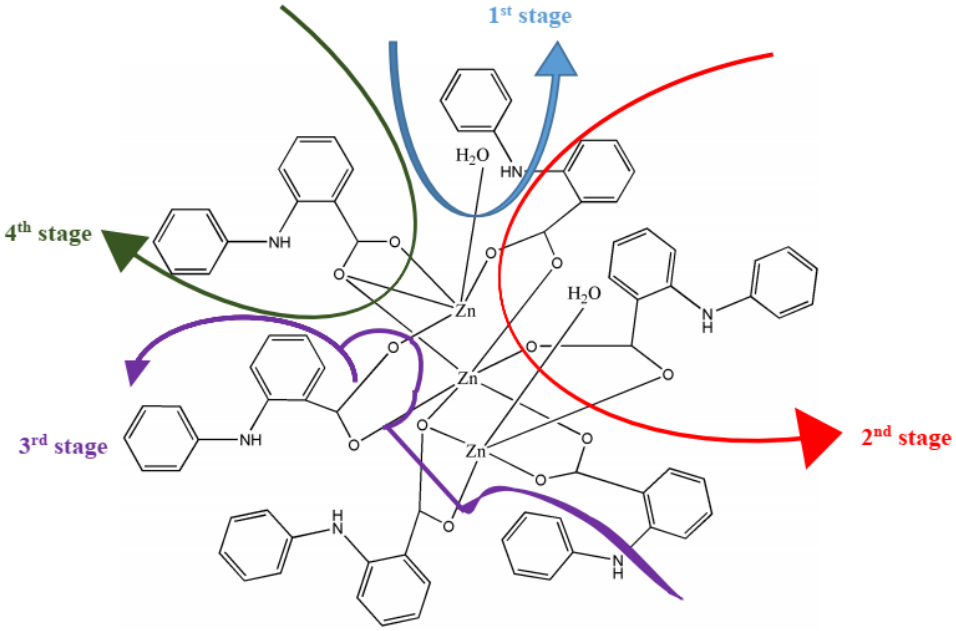


Figure 45: Proposed scheme of thermal degradation of [Zn3(H2O)2(NPA)6].

### 3.1.8. TGA/DTG thermogram of [Cd(2-Apy)2(dca)2]

The TGA thermogram of [Cd(2-Apy)2(dca)2] shows a mass loss in three major steps. The complex is stable up to 45 °C and shows no weigh loss below this temperature. The mass loss occurs between the temperature range 50 – 645 °C as shown in the Figure 46.

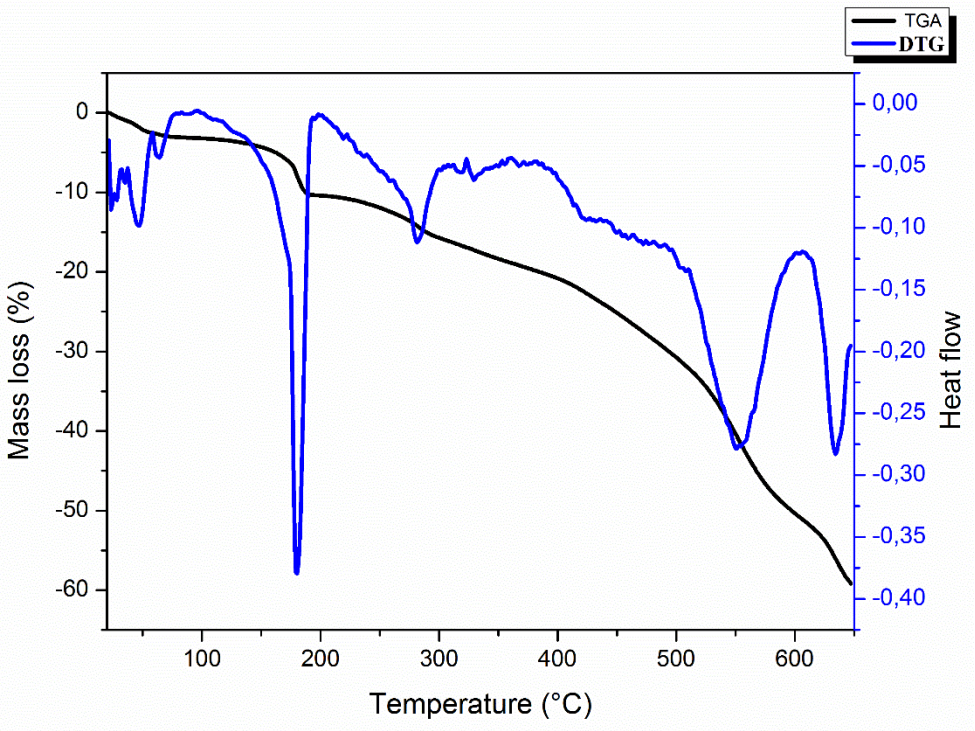


Figure 46: TGA/DTG thermograms of $[Cd(2\text{-}Apy)_2(dca)_2]$.

The weight loss (10.08 %) in the first step (50–177 °C) is probably due to the loss of two dca ($2C_2N_3$) fragments (calculated 9.48 %). The percentage loss of 6.68 % is recorded for the second step and occurs at the temperature range 220–320 °C, probably corresponding to the loss of two amino groups ($2NH_2$) from the two 2-Apy ligands (calculated 7.39 %). The third and the fourth steps, which occur at the temperature range of 450–645 °C, shows a mass loss of about 18.49 %. This may be due to probable loss of one remaining 2-Apy fragment (calculated 18.05 %). A stable mass is reached at temperature greater than 650 °C with a residual mass of 64.75 %, which is probably due to CdN deposition and the loss of $H_2CC_3CH_2$ gas fragment (calculated 65.08 %).

The proposed decomposition scheme for $[Cd(2\text{-}Apy)_2(dca)_2]$ complex is shown in the Figure 47.

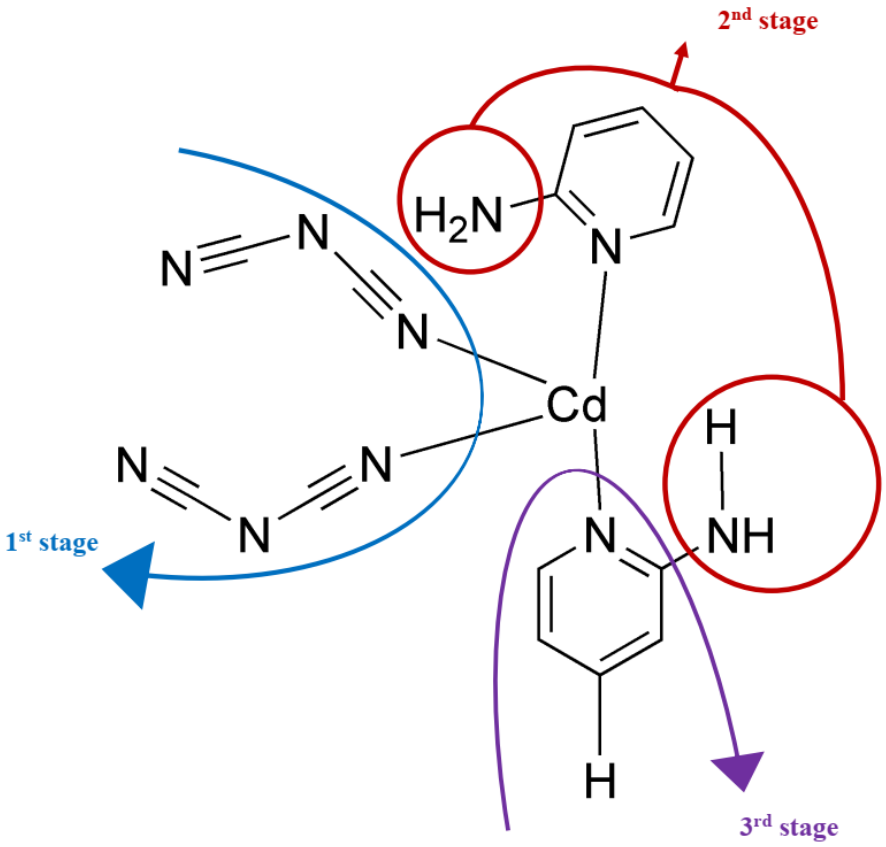


Figure 47: Proposed scheme of thermal degradation of $[Cd(2\text{-}Apy)_2(dca)_2]$.

The corresponding summary of the decomposition scheme of Mn(II), Zn(II), and Cd(II) complexes is shown in Table XVI.

**Table XVI : Mass loss at different temperatures for Mn(II), Zn(II), and Cd(II) complexes**

| Stage | TGA | | |
|---|---|---|---|
| | Temperature range (°C) | Decomposition % (calculated) | Peak Temperature (°C) |
| ***[Mn(2-Apy)$_2$(dca)$_2$] complex*** | | | |
| I | 130–250 | 33.11 (32.77) | 189 |
| II | 500–600 | 17.87 (17.32) | 576 |
| ***[Zn$_3$(H$_2$O)$_2$(NPA)$_6$] complex*** | | | |
| I | 200 – 245 | 6.49 (6.11) | 224 |
| II | 245 – 300 | 21.94 (22.18) | 276 |
| III | 304 – 387 | 32.55 (33.21) | 330 |
| IV | 394 – 572 | 14.15 (13.80) | 437 |
| ***[Cd(2-Apy)$_2$(dca)$_2$] complex*** | | | |
| I | 50–200 | 10.08 (9.48) | 177 |
| II | 220–320 | 6.68 (7.39) | 284 |
| III and IV | 450–645 | 18.49 (18.05) | 550 and 630 |

### 3.8. Hirsfeld surface analysis

In Hirsfeld surface analysis, a colour scheme is applied such that where the contact is shorter than the van der Waals separation, the point is coloured red, white is used for contacts around the van der Waals separation and blue is for longer contacts.

*Crystal Explorer* [144] was used to calculate Hirshfeld surface and subsequent fingerprint plots to quantify the intermolecular contacts present within the 3D supramolecular architecture of the complexes.

#### 3.8.1. Hirsfeld surface analysis for [Mn(2-Apy)$_2$(dca)$_2$] complex

The Mn(II) complex exhibits seven (07) types of intermolecular contacts to the Hirshfeld surface: H···N/N···H bond (37 %); H···C/C···H bond (27.3 %); H···H bond (17.7 %); C···C bond (7.2 %); N···Mn/Mn···N bond (5.1 %); C···N/N···C bond (3.3 %); N···N bond (2.4 %). The general Hirsfeld Surface all possible interactions are shown below.

Figure 22 shows the Hirsfeld surface of the Mn(II) complex with $d_{norm}$ interval ranging from -0.7380 to 1.3734 Å. The red dots on the figure indicate interactions with close contacts, smaller than Van Der Walls.

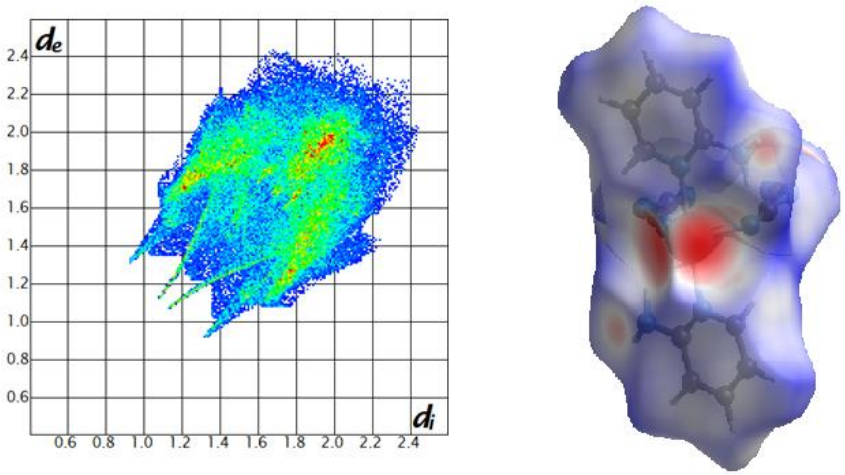


Figure 48: Hirshfeld surface mapped over $d_{norm}$ for the title compound [Mn(2-Apy)$_2$(dca)$_2$].

#### 3.8.1.1. H···N interactions

H···N interactions is the highest contributor (37 %) of the fingerprint plot on the Hirshfeld surface. The interactions arise between the phenyl H-atoms and the surrounding N-atoms of amino and dicyanamide groups, and vice-versa.

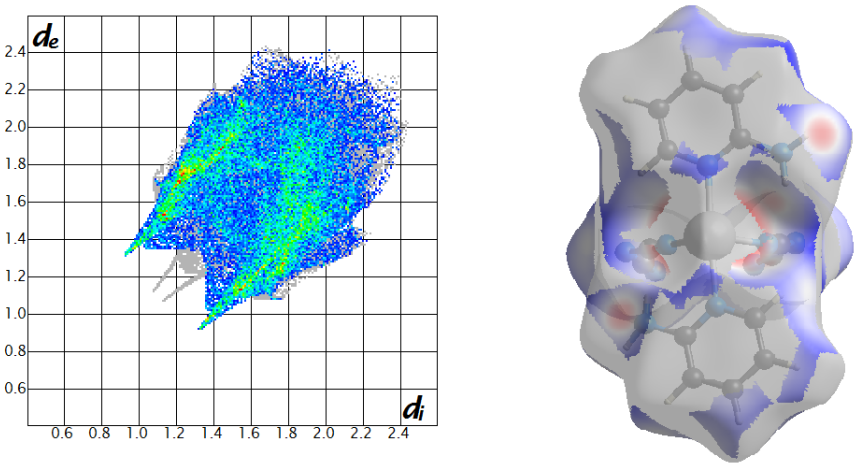


Figure 49: Hirshfeld surface and associated fingerprint plot of $[Mn(2\text{-}Apy)_2(dca)_2]$ showing C–H···N hydrogen bonds.

On the fingerprint plot above, H···N bond contact shows up as a pair of spikes. This might be considered as H-bonding. The stronger contact appears to occur between H-atoms of amino group and a neighbouring N-atom of neighbouring molecule. This is coloured in red as observed on the Hirsfeld surface.

### 3.8.1.2. C···H interactions

The second contributor of the fingerprint plot is the C···H stacking (comparable to C–H···π) with a percentage weight of 27.3 %, which gives rise to a pair of characteristic wings in the fingerprint plot.

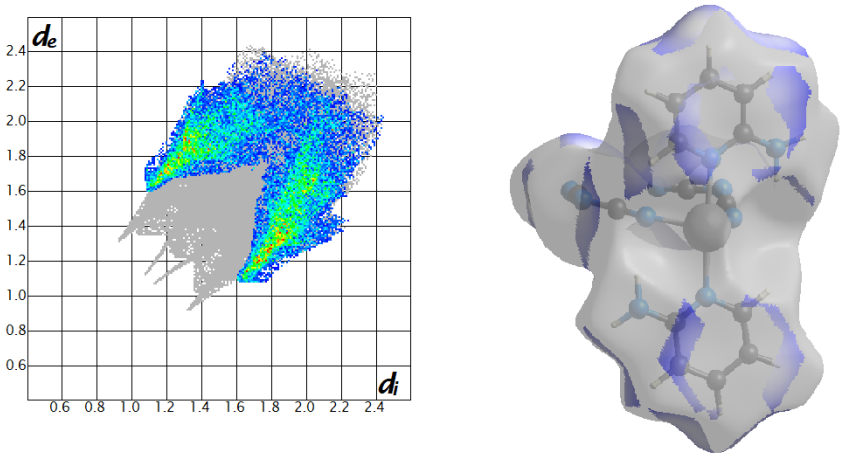


Figure 50: Hirshfeld surface and associated fingerprint plot of [Mn(2-Apy)2(dca)2] showing C–H···C hydrogen bonds.

The intreactions mainly occur between C-H bonds of pyridine ring with neigbouring molecules with $di + de \sim 2.7$ Å.

### 3.8.1.3. H···H interactions

H···H interactions is solely attributed to interactions between neighbouring aromatic hydrogens.

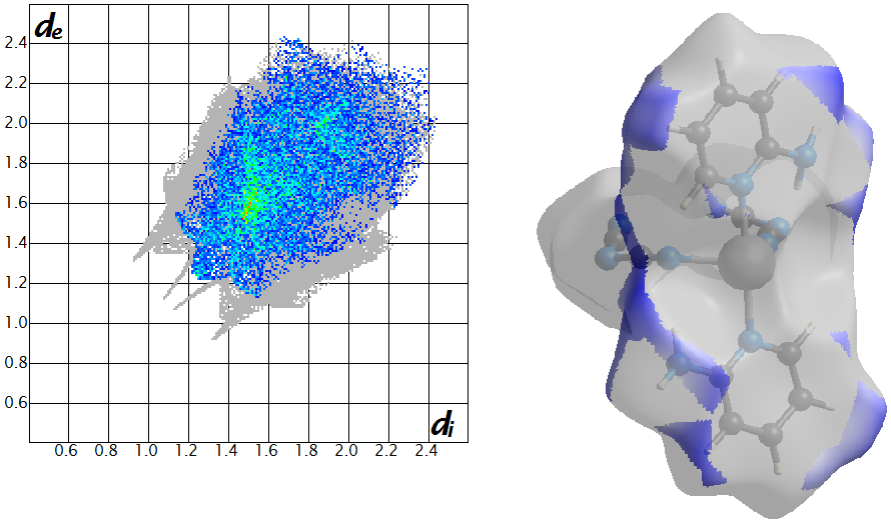


Figure 51: Hirshfeld surface and associated fingerprint plot of $[Mn(2\text{-}Apy)_2(dca)_2]$ showing C–H···H hydrogen bonds.

Its contribution to the fingerprint plot is 17.7 %, with *di* = *de* ~1.2 Å.

### 3.8.1.4. C···C interactions

With 7.2 % contribution of the fingerprint plot, C···C interaction is the fourth contributor to the Hirsfeld surface. It participates in a planar stacking arrangement of the molecule (the so called π···π stacking) between neighbouring pyridine groups.

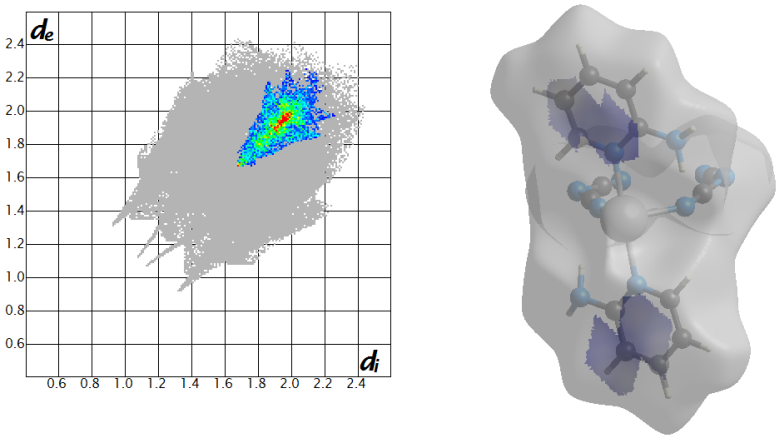


Figure 52: Hirshfeld surface and associated fingerprint plot of $[Mn(2\text{-}Apy)_2(dca)_2]$ showing C···C.

As shown from the fingerprint plot, the contact distance varies from (*d*i = *d*e) 1.7 – 2.2 Å.

### 3.8.1.5. Mn···N interactions

Mn interacts only with terminal N-atoms of dca and is shown as large and intense red spot around the metallic ion. This is indicative of very strong interactions attributed to the coordination bond between metallic ion and N atom of dca. The interaction contributes to 5.1 % to the fingerprint plot and can be seen as spikes on the fingerprint plot below.

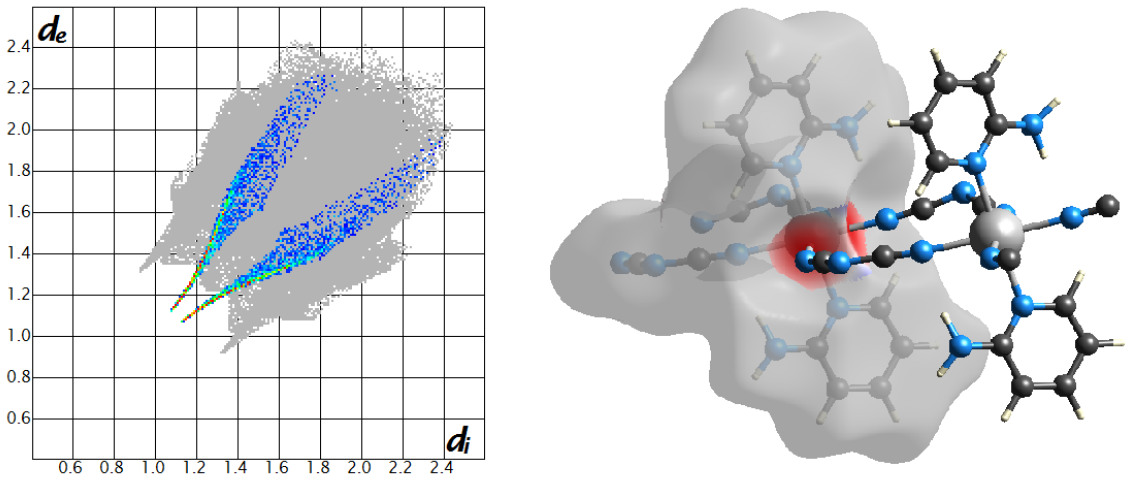


Figure 53: Hirshfeld surface and associated fingerprint plot of $[Mn(2\text{-}Apy)_2(dca)_2]$ showing Mn···N.

The Mn···N interaction is shown as spikes on the fingerprint plot at $de = di \sim 1.1$ Å.

### 3.8.1.6. C···N interactions

There is interaction between the C-atom at the para-position of the pyridine ring with the neighbouring N-atom of another pyridine ring on one side, and on the other side, the N- and C-atoms of dicyanamide interact respectively with C- and N–atoms of the neighbouring dicyanamide. This globally accounts for C···N interactions which contributes to about 3.3 % of the fingerprint plot as shown on the figure 54.

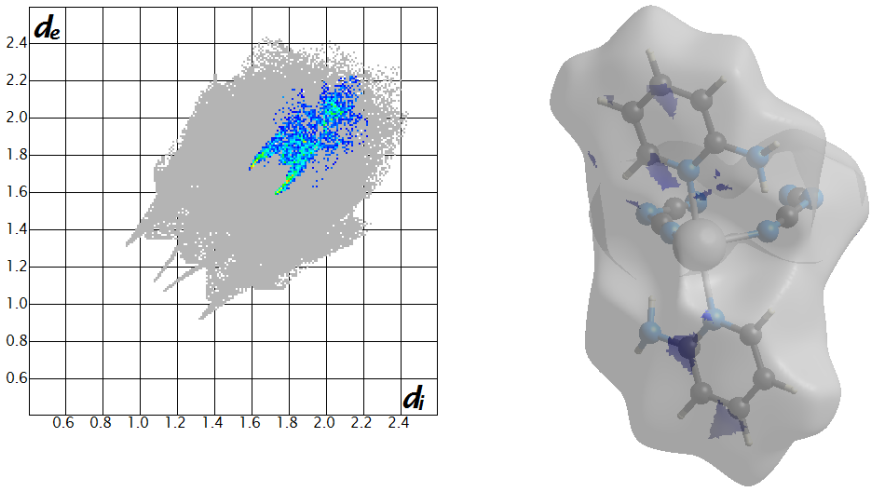


Figure 54: Hirshfeld surface and associated fingerprint plot of $[Mn(2\text{-}Apy)_2(dca)_2]$ showing C···N.

### 3.8.1.6. N···N interactions

The N···N interactions arise between the neighbouring N-atoms of pyridine rings and the terminal bonding N-atoms of dicyanamide.

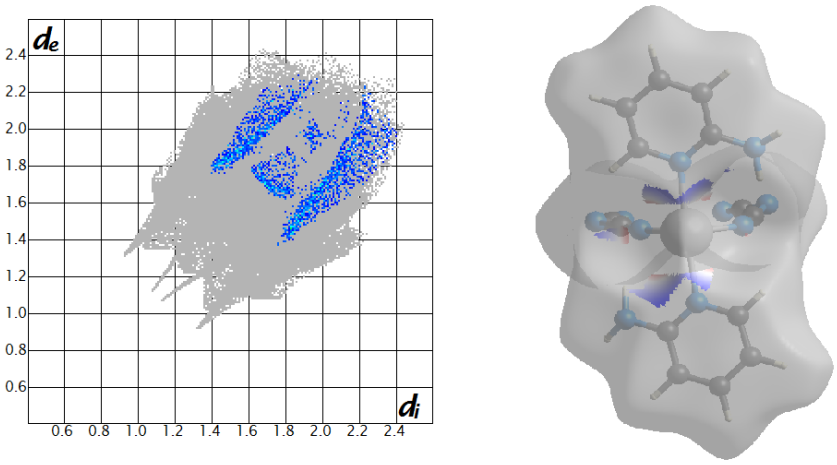


Figure 55: Hirshfeld surface and associated fingerprint plot of $[Mn(2\text{-}Apy)_2(dca)_2]$ showing N···N.

The N···N has the least contribution to the fingerprint plot with a percentage weight of 2.4 %, and with *d*e + *d*i ~ 3.2 Å.

### 3.8.2. Hirsfeld surface analysis for $[Zn_3(H_2O)_2(NPA)_6]$ complex

$[Zn_3(NPA)_6(H2O)_2]$ complex displays a number of intermolecular interactions between neighbouring atoms. The combined interactions are mapped on Figure 56. The figure indicates the total percentage contributions of the various intermolecular contacts to the Hirshfeld surface with $d_{norm}$ interval ranging from -0.6888 to 1.4062 Å. The most significant ones are: H···H bond (63.4 %); H···C/C···H bond (25.4 %); H···O/O···H bond (7.6 %); C···C bond (2.1 %); and H···N/N···H bond (0.9 %).

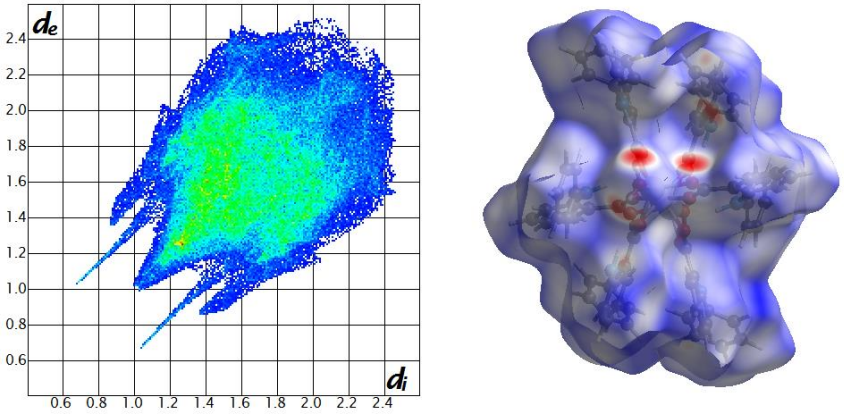


Figure 56: Hirshfeld surface mapped over $d_{norm}$ for the title compound $[Zn_3(H_2O)_2(NPA)_6]$.

### 3.8.2.1. H···H interactions

On the Hirshfeld surfaces, the H···H interactions appear as the largest region (63.4 %) of the fingerprint plot with a high concentration at *de* = *di* ~1.0 Å.

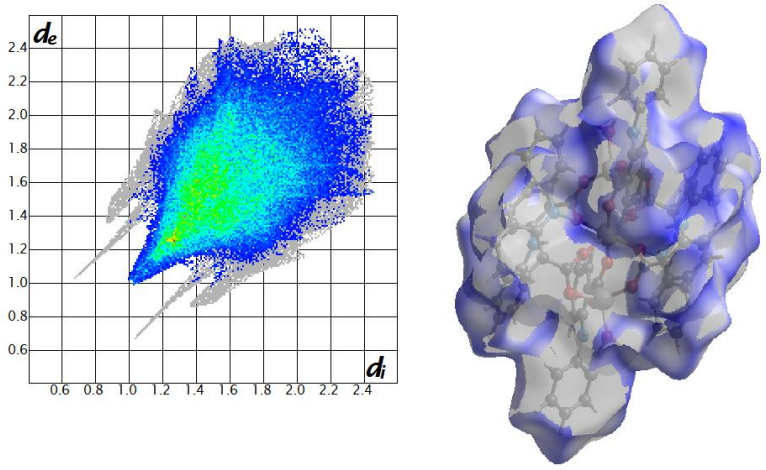


Figure 57: Hirshfeld surface and associated fingerprint plot of $[Zn_3(H_2O)_2(NPA)_6]$ showing C-H···H interactions.

The interaction arises as a result of interaction between neighbouring H-atoms from pyridine groups.

### 3.8.2.2. H···O interactions

Two sharp spikes (*de* + *di* ~ 1.8 Å) on the fingerprint plot are observed for the H···O/O···H bond contacts, corresponding to the C—H···O hydrogen bond contacts.

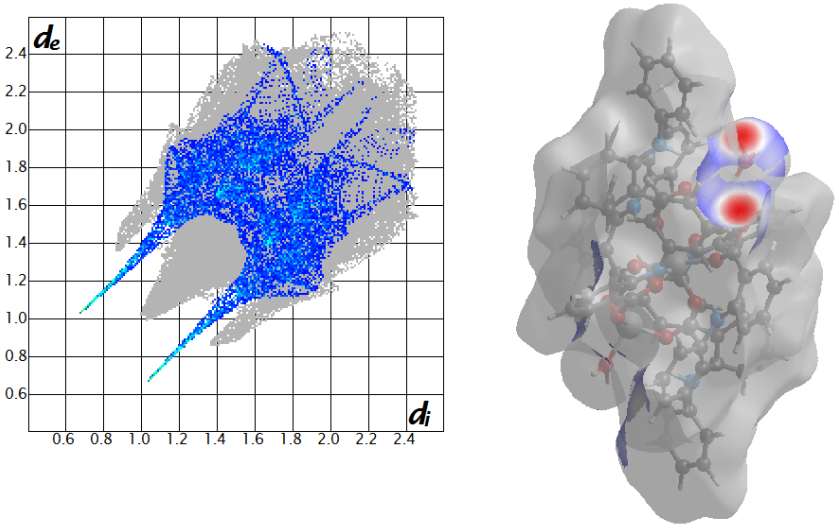


Figure 58: Hirshfeld surface and associated fingerprint plot of $[Zn_3(H_2O)_2(NPA)_6]$ showing C–H···O interactions.

The red spot on the Hirsfeld surface indicates bonds stronger than Van Der Waals forces. Therefore, C–H···O is attributed to strong hydrogen bond appearing between the free H-atoms of the bonded water molecule and the O-atom of the neighbouring carboxylate of NPA.

### 3.8.2.3. C···H interactions

The C···H/H···C contacts contribute to 25.4 % of the Hirshfeld area. These contacts also appear as two wings around *de* + *di* ~ 2.3 Å.

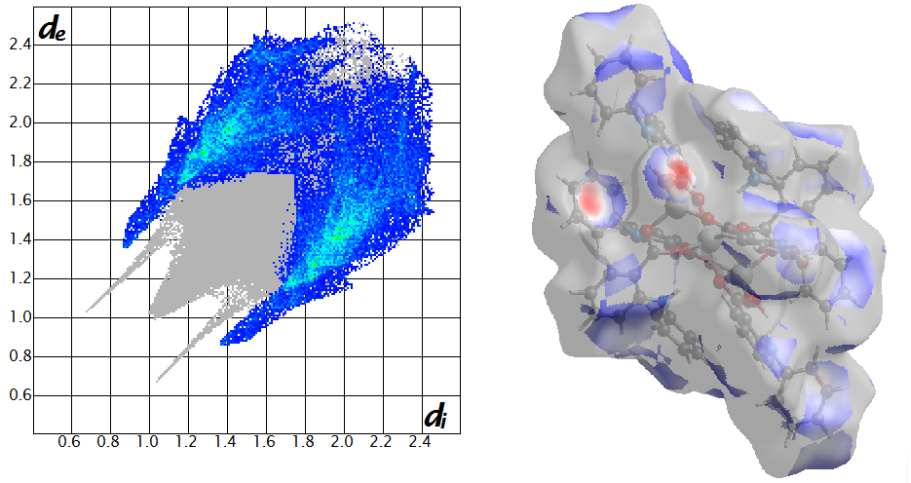


Figure 59: Hirshfeld surface and associated fingerprint plot of $[Zn_3(H_2O)_2(NPA)_6]$ showing C···H interactions.

Among these C···H intreactions, strong ones are observed, as shown as red spot on Hirsfeld surafce, and may be attributed to O–H···C between the free H-atoms of bonded water molecule and neigbouring centroid of benzene ring.

### 3.8.2.4. C···C interactions

C···C interactions counts for about 2.1% of the Hirsfeld surface. This arises only for centroid from benzene ring as shown in the figure below.

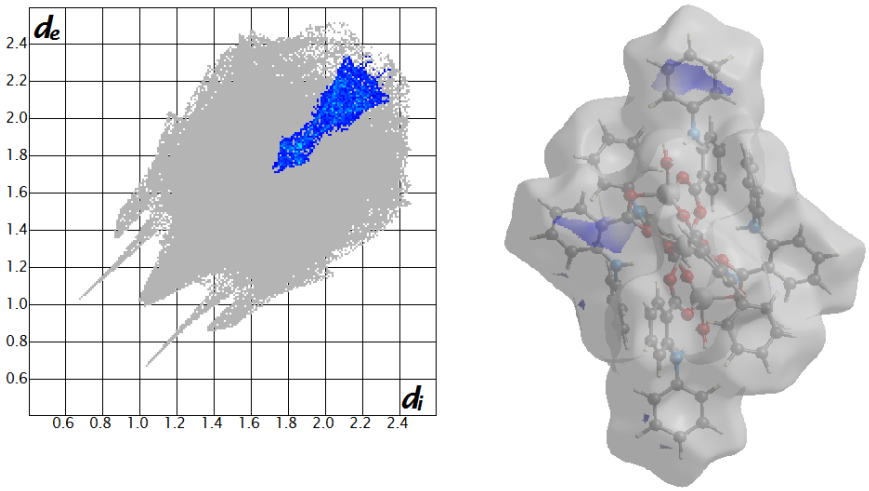


Figure 60: Hirshfeld surface and associated fingerprint plot of $[Zn_3(H_2O)_2(NPA)_6]$ showing C···C interactions.

The C···C interactions may be attributed to the perpendicular π-stacking that arise from the molecule. This is shown as blue spot on the Hirsfeld surface.

### 3.8.2.4. H···N interactions

The H···N/N···H bond contacts have *de* + *di* ~ 2.8 Å, corresponding to C-H···N bond interactions, has the least contribution at 0.9 % of the Hirsfeld surface. This appears as spikes as shown on the fingerprint plot in Figure 61.

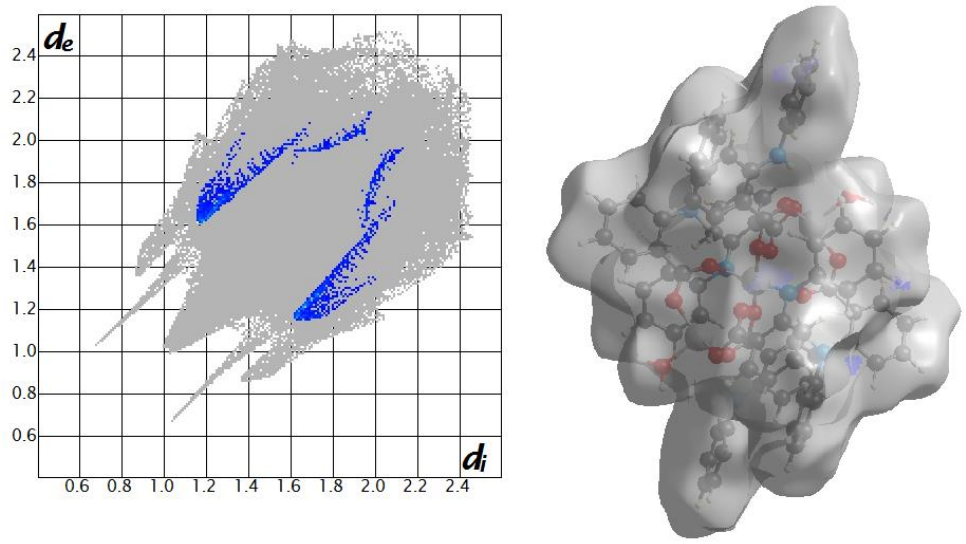


Figure 61: Hirshfeld surface and associated fingerprint plot of $[Zn_3(H_2O)_2(NPA)_6]$ showing N···H/ N···H interactions.

Therefore H···H, H···C/C···H bond (C–H···π); H···O/O···H interactions constitute 96.4 % of the packing arrangement of the supramolecular crystal structure in $[Zn_3(H_2O)_2(NPA)_6]$.

### 3.8.3. Hirsfeld surface analysis for $[Cd(2\text{-}Apy)_2(dca)_2]$ complex

The fingerprint plots of the individual contacts of Cd(II) complex is similar to that of Mn(II) complex in that they also possess seven (07) intermolecular contacts to the Hirshfeld surface with a $d_{norm}$ ranging from -0.5009 to 1.3625. However, the percent weight of each contact slightly differ from that of Mn(II) complex. Moreover, the interaction contributions obey to the same scheme as that of Mn(II) complex in that, the weight percent is highest for H···N/N···H interaction (40,1 %) and lowest for N···N interaction (1,3 %). The other interactions ranked with their respective weight are: H···C/C···H bond (28.5 %); H···H bond (15.5 %); C···C bond (6.4 %); N···Mn/Mn···N bond (4.6 %); C···N/N···C bond (3.5 %). As in Mn(II) complex, the C–H···π, H···H, and N···H/H···N interactions are the most prominent features. They constitute 84.1 % of the overall interactions of the crystal packing. The individual interactions are shown in Figure 62.

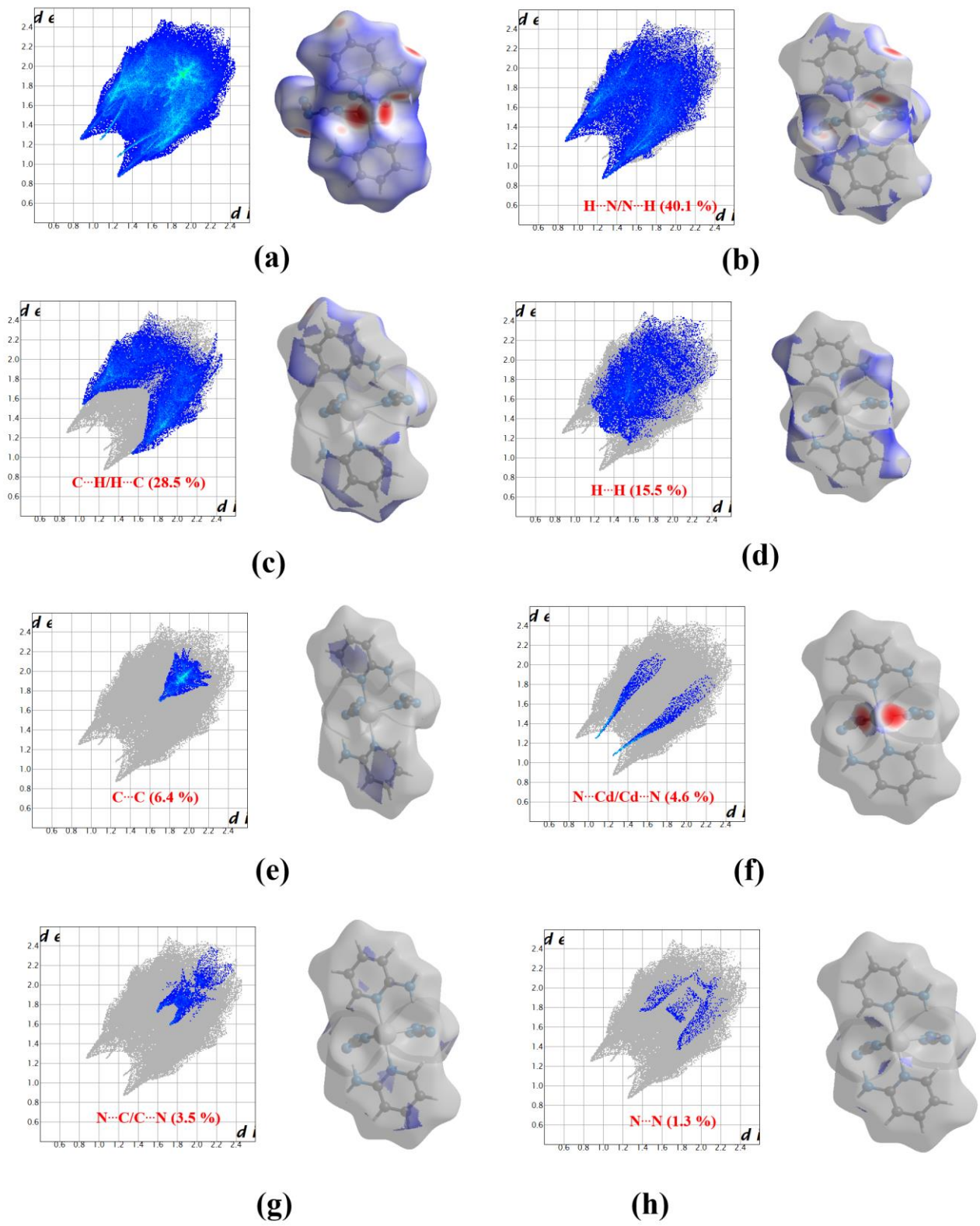


Figure 62 : Hirshfeld surface and associated fingerprint plot of $[Cd(2\text{-}Apy)_2(dca)_2]$. The close contacts in the Hirshfeld surface appear in red [$d_{norm}$ range: -0.5009: 1.3625].

The relative contribution of all the interactions in Mn(II), Zn(II), and Cd(II) supramolecular complexes are summarised in Figure 63.

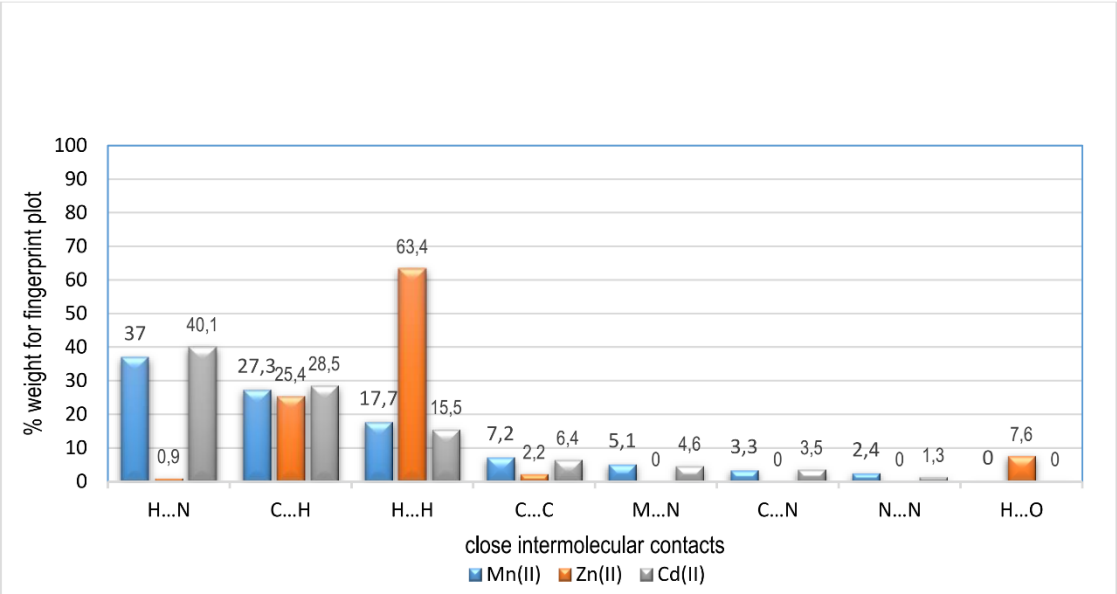


Figure 63: Percentage contributions to the Hirshfeld surface area for the various close intermolecular contacts for Mn(II), Zn(II) and Cd(II) compounds

It can be observed that Mn(II) and Cd(II) display the same individual interactions due to their similar configuration. Moreover, the trend in percentage weight of the individual interaction are also similar. However, these interactions are not all present in Zn(II) compound, which displays other individual interactions.

### 3.9. Frontier Molecular Orbital Theory

HOMO-LUMO is mainly a mathematical model that is used to represent electronic density around atoms. Therefore, they are indirect experimentally observable parameters, where usually, they are physically explained as the ionization potential for HOMO, and electron affinity for LUMO. [158] The HOMO-LUMO gap provides useful information about the compound properties. A molecule with a small HOMO-LUMO gap is more reactive and is softer, thus has a higher polarizable nature [159]. Therefore, the energy gap between HOMO–LUMO orbitals determines the chemical stability, chemical hardness (η) and softness (σ), chemical potential (μ), electronegativity (χ) and the electrophilicity ($\omega$) of a compound. These are formulated by the equations: [160–162]:

$$\eta = (-E_{HOMO} + E_{LUMO})/2 \quad \text{..... (1)}$$

$$\sigma = 1/\eta \quad \text{..... (2)}$$

$$\mu = -(-E_{HOMO} - E_{LUMO})/2 \quad \text{..... (3)}$$

$$\chi = (-E_{HOMO} - E_{LUMO})/2 \quad \text{..... (4)}$$

$$\omega = \mu^2/2\eta \quad \text{..... (5)}$$

where $E_{HOMO}$ and $E_{LUMO}$ are the energies of the HOMO and LUMO orbitals.

The energy levels for all the compounds were computed using the DFT-B3LYP/3-21G method. For all the complexes, the initial molecular geometry was taken from the crystal structures while initial molecular geometries of the ligands were drawn from Gaussian software and optimised.

### 3.9.1. HOMO-LUMO energy gap for N-Phenylanthranilate complex

Electron distributions in the frontier molecular orbitals (the highest occupied molecular orbital (HOMO) and the lowest unoccupied molecular orbital (LUMO)) of NPA ligand and Zn(II) complex were calculated and the values obtained range from 4.3731 eV in the free ligand to 4.2376 eV in the complex (Figure 64).

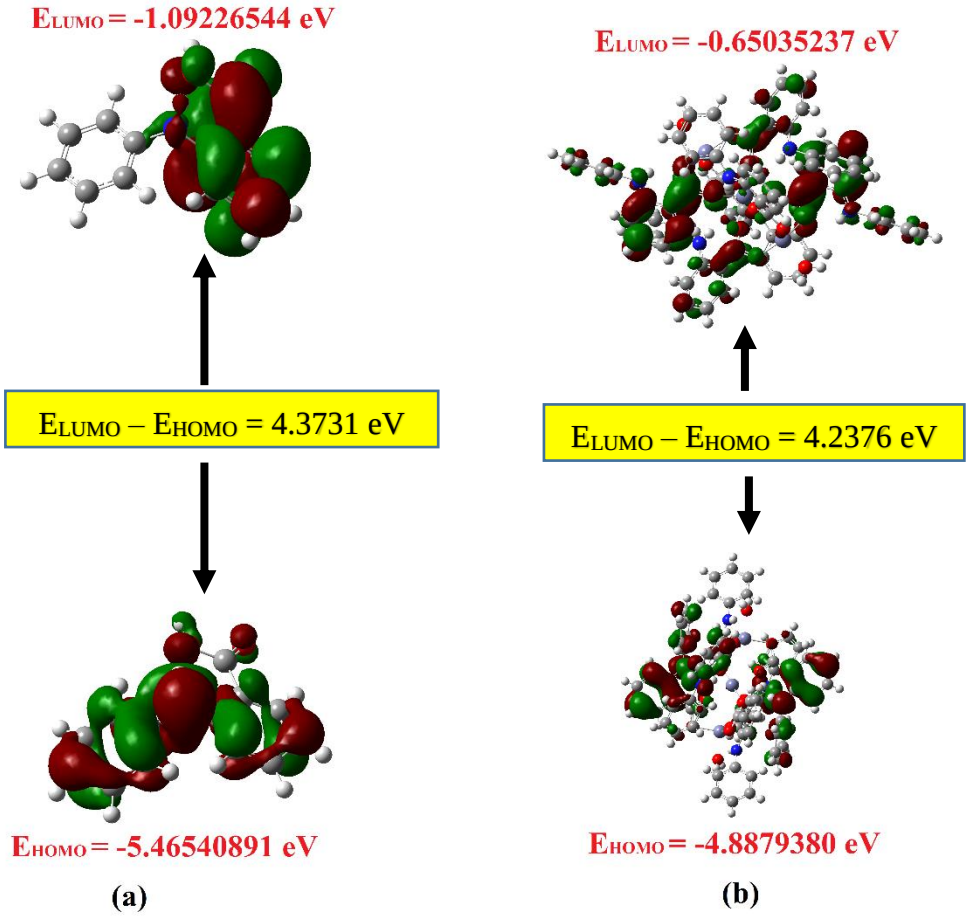


Figure 64: Frontier molecular orbital (HOMO-LUMO) and related transition energy of (a) NPA and (b) $[Zn_3(H_2O)_2(NPA)_6]$ complex.

As seen in Figure 64(a), in the ligand, the HOMO is delocalised on the entire bonds, whereas LUMO is generally localized on the phenyl arm containing carboxylic acid.

In the complex (Figure 64(b)), the HOMO is delocalised and very pronounced on the entire bonds of two of the six NPA ligands which are bonded to the two exterior zinc centres. The HOMO also occurs on the two other NPA ligands bonded to the exterior zinc centres, but is less pronounced and only present on the phenyl arm containing carboxylic acid. Therefore, the two axial NPA ligands are not involved with the HOMO. The LUMO is mainly localised on the phenyl arm containing carboxylic acid of the two axial NPA ligands which are not involved in the HOMO localisation. This indicates that there is a transfer of charge between the equatorial NPA ligands to the axial ligands.

The calculated values of reactivity descriptors of complex are given in Table XVII. The negative value of chemical potential (-2,7692eV) is an indication of the stability of the compound suggesting that it does not undergo decomposition into its constituents. In addition, the large energy gap of HOMO-LUMO (4,2376 eV) suggests that the molecule has good stability and therefore is less reactive.

### 3.9.2. HOMO-LUMO energy gap for 2-Aminopyridine complexes

Figure 65 shows the molecular orbital energy levels for 2-Apy, Mn(II) and Cd(II) complexes with their respective energy gaps.

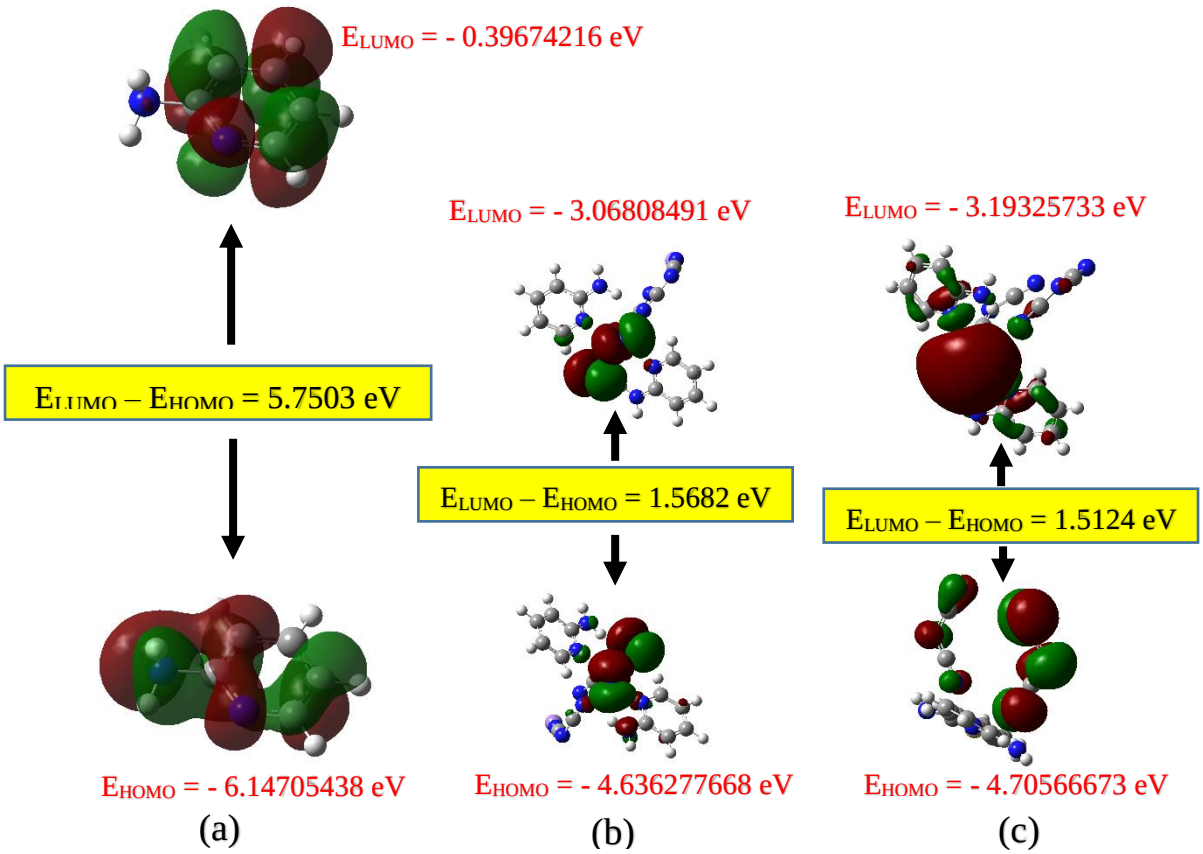


Figure 65: Frontier molecular orbital (HOMO-LUMO) and related transition energy of (a) 2-Apy free ligand, (b) $[Mn(2\text{-}Apy)_2(dca)_2]$, and (c) $[Cd(2\text{-}Apy)_2(dca)_2]$.

From Figure 65(a), the HOMO is delocalised on the entire bonds of 2-Apy, whereas LUMO is limited to the phenyl ring and does not involve the $NH_2$ group.

Figure 65(b) shows the HOMO-LUMO map of Mn(II) complex. It is seen from the figure that the HOMO is localised around the central metal, the coordinated immediate N-atoms from dca, and the N-atoms of 2-Apy ligands. The LUMO is localised in the same manner except for the N-atoms of 2-Apy which are not involved.

In the Cd(II) complex (Figure 65(b)), the HOMO are delocalised mainly at the linear dca ligands, while the LUMO are delocalised at the metal centre and the 2-Apy rings. This is a clear indication that charge transfer occurs between the dca ligands and the metal centre.

The computed energy gaps of HOMO-LUMO for Mn(II) and Cd(II) complexes have been found to be 1.5682 and 1.5124 eV respectively. Moreover, the magnitude of chemical hardness, supported by the HOMO–LUMO energy gap, for Mn(II) and Cd(II) complexes have been found to be respectively 0.7841 eV and 0.7562 eV (Table XVII). The small values of hardness imply higher reactivity and soft molecules in nature. The soft molecules undergo changes in electron density more easily and are therefore more reactive. Moreover, Mn(II) and Cd(II) have negative values of chemical potential (-3.8522 and -3.9495 eV, respectively) as shown in Table XVII, which is an indication that the complexes do not undergo decomposition into their components. The electrophilicity index values, ω, given in Table XVII for Mn(II) and Cd(II) complexes (5.8177and 5.8977 eV, respectively) related to chemical potential and hardness indicate that both compounds have similar electrophile strength.

The reactivity descriptors of the complexes are summarised in Table XVII.

**Table XVII: Computed HOMO and LUMO energies, HOMO-LUMO gap energies, hardness (η), chemical potential (μ), electronegativity (χ) and the electrophilicity (ω) all in eV, and softness (σ) in $eV^{-1}$**

| Complexes | HOMO | LUMO | $\Delta E_{gap}$ | η | σ | μ | χ | ω |
|---|---|---|---|---|---|---|---|---|
| $[Mn(2\text{-}Apy)_2(dca)_2]$ | -4.6363 | -3.0681 | 1.5682 | 0.7841 | 1.2753 | -3.8522 | 3.8522 | 5.8177 |
| $[Zn_3(H_2O)_2(NPA)_6]$ | -4.8880 | -0.6504 | 4.2376 | 2.1188 | 0.4720 | -2.7692 | 2.7692 | 8.1238 |
| $[Cd(2\text{-}Apy)_2(dca)_2]$ | -4.7057 | -3.1933 | 1.5124 | 0.7562 | 1.3224 | -3.9495 | 3.9495 | 5.8977 |

The above Table indicates that all the complexes do not decompose to their constituents as they all have negative values of chemical potential (μ), therefore they are all stable. Zn(II) complex possesses

the lowest electronegativity value (χ). It also possesses the lowest LUMO which signifies that it can be the best electron acceptor. This is confirmed by its highest electrophilicity index values (ω), meaning that it is the strongest electrophile among all compounds. Cd(II) complex is the softest molecule, has the highest chemical reactivity amongst all, therefore kinetically less stable.

### 3.10. Biological screening

The biological activity of the metal salts, ligands, anions, complexes of Mn(II), Zn(II), Cd(II), reference antibacterial (chloramphenicol) and anti-fungal drug (gentamicine) were evaluated against three microorganisms, comprised of one gram-positive and one gram-negative bacterial strains, and one fungal strain. For the antimicrobial inhibition, if the activity zone in millimetre is > 0, therefore the microbial strain is considered as sensitive to the compound. Beside the *in vitro* screening, molecular docking simulation of the novel complexes was computed for breast cancer mutant and SARS-CoV-2 proteins.

#### 3.10.1. *In vitro* screening

The ligands, co-ligand and their metal complexes were evaluated for their *in vitro* antimicrobial activities against *Staphylococcus aureus, Salmonella Typhi,* and *Candida albicans.*

The lists of the activities of the ligands, co-ligands, metal complexes and salts against the microbes are given on Table XVIII.

**Table XVIII: Zone of inhibition of the compounds (active if inhibition zone > 0)**

| Compounds | *Microorganisms* | | |
|---|---|---|---|
| | *Staphylococcus aureus* | *Salmonella typhi* | *Candida albicans* |
| *chloramphenicol* | 29.5±1.3 | 29.75±1.25 | / |
| *Gentamicine* | / | / | 31.75±1.70 |
| *2-Apy* | 1.9±0.5 | 0±0 | 0±0 |
| *NPA* | 1 ±0 | 0 ±0 | 3±5 |
| *dca* | 4.75±5.50 | 0 ±0 | 0.25±0.50 |
| $MnCl_2.4H_2O$ | 3.2 ±0.2 | 0 ±0 | 0.5±0.0 |
| $ZnCl_2$ | 0±0 | 0 ±0 | 1±0 |
| $CdCl_2.2H_2O$ | 2.1±0.2 | 1.7±0.3 | 3±2 |
| $[Mn(2\text{-}Apy)_2(dca)_2]$ | 12.5±0.6 | 0 ±0 | 1.25±0.96 |
| $[Zn_3(H_2O)_2(NPA)_6]$ | 13±1 | 3.75±4.85 | 0.5 ±0.6 |
| $[Cd(2\text{-}Apy)_2(dca)_2]$ | 19±2 | 14.5±2.2 | 26.5±5.0 |

The diameter of the susceptibility zones was measured in millimetres (mm). The susceptibility zones measured were clear zones around the disc inhibiting the microbial growth.

The inhibition zone for the bacterial species ranges from 0 to 19 mm, while that for the fungus species ranges from 0.5 to 26.5 mm.

*S. aureus* is active to all ligands, while *S. typhi* has shown no activity against the ligands. Only NPA and dca ligands have been active against *C. albicans.* Both Zn(II) and Cd(II) complexes are active against all microbial strains. However, the inhibition diameter vary from relatively low to high values. For instance, *C. albicans* showed a weak sensitivity toward Zn(II) complex. *S. typhi* have been found to be insensitive to Mn(II) compound. The activity of Mn(II) compound is however greater in *S. aureus* than in *C. albicans.* The reference antimicrobial agents were more active against the microbial strains than the synthesised metal complexes.

The general trend for the *in vitro* biological essay shows that, for microbial strains which are found to be sensitive to the newly synthesised complexes, their antimicrobial activities are higher than that of the free ligand. The exception occurs with *C. albicans.* Here, the NPA ligand has activity greater than the synthesised complexes.

The increased biological activity of the synthesised complexes could be explained on the basis of Overton's concept of cell permeability. According to this concept, the lipid membrane that surrounds the bacterial cell favors the passage of only the lipid soluble materials as liposolubility is an important factor, which controls the activity. [163] Studies have also shown that chelation tends to increase the antimicrobial activity of the complex more powerfully than the free organic compound. [163,164]

Below is the histogram showing comparative activity of the complexes against bacteria and fungus species.

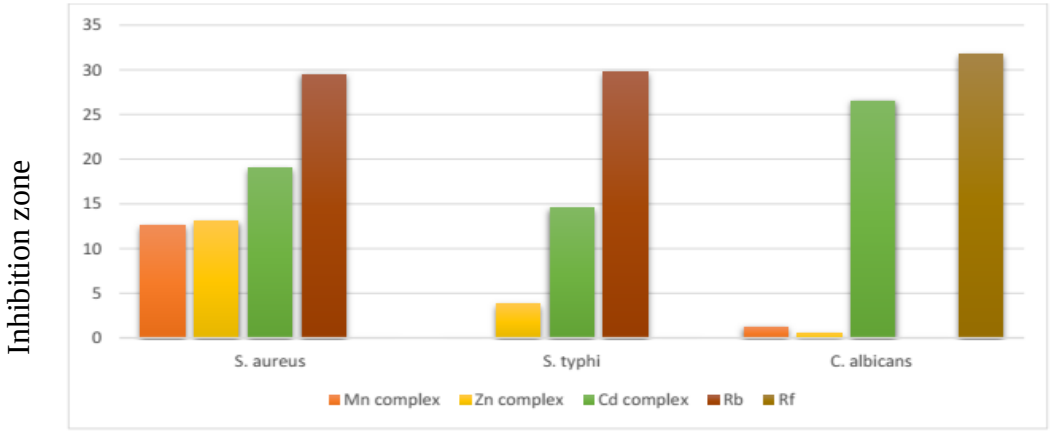


Figure 66: Histogram showing comparative activity of compounds against bacteria and fungus species (Rb = reference antibacterial agent; Rf = reference antifungal agent).

The activities of the metal complexes were confirmed by calculating the activity index according to the following relation; [97]

$$\text{Activity index (AI)} = \frac{\text{Inhibition Zone of compound}}{\text{Inhibition Zone of reference drug}} x100$$

The calculated values are presented in the table below.

**Table XIX: Activity index for the compounds against the microbial stains**

| Compounds | *Activity index (%)* | | |
|---|---|---|---|
| | *Staphylococcus aureus* | *Salmonella typhi* | *Candida albicans* |
| *[Mn(2-Apy)$_2$(dca)$_2$]* | 42 | 0 | 4 |
| *[Zn$_3$(H$_2$O)$_2$(NPA)$_6$]* | 44 | 13 | 2 |
| *[Cd(2-Apy)$_2$(dca)$_2$]* | 64 | 49 | 84 |

The above table shows that the activity index varies from 0 % for Mn(II) complex against *Salmonella typhi*, to up to 84 % for Cd(II) complex against *C. albicans.*

The resulting histogram is shown in Figure 67.

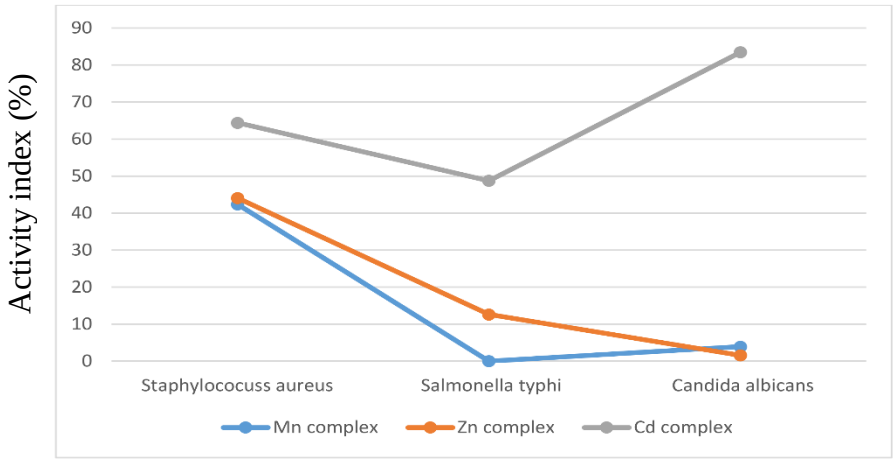


Figure 67: Activity index of the metal complexes.

From the data, it can be concluded that among the newly synthesised complexes, the best overall activity occurs with Cd(II) complex against *C. albicans*, while Mn(II) complex has no activity index against *S. typhi*. Cd(II) complex also showed the best activity index against the gram-positive bacteria *S. aureus* (64 %) and the gram-negative bacteria *S. typhi* (49 %).

The determination of the Minimum Inhibitory Concentration (MIC) and the Minimum Bactericidal/Fungicidal Concentration (MBC or MFC) is used as a research tool to determine *in vitro*,

the susceptibility of a pathogen to a given antimicrobial agent. The MIC is the lowest concentration that inhibits microorganism growth, while MBC (or MFC) is the lowest concentration required to kill a bacterium/fungus over a fixed, somewhat extended period, under specific conditions. [165] The MIC and MBC (or MFC) were determined for those compounds which were active in the disc diffusion method. The results are presented in Table XX.

**Table XX: Minimum inhibitory concentration (mg/L) and Minimum Bactericidal/Fungicidal Concentration (mg/L) of the complexes and reference compounds**

| Compounds | *Microorganisms* | | | | | | | | |
|---|---|---|---|---|---|---|---|---|---|
| | *Staphylococcus aureus* | | | *Salmonella typhi* | | | *Candida albicans* | | |
| | *MIC* | *MBC* | *r* | *MIC* | *MBC* | *r* | *MIC* | *MFC* | *r* |
| *Chloramphenicol* | 3 | 3 | 1 | 4 | 8 | 2 | / | | |
| *Gentamycin* | / | | | / | | | 3 | 3 | 1 |
| *[Mn(2-Apy)$_2$(dca)$_2$]* | 20 | >20 | >1 | / | | | 10 | 10 | 1 |
| *[Zn$_3$(H$_2$O)$_2$(NPA)$_6$]* | 20 | >20 | >1 | 20 | >20 | >1 | 20 | >20 | >1 |
| *[Cd(2-Apy)$_2$(dca)$_2$]* | 5 | 5 | 1 | 5 | 10 | 2 | 5 | 10 | 2 |

*If **r = MBC(or MFC)/MIC < 4** therefore bactericidal, and if **r > 4** bacteriostatic.*

The above table shows that the compounds exhibit variable MIC depending on the microbial strain. The MIC values of the novel synthesised compounds range from 5 mg/L to >20 mg/L. They are greater than those of the reference antimicrobial agents. The MBC (or MFC) values are at least twice the MIC values, with some exceptions as shown on Table XX above.

The ratio, *r* = MBC(or MFC)/MIC, is less than 4 for Cd(II) complex suggesting that it is bactericidal against all bacterial species. Mn(II) complex shows a bactericidal property only against *C. albicans*, but its *r* >1 for all other microbial strains. Zn(II) complex shows a ratio *r* >1 for all tested bacterial strains. This value does not define the bactericidal or bacteriostatic nature of the complexes against the microbial strains and therefore, further analyses have to be conducted for clarity.

### 3.10.2. *In silico* biological screening

Molecular docking has become the most frequently used computational method used for studying the interactions between coordination complexes and biological macromolecules. Docking allows the prediction of the preferred pose of a ligand inside a receptor binding site. The widely accepted selection criterion is that the best pose corresponds to the best energy score. [166] The crystallographic structures of proteins were retrieved from the Royal Collaboratory for Structural Bioinformatics, RCSB Protein

Data Bank (http://www.rcsb.org/pdb/). The active sites of the protein were simultaneously predicted using the MetaPocket 2.0 online server (https://projects.biotec.tu-dresden.de/metapocket/) [167] and Discovery studio software. The docking was carried on breast cancer mutant protein and SARS-CoV-2 protein.

### 3.10.2.1. *In silico* screening on breast cancer mutant

Human 17 beta-hydroxysteroid dehydrogenase type 1 (17β-HSD1) is a steroid-converting enzyme that promotes breast cancer cell proliferation. For molecular docking, the standard pocket site of the breast cancer mutant, (PDB Id: 3hb5) has been computed to be at the grid box centre values: $x$ = -16.008, $y$ = -2.917, and $z$ = -1.221 and offset values of 48, 38, and 50 respectively, with the grid spacing at 0.603 Å. One of the potential lead compound for its therapy is the inhibitor E2B {3-[3',17'beta-dihydroxyestra-1',3',5'(10')-trien-16'beta-methyl]benzamide}. [168] The computation of E2B has shown that its docking score at its best pose with the breast cancer protein is equal to -8.9 kcal/mol.

The 3D and 2D figures below (figures 68 to 70) provide detailed information on the interaction contexts of Mn(II), Zn(II), and Cd(II) complexes with the protein.

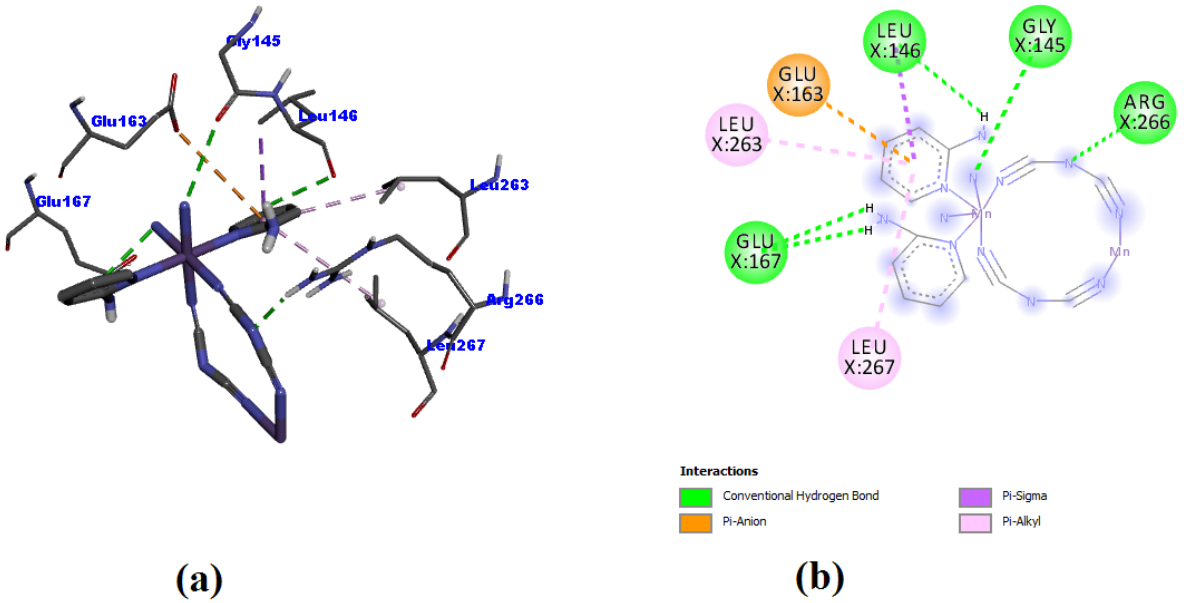


Figure 68: Non-bonding interactions in (a) 3D and (b) 2D representation of the best pose of [Mn(2-Apy)$_2$(dca)$_2$] complex with breast cancer mutant (PDB Id: 3HB5) at -6.3 kcal/mol.

From Figure 68, it is seen that Mn(II) complex binds to seven (07) different amino acid residues. The most recurrent interaction is hydrogen bond. It occurs with the amino acid residues Leu146, Gly145, Arg266, and Glu167. In addition to hydrogen bond, Leu146 forms π–sigma bond with pyridine ring of 2-Apy. Leu263 and Leu267 residues form π–alkyl with the metal complex. Moreover, π–anion interaction occurs with Glu163. The interaction lengths range from 2.130 to 5.480 Å.

Figure 69 below displays 3D and 2D interactions between the cancer protein and Zn(II) complex.

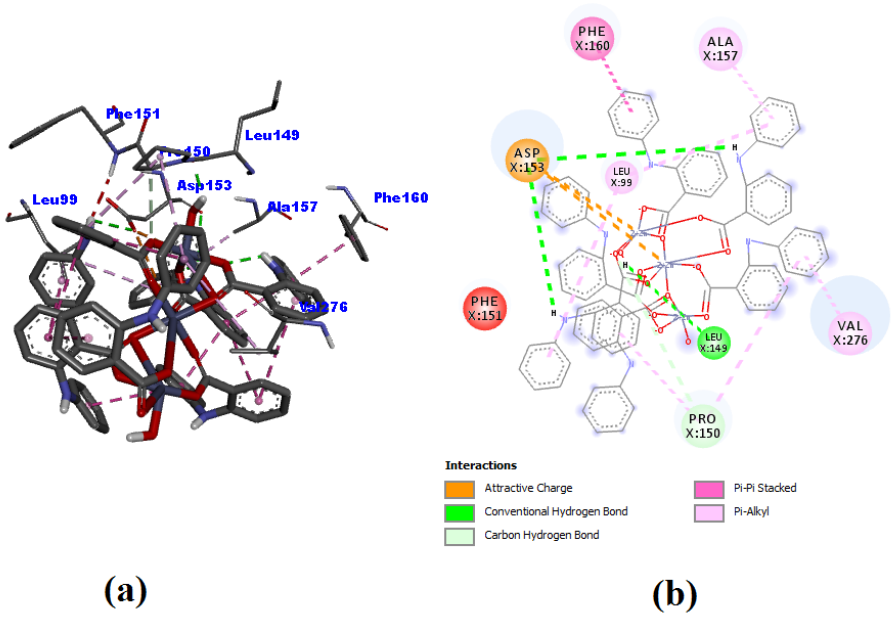


Figure 69: Non-bonding interactions in (a) 3D and (b) 2D representation of the best pose of $[Zn_3(H_2O)_2(NPA)_6]$ complex with breast cancer mutant (PDB Id: 3HB5) at -7.9 kcal/mol.

The molecular docking simulation of Zn(II) complex at its best pose (-7.6kcal/mol) shows that five different interactions arise with seven (07) amino acid residues. Asp153, Leu99, and Pro150 are crossed bonded with different benzyl groups of NPA ligand. Leu99 however displays only π–alkyl interactions. Asp153 displays both hydrogen bonding and attractive charge interactions, while Pro150 Carbon – hydrogen and π–alkyl interactions. Each of the other amino acid residues display one type of interaction with respect to the metal complex. The interaction lengths range from 1.850 to 5.451 Å and are summarised in Table XXI below.

Cd(II) complex interactions in 2D and 3D with breast cancer protein is shown in the figure below.

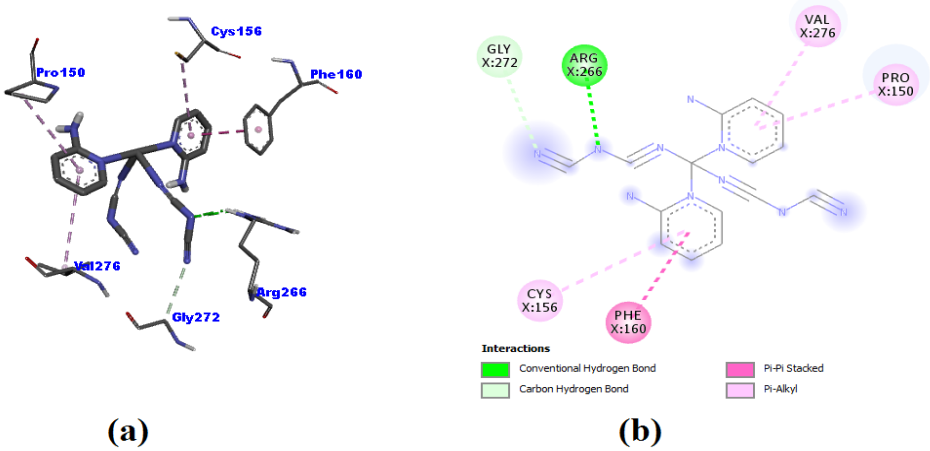


Figure 70: Non-bonding interactions in (a) 3D and (b) 2D representation of the best pose of $[Cd(2\text{-}Apy)_2(dca)_2]$ complex with breast cancer mutant (PDB Id: 3HB5) at -6.2 kcal/mol.

Cd(II) complex displays a binding affinity of -6.2 kcal/mol at its best binding mode. It binds to the breast cancer protein through four different interactions as seen on Figure 70(b). The most remarkable interactions are those with the pyridine rings. Here, each pyridine ring interacts with two different residues. If the residues Pro150 and Val276 interacts with the one ring through π–alkyl interactions, Phe160 and Cys156 respectively interact with the other ring through π···π stacked and π–alkyl interactions. Hydrogen bond do occur between Arg266 with the $\mu_3$ of dca N atom.

From the above docking simulations, it is obvious that Zn(II) complex binds more strongly to the breast cancer protein due to its architecture which favours various interactions. However, it has a lower binding affinity than E2B compound which has been computed at –8.9 kcal/mol. Therefore, it is the compound, among the synthesised ones, which bind most toward the breast cancer mutant protein, 3hb5, and its computed receptor surface and the surface image are shown on scheme I and II, appendix II.

The binding energy, the bond lengths with respect to each amino acid residue are summarised in the following table.

**Table XXI: Binding affinity and non-bonding interaction of Mn(II), Zn(II), and Cd(II) compounds against breast cancer mutant**

| Compound | Binding energy (Kca/mol) | Residues in contact | Intreaction type | Distance (Å) |
|---|---|---|---|---|
| $[Mn(2\text{-}Apy)_2(dca)_2]$ | – 6.3 | Arg266 | H – bond | 2.130 |
| | | Gly145 | H – bond | 3.393 |
| | | Leu146 | H – bond | 2.789 |
| | | Leu146 | π···sigma | 3.80 |
| | | Glu163 | π···anion | 4.927 |
| | | Glu167 | H – bond | 2.842 |
| | | Glu167 | H – bond | 2.588 |
| | | Leu263 | π···alkyl | 5.465 |
| | | Leu267 | π···alkyl | 5.480 |
| $[Zn_3(H_2O)_2(NPA)_6]$ | – 7.9 | Phe160 | π··· π stacked | 3.751 |
| | | Asp153 | Attractive charge | 2.10 |
| | | Asp153 | Attractive charge | 5.474 |
| | | Asp153 | H – bond | 2.982 |
| | | Asp153 | H – bond | 2.63 |
| | | Pro150 | C-H | 3.519 |
| | | Pro150 | π···alkyl | 4.623 |
| | | Pro150 | π···alkyl | 4.726 |
| | | Leu149 | H – bond | 1.850 |
| | | Val276 | π···alkyl | 4.872 |
| | | Ala157 | π···alkyl | 5.451 |
| | | Leu99 | π···alkyl | 4.806 |

| | | | | |
|---|---|---|---|---|
| | | Leu99 | π···alkyl | 4.695 |
| [Cd(2-Apy)$_2$(dca)$_2$] | – 6.2 | Gly272 | C-H bond | 3.432 |
| | | Arg266 | H – bond | 2.073 |
| | | Val276 | π···alkyl | 5.188 |
| | | Pro150 | π···alkyl | 5.064 |
| | | Phe160 | π··· π stacked | 3.91 |
| | | Cys156 | π···alkyl | 5.348 |

### 3.10.2.2. *In silico* screening on SARS-CoV-2

A new coronavirus, known as severe acute respiratory syndrome coronavirus 2, SARS-CoV-2, PDB Id: 6lu7, is the etiological agent responsible for the 2019-2020 viral pneumonia outbreak of coronavirus disease 2019 (Covid-19).

The grid box centre values at $x$ = -26.283, $y$ = 12.599, and $z$ = 58.966 and offset values of 62, 126, and 92 respectively were used for the molecular docking of SARS-CoV-2. The results were compared with respect to the standard binding site and shown in the red circles (Figure 71)

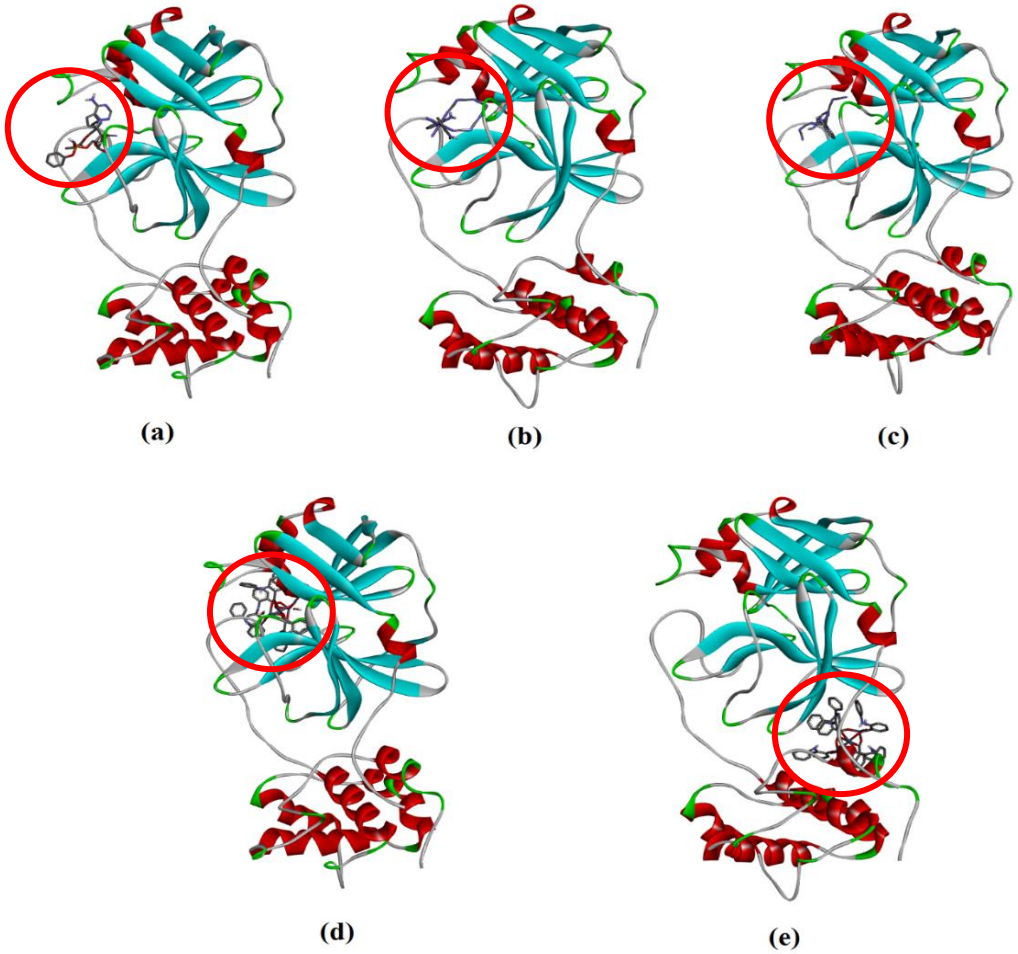


Figure 71: Cartoon representations of (a) Chloroquine (-8.0 kcal/mol), (b) [Mn(2-Apy)$_2$(dca)$_2$] (-6.7 kcal/mol), (c) [Mn(2-Apy)$_2$(dca)$_2$] (-5.9 kcal/mol), (d) [Zn$_3$(H$_2$O)$_2$(NPA)$_6$] (-6.2 kcal/mol) at the standard active site of SARS-CoV-2, and (e) [Zn$_3$(H$_2$O)$_2$(NPA)$_6$] at its best pose at -8.4 kcal/mol.

From Figure 71, it is shown that the binding affinity for SARS-CoV-2 protein is different for Zn(II) complex on one side, and for both Mn(II) and Cd(II) complexes on the other, at their best pose. In its best conformation, Mn(II) and Cd(II) compounds are mainly found at the standard pocket site, in-between the beta-sheets (in blue) and the turns and loops (in green an grey) (Figure 71(b) and (c)), whereas Zn(II) compound is located between the beta-sheets and the helices (in red) (Figure 71(e)).

3D and 2D figures provide with detailed information on how the compounds form non-bonding interactions with the SARS-CoV-2 protein (Figure 72, 73 and 74).

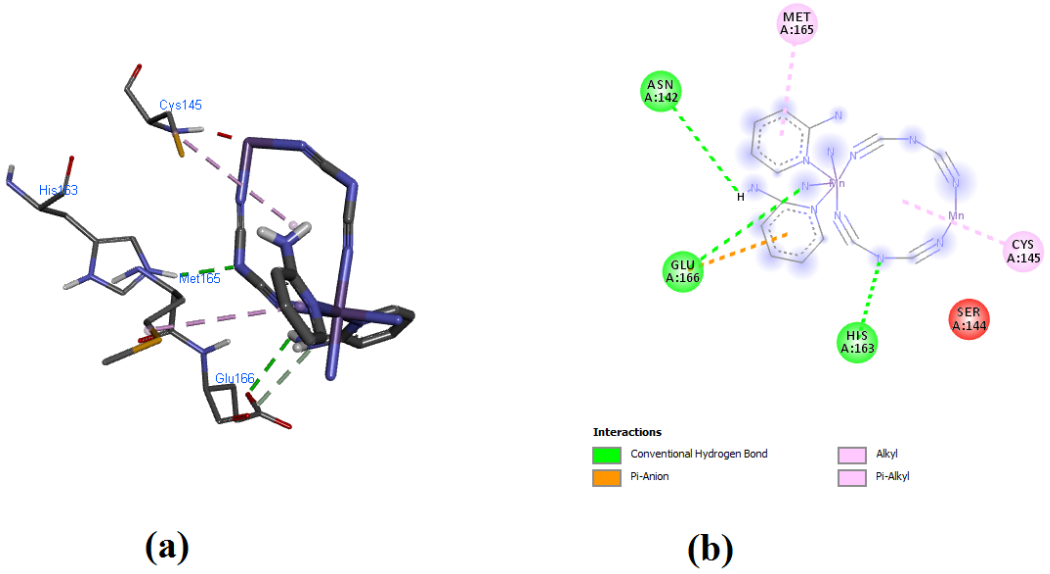


Figure 72: Non-bonding interactions in (a) 3D and (b) 2D representation of the best pose of $[Mn(2\text{-}Apy)_2(dca)_2]$ complex with SARS-CoV-2 (PDB Id: 6LU7) at -6.8 kcal/mol.

With a binding affinity of -6.7 kcal/mol, the interaction between the Mn(II) complex and the protein target in SARS-CoV-2, 6lu7, is characterized by the formation of three hydrogen bonds with Glu166, Asn142 and His163 from the A chain. $\pi\cdots$alkyl bond contact is also observed between Met165 and one pyridine ring.

More amino acid residues are involved in Zn(II) complex – SARS-CoV-2 non-bonding interactions (Figure 73).

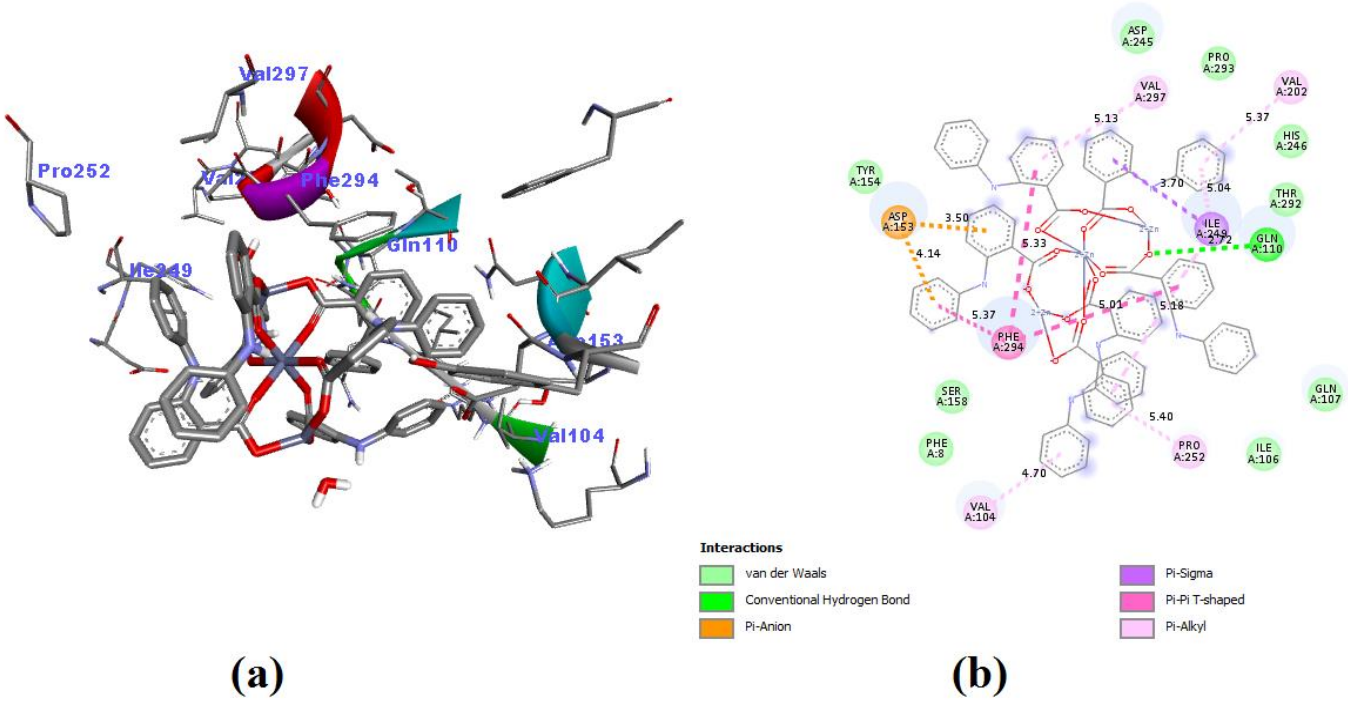


Figure 73: Non-bonding interactions in (a) 3D and (b) 2D representation of the best pose of $[Zn_3(H2O)_2(NPA)_6]$ complex with SARS-CoV-2 (PDB Id: 6LU7) at -8.4 kcal/mol.

According to the docking simulation, the best binding mode of the complex fragment indicated the formation of hydrogen bond contact through the interaction of the carboxylate O atom with amino acid residue Gln110 at a distance of 2.72 Å (Figure 73). The binding affinity of the best pose of the complex was computed at -8.4 kcal/mol. However, most of the bonding contacts between the complex and the target protein are from the benzyl groups of the complex as shown in Figure 73(b). The peculiarity is the formation of cross bonding contacts between the benzyl groups and amino acid residues as observed with π···anion bond contacts with Asp153; perpendicular π···π stacking with Phe294 at distances of 5.37, 5.33, and 5.01 Å; benzyl π···alkyl bond contacts with Pro252 at 5.40 Å, Ile249 at 5.18 Å, and Val202 at 5.37 Å.

Moreover, the formation of different types of contacts between the same amino acid residue with different benzyl groups are observed, such as the formation of both π···alkyl and π···sigma bonds contacts between Ile249 and three benzyl groups. Also, Val297 and Phe294 respectively formed π···alkyl bond and π···π stacking with the same benzyl group. Therefore, the complex offers a variety of binding affinity with the target protein with their respective distances as shown in Figure 73.

In the Cd(II) complex, four of the amino acid residues are involved in the interact as shown in the figure below.

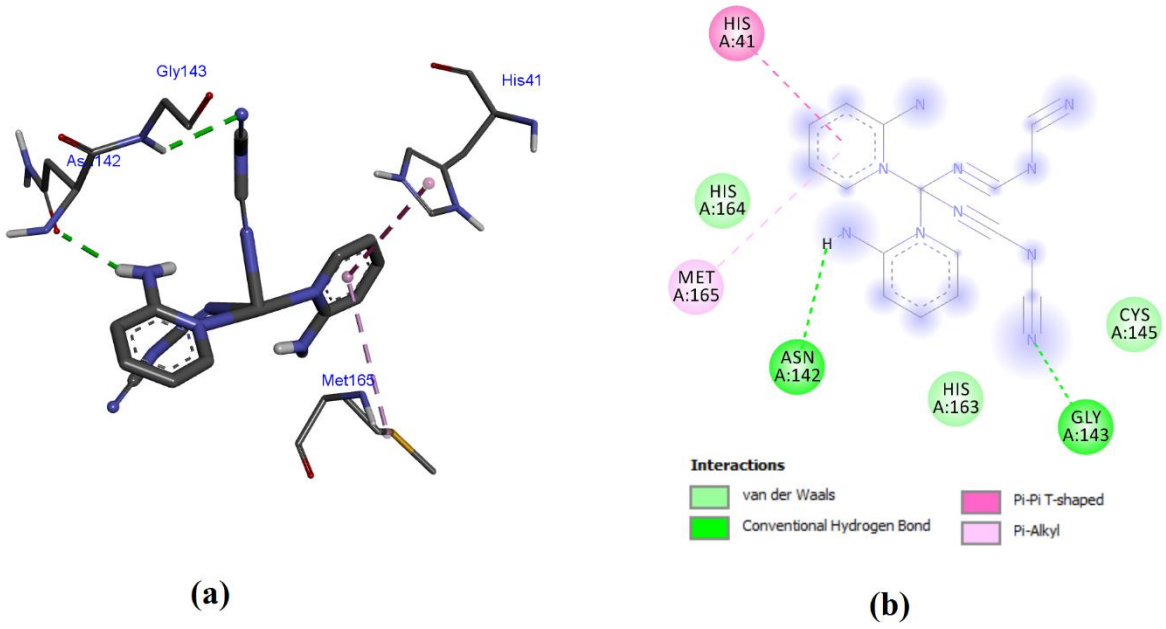


Figure 74: Non-bonding interactions in (a) 3D and (b) 2D representation of the best pose of $[Cd(2\text{-}Apy)_2(dca)_2]$ complex with SARS-CoV-2 (PDB Id: 6LU7) at -5.9 kcal/mol.

The binding affinity of the complex with respect to the protein target in SARS-CoV-2, 6lu7, is -5.9 kcal/mol. The interactions are characterised with the formation of two hydrogen bonds between both Gly143 and a terminal N atom of dca, and Asn142 and H atom of amino group of 2-apy. Moreover, one of the pyridine ring forms both π···alkyl bond contact with Met165 and π··· π bond contact with His141.

The non-bonding interactions and the respective lengths of Mn(II), Zn(II), and Cd(II) complexes with SARS-CoV-2 are shown on Table XXII.

**Table XXII: Binding affinity and non-bonding interaction of Mn(II), Zn(II), and Cd(II) compounds against SARS-COV-2**

| Compound | Binding energy (Kca/mol) | Residues in contact | Intreaction type | Distance (Å) |
|---|---|---|---|---|
| $[Mn(2\text{-}Apy)_2(dca)_2]$ | – 6.8 | Glu166 | H – bond | 2.873 |
| | | Glu166 | H – bond | 3.745 |
| | | His163 | π···alkyl | 2.475 |
| | | Cys145 | alkyl | 5.363 |
| | | Met165 | π···alkyl | 4.911 |
| $[Zn_3(H_2O)_2(NPA)_6]$ | – 8.4 | Phe294 | π···sigma | 3.929 |
| | | Phe294 | π···π | 5.006 |
| | | Phe294 | π···π | 5.328 |
| | | Phe294 | π···π | 5.369 |
| | | Gln110 | H – bond | 2.718 |

| | | | | |
|---|---|---|---|---|
| | | Asp153 | π···anion | 3.505 |
| | | Asp153 | π···anion | 4.139 |
| | | Ile249 | π···sigma | 3.702 |
| | | Ile249 | π···alkyl | 5.044 |
| | | Ile249 | π···alkyl | 5.183 |
| | | Val202 | π···alkyl | 5.368 |
| | | Val297 | π···alkyl | 5.126 |
| | | Pro252 | π···alkyl | 5.397 |
| | | Val104 | π···alkyl | 4.699 |
| $[Cd(2\text{-}Apy)_2(dca)_2]$ | – 5.9 | Met165 | π···alkyl | 5.084 |
| | | His41 | π···π | 4.735 |
| | | Asn142 | H – bond | 2.431 |
| | | Gly143 | H – bond | 2.600 |

Therefore, molecular docking studies show that Zn(II) complex has varied and great number of interactions as compared to Mn(II) and Cd(II) complexes. Moreover, Cd(II) complex has the lowest binding affinity toward SARS-CoV-2 protein, 6lu7.

The computed receptor surface and the surface image of Zn(II) complex against SARS-CoV-2 are shown on scheme III and IV, appendix II.

## CONCLUSION

The main objective of the present work was to synthesise N-Phenylanthranilic acid and 2-Aminopyridine coordination functional networks with Mn(II), Zn(II), and Cd(II) metals in simple solvents system.

Metal complexes of Mn(II), Zn(II), and Cd(II) with 2-Apy and NPA have been synthesised in simple, eco-friendly solvent systems and characterised. The X-ray crystal structures of two isostructural complexes of $[Mn(2\text{-}Apy)_2(dca)_2]$ and $[Cd(2\text{-}Apy)_2(dca)_2]$, as well as $[Zn_3(H_2O)_2(NPA)_6]$ complex have been reported.

$[Mn(2\text{-}Apy)_2(dca)_2]$ complex belongs to the monoclinic system with space group Cc, with $a$ = 6.0680(5) Å, $b$= 7.5050(3) Å, $c$ = 14.4658(4) Å, β = 113.087(2)°, $V$=1604.72(9) Å$^3$, and $Z$ = 4.

The trinuclear compound $[Zn_3(H_2O)_2(NPA)_6]$ crystallises in a triclinic crystal system with space group $P\bar{1}$, with $a$ = 11.0968(5) Å, $b$= 12.8319(6) Å, $c$ = 13.3134(6) Å, $\alpha$ = 111.703(2)°, β = 108.028(2)°, $\gamma$ = 93.125(2)°, $V$= 1643.97(13) Å$^3$, and $Z$ = 1. In this trinuclear complex, the central $Zn^{2+}$ ion is octahedrally coordinated to six O atoms from each NPA ligand, while the exterior $Zn^{2+}$ ions are each coordinated to one water molecule and three O atoms from three NPA ligands. This confer them a trigonal bipyramidal geometry according to the Addison's parameter.

The compound $[Cd(2\text{-}Apy)_2(dca)_2]$, as well as $[Mn(2\text{-}Apy)_2(dca)_2]$, belongs to the monoclinic system with space group Cc, $a$ = 16.1412(2) Å, $b$ = 7.6088(0) Å, $c$ = 14.5173(2) Å, β = 113.371(2)°, $V$=1636.66(4) Å$^3$, and $Z$ = 4.

Both compounds $[Mn(2\text{-}Apy)_2(dca)_2]$ and $[Cd(2\text{-}Apy)_2(dca)_2]$ form 1D polymeric chain along the *c*-axis in which each metal centre is in a distorted octahedra configuration. Both compounds are quite similar in their intra-chain metal-metal distance, with respective distances of 7.505 Å and 7.609 Å. If both compounds display π···π interactions through parallel centroids, intermolecular and intramolecular hydrogen bonds are present only in $[Mn(2\text{-}Apy)_2(dca)_2]$ complex. $[Cd(2\text{-}Apy)_2(dca)_2]$ complex however displays only intermolecular hydrogen bonding. The compound $[Zn_3(H_2O)_2(NPA)_6]$ is in a 3D configuration with intermolecular and intramolecular hydrogen bonding, as well as perpendicular π–interactions. These non-covalent bonding are responsible for the arrangement of the packing structure of the supramolecular coordination complex.

IR spectroscopy analyses show that all the three complexes are in a ternary configuration with the presence of metal centres and coordination to two different ligands. The coordination modes in the trinuclear compound is however complex. The conductimetry measurement have shown that all the

synthesised complexes are molecular in nature. All these results have been confirmed by single crystal X-ray analysis.

Elemental analysis results show that the percentages of the elements present in the complexes are close to theoretical values, confirming the expected formulae of the complexes. These are confirmed with TGA and by single crystal X-ray results.

The Hirsfeld surface analysis has check off seven (07) types of intermolecular contacts for both the $[Mn(2\text{-}Apy)_2(dca)_2]$ and $[Cd(2\text{-}Apy)_2(dca)_2]$ complexes, and five (05) for $[Zn_3(H_2O)_2(NPA)_6]$ complex.

The most prominent intermolecular interaction in both $[Mn(2\text{-}Apy)_2(dca)_2]$ and $[Cd(2\text{-}Apy)_2(dca)_2]$ complexes is the H···N/N···H bond contact, and contributes respectively at 37% and 40.1% on the Hirsfeld surface. Moreover, the C–H···π, H···H, and N···H/H···N intermolecular interactions for the compounds $[Mn(2\text{-}Apy)_2(dca)_2]$ and $[Cd(2\text{-}Apy)_2(dca)_2]$ constitute respectively 82.0% and 84.1% of the packing arrangement.

In the trinuclear complex $[Zn_3(H_2O)_2(NPA)_6]$, the highest contributor to the Hirsfeld surface is H···H bond contact and weight 63.4%. C–H···π, H···H, and O···H/H···O intermolecular interactions constitute up to 96.4% of the packing arrangement in this supramolecular coordination compound.

DFT calculations show that $[Zn_3(H_2O)_2(NPA)_6]$ possesses the lowest electronegativity value and that it is the best electron acceptor. On the other hand, $[Cd(2\text{-}Apy)_2(dca)_2]$ is the most reactive compound amongst all and this may be correlated with its highest biological activity.

*In vitro* biological activity of the ligands and their metal complexes were studied. The evaluation was carried on three microbial strains: a gram-positive bacterium, *Staphylococcus aureus*; a gram-negative bacterium, *Salmonella typhi*; and a fungus, *Candida albicans.* $[Zn_3(H_2O)_2(NPA)_6]$ and $[Cd(2\text{-}Apy)_2(dca)_2]$ complexes showed activities against all microbial strains, while $[Mn(2\text{-}Apy)_2(dca)_2]$ was only sensitive to *Staphylococcus aureus* and *Candida albicans* strains. $Cd(2\text{-}Apy)_2(dca)_2]$ complex however showed the highest activity index amongst all complexes. Molecular docking was also carried out to determine the binding affinity of these complexes on the breast cancer (PDB ID: 3hb5) and SARS-CoV-2 (PDB ID: 6lu7) proteins. This showed that $[Zn_3(H_2O)_2(NPA)_6]$ has the best binding affinity against all tested proteins. Moreover, its binding affinity is higher than that of Chloroquine, which would indicate that it would be a potential candidate for the inhibition of SARS-CoV-2. The docking study also reveals that $[Cd(2\text{-}Apy)_2(dca)_2]$ potentially has the lowest binding affinity against the tested proteins.

# PERSPECTIVES

If the immediate objectives of the present work have been attained, the following are envisaged:

- Synthesise the nanomaterial from the compounds using the top-bottom method and carry out their biological analyses;
- Carry out *in vitro* biological essay of the complexes on cancer strains to determine the extent of their biological versality;
- Carry out pharmacokinetic studies and toxicological profile of the complexes;
- Carry out DFT calculations at a higher basis set so as to have accurate values of chemical descriptors of the complexes;
- Carry out photoluminescent studies on the synthesised compounds.

These actions will not only improve the quality of the present work, but will serve also as directions for further research.

# Appendix I

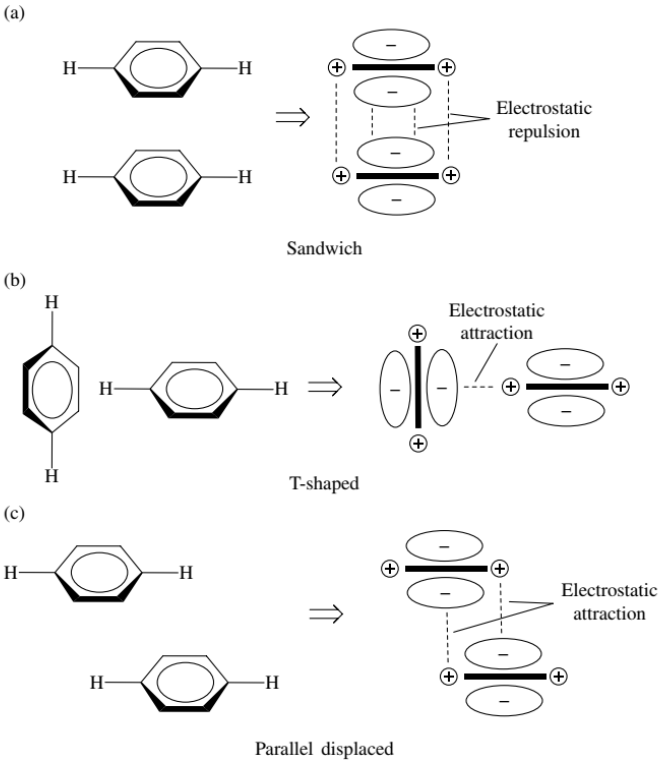


Scheme I : Stacking patterns in benzene ring

## Appendix II

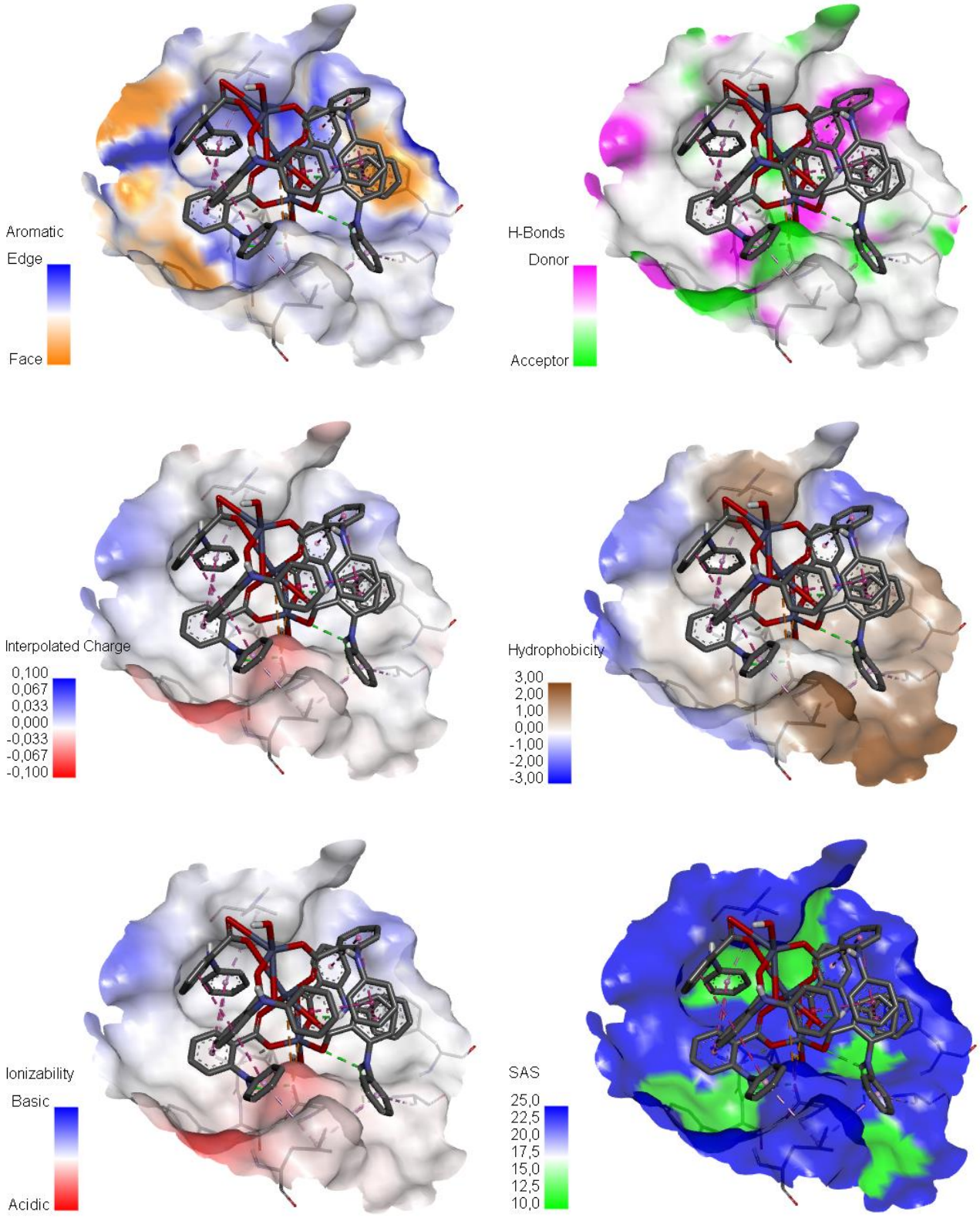


Scheme I: Receptor surfaces of Zn(II) complex against breast cancer protein (PDB ID: 3hb5) at its best pose (– 7.9 kcal/mol).

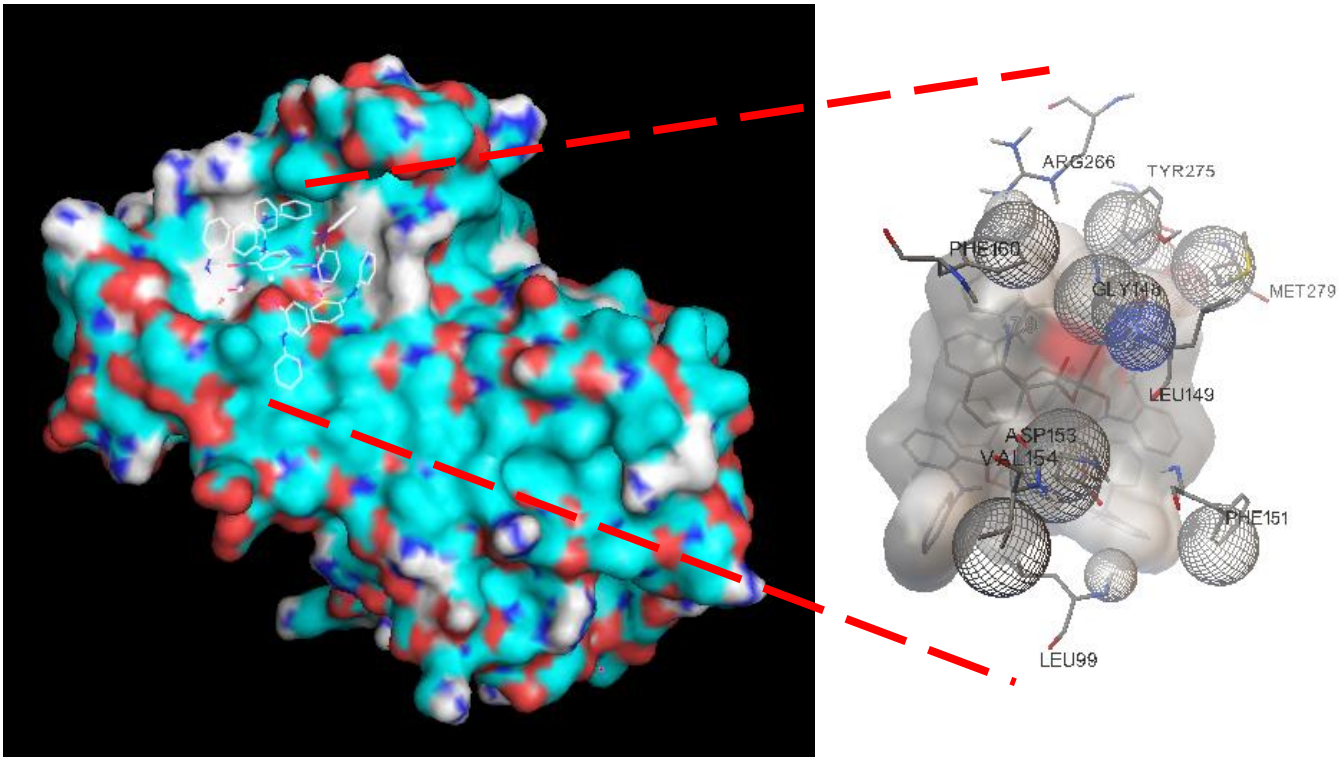


Scheme II: Surface image of Zn(II) complex in breast cancer mutant protein (PDB ID: 3hb5)

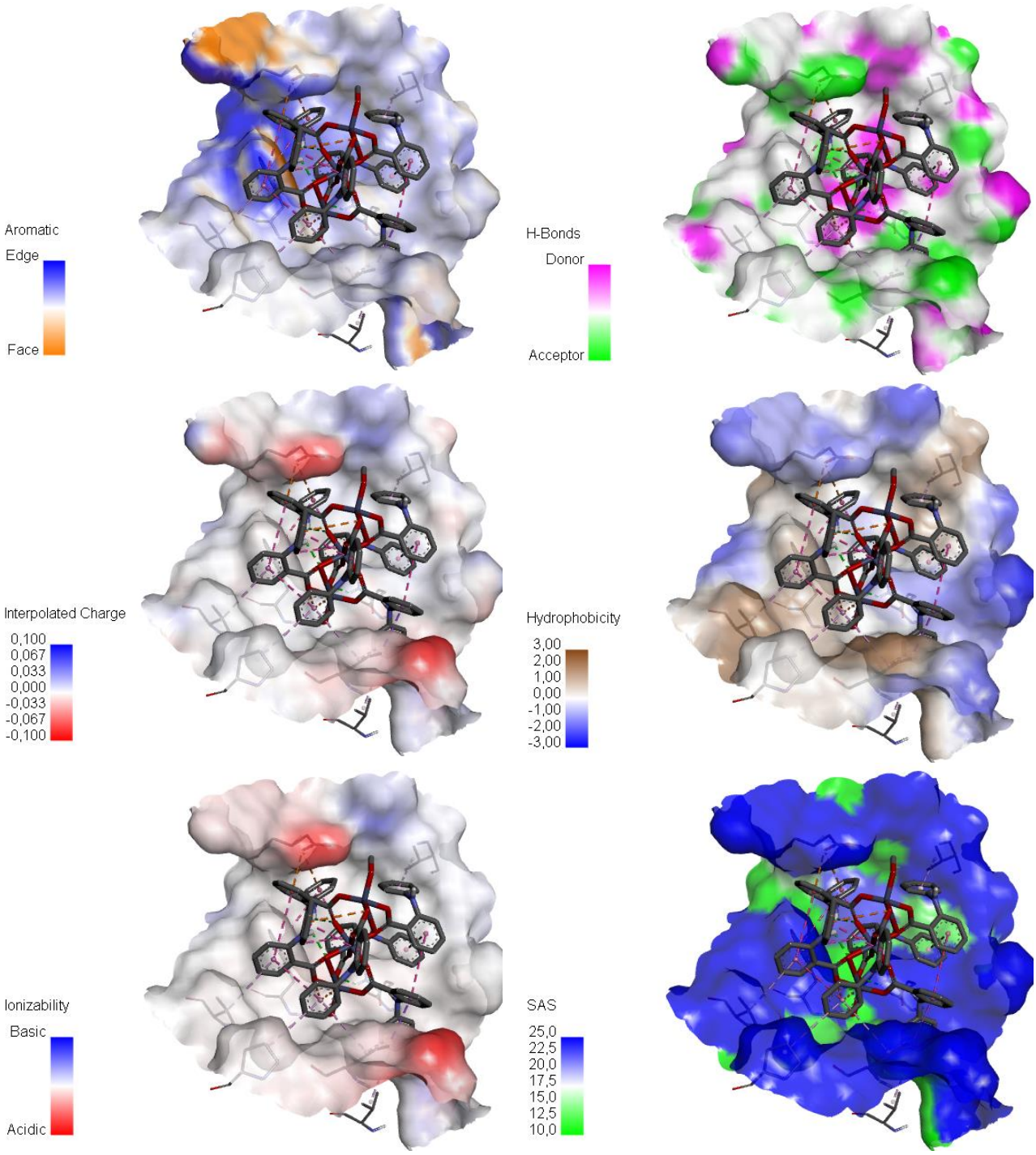


Scheme III: Receptor surfaces of Zn(II) complex against SARS-CoV-2 protein (PBD ID: 6lu7) at its best pose (– 8.4 kcal/mol).

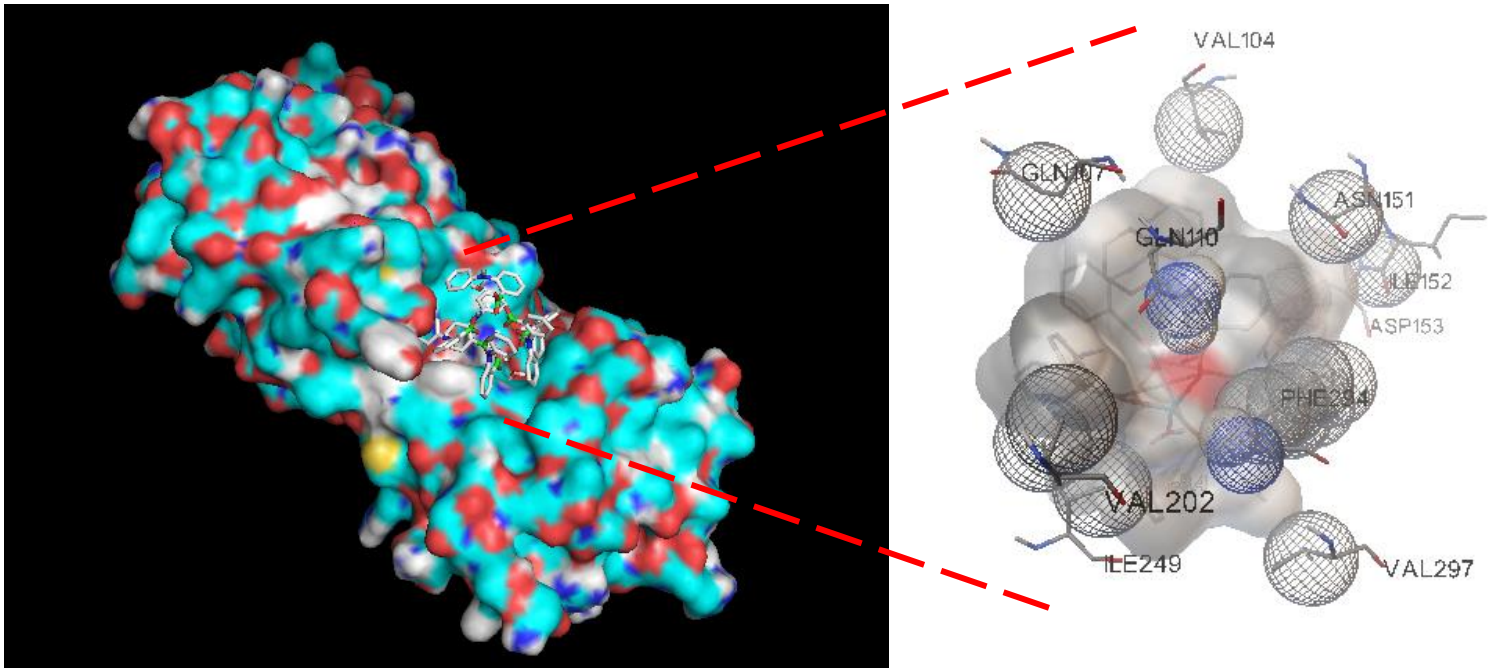


Scheme IV: Surface image of Zn(II) complex in SARS-CoV-2 protein (PDB ID: 6lu7)

## References


(1) Holliday, B. J.; Mirkin, C. A. Strategies for the Construction of Supramolecular Compounds through Coordination Chemistry. *Angew. Chem. Int. Ed.* **2001**, *40* (11), 2022–2043. https://doi.org/10.1002/1521-3773(20010601)40:11<2022::AID-ANIE2022>3.0.CO;2-D.

(2) Casini, A.; Woods, B.; Wenzel, M. The Promise of Self-Assembled 3D Supramolecular Coordination Complexes for Biomedical Applications. *Inorganic Chemistry* **2017**, 15. https://doi.org/10.1021/acs.inorgchem.7b0259.

(3) Ernst, K.-H.; Wild, F. R. W. P.; Blacque, O.; Berke, H. Alfred Werner's Coordination Chemistry: New Insights from Old Samples. *Angew. Chem. Int. Ed.* **2011**, *50* (46), 10780–10787. https://doi.org/10.1002/anie.201104477.

(4) Lehn, J.-M. Supramolecular Chemistry—Scope and Perspectives Molecules, Supermolecules, and Molecular Devices(Nobel Lecture). *Angew. Chem. Int. Ed. Engl.* **1988**, *27* (1), 89–112. https://doi.org/10.1002/anie.198800891.

(5) Whitesides, G. M.; Mathias, J. P.; Seto, C. T. Molecular Self-Assembly and Nanochemistry: A Chemical Strategy for the Synthesis of Nanostructures. *Science* **1991**, *254*, 1312–1319.

(6) Bäumer, N.; Matern, J.; Fernández, G. Recent Progress and Future Challenges in the Supramolecular Polymerization of Metal-Containing Monomers. *Chem. Sci.* **2021**, *12* (37), 12248–12265. https://doi.org/10.1039/D1SC03388C.

(7) Palmer, L. C.; Stupp, S. I. Molecular Self-Assembly into One-Dimensional Nanostructures. *Acc. Chem. Res.* **2008**, *41* (12), 1674–1684. https://doi.org/10.1021/ar8000926.

(8) Hayati, P.; Angel, G. The Role of Non-Covalent Interactions on Supramolecular Assembly of Coordination Compounds of Mercury(II) Based on Substituted Pyridine Mixed Ligands. A Survey of Different Conditions on Morphology of New Flower and Ribbon Like Submicro Structures. *Inorganica Chimica Acta* **2018**, 39. https://doi.org/10.1016/j.ica.2018.04.024.

(9) Malinowski, J.; Zych, D.; Jacewicz, D.; Gawdzik, B.; Drzeżdżon, J. Application of Coordination Compounds with Transition Metal Ions in the Chemical Industry—A Review. *IJMS* **2020**, *21* (15), 5443. https://doi.org/10.3390/ijms21155443.

(10) *Comprehensive Coordination Chemistry II: From Biology to Nanotechnology*, 1st ed.; McCleverty, J. A., Meyer, T. J., Eds.; Elsevier Pergamon: Amsterdam ; Boston, 2004.

(11) Hfidhi, N.; bkhairia, I.; Atoui, D.; Boonmak, J.; Nasri, M.; Ben Salem, R.; Youngme, S.; Naïli, H. Catalytic and Biological Valorization of a Supramolecular Mononuclear Copper Complex Based 4-Aminopyridine: Catalytic and Biological Valorization of a Copper Complex. *Appl Organometal Chem* **2019**, *33* (4), e4793. https://doi.org/10.1002/aoc.4793.

(12) Jin, S.; Wang, D. Construction of Six Non-Covalent-Bonded Supramolecules from Reactions of Cadmium(II), and Zinc(II) with 3,5-Dimethylpyrazole and Carboxylate Ligands. *Inorganica Chimica Acta* **2014**, *415*, 31–43. https://doi.org/10.1016/j.ica.2014.02.027.

(13) Tan, Y.; Xiong, J.; Gao, J.; Xu, Q.; Fu, C.; Tang, Y.; Yang, S. Synthesis , Crystal Structures , and Properties of Three Metal Complexes with N-Phenylanthranilic Acid. *Journal of Molecular Structure* **2015**, *1086*, 49–55. https://doi.org/10.1016/j.molstruc.2015.01.005.

(14) Anthony, E. J.; Bolitho, E. M.; Bridgewater, H. E.; Carter, O. W. L.; Donnelly, J. M.; Imberti, C.; Lant, E. C.; Lermyte, F.; Needham, R. J.; Palau, M.; Sadler, P. J.; Shi, H.; Wang, F.-X.; Zhang, W.-Y.; Zhang, Z. Metallodrugs Are Unique: Opportunities and Challenges of Discovery and Development. *Chem. Sci.* **2020**, *11* (48), 12888–12917. https://doi.org/10.1039/D0SC04082G.

(15) Kovala-Demertzi, D.; Hadjipavlou-Litina, D.; Staninska, M.; Primikiri, A.; Kotoglou, C.; Demertzis, M. A. Anti-Oxidant, *in Vitro* , *in Vivo* Anti-Inflammatory Activity and Antiproliferative Activity of Mefenamic Acid and Its Metal Complexes with Manganese(II), Cobalt(II), Nickel(II), Copper(II) and Zinc(II). *Journal of Enzyme Inhibition and Medicinal Chemistry* **2009**, *24* (3), 742–752. https://doi.org/10.1080/14756360802361589.

(16) Ros, T. G.; Van Der Lee, M. K.; Van Dillen, A. J.; Geus, J. W.; Koningsberger, D. C. Rhodium Complexes with N-Phenyl Anthranilic Acid Ligands as Catalysts for Hydrogenation. *Journal of Molecular Catalysis A: Chemical* **2002**, *186* (1–2), 13–24. https://doi.org/10.1016/S1381-1169(02)00062-6.

(17) Tas, M.; Yes, O. Z.; Bu, O. Novel Copper(II) Complexes of N-Phenylanthranilic Acid Containing Ethanol and Hydroxo Ligands. *Journal of Inorganic and Organometallic Polymers* **2010**, *20*, 298–305. https://doi.org/10.1007/s10904-010-9348-7.

(18) Rajalakshmi, R. T.; Bheeter, S. R.; Vasanth, N. Synthesis and Characterisaion of Biologically Active Metal Complexes of N-Phenyl Anthranilic Acid. *ReTeLL 15*, 8 pages.

(19) Mautner, F. A.; Jantscher, P.; Fischer, R. C.; Torvisco, A.; Vicente, R.; Karsili, T. N. V.; Massoud, S. S. Synthesis and Characterization of 1D Coordination Polymers of Metal(II)-Dicyanamido Complexes. *Polyhedron* **2019**, *166*, 36–43. https://doi.org/10.1016/j.poly.2019.03.038.

(20) Suckert, S.; Terraschke, H.; Reinsch, H.; Näther, C. Synthesis, Crystal Structures, Thermal, Magnetic and Luminescence Properties of Mn(II) and Cd(II) Thiocyanate Coordination Compounds with 4-(Boc-Amino)Pyridine as Co-Ligand. *Inorganica Chimica Acta* **2017**, *461*, 290–297. https://doi.org/10.1016/j.ica.2017.03.002.

(21) Gong, Y.; Hu, C.; Li, H.; Tang, W.; Huang, K.; Hou, W. Synthesis, Crystal Structure and Calcination of Three Novel Complexes Based on 2-Aminopyridine and Polyoxometalates. *Journal of Molecular Structure* **2006**, *784* (1–3), 228–238. https://doi.org/10.1016/j.molstruc.2005.09.009.

(22) Bolliger, J. L.; Oberholzer, M.; Frech, C. M. Access to 2-Aminopyridines - Compounds of Great Biological and Chemical Significance. *Advanced Synthesis and Catalysis* **2011**, *353* (6), 945–954. https://doi.org/10.1002/adsc.201000942.

(23) Nomiya, K.; Yokoyama, H. Syntheses, Crystal Structures and Antimicrobial Activities of Polymeric Silver(i) Complexes with Three Amino-Acids [Aspartic Acid (H2asp), Glycine (Hgly) and Asparagine (Hasn)]Note: For Ease of Reference during Discussion of Their Anions, H2asp, Hgly and Hasn Have Been Used as the Abbreviations for the Neutral Amino-Acids, Rather than the Conventional Asp, Gly and Asn, Respectively. *J. Chem. Soc., Dalton Trans.* **2002**, No. 12, 2483–2490. https://doi.org/10.1039/b200684g.

(24) Williams, D. R. Anticancer Drug Design Involving Complexes of Amino-Acids and Metal Ions. *Inorganica Chimica Acta Reviews* **1972**, *6*, 123–133. https://doi.org/10.1016/0073-8085(72)80014-7.

(25) Aiyelabola, T. O.; Isabirye, D. A.; Akinkunmi, E. O.; Ogunkunle, O. A.; Ojo, I. A. O. Synthesis, Characterization, and Antimicrobial Activities of Coordination Compounds of Aspartic Acid. *Journal of Chemistry* **2016**, *2016*, 1–8. https://doi.org/10.1155/2016/7317015.

(26) Alnomsy, A. K. Synthesis and Properties of Pyridine Containing Drugs and Heterocycles, University of Sussex, United Kingdom, 2016. http://sro.sussex.ac.uk/.

(27) Bendella, C. Synthèse et caractérisation des dérivés de la 2-aminopyridine et de leurs complexes de métaux de transition. Evaluation de leur activité antioxydante. Master, Université Abou-Bekr Belkaid, Tlemcen, Algérie, 2018.

(28) Tan, Y.-H.; Xiong, J.-B.; Gao, J.-X.; Xu, Q.; Fu, C.-W.; Tang, Y.-Z.; Yang, S.-P.; Wen, H.-R. Synthesis, Crystal Structures, and Properties of Three Metal Complexes with N-Phenylanthranilic Acid. *Journal of Molecular Structure* **2015**, *1086*, 49–55. https://doi.org/10.1016/j.molstruc.2015.01.005.

(29) Tas, M.; Yes, O. Z.; Bu, O. Novel Copper ( II ) Complexes of N -Phenylanthranilic Acid Containing Ethanol and Hydroxo Ligands. *Journal of Inorganic and Orgnanometallic Polymers* **2010**, *20*, 298–305. https://doi.org/10.1007/s10904-010-9348-7.

(30) Sim, S. A.; Saunders, G. C.; Lane, J. R.; Henderson, W. Synthesis and Characterisation of Organo-Platinum(II) Complexes of the N,O-Donor Ligands Hippuric Acid (N-Benzoylglycine) and N-Phenylanthranilic Acid. *Inorganica Chimica Acta* **2016**, *450*, 285–292. https://doi.org/10.1016/j.ica.2016.05.053.

(31) *Transition Metal Catalyzed Carbonylative Synthesis of Heterocycles*; Springer Berlin Heidelberg: New York, NY, 2015.

(32) Dojer, B.; Pevec, A.; Jagodič, M.; Kristl, M.; Drofenik, M. Three New Cobalt(II) Carboxylates with 2-, 3- and 4-Aminopyridine: Syntheses, Structures and Magnetic Properties. *Inorganica Chimica Acta* **2012**, *383*, 98–104. https://doi.org/10.1016/j.ica.2011.10.056.

(33) Amah, C. B. Y.; Agwara, M. O.; Yufanyi, D. M.; Conde, M. A.; Jagan, R.; Oben Eyong, K. Synthesis, Crystal Structure, and Antimicrobial Properties of a Novel 1-D Cobalt Coordination Polymer with Dicyanamide and 2-Aminopyridine. *International Journal of Inorganic Chemistry* **2015**, *2015*, 1–8. https://doi.org/10.1155/2015/106838.

(34) Liu, X.-H.; Zhang, L.; Lu, Q.; Xiao, Z.-P. Crystal Structure of Acetatohydroxy(2-Aminopyridine)Manganese(II), C7H10MnN2O3. *Zeitschrift für Kristallographie - New Crystal Structures* **2008**, *223* (2), 119–120. https://doi.org/10.1524/ncrs.2008.0050.

(35) Mautner, F. A.; Egger, A.; Sodin, B.; Goher, M. A. S.; Abu-Youssef, M. A. M.; Massoud, A.; Escuer, A.; Vicente, R. Two New Azido Bridging Mn(II) 1D Systems: Synthesis and Characterization of Trans-[Mn(N3)2(2-Aminopyridine)2]n and Trans-[Mn(N3)2(4-Azidopyridine)2]n. *Journal of Molecular Structure* **2010**, *969* (1–3), 192–196. https://doi.org/10.1016/j.molstruc.2010.02.012.

(36) Nieto, S.; Pe, J. Metal Complexes with Two Different Hydrogen-Bond Donor Ligands as Anion Hosts w. **2009**, 3279–3281. https://doi.org/10.1039/b823460d.

(37) Kanematsu, N.; Ebihara, M.; Kawamura, T. Preparation, Structure and Electrochemical Behavior of Dinuclear Cyclooctadiene-Chelated Ir(I) Complexes with 2-Aminopyridinato Bridges. *Inorganica Chimica Acta* **1999**, *292* (2), 244–248. https://doi.org/10.1016/S0020-1693(99)00218-2.

(38) Sadimenko, A. P. Organometallic Complexes of Aminopyridines. In *Advances in Heterocyclic Chemistry*; Elsevier, 2011; Vol. 102, pp 229–286. https://doi.org/10.1016/B978-0-12-385464-3.00003-0.

(39) Stuart R. Batten Suzanne M. Neville and David R. Tuner. *Coordination Polymers: Design, Analysis and Application*; House, T. G., Ed.; RSC Publishing: Cambridge, 2009. https://doi.org/10.1016/j.molstruc.2006.03.065.

(40) Zhu, H.; Shao, S.; Ma, J.; Qiu, X.; Sun, L.; Yang, S. Dibenzoato-Di(2-Aminopyridine)Nickel(II). *Acta Crystallographica Section E* **2003**, *E59*, 843–844. https://doi.org/10.1107/S1600536803019329.

(41) Mitra, M.; Manna, P.; Seth, S. K.; Das, A.; Meredith, J.; Helliwell, M.; Bauza´, A.; Choudhury, S. R.; Frontera, A.; Mukhopadhyay, M. Salt-Bridge–p (Sb–p) Interactions at Work: Associative Interactions of Sb–p, p–p and Anion–p in Cu(II)-Malonate–2-Aminopyridine–Hexafluoridophosphate Ternary System. *CrystEngComm* **2013**, *15*, 686–696. https://doi.org/DOI: 10.1039/c2ce26790j.

(42) Hobza, P.; Jirˇ, C. Non-Covalent Interactions in Biomacromolecules. *Phys. Chem. Chem. Phys.* **2007**, *9*, 5291–5303. https://doi.org/10.1039/b704781a.

(43) Karshikoff, A. *Non-Covalent Interactions in Proteins*; Imperial College Press ; Distributed by World Scientific: London ; Hackensack, N.J. : Singapore, 2006.

(44) Mahmudov, K. T.; Kopylovich, M. N.; Guedes, M. F. C.; Pombeiro, J.L, A. Non-Covalent Interactions in the Synthesis of Coordination Compounds : Recent Advances. *Coordination Chemistry Reviews* **2016**, No. November 2017. https://doi.org/10.1016/j.ccr.2016.09.002.

(45) Gilli, G.; Gilli, P. Towards an Unified Hydrogen-Bond Theory. *Journal of Molecular Structure* **2000**, *552*, 1–15.

(46) Arunan, E.; Desiraju, G. R.; Klein, R. A.; Sadlej, J.; Scheiner, S.; Alkorta, I.; Clary, D. C.; Crabtree, obert H.; Dannenberg, J. J.; Hobza, P.; Kjaergaard, H. G.; Legon, A. C.; Mennucci, B.; Nesbitt, D. J. Definition of the Hydrogen Bond. *Pure and Applied Chemistry* **2011**, *83* (8), 1619–1636.

(47) Maharramov, A. M.; Mahmudov, K. T.; Kopylovich, M. N.; Pombeiro, A. J. L. *Non-Covalent Interactions in the Synthesis and Design of New Compounds*, First Edit.; Maharramov, A. M., Mahmudov, K. T., Kopylovich, M. N., Pombeiro, A. J. L., Eds.; John Wiley & Sons, Inc., 2016; Vol. 09.

(48) Hunter, C. A.; Sanders, J. K. M. The Nature of π-π Interactions. *Journal of American Chemical Society* **1990**, *112* (2), 5525–5534.

(49) Tan, Y.; Xiong, J.; Gao, J.; Xu, Q.; Fu, C.; Tang, Y.; Yang, S. Synthesis , Crystal Structures , and Properties of Three Metal Complexes with N-Phenylanthranilic Acid. *JOURNAL OF MOLECULAR STRUCTURE* **2015**, *1086*, 49–55. https://doi.org/10.1016/j.molstruc.2015.01.005.

(50) Yenikaya, C.; Poyraz, M.; Sarı, M.; Demirci, F.; İlkimen, H.; Büyükgüngör, O. Synthesis, Characterization and Biological Evaluation of a Novel Cu(II) Complex with the Mixed Ligands 2,6-Pyridinedicarboxylic Acid and 2-Aminopyridine. *Polyhedron* **2009**, *28* (16), 3526–3532. https://doi.org/10.1016/j.poly.2009.05.079.

(51) Rao, C.; Reddy, B. NSAIDs and Chemoprevention. *CCDT* **2004**, *4* (1), 29–42. https://doi.org/10.2174/1568009043481632.

(52) Thun, M. J.; Henley, S. J.; Patrono, C. Nonsteroidal Anti-Inflammatory Drugs as Anticancer Agents: Mechanistic, Pharmacologic, and Clinical Issues. *JNCI Journal of the National Cancer Institute* **2002**, *94* (4), 252–266. https://doi.org/10.1093/jnci/94.4.252.

(53) Endo, S.; Matsunaga, T.; Soda, M.; Tajima, K.; Zhao, H.-T.; El-Kabbani, O.; Hara, A. Selective Inhibition of the Tumor Marker AKR1B10 by Antiinflammatory N-Phenylanthranilic Acids and Glycyrrhetic Acid. *Biol. Pharm. Bull.* **2010**, *33* (5), 886–890. https://doi.org/10.1248/bpb.33.886.

(54) Zapała, L.; Kosińska, M.; Woźnicka, E.; Byczyński, Ł.; Ciszkowicz, E. Thermochimica Acta Comparison of Spectral and Thermal Properties and Antibacterial Activity of New Binary and Ternary Complexes of Sm ( III ), Eu ( III ) and Gd ( III ) Ions with N -Phenylanthranilic Acid and 1 , 10-Phenanthroline. *Thermochimica Acta* **2019**, *671* (September 2018), 134–148. https://doi.org/10.1016/j.tca.2018.11.019.

(55) Thanh, N. T. K.; Stevenson, G.; Obatomi, D. K.; Aicher, B.; Baumeister, M.; Bach, P. H. Urinary Lipid Changes during the Development of Chemically-Induced Renal Papillary Necrosis: A Study Using Mefenamic Acid and *N* -Phenylanthranilic Acid. *Biomarkers* **2001**, *6* (6), 417–427. https://doi.org/10.1080/13547500110057407.

(56) Betton, G. R.; Kenne, K.; Somers, R.; Marr, A. Protein Biomarkers of Nephrotoxicity; a Review and Findings with Cyclosporin A, a Signal Transduction Kinase Inhibitor and N-Phenylanthranilic Acid. *CBM* **2005**, *1* (1), 59–67. https://doi.org/10.3233/CBM-2005-1107.

(57) Betton, G. R.; Ennulat, D.; Hoffman, D.; Gautier, J.-C.; Harpur, E.; Pettit, S. Biomarkers of Collecting Duct Injury in Han-Wistar and Sprague-Dawley Rats Treated with N-Phenylanthranilic Acid. *Toxicol Pathol* **2012**, *40* (4), 682–694. https://doi.org/10.1177/0192623311436174.

(58) Borowski, A. F. Rhodium Complexes with N-Phenylanthranilic Acid . Synthesis , Structural Investigations and Catalytic Activity in Hydrogenation of Some Aromatic and Heteroaromatic Compounds. **1983**, *270*, 266–270.

(59) Nassab, R. H.; Bakhshi, M.; Amini, M. K. Adsorptive Cathodic Stripping Voltammetric Determination of Uranium(VI) in Presence of N-Phenylanthranilic Acid. *Electroanalysis* **2014**, *26*, 1598–1605. https://doi.org/10.1002/elan.201400107.

(60) Sriramam, K. Some Observations on the Redox Behaviour of N-Phenylanthranilic Acid Indicator in Iron(II) Titrations. *Talanta* **1973**, *20* (4), 383–390. https://doi.org/10.1016/0039-9140(73)80166-3.

(61) IUPAC. *Compendium of Chemical Terminology*, 2nd ed.; McNaught, A. D., Wilkinson, A., Eds.; Blackwell Scientific Publications: Oxford, 1997; Vol. 67. https://doi.org/10.1351/goldbook.

(62) Zheng, L. Synthesis , Crystal Structures, and Magnetic Properties of Ternary M(II)-Dicyanamide-Hydroxypyridine Complexes. *Journal of Inorganic Chemistry* **2013**, *2013*, 1–10.

(63) Carranza, J.; Sletten, J.; Lloret, F.; Julve, M. Structural Analysis and Magnetic Properties of the Copper(II) Dicyanamide Complexes [Cu2(Dmphen)2(Dca)4], [Cu(Dmphen)(Dca)(NO3)]n and [Cu(4,4′-Dmbpy)(H2O)(Dca)2] (Dca=dicyanamide; Dmphen=2,9-Dimethyl-1,10-Phenanthroline; 4,4′-Dmbpy=4,4′-Dimethyl-2,2′-Bipyridine). *Inorganica Chimica Acta* **2004**, *357* (11), 3304–3316. https://doi.org/10.1016/j.ica.2004.01.044.

(64) Triki, S.; Thétiot, F.; Gala-Mascaros, J.-R.; Pala, J. S.; Dunbar, K. R. New Compounds with Bridging Dicyanamide and Bis-Chelating 2,2'- -Bipyrimidine Ligands: Syntheses, Structural Characterisation and Magnetic Properties of the Two-Dimensional Materials [Fe(Dca)4(Bpym)].H2O and [Fe(Dca)4(Bpym)(H2O)2]. *New Journal of Chemistry* **2001**, *25*, 954–958. https://doi.org/10.1039/b102188p.

(65) Wang, Z.; Liu, T.; Long, X.; Li, Y.; Bai, F.; Yang, S. Understanding the Diverse Coordination Understanding the Diverse Coordination Modes of Thiocyanate. *The Journal of Physical chemistry* **2019**. https://doi.org/10.1021/acs.jpcc.9b01457.

(66) Norbury, A. H. Coordination Chemistry of The Cyanate, Thiocyanate, and Selenocyanate Ions. In *Advances in Inorganic Chemistry and Radiochemistry*; Elsevier, 1975; p 231—386. https://doi.org/10.1016/s0065-2792(08)60064-3.

(67) Alam, MD. M.; Ahmed, F.; Begum, R.; Rahman, S. M. M.; Siddiquey, I. A.; Karim, M. R.; Saiful, I. S. Synthesis and Characterization of a Thiocyanate Bridged Dinuclear Cu(II) Complex Containing Macrocyclic Ligand Derived From Pyridine-2,6-Dicarboxaldehyde and 1, 2-Bis(2-Aminoethoxy) Ethane. *Journal of Bangladesh Academy of Science* **2012**, *36* (1), 89–96.

(68) Chunga, Y.-H.; Linb, H.-H.; Weib, H.-H. Synthesis , Crystal Structure , and Magnetic Properties of ( X - : Cyanate , Dicyanamide , Acetate , Thiocyanato ). *Journal of the Chinese Chemical Society* **2005**, *52* (5), 877–884.

(69) Khan, S.; Sproules, S.; Natrajan, L.; Harms, K.; Chattopadhyay, S. End-on Cyanate or End-to-End Thiocyanate Bridged Dinuclear Copper(II) Complexes with a Tridentate Schiff Base Blocking Ligand: Synthesis, Structure and Magnetic Studies. *New Journal of Chemistry* **2017**. https://doi.org/10.1039/C7NJ03990E.

(70) Chandler, J. D.; Day, B. J. Biochemical Mechanisms and Therapeutic Potential of the Pseudohalide Thiocyanate in Human Health. **2015**, *49* (6), 695–710. https://doi.org/10.3109/10715762.2014.1003372.Biochemical.

(71) Chandler, J. D.; Day, B. J. THIOCYANATE: A Potentially Useful Therapeutic Agent with Host Defense and Antioxidant Properties. *Biochemical Pharmacology* **2012**, *84* (11), 1381–1387. https://doi.org/10.1016/j.bcp.2012.07.029.

(72) Nadeem, S.; Sirajuddin, M.; Ahmad, S.; Yaqub, S.; Ali, M. I.; Tirmizi, S. A.; Ali, S.; Hameed, A. Synthesis, Spectral Characterization, In Vitro Antibacterial Evaluation and POM Analyses of Palladium(II) Thiocyanate Complexes of Thioamides. *Pharmaceutical Chemistry Journal* **2017**, *51* (9), 793–799. https://doi.org/10.1007/s11094-017-1695-z.

(73) Manimaran, P.; Balasubramaniyan, S. Synthesis, Characterization and Biological Evaluation of Fe(III) and Cu(II) Complexes with 2,4-Dinitrophenyl Hydrazine and Thiocyanate Ions. *Asian Journal of Chemistry* **2019**, *31* (4), 780–784.

(74) Human, Z.; Munyaneza, A.; Omondi, B.; Sanabria, N. M.; Meijboom, R.; Marianne, C. J. The Induction of Cell Death by Phosphine Silver(I) Thiocyanate Complexes in SNO-Esophageal Cancer Cells. *Biometals* **2014**, No. I. https://doi.org/10.1007/s10534-014-9817-5.

(75) Salomon, E.; Keren, N.; Kanteev, M.; Adir, N. Manganese in Biological Systems: Transport and Function. In *PATAI'S Chemistry of Functional Groups*; Rappoport, Z., Ed.; John Wiley & Sons, Ltd: Chichester, UK, 2011; p pat0540. https://doi.org/10.1002/9780470682531.pat0540.

(76) Zhu, W.; Richards, N. G. J. Biological Functions Controlled by Manganese Redox Changes in Mononuclear Mn-Dependent Enzymes. *Essays in Biochemistry* **2017**, *61* (2), 259–270. https://doi.org/10.1042/EBC20160070.

(77) Sousa, C.; Moutinho, C.; Vinha, A. F.; Matos, C. Trace Minerals in Human Health: Iron, Zinc, Copper, Manganese and Fluorine. *13*, 24.

(78) Kehres, D. G.; Maguire, M. E. Emerging Themes in Manganese Transport, Biochemistry and Pathogenesis in Bacteria. *FEMS Microbiology Reviews* **2003**, 28.

(79) Chen, P. Manganese Metabolism in Humans. *Front Biosci* **2018**, *23* (9), 1655–1679. https://doi.org/10.2741/4665.

(80) *Handbook on the Toxicology of Metals*, 3rd ed.; Nordberg, G., Ed.; Academic Press: Amsterdam ; Boston, 2007.

(81) Prihantono; Rizal, I.; Indah, R.; Warsinggih. Potential Anticancer Activity of Mn (II) Complexes Containing Arginine Dithiocarbamate Ligand on MCF-7 Breast Cancer Cell Lines. *Annals of Medicine and Surgery* **2020**, *60*, 396–402. https://doi.org/10.1016/j.amsu.2020.11.018.

(82) Tarushi, A.; Geromichalos, G. D.; Kessissoglou, D. P.; Psomas, G. Manganese Coordination Compounds of Mefenamic Acid: In Vitro Screening and in Silico Prediction of Biological Activity. *Journal of Inorganic Biochemistry* **2019**, *190*, 1–14. https://doi.org/10.1016/j.jinorgbio.2018.09.017.

(83) Zhang, F.; Lin, Q.-Y.; Zheng, X.-L.; Zhang, L.-L.; Yang, Q.; Gu, J.-Y. Crystal Structures, Interactions with Biomacromolecules and Anticancer Activities of Mn(II), Ni(II), Cu(II) Complexes of Demethylcantharate and 2-Aminopyridine. *J Fluoresc* **2012**, *22* (5), 1395–1406. https://doi.org/10.1007/s10895-012-1078-5.

(84) Oliveira, C. G.; Maia, P. I. da S.; Souza, P. C.; Pavan, F. R.; Leite, C. Q. F.; Viana, R. B.; Batista, A. A.; Nascimento, O. R.; Deflon, V. M. Manganese(II) Complexes with Thiosemicarbazones as Potential Anti-Mycobacterium Tuberculosis Agents. *Journal of Inorganic Biochemistry* **2014**, *132*, 21–29. https://doi.org/10.1016/j.jinorgbio.2013.10.011.

(85) McCarron, P.; McCann, M.; Devereux, M.; Kavanagh, K.; Skerry, C.; Karakousis, P. C.; Aor, A. C.; Mello, T. P.; Santos, A. L. S.; Campos, D. L.; Pavan, F. R. Unprecedented in Vitro Antitubercular Activitiy of Manganese(II) Complexes Containing 1,10-Phenanthroline and Dicarboxylate Ligands: Increased Activity, Superior Selectivity, and Lower Toxicity in Comparison to Their Copper(II) Analogs. *Frontiers in Microbiology* **2018**, *9* (1432), 1–10. https://doi.org/10.3389/fmicb.2018.01432.

(86) Osredkar, J.; Sustar, N. Copper and Zinc , Biological Role and Significance of Copper / Zinc Imbalance Journal of Clinical Toxicology. *Journal of Clinical Toxicology* **2011**, 1–18. https://doi.org/10.4172/2161-0495.S3-001.

(87) Vallee, B. L.; Falchuk, K. H. The Biochemical Basis of Zinc Physiology. *Physiological Reviews* **1993**, *73* (1), 79–118.

(88) Orlova, M. A.; Orlov, A. P. Role of Zinc in an Organism and Its Influence on Processes Leading to Apoptosis. *British Journal of Medecine & Medical Research* **2011**, *1* (4), 239–305.

(89) Devi, C. B.; Nandakishore, T.; Sangeeta, N.; Basar, G.; Devi, N. O.; Jamir, S.; Singh, M. A. Zinc in Human Health. *Journal of Dental and Medical Sciences* **2014**, *13* (7), 18–23.

(90) Skrajnowska, D.; Bobrowska-Korczak, B. Role of Zinc in Immune System and Anti-Cancer Defense Mechanisms. *Nutrients* **2019**, *11* (10), 2273. https://doi.org/10.3390/nu11102273.

(91) Costello, L. C.; Franklin, R. B. Cytotoxic/Tumor Suppressor Role of Zinc for the Treatment of Cancer: An Enigma and an Opportunity. *Expert Review Anticancer Therapy* **2012**, *12* (1), 121–128. https://doi.org/10.1586/era.11.190.Cytotoxic/tumor.

(92) Skrajnowska, D.; Bobrowska-Korczak, B. Role of Zinc in Immune System and Anti-Cancer. *Nutrients* **2019**, *11* (2273), 28.

(93) Jin, S.; Wang, D. Construction of Six Non-Covalent-Bonded Supramolecules from Reactions of Cadmium(II), and Zinc(II) with 3,5-Dimethylpyrazole and Carboxylate Ligands. *Inorganica Chimica Acta* **2014**, *415*, 31–43. https://doi.org/10.1016/j.ica.2014.02.027.

(94) Borsari, M. Cadmium: Inorganic & Coordination Chemistry. *Encyclopedia of Inorganic Chemistry* **2006**, 1–18. https://doi.org/DOI: 10.1002/0470862106.ia030.

(95) Oliviera da Silva, A. L.; Barrocas, P. R. G.; Jacob, S. do C.; Moriera, J. C. Dietary Intake and Health Effects of Selected Toxic Elements. *Brazilian Journal of Plant Physiology* **2005**, *17* (1), 79–93.

(96) Genchi, G.; Sinicropi, M. S.; Lauria, G.; Carocci, A.; Catalano, A. The Effects of Cadmium Toxicity. *International Journal of Environmental Research and Public Health* **2020**, *17* (3782), 1–22.

(97) Sharma, H.; Rawal, N.; Mathew, B. B. The Characteristics, Toxicity and Effects of Cadmium. *International Journal of Nanotechnology and Nanoscience* **2015**, *3*, 1–9.

(98) Saghatforoush, L. A.; Valencia, L.; Chalabian, F.; Ghammamy, S. Synthesis, Characterization, Crystal Structure, and Biological Studies of a Cadmium(II) Complex with a Tridentate Ligand 4 -Chloro-2,2 :6 ,2 -Terpyridine. *Bioinorganic Chemistry and Applications* **2011**, 8. https://doi.org/10.1155/2011/803292.

(99) Golcu, A.; Tumer, M.; Demirelli, H.; Wheatley, R. A. Cd(II) and Cu(II) Complexes of Polydentate Schiff Base Ligands: Synthesis, Characterization, Properties and Biological Activity. *Inorganica Chimica Acta* **2005**, *358* (6), 1785–1797. https://doi.org/10.1016/j.ica.2004.11.026.

(100) Tümer, M. Polydentate Schiff-Base Ligands and Their Cd(II) and Cu(II) Metal Complexes: Synthesis, Characterization, Biological Activity and Electrochemical Properties. *Journal of Coordination Chemistry* **2007**, *60* (19), 2051–2065.

(101) Karadağ, A.; Korkmaz, N.; Aydın, A.; Akbaş, H.; Tekin, Ş.; Yerli, Y.; Şen, F. Metalo Components Exhibiting Significant Anticancer and Antibacterial Properties: A Novel Sandwich-Type like Polymeric Structure. *Sci Rep* **2020**, *10* (1), 12472. https://doi.org/10.1038/s41598-020-69416-x.

(102) Sato, A.; Yamaguchi, T.; Hamada, M.; Ono, D.; Sonoda, S.; Oshiro, T.; Nagashima, M.; Kato, K.; Okazumi, S.; Katoh, R.; Ishii, Y.; Tateda, K. Morphological and Biological Characteristics of *Staphylococcus Aureus* Biofilm Formed in the Presence of Plasma. *Microbial Drug Resistance* **2019**, *25* (5), 668–676. https://doi.org/10.1089/mdr.2019.0068.

(103) Cohen, M. L. Staphylococcus Aureus: Biology, Mechanisms of Virulence, Epidemiology. *The Journal of Pediatrics* **1986**, *108* (5), 796–799. https://doi.org/10.1016/S0022-3476(86)80747-8.

(104) Tong, S. Y. C.; Davis, J. S.; Eichenberger, E.; Holland, T. L.; Fowler, V. G. Staphylococcus Aureus Infections: Epidemiology, Pathophysiology, Clinical Manifestations, and Management. *Clin Microbiol Rev* **2015**, *28* (3), 603–661. https://doi.org/10.1128/CMR.00134-14.

(105) Chen, K.; Huang, Y.; Song, Q.; Wu, C.; Chen, X.; Zeng, L. Drug-Resistance Dynamics of Staphylococcus Aureus between 2008 and 2014 at a Tertiary Teaching Hospital, Jiangxi Province, China. *BMC Infect Dis* **2017**, *17* (1), 97. https://doi.org/10.1186/s12879-016-2172-0.

(106) Schaumburg, F.; Alabi, A. S.; Peters, G.; Becker, K. New Epidemiology of Staphylococcus Aureus Infection in Africa. *Clinical Microbiology and Infection* **2014**, *20* (7), 589–596. https://doi.org/10.1111/1469-0691.12690.

(107) Kesah, C.; Ben Redjeb, S.; Odugbemi, T. O.; Boye, C. S.-B.; Dosso, M.; Ndinya Achola, J. O.; Koulla-Shiro, S.; Benbachir, M.; Rahal, K.; Borg, M. Prevalence of Methicillin—Resistant Staphylococcus Aureus in Eight African Hospitals and Malta. *Clinical Microbiology and Infection* **2003**, *9* (2), 153–156. https://doi.org/10.1046/j.1469-0691.2003.00531.x.

(108) Monaco, M.; Pimentel de Araujo, F.; Cruciani, M.; Coccia, E. M.; Pantosti, A. Worldwide Epidemiology and Antibiotic Resistance of Staphylococcus Aureus. In *Staphylococcus aureus*; Bagnoli, F., Rappuoli, R., Grandi, G., Eds.; Current Topics in Microbiology and Immunology; Springer International Publishing: Cham, 2016; Vol. 409, pp 21–56. https://doi.org/10.1007/82_2016_3.

(109) Harris, L.; Foster, S.; Richards, R. An Introduction to Staphylococcus Aureus, and Techniques for Identifying and Quantifying s. Aureus Adhesins in Relation to Adhesion to Biomaterials: Review. *eCM* **2002**, *4*, 39–60. https://doi.org/10.22203/eCM.v004a04.

(110) Ghalehnoo, Z. R. Diagnosis, Treatment and Prevention of Staphylococcus Aureus. *International Journal of Medical and Health Research* **2018**, *4* (11), 68–70.

(111) Abás, E.; Aguirre-Ramírez, D.; Laguna, M.; Grasa, L. Selective Anticancer and Antimicrobial Metallodrugs Based on Gold(III) Dithiocarbamate Complexes. *Biomedicines* **2021**, *9* (12), 1775. https://doi.org/10.3390/biomedicines9121775.

(112) Andrews-Polymenis, H. L.; Baumler, A. J.; McCormick, B. A.; Fang, F. C. Taming the Elephant: Salmonella Biology, Pathogenesis, and Prevention□. *INFECT. IMMUN.* **2010**, *78*, 14.

(113) Njoya, H. F.; Awolu, M. M.; Christopher, T. B.; Duclerc, J. F.; Ateudjieu, J.; Wirsiy, F. S.; Atuhaire, C.; Cumber, S. N. Prevalence and Awareness of Mode of Transmission of Typhoid Fever in Patients

Diagnosed with Salmonella Typhi and Paratyphi Infections at the Saint Elisabeth General Hospital Shisong, Bui Division, Cameroon. *Panafrican Medical Journal* **2021**, *40* (83), 9 pages.

(114) Veeraraghavan, B.; Pragasam, A. K.; Bakthavatchalam, Y. D.; Ralph, R. Typhoid Fever: Issues in Laboratory Detection, Treatment Options & Concerns in Management in Developing Countries. **2018**, 12.

(115) Marchello, C. S.; Carr, S. D.; Crump, J. A. A Systematic Review on Antimicrobial Resistance among Salmonella Typhi Worldwide. *The American Journal of Tropical Medicine and Hygiene* **2020**, *103* (6), 2518–2527. https://doi.org/10.4269/ajtmh.20-0258.

(116) Rodríguez, I.; Fernández-Vega, L.; Maser-Figueroa, A. N.; Sang, B.; González-Pagán, P.; Tinoco, A. D. Exploring Titanium(IV) Complexes as Potential Antimicrobial Compounds. *Antibiotics* **2022**, *11* (2), 158. https://doi.org/10.3390/antibiotics11020158.

(117) Anh, D. N.; Hung, D. N.; Tien, T. V.; Dinh, V. N.; Son, V. T.; Luong, N. V.; Van, N. T.; Quynh, N. T. N.; Van Tuan, N.; Tuan, L. Q.; Bac, N. D.; Luc, N. K.; Anh, L. T.; Trung, D. M. Prevalence, Species Distribution and Antifungal Susceptibility of Candida Albicans Causing Vaginal Discharge among Symptomatic Non-Pregnant Women of Reproductive Age at a Tertiary Care Hospital, Vietnam. *BMC Infect Dis* **2021**, *21* (1), 523. https://doi.org/10.1186/s12879-021-06192-7.

(118) Mareković, I.; Pleško, S.; Rezo Vranješ, V.; Herljević, Z.; Kuliš, T.; Jandrlić, M. Epidemiology of Candidemia: Three-Year Results from a Croatian Tertiary Care Hospital. *JoF* **2021**, *7* (4), 267. https://doi.org/10.3390/jof7040267.

(119) Ben-Ami, R. Treatment of Invasive Candidiasis: A Narrative Review. *JoF* **2018**, *4* (3), 97. https://doi.org/10.3390/jof4030097.

(120) Guinea, J. Global Trends in the Distribution of Candida Species Causing Candidemia. *Clinical Microbiology and Infection* **2014**, *20*, 5–10. https://doi.org/10.1111/1469-0691.12539.

(121) Pugliese, A.; Torre, D.; Baccino, F. M.; Perri, G. D.; Cantamessa, C.; Gerbaudo, L.; Saini, A.; Vidotto, V. Candida Albicans and HIV-1 Infection. *Cell Biochem. Funct.* **2000**, *18* (4), 235–241. https://doi.org/10.1002/1099-0844(200012)18:4<235::AID-CBF877>3.0.CO;2-L.

(122) Kechia, F. A.; Dohbit, J. S.; Kouotou, E. A.; Iwewe, S. Y.; Dzoyem, J. P.; Mbopuwouo, N. M.; Moyou, S. R. Profil Épidémiologique et Étiologique de la Candidose Vulvo-Vaginale chez la Femme Enceinte à Yaoundé (Cameroun). **2015**, *16*, 6.

(123) Martins, N.; Ferreira, I. C. F. R.; Barros, L.; Silva, S.; Henriques, M. Candidiasis: Predisposing Factors, Prevention, Diagnosis and Alternative Treatment. *Mycopathologia* **2014**, *177* (5–6), 223–240. https://doi.org/10.1007/s11046-014-9749-1.

(124) Arendrup, M. C.; Patterson, T. F. Multidrug-Resistant Candida: Epidemiology, Molecular Mechanisms, and Treatment. *The Journal of Infectious Diseases* **2017**, *216* (suppl_3), S445–S451. https://doi.org/10.1093/infdis/jix131.

(125) Berman, J. Candida Albicans. *Current Biology* **2012**, *22* (16), R620–R622. https://doi.org/10.1016/j.cub.2012.05.043.

(126) Costa-de-Oliveira, S.; Rodrigues, A. G. Candida Albicans Antifungal Resistance and Tolerance in Bloodstream Infections: The Triad Yeast-Host-Antifungal. *Microorganisms* **2020**, *8* (2), 154. https://doi.org/10.3390/microorganisms8020154.

(127) Baskar, R.; Lee, K. A.; Yeo, R.; Yeoh, K. Cancer and Radiation Therapy: Current Advances and Future Directions. *International Journal of Medical Science* **2012**, *9* (3), 193–199. https://doi.org/10.7150/ijms.3635.

(128) Orock GE, E.; P, N.; As, D. Current Cancer Incidence and Trends in Yaounde, Cameroon. *OGH Reports* **2012**, *1* (1), 58–63. https://doi.org/10.5530/ogh.2012.1.14.

(129) Baskar, R.; Lee, K. A.; Yeo, R.; Yeoh, K.-W. Cancer and Radiation Therapy: Current Advances and Future Directions. *International Journal of Medical Sciences* **2012**, *9* (3), 193–199. https://doi.org/10.7150/ijms.3635.

(130) Hanahan, D.; Weinberg, R. A. The Hallmarks of Cancer. *Cell* **2000**, *100* (1), 57–70. https://doi.org/10.1016/S0092-8674(00)81683-9.

(131) Chang, A. H.; Parsonnet, J. Role of Bacteria in Oncogenesis. *CMR* **2010**, *23* (4), 837–857. https://doi.org/10.1128/CMR.00012-10.

(132) Parsonnet, J. Bacterial Infection as a Cause of Cancer. *Environmental Health Perspectives* **1995**, *103*, 6.

(133) Blaser, M. J. Understanding Microbe-Induced Cancers. *Cancer Prev Res* **2008**, *1* (1), 15–20. https://doi.org/10.1158/1940-6207.CAPR-08-0024.

(134) Urruticoechea, A.; Alemany, R.; Balart, J.; Villanueva, A.; Vinals, F.; Capella, G. Recent Advances in Cancer Therapy: An Overview. *CPD* **2010**, *16* (1), 3–10. https://doi.org/10.2174/138161210789941847.

(135) Rafique, S.; Idrees, M.; Nasim, A.; Akbar, H.; Athar, A. Transition Metal Complexes as Potential Therapeutic Agents. *Biotechnology and Molecular Biology Reviews* **2010**, *5* (2), 38–45.

(136) Galluzzi, L.; Senovilla, L.; Vitale, I.; Michels, J.; Martins, I.; Kepp, O.; Castedo, M.; Kroemer, G. Molecular Mechanisms of Cisplatin Resistance. *Oncogene* **2012**, *31*, 1869–1883. https://doi.org/10.1038/onc.2011.384.

(137) Zhang, P.; Sadler, P. J. Redox-Active Metal Complexes for Anticancer Therapy: Redox-Active Metal Complexes for Anticancer Therapy. *Eur. J. Inorg. Chem.* **2017**, *2017* (12), 1541–1548. https://doi.org/10.1002/ejic.201600908.

(138) Alanagreh, L.; Alzoughool, F.; Atoum, M. The Human Coronavirus Disease COVID-19: Its Origin, Characteristics, and Insights into Potential Drugs and Its Mechanisms. *Pathogens* **2020**, *9* (5), 331. https://doi.org/10.3390/pathogens9050331.

(139) Shereen, M. A.; Khan, S.; Kazmi, A.; Bashir, N.; Siddique, R. COVID-19 Infection: Origin, Transmission, and Characteristics of Human Coronaviruses. *Journal of Advanced Research* **2020**, *24*, 91–98. https://doi.org/10.1016/j.jare.2020.03.005.

(140) Rossi, G. A.; Sacco, O.; Mancino, E.; Cristiani, L.; Midulla, F. Differences and Similarities between SARS-CoV and SARS-CoV-2: Spike Receptor-Binding Domain Recognition and Host Cell Infection with Support of Cellular Serine Proteases. *Infection* **2020**, *48* (5), 665–669. https://doi.org/10.1007/s15010-020-01486-5.

(141) Nadeem, M. S.; Zamzami, M. A.; Choudhry, H.; Murtaza, B. N.; Kazmi, I.; Ahmad, H.; Shakoori, A. R. Origin, Potential Therapeutic Targets and Treatment for Coronavirus Disease (COVID-19). **2020**, 13.

(142) Kadioglu, O.; Saeed, M.; Greten, H. J.; Efferth, T. *Identification of Novel Compounds against Three Targets of SARS CoV-2 Coronavirus by Combined Virtual Screening and Supervised Machine Learning*; preprint; nCoV, 2020. https://doi.org/10.2471/BLT.20.255943.

(143) Naqvi, A. A. T.; Fatima, K.; Mohammad, T.; Fatima, U.; Singh, I. K.; Singh, A.; Atif, S. M.; Hariprasad, G.; Hasan, G. M.; Hassan, I. Insights into SARS-CoV-2 Genome, Structure, Evolution, Pathogenesis and Therapies: Structural Genomics Approach. 50.

(144) Spackman, M. A.; Jayatilaka, D. Hirshfeld Surface Analysis. *CrystEngComm* **2009**, *11* (1), 19–32. https://doi.org/10.1039/B818330A.

(145) McKinnon, J. J.; Jayatilaka, D.; Spackman, M. A. Towards Quantitative Analysis of Intermolecular Interactions with Hirshfeld Surfaces. *Chem. Commun.* **2007**, No. 37, 3814. https://doi.org/10.1039/b704980c.

(146) Trott, O.; Olson, A. J. AutoDock Vina: Improving the Speed and Accuracy of Docking with a New Scoring Function, Efficient Optimization, and Multithreading. *J. Comput. Chem.* **2009**, 455–461. https://doi.org/10.1002/jcc.21334.

(147) Mautner, F. A.; Albering, J. H.; Mikuriya, M.; Massoud, S. S. Dicyanamido-Metal(II) Complexes. Part 5: First Example for a Unit Cell Containing Dinuclear and 1-D Polymeric Cu(II) Complexes Bridging

by Dicyanamide. *Inorganic Chemistry Communications* **2010**, *13* (6), 796–799. https://doi.org/10.1016/j.inoche.2010.03.051.

(148) Nakamoto, K. *Infrared and Raman Spectra of Inorganic and Coordination Compounds*, 4th Edition.; John Wiley & Sons: New York, 1986.

(149) Mbani, A. L. O.; Yufanyi, D. M.; Tabong, C. D.; Hubert, N. J.; Yuoh, A. C. B.; Paboudam, A. G.; Ondoh, A. M. Synthesis, Crystal Structure, DFT Studies and Hirshfeld Surface Analysis of Manganese(II) and Cadmium(II) Coordination Polymers of 2-Aminopyridine and Dicyanamide. *Journal of Molecular Structure* **2022**, *1261*, 132956. https://doi.org/10.1016/j.molstruc.2022.132956.

(150) Manson, J. L.; Schlueter, J. A.; Nygren, C. L. Mn(Dca)2(Pym)2 and Mn(Dca)2(Pym)(H2O) {dca = Dicyanamide; Pym = Pyrimidine}: New Coordination Polymers Exhibiting 1- and 2-D Topologies. *Dalton Trans.* **2007**, No. 6, 646. https://doi.org/10.1039/b612474g.

(151) Wriedt, M.; Näther, C. Directed Synthesis of μ-1,3,5 Bridged Dicyanamides by Thermal Decomposition of μ-1,5 Bridged Precursor Compounds. *Dalton Transactions* **2011**, *40*, 886–898. https://doi.org/10.1039/c0dt00864h.

(152) Mautner, F. A.; Traber, M.; Fischer, R. C.; Massoud, S. S.; Vicente, R. Synthesis, Crystal Structures, Spectral and Magnetic Properties of 1-D Polymeric Dicyanamido-Metal(II) Complexes. *Polyhedron* **2017**, *138*, 13–20. https://doi.org/10.1016/j.poly.2017.09.004.

(153) Domagała, M.; Grabowski, S. J. X–H p and X–H N Hydrogen Bonds – Acetylene and Hydrogen Cyanide as Proton Acceptors. *Chemical Physics* **2009**, *363*, 42–48. https://doi.org/10.1016/j.chemphys.2009.07.007.

(154) Ramabhadran, R. O.; Hua, Y.; Flood, A. H.; Raghavachari, K. C vs N: Which End of the Cyanide Anion Is a Better Hydrogen Bond Acceptor? *J. Phys. Chem. A* **2014**, *118* (35), 7418–7423. https://doi.org/10.1021/jp412816w.

(155) Mbani O., A. L.; Bonnand, E. F.; Paboudam, A. G.; Brannon, J. P.; Gardner-Ricossa, K. D.; Stieber, S. C. E.; Agwara, M. O. Synthesis, Structural Analysis, and Docking Studies with SARS-CoV-2 of a Trinuclear Zinc Complex with *N* -Phenylanthranilic Acid Ligands. *Acta Crystallogr C Struct Chem* **2022**, *78* (4), 231–239. https://doi.org/10.1107/S205322962200239X.

(156) Addison, A. W.; Rao, T. N.; Reedijk, J.; van Rijn, J.; Verschoor, G. C. Synthesis, Structure, and Spectroscopic Properties of Copper(II) Compounds Containing Nitrogen-Sulphur Donor Ligands; the Crystal and Molecular Structure of Aqua[1,7-Bis(N-Methylbenzimidazol-2'-Yl)- 2,6-Dithiaheptane]Copper(II) Perchlorate. *J. Chem. Soc., Dalton Trans.* **1984**, No. 7, 1349–1356. https://doi.org/10.1039/DT9840001349.

(157) Tai, X.-S.; Feng, Y.-M. Crystal Structure of Diaqua(Bis(2-Aminopyridine))Dinitratocadmium(II) Monohydrate, [Cd(H2O)2(C10H12N4)2(NO3)2] · H2O. *Zeitschrift für Kristallographie - New Crystal Structures* **2008**, *223* (1), 39–40. https://doi.org/10.1524/ncrs.2008.0019.

(158) Gutiérrez, G.; Gordillo, M. A.; Chaur, M. N. A DFT Study on Dichloro {(E)-4-Dimethylaminog N′-[(Pyridin-2-Yl)Methylidene-κN] Benzohydrazide-κO}M2+(M = Zn, Cu, Ni, Fe, Mn, Ca and Co) Complexes: Effect of the Metal over Association Energy and Complex Geometry. *Revista Colombiana de Química* **2016**, *45* (3), 28–32. http://dx.doi.org/10.15446/rev.colomb.quim.v45n3.57351.

(159) Sivajeyanthi, P.; Jeevaraj, M.; Edison, B.; Balasubramani, K. Crystal Structure, Hirshfeld Surface Analysis and Frontier Molecular Orbital Analysis of (E)-4-BromoN'-(2,3-Dichlorobenzylidene)Benzohydrazide. *Acta Crystallographica Section E* **2019**, *75*, 324–327. https://doi.org/10.1107/S2056989019001816.

(160) Adejumo, T. T.; Tzouras, N. V.; Zorba, L. P.; Radanovic, D.; Pevec, A.; Grubišic, S.; Mitic, D.; Andelkovic, K. K.; Vougioukalakis, G. C.; Cobeljic, B.; Turel, I. Synthesis, Characterization, Catalytic Activity, and DFT Calculations of Zn(II) Hydrazone Complexes. *Molecules* **2020**, *25* (4043), 1–18. https://doi.org/10.3390/molecules25184043.

(161) Benhamed, K.; Boukli-Hacene, L.; Harek, Y. Crystal Structure and DFT Calculation Studies of Ni(II) Cinnamaldehyde Thiosemicarbazone Complex. *Mediterranean Journal of Chemistry* **2015**, *4* (5), 209–218. http://dx.doi.org/10.13171/mjc.4.5.2015.18.11.23/boukli.

(162) Moniruzzaman; ABEDUL Hoque, M.; Ahsan, A.; Belayet hossain, M. Molecular Docking, Pharmacokinetic, and DFT Calculation of Naproxen and Its Degradants. *Biomedical Journal of Scientific and Technical Research* **2018**, *9* (5), 1–6. https://doi.org/10.26717/BJSTR.2018.09.001852.

(163) Beyene, B. B.; Mihirteu, A. M.; Ayana, M. T.; Yibeltal, A. W. Synthesis, Characterization and Antibacterial Activity of Metalloporphyrins: Role of Central Metal Ion. *Results in Chemistry* **2020**, *2*, 100073. https://doi.org/10.1016/j.rechem.2020.100073.

(164) Agwara, M. O.; Ndifon, P. T.; Ndosiri, N. B.; Paboudam, A. G.; Yufanyi, D. M.; Mohamadou, A. Synthesis, Characterisation and Antimicrobial Activities of Cobalt(II), Copper(II) and Zinc(II) Mixed-Ligand Complexes Containing 1,10-Phenanthroline and 2,2'-Bipyridine. *Bull. Chem. Soc. Eth.* **2010**, *24* (3). https://doi.org/10.4314/bcse.v24i3.60680.

(165) Andrews, J. M. Determination of Minimum Inhibitory Concentrations. *Journal of Antimicrobial chemotherapy* **2001**, *48* (Suppl. S1), 5–16.

(166) Azam, S. S.; Abbasi, S. W. Molecular Docking Studies for the Identification of Novel Melatoninergic Inhibitors for Acetylserotonin-O-Methyltransferase Using Different Docking Routines. *Theor Biol Med Model* **2013**, *10* (1), 63. https://doi.org/10.1186/1742-4682-10-63.

(167) Adasme, M. F.; Linnemann, K. L.; Bolz, S. N.; Kaiser, F.; Salentin, S.; Haupt, V. J.; Schroeder, M. PLIP 2021: Expanding the Scope of the Protein–Ligand Interaction Profiler to DNA and RNA. *Nucleic Acids Research 49* (530–534).

(168) Mazumdar, M.; Lin, S.-X. Binary and Ternary Crystal Structures of a Novel Inhibitor of 17 Beta-HSD Type 1: A Lead Compound for Breast Cancer Therapy. *2* **2009**. https://doi.org/10.2210/pdb3HB5/pdb.

# Articles from the work

STRUCTURAL CHEMISTRY

ISSN: 2053-2296
journals.iucr.org/c

# Synthesis, structural analysis, and docking studies with SARS-CoV-2 of a trinuclear zinc complex with *N*-phenylanthranilic acid ligands

**Armel L. Mbani O., Evan F. Bonnand, Awawou G. Paboudam, Jacob P. Brannon, Kevyn D. Gardner-Ricossa, S. Chantal E. Stieber and Moise O. Agwara**

*Acta Cryst.* (2022). C**78**, 231–239

STRUCTURAL CHEMISTRY
ISSN 2053-2296

# Synthesis, structural analysis, and docking studies with SARS-CoV-2 of a trinuclear zinc complex with *N*-phenylanthranilic acid ligands

Armel L. Mbani O.,[a] Evan F. Bonnand,[b] Awawou G. Paboudam,[a] Jacob P. Brannon,[b] Kevyn D. Gardner-Ricossa,[b] S. Chantal E. Stieber[b]* and Moise O. Agwara[a]

[a]Faculty of Science, Department of Inorganic Chemistry, University of Yaoundé I, PO Box 812, Yaoundé, Cameroon, and [b]Department of Chemistry & Biochemistry, California State Polytechnic University, Pomona, 3801 W. Temple Ave., Pomona, CA 91768, USA. *Correspondence e-mail: sestieber@cpp.edu

Received 15 November 2021
Accepted 1 March 2022

Edited by L. Dawe, Wilfrid Laurier University, Waterloo, Ontario, Canada

**Keywords:** trinuclear; phenylanthranilic acid; NPA; zinc; inorganic chemistry; organometallic; SARS-CoV-2; molecular docking; crystal structure.

**CCDC reference**: 2155769

**Supporting information**: this article has supporting information at journals.iucr.org/c

The structure of a trinuclear zinc complex, hexakis($\mu_2$-2-anilinobenzoato)diaquatrizinc(II), $[Zn_2(C_{13}H_{10}NO_2)_6(H_2O)_2]$ or $(NPA)_6Zn_3(H_2O)_2$ (NPA is 2-anilinobenzoate or *N*-phenylanthranilate), is reported. The complex crystallizes in the triclinic space group $P\overline{1}$ and the central $Zn^{II}$ atom is located on an inversion center. The NPA ligand is found to coordinate *via* the carboxylate O atoms with unique C—O bond lengths that support an unequal distribution of resonance over the carboxylate fragment. The axial $H_2O$ ligands form hydrogen bonds with neighboring molecules that stabilize the supramolecular system in rigid straight chains, with an angle of 180° along the *c* axis. $\pi$ stacking is the primary stabilization along the *a* and *b* axes, resulting in a highly ordered supramolecular structure. Docking studies show that this unique supramolecular structure of a trinuclear zinc complex has potential for binding to the main protease ($M^{pro}$) in SARS-CoV-2 in a different location from Remdesivir, but with a similar binding strength.

## 1. Introduction

The design of zinc complexes as antiviral agents from simple, relatively cheap, and available ligands is of great interest in supramolecular chemistry and materials science (Batten *et al.*, 2009). Coronaviruses such as SARS-CoV can be targeted by $Zn^{2+}$ when combined with ionophores to increase $Zn^{2+}$ concentrations inside the cell (te Velthuis *et al.*, 2010). $Zn^{2+}$ has been proposed for use as a supplement in reducing COVID-19 morbidity (Derwand & Scholz, 2020), with possible impacts on virus replication, neurological damage, and inflammation (Cereda *et al.*, 2022). Current proposed modes of action are through inhibition of DNA and RNA replication (te Velthuis *et al.*, 2010), so the main protease of SARS-CoV-2 ($M^{pro}$) is of particular interest for developing antiviral agents. $M^{pro}$ plays a key role in the replication and transcription of SARS-CoV-2 and is the target of Remdesivir, the first therapeutic approved by the FDA for COVID-19 treatment (Beigel *et al.*, 2020). Molecular docking studies of Remdesivir with $M^{pro}$, as compared to other potential antiviral agents, established that Remdesivir binds most strongly to $M^{pro}$ based on the most favorable docking score (Naik *et al.*, 2020). This establishes molecular docking as a possible tool for screening potential antiviral agents. The current work presents the synthesis of a novel trinuclear zinc complex and analysis of its molecular docking to $M^{pro}$.

Polynuclear complexes can be synthesized using ligands with multidentate moieties (El-Boraey & El-Salamony, 2019),

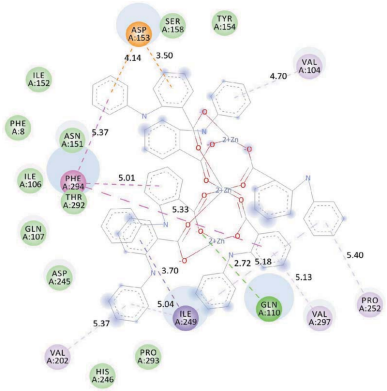

and amino acid-based ligands are often targeted because of their potential pharmacological properties (Aiyelabola *et al.*, 2016). Although the naturally occurring $\alpha$-amino acids have been studied extensively, synthetic $\beta$-amino acids have only more recently been considered for applications in coordination chemistry. This work focuses on *N*-phenylanthranilic acid (NPA), which is a $\beta$-amino acid. In $\beta$-amino acids, the amino group is bound to the $\beta$-carbon, which is one atom further removed from the carboxylic acid group. This contrasts with $\alpha$-amino acids, in which the carbonyl C atom of the carboxylic acid group and the N atom of the amino group are bound to the same C atom, the $\alpha$-carbon. Of note are the two arene arms in NPA, which can rotate freely around the amino group. This capacity for rotation minimizes steric hindrance and can therefore lead to interesting structures with versatile motifs.

NPA is reported to act as a chelating ligand for metals, with potential for coordination through both the N atom of the amino group (N) and the O atoms of the carboxyl group ($-COO^-$) (Ros *et al.*, 2002). NPA can also bind either through one carboxylate O atom, as in the motif $Zn(Hdmpz)_2(L_2)_2$ (Hdmpz is 3,5-dimethylpyrazole and $L_2$ is *N*-phenylanthranilate), or through both carboxylate O atoms, as in the dinuclear motif $[Cu_2(C_6H_5NHC_6H_4COO)_4(CH_3CH_2OH)_2]$ (Jin & Wang, 2014; Taş *et al.*, 2010). NPA ligands were reported to coordinate to rhodium for synthesizing hydrogenation catalysts, as seen in RhPAA (PAA is *N*-phenylanthranilic acid) (Ros *et al.*, 2002). Here, NPA was found to interact with the rhodium center *via* both the amine and carboxyl groups. Recent reports of NPA ligands coordinated to the lanthanides samarium, europium, and gadolinium in a search for novel antibacterial complexes provide several examples of NPA complexes in which the ligand is coordinated to two or three metal centers (Zapała *et al.*, 2019). Analysis of the complexes revealed that NPA coordinates to all of these lanthanides only *via* the carboxylate group. Similar NPA coordination was reported in terbium complexes for luminescence studies (Fu *et al.*, 2008).

Among the first NPA complexes with 3*d* transition metals reported were with $Cu^{II}$ metal centers in tetrakis[$\mu$-2-(phenylamino)benzoato-$\kappa^2O,O'$]bis[(ethanol)copper(II)] and bis[$\mu$-2-(phenylamino)benzoato-$\kappa^2O,O'$]bis[(hydroxido)copper(II)] (Taş *et al.*, 2010). Both of these complexes contain two copper centers, with NPA ligands that bridge between the two $Cu^{II}$ centers *via* the carboxylate groups. Mononuclear metal complexes of NPA were reported for Cd and Zn with an additional 2,2′-bipyridine or 3,5-dimethylpyrazole ligand, and for Mn with an additional phenanthroline ligand (Jin & Wang, 2014; Tan *et al.*, 2015).

Little attention has been focused on pharmaceutical agents and coordination compounds of NPA with Zn in a polynuclear motif, although several studies involving trinuclear zinc complexes with a variety of ligands have been reported (Liu *et al.*, 2013; Yu *et al.*, 2007; Neels & Stoeckli-Evans, 1999; Akine *et al.*, 2004; Karmakar *et al.*, 2019; Diop *et al.*, 2014). A recurring theme in this area of research is the exploration of photoluminescence (Fu *et al.*, 2008) and applications in DNA intercalation (Biswas *et al.*, 2014).

In this article, the synthesis and structural characterization of a trinuclear Zn complex with NPA ligands is reported (Scheme 1). The complex was analyzed using NMR and single-crystal X-ray diffraction to confirm the NPA coordination and structural motifs. Docking studies with SARS-COV-2 were conducted to probe the potential for the new complex to act as an antiviral agent.

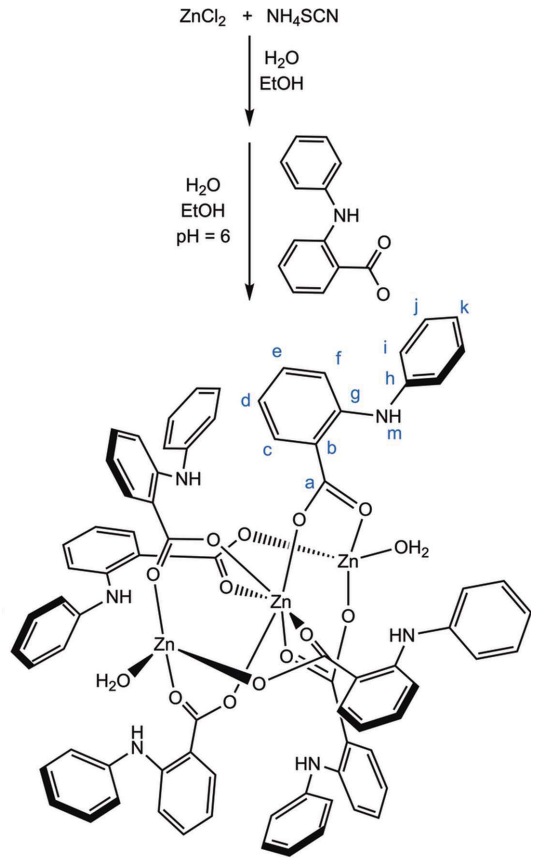


Scheme 1

## 2. Experimental

All procedures were conducted on the bench in the presence of air and moisture, and all reagents were obtained commercially and used without further purification. Elemental analysis for C, H, and N was conducted using a Costech ECS 4010 CHNSO analyzer. $^1$H and $^{13}$C NMR were conducted using a Varian 400 MHz spectrometer and calibrated to residual dimethyl sulfoxide (DMSO). Associated NMR data (Brannon *et al.*, 2021) and molecular docking data (Mbani *et al.*, 2021) were deposited on *Zenodo* (https://zenodo.org/).

### 2.1. Synthesis and crystallization of $(NPA)_6Zn_3(H_2O)_2$

$ZnCl_2$ (0.272 g, 0.002 mol) and $NH_4SCN$ (0.144 g, 0.002 mol) were dissolved in a water–ethanol solution (~10 ml, 1:5 *v*/*v*) and placed in a 100 ml Erlenmeyer flask with stirring at room temperature for about 30 min. To this solution was added an ethanolic solution (20 ml) of NPA (0.426 g, 0.002 mol). The pH of the resulting solution was adjusted to about 6 using 10% $Et_3N$ solution and stirring was continued for 24 h. A transparent crystalline complex was obtained from the solution

**Table 1**
Experimental details.

| | |
|---|---|
| Crystal data | |
| Chemical formula | $[Zn_3(C_{13}H_{10}NO_2)_6(H_2O)_2]$ |
| $M_r$ | 1505.46 |
| Crystal system, space group | Triclinic, $P\overline{1}$ |
| Temperature (K) | 100 |
| $a, b, c$ (Å) | 11.0968 (5), 12.8319 (6), 13.3134 (6) |
| $\alpha, \beta, \gamma$ (°) | 111.703 (2), 108.028 (2), 93.125 (2) |
| $V$ (Å$^3$) | 1643.97 (13) |
| $Z$ | 1 |
| Radiation type | Mo $K\alpha$ |
| $\mu$ (mm$^{-1}$) | 1.16 |
| Crystal size (mm) | 0.3 × 0.1 × 0.03 |
| | |
| Data collection | |
| Diffractometer | Bruker Kappa Venture D8 |
| Absorption correction | Multi-scan (*SADABS*; Bruker, 2017) |
| $T_{min}$, $T_{max}$ | 0.664, 0.748 |
| No. of measured, independent and observed [$I > 2\sigma(I)$] reflections | 86106, 10025, 8556 |
| $R_{int}$ | 0.044 |
| (sin $\theta/\lambda)_{max}$ (Å$^{-1}$) | 0.714 |
| | |
| Refinement | |
| $R[F^2 > 2\sigma(F^2)]$, $wR(F^2)$, $S$ | 0.030, 0.078, 1.03 |
| No. of reflections | 10025 |
| No. of parameters | 477 |
| H-atom treatment | H atoms treated by a mixture of independent and constrained refinement |
| $\Delta\rho_{max}$, $\Delta\rho_{min}$ (e Å$^{-3}$) | 0.65, −0.85 |

Computer programs: *APEX3* (Bruker, 2017), *SAINT* (Bruker, 2017), *SHELXT* (Sheldrick, 2015*a*), *SHELXL2017* (Sheldrick, 2015*b*), *Mercury* (Macrae *et al.*, 2020), and *OLEX2* (Dolomanov *et al.*, 2009).

(yield 0.273 g, 54%, based on NPA) by slow evaporation for several days, producing crystals suitable for X-ray analysis. Analysis calculated (%) for $C_{78}H_{64}N_6O_{14}Zn_3$: C 62.23, H 4.28, N 5.58; found: C 62.04, 3.83 H, N 5.67. $^1$H NMR (399.777 MHz, DMSO-$d_6$, 295 K): $\delta$ 6.80 (*m*, 1H; $H_d$), 7.02 (*t*, $J$ = 8.0 Hz, 1H; $H_k$), 7.22 (*d*, $J$ = 8.0 Hz, 2H; $H_i$), 7.33 (*m*, 4H; $H_e$, $H_f$, $H_j$), 8.03 (*d*, $J$ = 8.0 Hz, 1H; $H_c$), 10.42 (*br s*, 1H; $H_m$). $^{13}$C NMR (100.535 MHz, DMSO-$d_6$, 295 K): $\delta$ 113.7 ($C_f$), 117.5 ($C_d$), 117.7 ($C_b$), 120.2 ($C_i$), 122.1 ($C_k$), 129.7 ($C_j$), 132.5 ($C_e$), 132.9 ($C_c$), 141.8 ($C_h$), 146.0 ($C_g$), 173.3 ($C_a$).

### 2.2. Crystallographic details

Crystal data, data collection and structure refinement details are summarized in Table 1. H atoms were placed at ideal positions excluding the H atoms on the solvent water molecules and nitrogen, which were placed manually at q-peaks.

### 2.3. Molecular docking

Molecular docking studies were conducted with *AutoDock* (Version 4.2; Trott & Olson, 2010) and *CB-Dock* (Liu *et al.*, 2020; Cao & Li, 2014). The three-dimensional (3D) structure of the main protease ($M^{pro}$) of SARS-COV-2 (PDB ID: 6lu7) was reported previously with a bound N3 Michael addition inhibitor (Jin *et al.*, 2020). The N3 inhibitor, water molecules, and cocrystallized ligands were removed from the .pdb file prior to commencing docking studies with the new structural coordinates of $(NPA)_6Zn_3(H_2O)_2$. Preparation of the com-

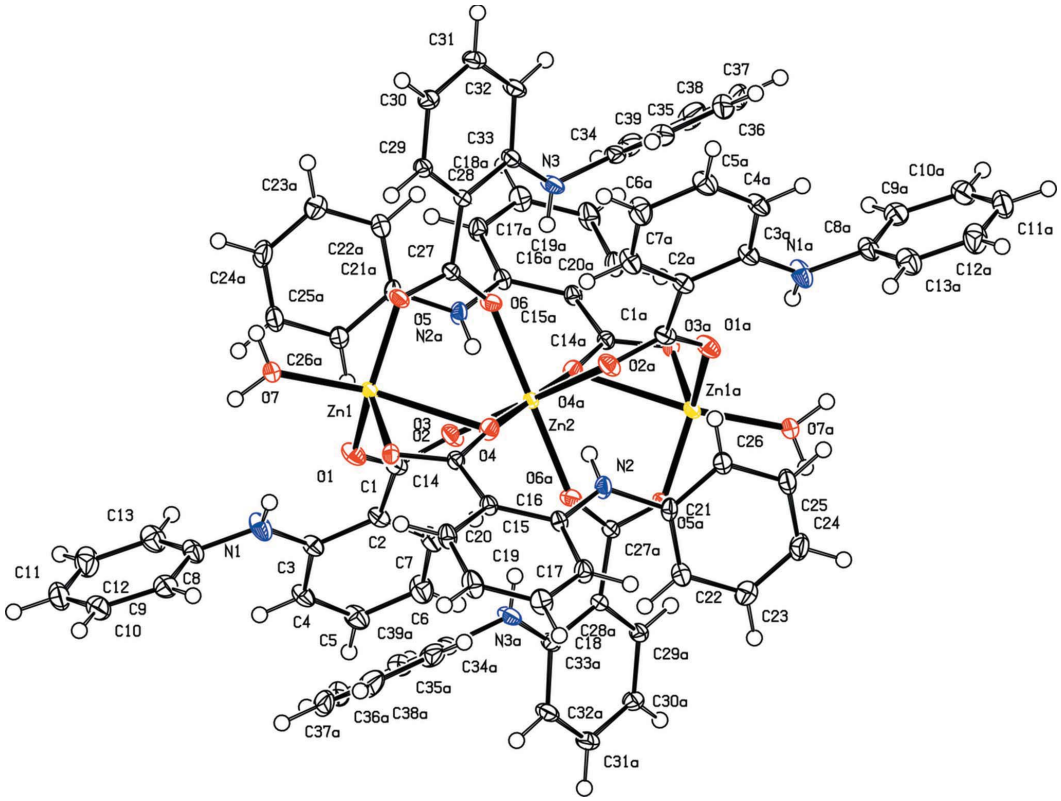


**Figure 1**
View of $(NPA)_6Zn_3(H_2O)_2$, drawn with 50% probability displacement ellipsoids. [Symmetry code: (a) $-x + 1, -y + 1, -z + 1$.]

pounds and proteins, polar H atoms, and partial charges (Kollman charges) were performed using *AutoDock Tools* (Version 1.5.6) that saved them as a .pdbqt file. *AutoDock Vina* (Version 1.1.2) was used with grid box center values at $x$ = −26.283, $y$ = 12.599, and $z$ = 58.966, and offset values of 62, 126, and 92, respectively. The 3D results of the interactions between the target and compound were analyzed and illustrated with the software *Discovery Studio* (Version 17.2) and *Chimera* (Pettersen *et al.*, 2004).

## 3. Results and discussion

$(NPA)_6Zn_3(H_2O)_2$ was synthesized from equimolar amounts of $ZnCl_2$ and $NH_4SCN$, followed by the addition of NPA, and adjusting the pH to 6 with triethylamine. Slow evaporation yielded transparent crystals in 54% yield that were characterized by $^1H$, $^{13}C$, COSY (correlated spectroscopy), HMBC (heteronuclear multiple bond correlation), and HSQC (heteronuclear single quantum coherence) NMR spectroscopy. The $^1H$ NMR spectrum in DMSO-$d_6$ revealed nine protons from the arene groups in the range 6.5–7.8 ppm, with the N—H proton found at 10.40 ppm. The observed signals are shifted from the free amino acid resonances at 6.5–7.4 ppm for the arene protons and 9.31 ppm for the N—H proton (Saito *et al.*, 2018), supporting coordination.

Crystallographic analysis reveals that $(NPA)_6Zn_3(H_2O)_2$ crystallizes in the triclinic space group $P\overline{1}$ and no solvent molecules are found to be trapped in the structure (Fig. 1). The structure is centrosymmetric, with the Zn2 atom located on an inversion center. The asymmetric unit contains two Zn centers (Zn1 and Zn2), about which three NPA ligands and one $H_2O$ ligand are coordinated. The full molecule fills the unit cell, which contains three Zn atoms, six coordinated NPA ligands, and two coordinated terminal $H_2O$ ligands.

The central $Zn^{II}$ atom, Zn2, is hexacoordinated exclusively by O atoms from the carboxylate groups of the NPA ligands. This central $Zn^{II}$ atom has an approximately octahedral molecular geometry, with bond angles ranging from 83.78 (4)° for O2—Zn2—O4$^i$ to 96.22 (4)° for O2—Zn2—O4 [symmetry code: (i) $-x+1, -y+1, -z+1$]. The ligand bond lengths range from 2.0219 (11) Å for Zn2—O2, to 2.0775 (10) Å for Zn2—O6, to 2.1762 (10) Å for Zn2—O4. The N atoms of the NPA ligands are not found to be involved in any coordination interaction with the $Zn^{II}$ centers, which is consistent with predictions from hard–soft acid–base theory (HSAB). However, the H atoms on the N atoms are involved in intramolecular hydrogen bonding with the carboxylate O atoms of NPA (Fig. 2). The hydrogen-bond distances within the asymmetric unit were all around a similar length, with distances of

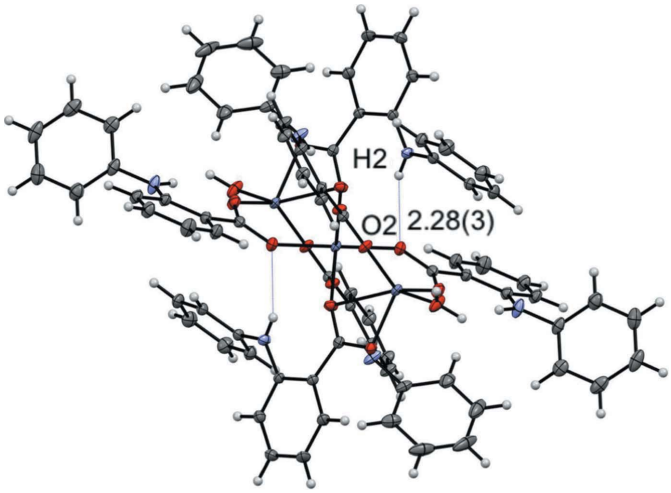


**Figure 3**
View of $(NPA)_6Zn_3(H_2O)_2$, drawn with 50% probability displacement ellipsoids, highlighting the intramolecular hydrogen bonding. The distances is in Å.

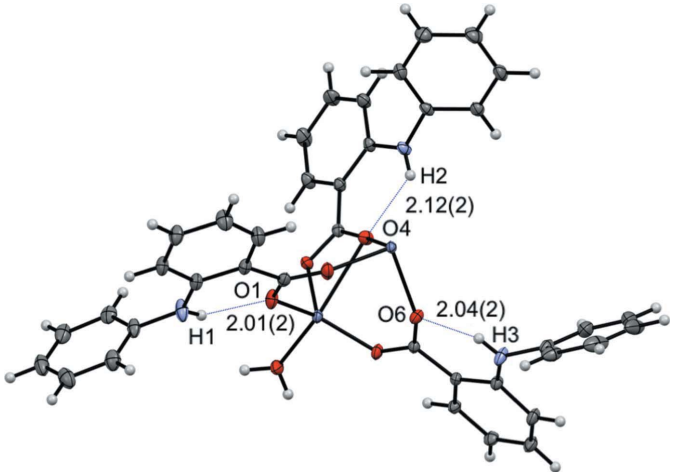


**Figure 2**
View of half the asymmetric unit of $(NPA)_6Zn_3(H_2O)_2$, drawn with 50% probability displacement ellipsoids, highlighting the intramolecular hydrogen bonding. Distances are in Å.

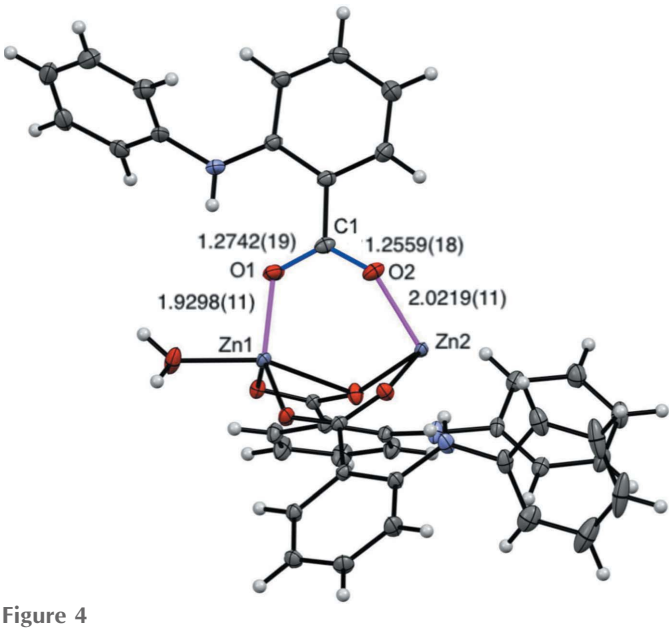


**Figure 4**
View of half the asymmetric unit of $(NPA)_6Zn_3(H_2O)_2$, drawn with 50% probability displacement ellipsoids, highlighting the Zn—O and carboxylate bond distances (Å).

2.01 (2) Å for O1···H1, 2.12 (2) Å for O4···H2, and 2.04 (2) Å for O6···H3. However, it should be noted that H atoms were fixed, or placed at calculated positions, which will affect the hydrogen-bond distances. Intramolecular hydrogen bonding between the two symmetry-generated halves of the molecule was found between H2 and O2$^{i}$ with a distance of 2.28 (3) Å (Fig. 3).

The exterior Zn$^{II}$ centers Zn1 and Zn1$^{i}$ are pentacoordinated, with only O atoms coordinated to these centers. The Zn1—O bond lengths are generally shorter than the Zn2—O bond lengths, with Zn1—O1 at 1.9298 (11) Å, Zn1—O3 at 1.9920 (10) Å, and Zn1—O5 at 1.9063 (10) Å. However, the notable outlier is that one of the O atoms coordinated to Zn1 comes from an $H_2O$ ligand, with Zn1—O7 at 2.0274 (12) Å. Because the Zn1 and Zn1$^{i}$ centers are pentacoordinated, there are two modes which can be used to classify their geometry: square pyramidal or trigonal bipyramidal. This distinction is made mathematically by utilizing the Addison parameter (Addison *et al.*, 1984). In this analysis, a trigonal index ($\tau$) is assigned according to the equation $\tau = (\beta - \alpha)/60$, where $\beta$ and $\alpha$ are the largest angles about the metal center. If the resulting value for $\tau$ is closer to 0, the center is classified as having a square pyramidal geometry. Conversely, if $\tau$ lies closer to 1, the center is classified as having a trigonal bipyramidal geometry. This analysis for Zn1 and Zn1$^{i}$ yielded the value $\tau = 0.566$, indicating that the molecular geometry of Zn1 and its symmetry-generated counterpart Zn1$^{i}$ are best described as trigonal bipyramidal in nature.

For all three NPA ligands of the asymmetric unit, both of the carboxylate O atoms are involved in coordination to Zn. This indicates that the formal negative charge of the ligand is delocalized between both O atoms instead of being localized on a single O atom. Each of the bond lengths between C and O atoms of the carboxylate groups are statistically different, indicating that the resonance is not shared equally. In all cases, the longer carboxylate C—O bond lengths are found for O atoms that are coordinated to Zn1, while shorter carboxylate C—O bond lengths are found for O atoms that are coordinated to Zn2 (Fig. 4). The longer carboxylate C—O bond lengths for C1—O1 at 1.2742 (19) Å, C14—O3 at 1.2866 (17) Å, and C27—O5 at 1.2788 (17) Å correlate with shorter Zn1—O bond lengths of Zn1—O1 at 1.9298 (11) Å, Zn1—O3 at 1.9920 (10) Å, and Zn1—O5 at 1.9063 (10) Å, respectively. By contrast, the shorter carboxylate C—O bond lengths for C1—O2 at 1.2559 (18) Å, C14—O4 at 1.2572 (17) Å, and C27—O6 at 1.2555 (17) Å correlate with

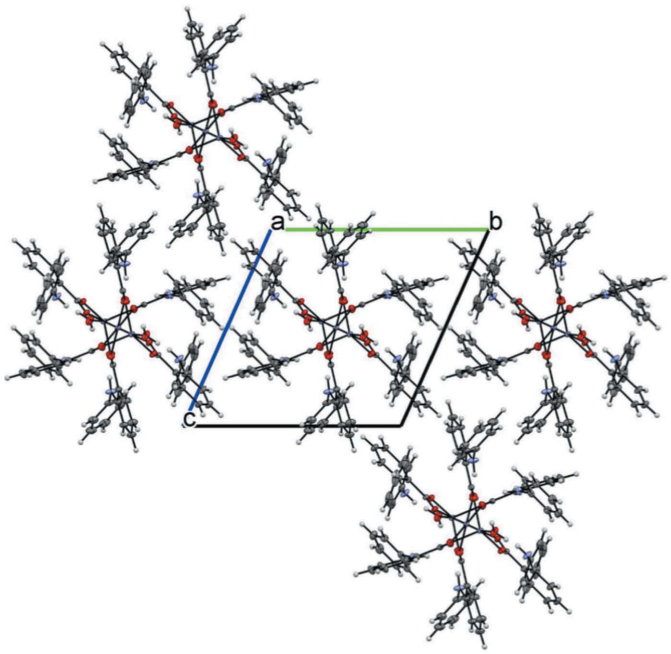


**Figure 6**
View of the macromolecular packing of $(NPA)_6Zn_3(H_2O)_2$, drawn with 50% probability displacement ellipsoids, viewed along the *c* axis.

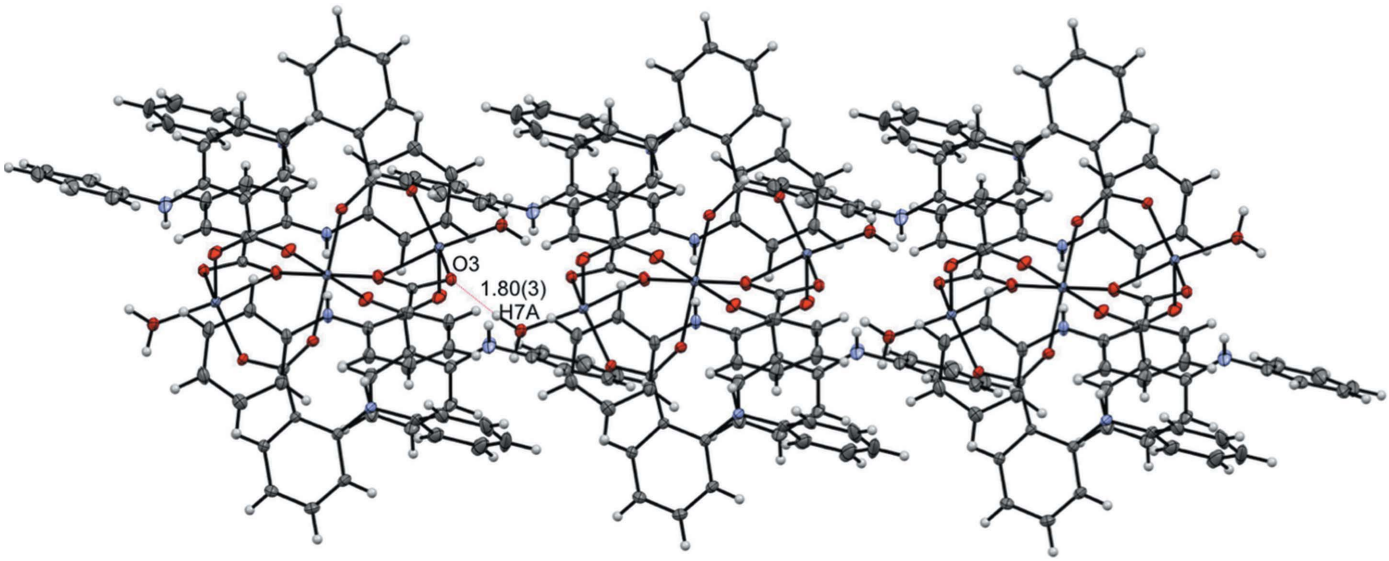


**Figure 5**
View of three molecules of $(NPA)_6Zn_3(H_2O)_2$, drawn with 50% probability displacement ellipsoids, highlighting the intermolecular hydrogen bonding. The distance is in Å.

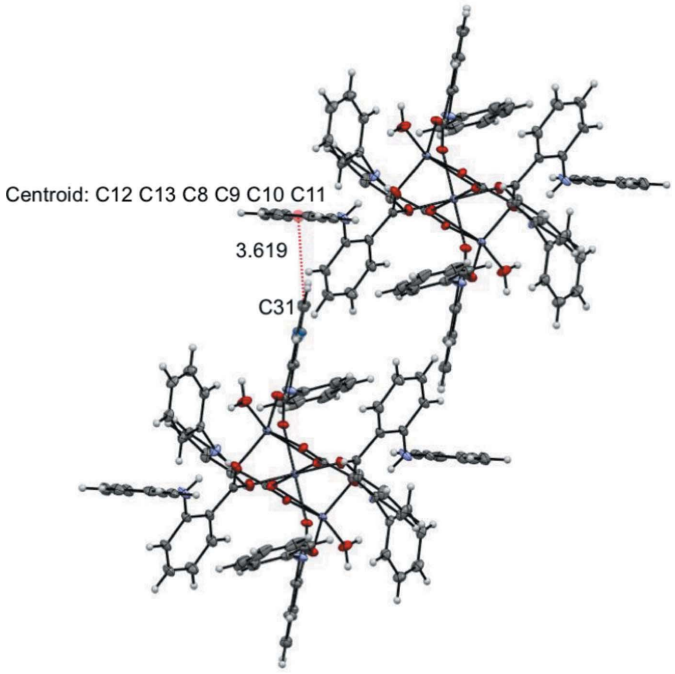


**Figure 7**
View of two molecules of $(NPA)_6Zn_3(H_2O)_2$, drawn with 50% probability displacement ellipsoids, highlighting the perpendicular $\pi$ stacking. The distance is in Å.

longer Zn2—O bond lengths of Zn2—O2 at 2.0219 (11) Å, Zn2—O4 at 2.1762 (10) Å, and Zn2—O6 at 2.0775 (10) Å, respectively. The longer Zn2—O bond lengths are likely due to increased steric hindrance around the central Zn2 atom and additional intramolecular hydrogen bonding of the O atoms (O2, O4, and O6) with a neighboring NPA ligand, causing additional torsion and strain (Fig. 3).

The two water ligands are located axially along the complex. Each water ligand is involved in hydrogen bonding from an H atom to a carboxylate O of the next unit cell, with a distance of 1.80 (3) Å for H7*A*···O3. As a result, each complex donates and accepts a hydrogen bond at each end, for a total of four intermolecular hydrogen bonds per molecule. Owing to symmetry-generated elements, it can be seen that all four hydrogen bonds arise from one unique bond (Fig. 5). These intermolecular hydrogen bonds are the main factor determining the arrangement of adjacent complexes. Due to the centrosymmetric nature of the complex and the axial hydrogen bonding, adjacent complexes attach end-on to form rigid straight chains, as shown in Fig. 5. The angle each chain forms is precisely 180°, such that the molecules stack perfectly when viewing a chain of complexes down the *c* axis (Fig. 6).

Multiple chains of the complex are stacked side-by-side (Fig. 7), with the arene groups of the NPA ligands of adjacent complexes in close proximity to one another. Perpendicular $\pi$ stacking is observed between the centroid defined by atoms C8–C13 and atom C31, with a distance of 3.619 Å and an angle of 83.4° (Fig. 7). $\pi$ stacking is the primary contact connecting adjacent chains of molecules along the *a* and *b* axes, while hydrogen bonding is the primary contact along the *c* axis.

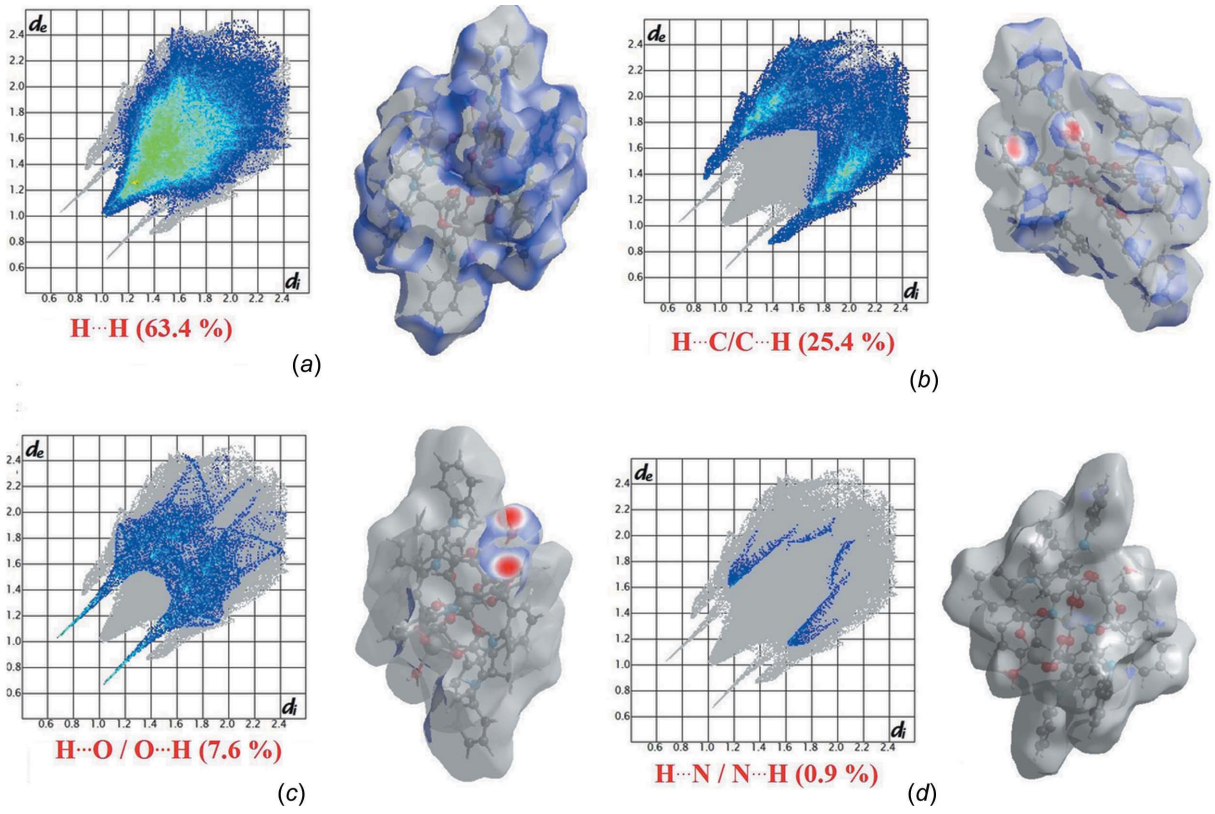


**Figure 8**
Hirshfeld fingerprint plots for $(NPA)_6Zn_3(H_2O)_2$ with highlighted contributions.

Hirshfeld surface and fingerprint plots were calculated using the *CrystalExplorer* program to further quantify the intermolecular contacts present in the 3D supramolecular architecture of the complex (Spackman & Jayatilaka, 2009; Spackman & McKinnon, 2002). Significant intermolecular interactions are mapped (Fig. 8) that indicate the percentage contributions of the intermolecular contacts to the Hirshfeld surface. Significant contacts include 63.4% H···H, 25.4% H···C/C···H, 7.6% H···O/O···H, and 0.9% H···N/N···H. The largest contribution of 63.4% for H···H interactions has a high concentration at $d_e = d_i \sim 1.02$ Å, as indicated by the red regions [Fig. 8(*a*)]. Two sharp spikes at $d_e + d_i \sim 1.71$ Å were observed for H···O/O···H interactions and indicate strong hydrogen bonding [Fig. 8(*b*)]. For H···C/C···H contacts, two spikes appear at $d_e + d_i \sim 2.25$ Å, while the H···N/N···H contacts have $d_e + d_i \sim 2.8$ Å.

The newly determined structure of $(NPA)_6Zn_3(H_2O)_2$ was used in a molecular docking study with the main protease ($M^{pro}$) of SARS-COV-2 using *AutoDock* (Version 4.2) and *CB-Dock* to probe the potential utility of $(NPA)_6Zn_3(H_2O)_2$ as an antiviral agent for SARS-COV-2. The structure of $M^{pro}$ (PDB ID: 6lu7) was reported previously with a bound N3 Michael addition inhibitor (Jin *et al.*, 2020) [Fig. 9(*b*)]. The N3 inhibitor, water molecules, and cocrystallized ligands were removed for docking studies with $(NPA)_6Zn_3(H_2O)_2$. Our docking results found the most stable confirmation with a docking score of $-8.4$ kcal mol$^{-1}$ using *AutoDock* and $-8.2$ kcal mol$^{-1}$ using *CB-Dock*. This suggests that $(NPA)_6Zn_3(H_2O)_2$ could be a strong inhibitor for $M^{pro}$ because the docking scores are on the same order of magnitude as those reported for Remdesivir at $-8.2$ kcal mol$^{-1}$ and Baloxavir marboxil at $-7.4$ kcal mol$^{-1}$ (Naik *et al.*, 2020). The main difference between the docking of $(NPA)_6Zn_3(H_2O)_2$ and Remdesivir is that a different binding location was found for $(NPA)_6Zn_3(H_2O)_2$ [Fig. 9(*b*)]. When using *CB-Dock*, we identified that $(NPA)_6Zn_3(H_2O)_2$ could also bind in the standard binding pocket with a docking score of $-6.0$ kcal mol$^{-1}$ [Fig. 9(*c*)]. While this is not as favorable a docking score as that of Remdesivir, it is on the same order of magnitude as scores reported for Oseltamivir at $-6.1$ kcal mol$^{-1}$ and Chloroquine at $-5.7$ kcal mol$^{-1}$ (Naik *et al.*, 2020). Combined, these results suggest that $(NPA)_6Zn_3(H_2O)_2$ has potential for inhibiting $M^{pro}$ of SARS-CoV-2.

Fig. 9 shows the 3D interaction between $(NPA)_6Zn_3(H_2O)_2$ and $M^{pro}$, which demonstrates that $(NPA)_6Zn_3(H_2O)_2$ targets a different area of the protein from N3. The strongest binding mode computed at $-8.4$ kcal mol$^{-1}$ of $(NPA)_6Zn_3(H_2O)_2$ included one hydrogen-bond contact between the $(NPA)_6Zn_3(H_2O)_2$ carboxylate O atom (such as O1) with amino acid residue Gln110 at a distance of 2.72 Å (Fig. 10). However, most of the stabilizing contacts result from $\pi$ interactions with the benzyl groups (such as C8–C13) in $(NPA)_6Zn_3(H_2O)_2$. Benzyl $\pi$···anion contacts were detected with Asp153 at distances of 3.50 and 4.14 Å. Perpendicular $\pi$–$\pi$ stacking was observed with Phe294 at distances of 5.33, 5.37, and 5.01 Å. Benzyl $\pi$···alkyl bond contacts were detected with Pro252 at 5.40 Å, Ile249 at 5.18 Å and 5.04 Å, and Val202 at 5.37 Å. Combined, the docking studies support that $(NPA)_6Zn_3$-

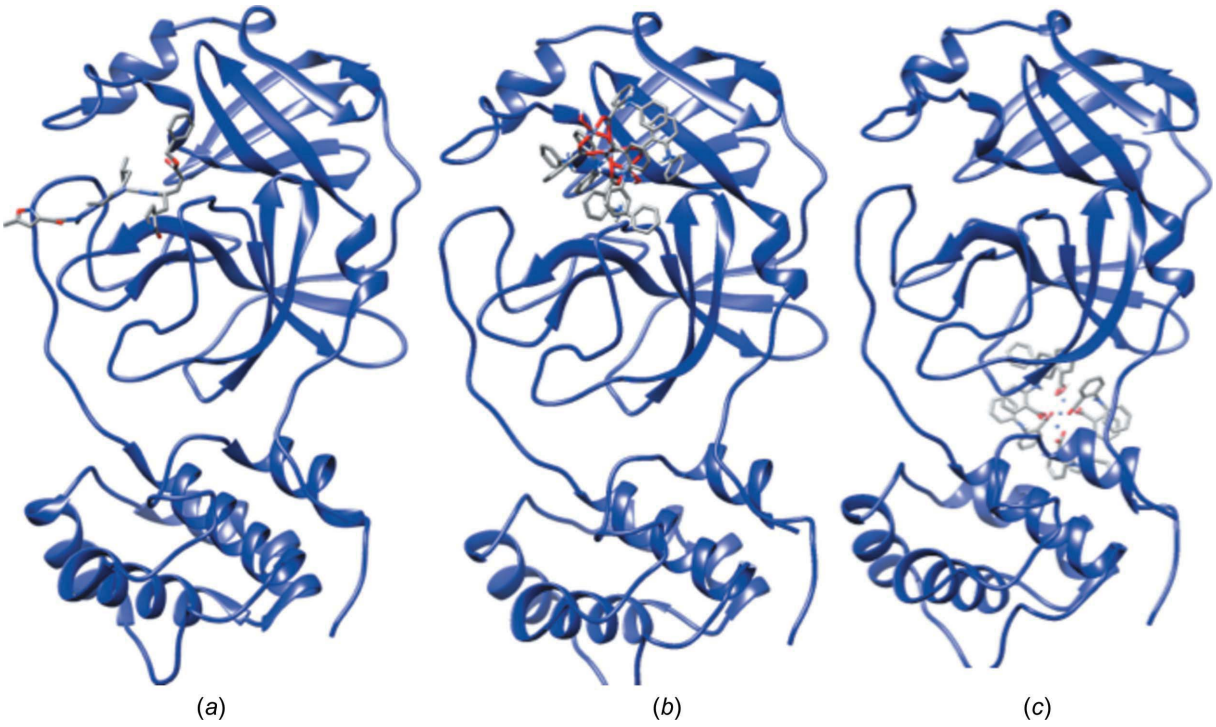


**Figure 9**
Cartoon representation of $M^{pro}$ with (*a*) the reported N3 inhibitor, (*b*) $(NPA)_6Zn_3(H_2O)_2$ at the standard pocket site and (*c*) $(NPA)_6Zn_3(H_2O)_2$ at the new binding site.

$(H_2O)_2$ could bind to $M^{pro}$ at a different binding site than the most widely studied pocket site in $M^{pro}$ where N3 and Remdesivir are known to bind.

## 4. Conclusion

The trinuclear zinc complex $(NPA)_6Zn_3(H_2O)_2$ was synthesized and characterized crystallographically. The crystal structure is symmetric about the central $Zn^{II}$ atom (Zn2), which has approximate octahedral geometry, flanked by outer $Zn^{II}$ atoms (Zn2 and Zn2$^{i}$) with highly contorted trigonal bipyramidal molecular geometries. The macromolecular stabilization is facilitated by intramolecular hydrogen bonding within the NPA ligand, hydrogen bonding between $H_2O$ and carboxylate O atoms of adjacent molecules, and perpendicular $\pi$ stacking between adjacent molecules. Hydrogen bonding is only observed along the crystallographic *a* axis, while $\pi$ stacking is only observed along the *b* and *c* axes. Most notably, the supramolecular stabilization results in a perfect alignment of $(NPA)_6Zn_3(H_2O)_2$ molecules along the *a* axis, such that only one molecule is seen when looking down this axis. Molecular docking studies of $(NPA)_6Zn_3(H_2O)_2$ with the $M^{pro}$ portion of SARS-COV-2 suggest that $(NPA)_6Zn_3(H_2O)_2$ could bind to $M^{pro}$ with a similar docking score as Remdesivir, but at a different binding site than the typically targeted pocket site where Remdesivir binds. $(NPA)_6Zn_3(H_2O)_2$ also binds to the same pocket as Remdesivir, with a slightly less favorable docking score, but on the same order of magnitude as other $M^{pro}$ inhibitors. This suggests that trinuclear Zn complexes should be further explored for antiviral activity for SARS-CoV-2.


## Acknowledgements

We thank Phil S. Beauchamp for helpful NMR discussions.

## Funding information

Funding for this research was provided by: National Science Foundation, Directorate for Mathematical and Physical Sciences (grant No. 1847926 to S. Chantal E. Stieber); U.S.


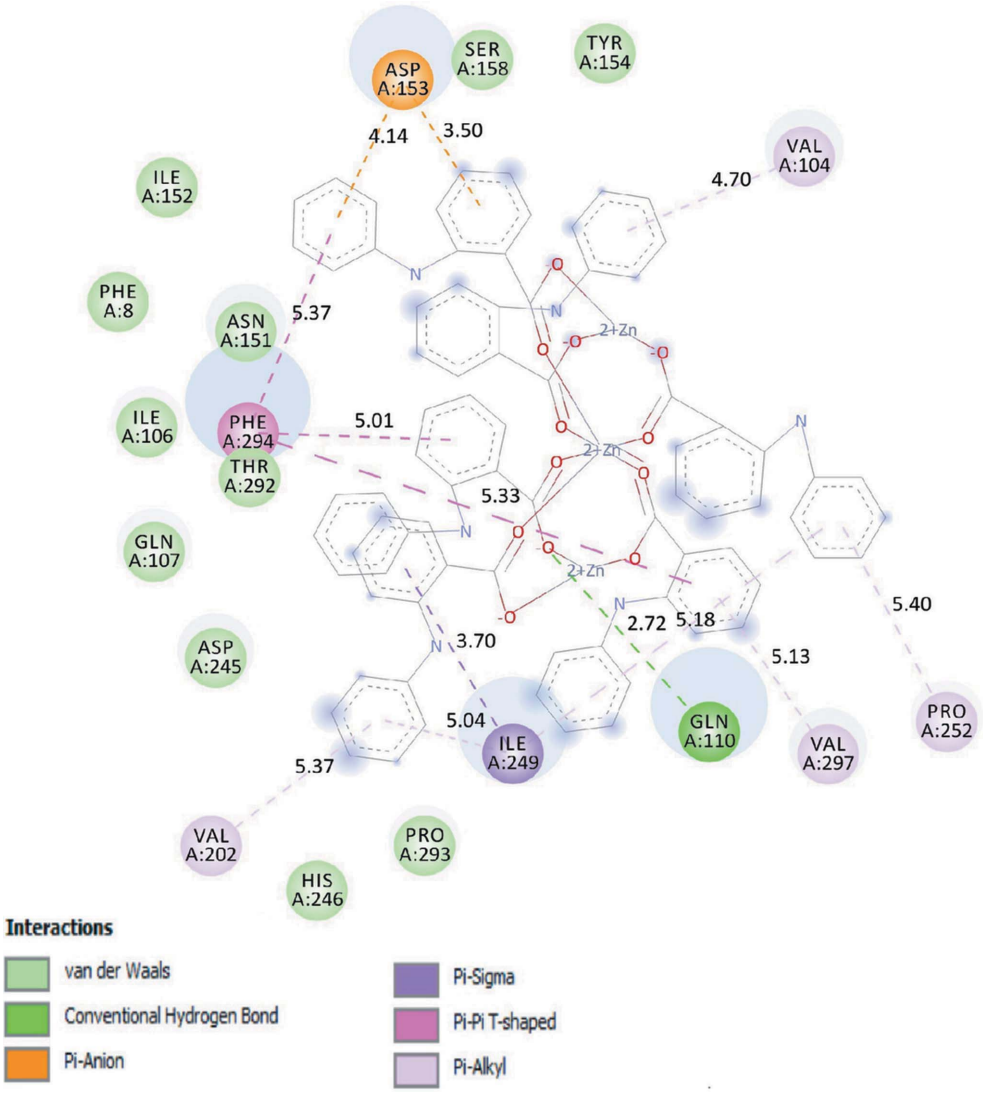


**Figure 10**
Enlarged view of the newly identified $(NPA)_6Zn_3(H_2O)_2$–$M^{pro}$ binding pocket with the key residue interactions and distances (Å).

Department of Defense, U.S. Army (grant No. W911NF-17-1-0537 to S. Chantal E. Stieber).

## References


Addison, A. W., Rao, T. N., Reedijk, J., van Rijn, J. & Verschoor, G. C. (1984). *J. Chem. Soc. Dalton Trans.* pp. 1349–1356.

Aiyelabola, T. O., Isabirye, D. A., Akinkunmi, E. O., Ogunkunle, O. A. & Ojo, I. A. O. (2016). *J. Chem.* **2016**, 7317015.

Akine, S., Taniguchi, T. & Nabeshima, T. (2004). *Inorg. Chem.* **43**, 6142–6144.

Batten, S. R., Neville, S. M. & Tuner, D. R. (2009). In *Coordination Polymers: Design, Analysis and Application*, edited by T. G. House. Cambridge: RSC Publishing.

Beigel, J. H., Tomashek, K. M., Dodd, L. E., Mehta, A. K., Zingman, B. S., Kalil, A. C., Hohmann, E., Chu, H. Y., Luetkemeyer, A., Kline, S., Lopez de Castilla, D., Finberg, R. W., Dierberg, K., Tapson, V., Hsieh, L., Patterson, T. F., Paredes, R., Sweeney, D. A., Short, W. R., Touloumi, G., Lye, D. C., Ohmagari, N., Oh, M. D., Ruiz-Palacios, G. M., Benfield, T., Fätkenheuer, G., Kortepeter, M. G., Atmar, R. L., Creech, C. B., Lundgren, J., Babiker, A. G., Pett, S., Neaton, J. D., Burgess, T. H., Bonnett, T., Green, M., Makowski, M., Osinusi, A., Nayak, S., Lane, H. C. & ACTT-1 Study Group Members (2020). *N. Engl. J. Med.* **383**, 1813–1826.

Biswas, B., Kole, N., Patra, M., Dutta, S. & Ganguly, M. (2014). *J. Chem. Sci.* **125**, 1445–1453.

Brannon, J. P., Gardner-Ricossa, K. D., Mbani, O. A. L., Paboudam, A. G., Agwara, M. O., Bonnand, E. F. & Stieber, S. C. E. (2021). *Zenodo*, doi: 10.5281/zenodo.4694912.

Bruker (2017). *APEX3*, *SAINT*, and *SADABS*. Bruker AXS Inc., Madison, Wisconsin, USA.

Cao, Y. & Li, L. (2014). *Bioinformatics*, **30**, 1674–1680.

Cereda, G., Ciappolino, V., Boscutti, A., Cantu, F., Oldani, L., Delvecchio, G. & Brambilla, P. (2022). *Adv. Nutr.* **13**, 66–79.

Derwand, R. & Scholz, M. (2020). *Med. Hypotheses*, **142**, 109815.

Diop, M., Aly-Gaye, P., Bouyagui-Tamboura, F., Gaye, M., Pérez-Lourido, P., Valencia, L. & Castro, G. (2014). *Z. Anorg. Allg. Chem.* **640**, 1392–1396.

Dolomanov, O. V., Bourhis, L. J., Gildea, R. J., Howard, J. A. K. & Puschmann, H. (2009). *J. Appl. Cryst.* **42**, 339–341.

El-Boraey, H. A. & El-Salamony, M. A. (2019). *J. Inorg. Organomet. Polym.* **29**, 684–700.

Fu, Y., Zhang, J., Lv, Y. & Cao, W. (2008). *Spectrochim. Acta A Mol. Biomol. Spectrosc.* **70**, 646–650.

Jin, S. & Wang, D. (2014). *Inorg. Chim. Acta*, **415**, 31–43.

Jin, Z., Du, X., Xu, Y., Deng, Y., Liu, M., Zhao, Y., Zhang, B., Li, X., Zhang, L., Peng, C., Duan, Y., Yu, J., Wang, L., Yang, K., Liu, F., Jiang, R., Yang, X., You, T., Liu, X., Yang, X., Bai, F., Liu, H., Liu, X., Guddat, L. W., Xu, W., Xiao, G., Qin, C., Shi, Z., Jiang, H., Rao, Z. & Yang, H. (2020). *Nature*, **582**, 289–293.

Karmakar, M., Roy, S. & Chattopadhyay, S. (2019). *New J. Chem.* **43**, 10093–10102.

Liu, X., Du, P. & Cao, R. (2013). *Nat. Commun.* **4**, 2375.

Liu, Y., Grimm, M., Dai, W., Hou, M., Xiao, Z. & Cao, Y. (2020). *Acta Pharmacol. Sin.* **41**, 138–144.

Macrae, C. F., Sovago, I., Cottrell, S. J., Galek, P. T. A., McCabe, P., Pidcock, E., Platings, M., Shields, G. P., Stevens, J. S., Towler, M. & Wood, P. A. (2020). *J. Appl. Cryst.* **53**, 226–235.

Mbani, O. A. L., Paboudam, A. G., Stieber, S. C. E. & Agwara, M. O. (2021). *Zenodo*, doi: 10.5281/zenodo.5703439.

Naik, V. R., Munikumar, M., Ramakrishna, U., Srujana, M., Goudar, G., Naresh, P., Kumar, B. N. & Hemalatha, R. (2020). *J. Biomol. Struct. Dyn.* pp. 2–14.

Neels, A. & Stoeckli-Evans, H. (1999). *Inorg. Chem.* **38**, 6164–6170.

Pettersen, E. F., Goddard, T. D., Huang, C. C., Couch, G. S., Greenblatt, D. M., Meng, E. C. & Ferrin, T. E. (2004). *J. Comput. Chem.* **25**, 1605–1612.

Ros, T. G., van der Lee, M. K., van Dillen, A. J., Geus, J. W. & Koningsberger, D. C. (2002). *J. Mol. Catal. A Chem.* **186**, 13–24.

Saito, T., Yamaji, T., Hayamizu, K., Yanagisawa, M. & Yamamoto, O. (2018). Spectral Database for Organic Compounds SDBS, National Institute of Advanced Industrial Science and Technology (AIST), Japan.

Sheldrick, G. M. (2015*a*). *Acta Cryst.* A**71**, 3–8.

Sheldrick, G. M. (2015*b*). *Acta Cryst.* C**71**, 3–8.

Spackman, M. A. & Jayatilaka, D. (2009). *CrystEngComm*, **11**, 19–32.

Spackman, M. A. & McKinnon, J. J. (2002). *CrystEngComm*, **4**, 378–392.

Tan, Y., Xiong, J., Gao, J., Xu, Q., Fu, C., Tang, Y., Yang, S. & Wen, H. (2015). *J. Mol. Struct.* **1086**, 49–55.

Taş, M., Yeşilel, O. Z. & Büyükgüngör, O. (2010). *J. Inorg. Organomet. Polym.* **20**, 298–305.

te Velthuis, A. J. W., van den Worm, S. H. E., Sims, A. C., Baric, R. S., Snijder, E. J. & van Hemert, M. J. (2010). *PLoS Pathog.* **6**, e1001176.

Trott, O. & Olson, A. J. (2010). *J. Comput. Chem.* **31**, 455–461.

Yu, T., Zhang, K., Zhao, Y., Yang, C., Zhang, H., Fan, D. & Dong, W. (2007). *Inorg. Chem. Commun.* **10**, 401–403.

Zapała, L., Kosińska, M., Woźnicka, E., Byczyński, Ł., Ciszkowicz, E., Lecka-Szlachta, K., Zapała, W. & Chutkowski, M. (2019). *Thermochim. Acta*, **671**, 134–148.

# supporting information

*Acta Cryst.* (2022). C**78**, 231-239 [https://doi.org/10.1107/S205322962200239X]

## Synthesis, structural analysis, and docking studies with SARS-CoV-2 of a trinuclear zinc complex with *N*-phenylanthranilic acid ligands

**Armel L. Mbani O., Evan F. Bonnand, Awawou G. Paboudam, Jacob P. Brannon, Kevyn D. Gardner-Ricossa, S. Chantal E. Stieber and Moise O. Agwara**

### Computing details

Data collection: *APEX3* (Bruker, 2017); cell refinement: *SAINT* (Bruker, 2017); data reduction: *SAINT* (Bruker, 2017); program(s) used to solve structure: SHELXT (Sheldrick, 2015*a*); program(s) used to refine structure: *SHELXL2017* (Sheldrick, 2015*b*); molecular graphics: *Mercury* (Macrae *et al.*, 2020); software used to prepare material for publication: OLEX2 (Dolomanov *et al.*, 2009).

### Hexakis($\mu_2$-2-anilinobenzoato)diaquatrizinc(II)

*Crystal data*

$[Zn_3(C_{13}H_{10}NO_2)_6(H_2O)_2]$
$M_r$ = 1505.46
Triclinic, $P\overline{1}$
$a$ = 11.0968 (5) Å
$b$ = 12.8319 (6) Å
$c$ = 13.3134 (6) Å
$\alpha$ = 111.703 (2)°
$\beta$ = 108.028 (2)°
$\gamma$ = 93.125 (2)°
$V$ = 1643.97 (13) Å$^3$
$Z$ = 1
$F(000)$ = 776
$D_x$ = 1.521 Mg m$^{-3}$
Mo $K\alpha$ radiation, $\lambda$ = 0.71073 Å
Cell parameters from 9800 reflections
$\theta$ = 2.5–38.9°
$\mu$ = 1.16 mm$^{-1}$
$T$ = 100 K
Prism, clear colourless
0.3 × 0.1 × 0.03 mm

*Data collection*

Bruker Kappa Venture D8 diffractometer
Radiation source: microfocus sealed X-ray tube, Incoatec I$\mu$s
Mirror optics monochromator
Detector resolution: 7.9 pixels mm$^{-1}$
$\omega$ and $\varphi$ scans
Absorption correction: multi-scan (SADABS; Bruker, 2017)
$T_{min}$ = 0.664, $T_{max}$ = 0.748
86106 measured reflections
10025 independent reflections
8556 reflections with $I > 2\sigma(I)$
$R_{int}$ = 0.044
$\theta_{max}$ = 30.5°, $\theta_{min}$ = 2.9°
$h$ = −15→15
$k$ = −18→18
$l$ = −19→19

*Refinement*

Refinement on $F^2$
Least-squares matrix: full
$R[F^2 > 2\sigma(F^2)]$ = 0.030
$wR(F^2)$ = 0.078
$S$ = 1.03
10025 reflections
477 parameters
0 restraints
Primary atom site location: dual
Hydrogen site location: mixed
H atoms treated by a mixture of independent and constrained refinement

$w = 1/[\sigma^2(F_o^2) + (0.0319P)^2 + 1.352P]$
where $P = (F_o^2 + 2F_c^2)/3$
$(\Delta/\sigma)_{max} = 0.001$

$\Delta\rho_{max} = 0.65$ e Å$^{-3}$
$\Delta\rho_{min} = -0.84$ e Å$^{-3}$

*Special details*

**Geometry**. All esds (except the esd in the dihedral angle between two l.s. planes) are estimated using the full covariance matrix. The cell esds are taken into account individually in the estimation of esds in distances, angles and torsion angles; correlations between esds in cell parameters are only used when they are defined by crystal symmetry. An approximate (isotropic) treatment of cell esds is used for estimating esds involving l.s. planes.

**Refinement**. $(NPA)_6Zn_3(H_2O)_2$ was mounted on a Bruker Kappa Venture D8 instrument on a Kapton sample holder that was then placed in a liquid nitrogen stream to cool the sample down to 100 K. The sample was run with a molybdenum micro source (Mo *Kα*, *λ*= 0.71073 Å) using a Photon II detector. The unit cell of was determined prior to full data collection, and data were integrated using the Bruker SAINT program using SADABS for absorption correction. Structural refinement was conducted using APEX3 and OLEX2 software that interfaced with the SHELXL PC Suite (Dolomanov *et al.*, 2009; Sheldrick, Sheldrick, 2015*b*). All non-H atoms were refined using anisotropic thermal parameters.

*Fractional atomic coordinates and isotropic or equivalent isotropic displacement parameters (Å²)*

| | *x* | *y* | *z* | $U_{iso}$*/$U_{eq}$ |
|---|---|---|---|---|
| Zn1 | 0.21623 (2) | 0.57673 (2) | 0.53262 (2) | 0.01224 (4) |
| Zn2 | 0.500000 | 0.500000 | 0.500000 | 0.01101 (5) |
| O3 | 0.18796 (10) | 0.46312 (9) | 0.59622 (9) | 0.01493 (19) |
| O5 | 0.33767 (10) | 0.71566 (9) | 0.63184 (9) | 0.0163 (2) |
| O6 | 0.50591 (10) | 0.67473 (9) | 0.57499 (9) | 0.0156 (2) |
| O4 | 0.38584 (10) | 0.46623 (9) | 0.59513 (10) | 0.0169 (2) |
| O7 | 0.05686 (11) | 0.64469 (11) | 0.54001 (12) | 0.0257 (3) |
| O2 | 0.34886 (11) | 0.47459 (10) | 0.35584 (9) | 0.0199 (2) |
| O1 | 0.15384 (11) | 0.48147 (10) | 0.36899 (9) | 0.0207 (2) |
| N2 | 0.52659 (12) | 0.32556 (11) | 0.66916 (12) | 0.0165 (2) |
| N3 | 0.70966 (13) | 0.84458 (12) | 0.65803 (12) | 0.0209 (3) |
| N1 | −0.05046 (13) | 0.40036 (14) | 0.17526 (12) | 0.0248 (3) |
| C29 | 0.47282 (14) | 0.91895 (12) | 0.80522 (13) | 0.0152 (3) |
| H29 | 0.392254 | 0.886158 | 0.802241 | 0.018* |
| C28 | 0.52736 (13) | 0.85540 (11) | 0.72560 (12) | 0.0128 (2) |
| C16 | 0.41632 (13) | 0.28630 (12) | 0.68010 (12) | 0.0137 (2) |
| C33 | 0.64919 (14) | 0.90238 (12) | 0.73231 (12) | 0.0154 (3) |
| C2 | 0.16772 (14) | 0.37100 (13) | 0.18719 (12) | 0.0165 (3) |
| C26 | 0.75406 (14) | 0.31903 (13) | 0.72482 (13) | 0.0169 (3) |
| H26 | 0.771698 | 0.394102 | 0.783266 | 0.020* |
| C3 | 0.03344 (14) | 0.35001 (13) | 0.12401 (12) | 0.0169 (3) |
| C21 | 0.62687 (14) | 0.26427 (13) | 0.65586 (13) | 0.0153 (3) |
| C30 | 0.53243 (15) | 1.02765 (12) | 0.88784 (13) | 0.0175 (3) |
| H30 | 0.494528 | 1.068533 | 0.941905 | 0.021* |
| C32 | 0.70667 (15) | 1.01528 (13) | 0.81453 (14) | 0.0203 (3) |
| H32 | 0.786401 | 1.049860 | 0.817622 | 0.024* |
| C7 | 0.24937 (16) | 0.31571 (15) | 0.13244 (14) | 0.0225 (3) |
| H7 | 0.339316 | 0.331356 | 0.175194 | 0.027* |
| C17 | 0.41055 (15) | 0.19384 (13) | 0.71268 (14) | 0.0183 (3) |
| H17 | 0.481000 | 0.154891 | 0.720440 | 0.022* |

| | | | | |
|---|---|---|---|---|
| C22 | 0.60164 (15) | 0.15393 (14) | 0.57133 (14) | 0.0201 (3) |
| H22 | 0.515144 | 0.116452 | 0.523614 | 0.024* |
| C19 | 0.19940 (15) | 0.21460 (15) | 0.72331 (15) | 0.0228 (3) |
| H19 | 0.127418 | 0.191002 | 0.739352 | 0.027* |
| C18 | 0.30479 (16) | 0.15924 (15) | 0.73335 (15) | 0.0218 (3) |
| H18 | 0.303180 | 0.096516 | 0.754887 | 0.026* |
| C20 | 0.20171 (14) | 0.30396 (14) | 0.68974 (13) | 0.0182 (3) |
| H20 | 0.130606 | 0.342222 | 0.683176 | 0.022* |
| C15 | 0.30715 (13) | 0.33982 (12) | 0.66494 (12) | 0.0138 (2) |
| C25 | 0.85502 (15) | 0.26398 (14) | 0.70820 (15) | 0.0215 (3) |
| H25 | 0.941724 | 0.302140 | 0.754172 | 0.026* |
| C34 | 0.84477 (15) | 0.86983 (13) | 0.68544 (15) | 0.0193 (3) |
| C14 | 0.29532 (13) | 0.42742 (12) | 0.61725 (12) | 0.0129 (2) |
| C31 | 0.64947 (15) | 1.07621 (13) | 0.89027 (14) | 0.0201 (3) |
| H31 | 0.690087 | 1.151989 | 0.944656 | 0.024* |
| C4 | −0.01196 (15) | 0.27355 (14) | 0.00644 (13) | 0.0195 (3) |
| H4 | −0.101030 | 0.259682 | −0.038487 | 0.023* |
| C27 | 0.45353 (13) | 0.74034 (12) | 0.63763 (12) | 0.0129 (2) |
| C24 | 0.82974 (16) | 0.15365 (15) | 0.62484 (16) | 0.0247 (3) |
| H24 | 0.898868 | 0.115683 | 0.614252 | 0.030* |
| C1 | 0.22793 (14) | 0.44702 (12) | 0.31205 (12) | 0.0161 (3) |
| C23 | 0.70285 (17) | 0.09865 (15) | 0.55673 (16) | 0.0248 (3) |
| H23 | 0.685355 | 0.022754 | 0.499856 | 0.030* |
| C5 | 0.07081 (16) | 0.21858 (15) | −0.04435 (13) | 0.0224 (3) |
| H5 | 0.037349 | 0.165888 | −0.123144 | 0.027* |
| C35 | 0.93108 (17) | 0.88179 (14) | 0.79226 (17) | 0.0273 (4) |
| H35 | 0.899654 | 0.873909 | 0.848340 | 0.033* |
| C9 | −0.27061 (16) | 0.33864 (14) | 0.15414 (14) | 0.0224 (3) |
| H9 | −0.238626 | 0.311924 | 0.213239 | 0.027* |
| C8 | −0.18516 (15) | 0.38650 (14) | 0.11840 (13) | 0.0207 (3) |
| C6 | 0.20304 (17) | 0.23893 (16) | 0.01791 (15) | 0.0268 (3) |
| H6 | 0.259623 | 0.200922 | −0.017628 | 0.032* |
| C10 | −0.40284 (17) | 0.32986 (15) | 0.10340 (16) | 0.0274 (4) |
| H10 | −0.460956 | 0.299287 | 0.129504 | 0.033* |
| C39 | 0.89097 (18) | 0.88128 (14) | 0.60371 (17) | 0.0258 (3) |
| H39 | 0.832464 | 0.873032 | 0.530741 | 0.031* |
| C13 | −0.23263 (17) | 0.42410 (16) | 0.03090 (15) | 0.0265 (3) |
| H13 | −0.174607 | 0.457781 | 0.006907 | 0.032* |
| C11 | −0.44982 (17) | 0.36558 (17) | 0.01499 (16) | 0.0312 (4) |
| H11 | −0.540240 | 0.358033 | −0.020802 | 0.037* |
| C12 | −0.36467 (18) | 0.41245 (18) | −0.02135 (16) | 0.0309 (4) |
| H12 | −0.396992 | 0.436662 | −0.082321 | 0.037* |
| C36 | 1.06257 (19) | 0.90516 (17) | 0.8164 (2) | 0.0407 (5) |
| H36 | 1.121435 | 0.913366 | 0.889251 | 0.049* |
| C38 | 1.0236 (2) | 0.90494 (16) | 0.6292 (2) | 0.0392 (5) |
| H38 | 1.055534 | 0.913039 | 0.573478 | 0.047* |
| C37 | 1.10874 (19) | 0.91665 (17) | 0.7347 (3) | 0.0463 (6) |
| H37 | 1.199117 | 0.932597 | 0.751558 | 0.056* |

| | | | | |
|---|---|---|---|---|
| H3 | 0.671 (2) | 0.7818 (19) | 0.6117 (19) | 0.022 (5)* |
| H2 | 0.533 (2) | 0.386 (2) | 0.6618 (19) | 0.028 (6)* |
| H1 | −0.023 (2) | 0.436 (2) | 0.247 (2) | 0.030 (6)* |
| H7A | −0.026 (3) | 0.615 (2) | 0.494 (3) | 0.055 (8)* |
| H7B | 0.059 (3) | 0.714 (3) | 0.578 (2) | 0.050 (8)* |

*Atomic displacement parameters (Å²)*

| | $U^{11}$ | $U^{22}$ | $U^{33}$ | $U^{12}$ | $U^{13}$ | $U^{23}$ |
|---|---|---|---|---|---|---|
| Zn1 | 0.00879 (7) | 0.01233 (8) | 0.01258 (8) | −0.00010 (5) | 0.00274 (6) | 0.00297 (6) |
| Zn2 | 0.00780 (10) | 0.01103 (10) | 0.01193 (10) | 0.00122 (7) | 0.00275 (8) | 0.00293 (8) |
| O3 | 0.0114 (4) | 0.0154 (5) | 0.0185 (5) | 0.0039 (4) | 0.0047 (4) | 0.0077 (4) |
| O5 | 0.0103 (4) | 0.0150 (5) | 0.0184 (5) | −0.0016 (4) | 0.0047 (4) | 0.0020 (4) |
| O6 | 0.0153 (5) | 0.0124 (4) | 0.0168 (5) | −0.0005 (4) | 0.0075 (4) | 0.0025 (4) |
| O4 | 0.0158 (5) | 0.0182 (5) | 0.0230 (5) | 0.0051 (4) | 0.0110 (4) | 0.0115 (4) |
| O7 | 0.0115 (5) | 0.0166 (5) | 0.0392 (7) | 0.0030 (4) | 0.0039 (5) | 0.0049 (5) |
| O2 | 0.0152 (5) | 0.0220 (5) | 0.0175 (5) | −0.0016 (4) | −0.0004 (4) | 0.0084 (4) |
| O1 | 0.0172 (5) | 0.0243 (6) | 0.0132 (5) | −0.0028 (4) | 0.0022 (4) | 0.0032 (4) |
| N2 | 0.0115 (5) | 0.0190 (6) | 0.0252 (6) | 0.0053 (5) | 0.0086 (5) | 0.0135 (5) |
| N3 | 0.0144 (6) | 0.0165 (6) | 0.0230 (6) | −0.0039 (5) | 0.0095 (5) | −0.0027 (5) |
| N1 | 0.0155 (6) | 0.0360 (8) | 0.0114 (6) | 0.0019 (6) | 0.0021 (5) | 0.0001 (6) |
| C29 | 0.0127 (6) | 0.0144 (6) | 0.0173 (6) | 0.0016 (5) | 0.0061 (5) | 0.0047 (5) |
| C28 | 0.0108 (6) | 0.0115 (6) | 0.0136 (6) | 0.0007 (5) | 0.0027 (5) | 0.0039 (5) |
| C16 | 0.0107 (6) | 0.0174 (6) | 0.0140 (6) | 0.0024 (5) | 0.0044 (5) | 0.0076 (5) |
| C33 | 0.0118 (6) | 0.0147 (6) | 0.0162 (6) | −0.0003 (5) | 0.0048 (5) | 0.0029 (5) |
| C2 | 0.0149 (6) | 0.0177 (6) | 0.0136 (6) | −0.0009 (5) | 0.0028 (5) | 0.0054 (5) |
| C26 | 0.0138 (6) | 0.0192 (7) | 0.0198 (7) | 0.0035 (5) | 0.0055 (5) | 0.0107 (6) |
| C3 | 0.0145 (6) | 0.0192 (7) | 0.0137 (6) | −0.0004 (5) | 0.0036 (5) | 0.0049 (5) |
| C21 | 0.0120 (6) | 0.0200 (7) | 0.0202 (7) | 0.0062 (5) | 0.0078 (5) | 0.0126 (6) |
| C30 | 0.0179 (7) | 0.0146 (6) | 0.0170 (6) | 0.0030 (5) | 0.0069 (5) | 0.0025 (5) |
| C32 | 0.0150 (7) | 0.0159 (7) | 0.0227 (7) | −0.0037 (5) | 0.0065 (6) | 0.0012 (6) |
| C7 | 0.0152 (7) | 0.0283 (8) | 0.0194 (7) | 0.0011 (6) | 0.0036 (6) | 0.0074 (6) |
| C17 | 0.0150 (6) | 0.0216 (7) | 0.0225 (7) | 0.0048 (5) | 0.0064 (5) | 0.0137 (6) |
| C22 | 0.0141 (6) | 0.0226 (7) | 0.0221 (7) | 0.0035 (6) | 0.0045 (6) | 0.0092 (6) |
| C19 | 0.0158 (7) | 0.0331 (9) | 0.0286 (8) | 0.0032 (6) | 0.0106 (6) | 0.0203 (7) |
| C18 | 0.0192 (7) | 0.0263 (8) | 0.0273 (8) | 0.0036 (6) | 0.0082 (6) | 0.0190 (7) |
| C20 | 0.0135 (6) | 0.0250 (7) | 0.0213 (7) | 0.0047 (5) | 0.0083 (5) | 0.0132 (6) |
| C15 | 0.0117 (6) | 0.0161 (6) | 0.0151 (6) | 0.0023 (5) | 0.0055 (5) | 0.0074 (5) |
| C25 | 0.0120 (6) | 0.0263 (8) | 0.0285 (8) | 0.0047 (6) | 0.0057 (6) | 0.0148 (7) |
| C34 | 0.0147 (7) | 0.0127 (6) | 0.0292 (8) | 0.0004 (5) | 0.0109 (6) | 0.0048 (6) |
| C14 | 0.0115 (6) | 0.0139 (6) | 0.0118 (6) | 0.0025 (5) | 0.0044 (5) | 0.0035 (5) |
| C31 | 0.0190 (7) | 0.0144 (6) | 0.0192 (7) | −0.0009 (5) | 0.0047 (6) | 0.0008 (5) |
| C4 | 0.0152 (7) | 0.0232 (7) | 0.0136 (6) | −0.0021 (6) | 0.0028 (5) | 0.0033 (6) |
| C27 | 0.0112 (6) | 0.0130 (6) | 0.0128 (6) | 0.0006 (5) | 0.0029 (5) | 0.0048 (5) |
| C24 | 0.0183 (7) | 0.0272 (8) | 0.0349 (9) | 0.0108 (6) | 0.0135 (7) | 0.0151 (7) |
| C1 | 0.0168 (7) | 0.0149 (6) | 0.0145 (6) | −0.0004 (5) | 0.0021 (5) | 0.0069 (5) |
| C23 | 0.0225 (8) | 0.0220 (7) | 0.0297 (8) | 0.0072 (6) | 0.0112 (7) | 0.0084 (7) |
| C5 | 0.0206 (7) | 0.0264 (8) | 0.0135 (6) | −0.0002 (6) | 0.0048 (6) | 0.0025 (6) |

| | | | | | | |
|---|---|---|---|---|---|---|
| C35 | 0.0219 (8) | 0.0187 (7) | 0.0367 (9) | 0.0010 (6) | 0.0053 (7) | 0.0110 (7) |
| C9 | 0.0220 (7) | 0.0215 (7) | 0.0176 (7) | 0.0034 (6) | 0.0087 (6) | 0.0003 (6) |
| C8 | 0.0146 (7) | 0.0243 (7) | 0.0136 (6) | 0.0016 (6) | 0.0038 (5) | −0.0011 (6) |
| C6 | 0.0212 (8) | 0.0337 (9) | 0.0211 (8) | 0.0064 (7) | 0.0088 (6) | 0.0052 (7) |
| C10 | 0.0193 (8) | 0.0256 (8) | 0.0283 (8) | 0.0018 (6) | 0.0116 (7) | −0.0009 (7) |
| C39 | 0.0270 (8) | 0.0187 (7) | 0.0393 (10) | 0.0077 (6) | 0.0219 (8) | 0.0112 (7) |
| C13 | 0.0227 (8) | 0.0318 (9) | 0.0191 (7) | 0.0023 (7) | 0.0061 (6) | 0.0056 (7) |
| C11 | 0.0163 (7) | 0.0332 (9) | 0.0279 (9) | 0.0066 (7) | 0.0037 (6) | −0.0018 (7) |
| C12 | 0.0258 (9) | 0.0375 (10) | 0.0207 (8) | 0.0102 (7) | 0.0028 (7) | 0.0065 (7) |
| C36 | 0.0194 (8) | 0.0237 (9) | 0.0672 (15) | 0.0031 (7) | −0.0011 (9) | 0.0195 (9) |
| C38 | 0.0336 (10) | 0.0251 (9) | 0.0799 (16) | 0.0133 (8) | 0.0415 (11) | 0.0253 (10) |
| C37 | 0.0161 (8) | 0.0241 (9) | 0.105 (2) | 0.0072 (7) | 0.0233 (11) | 0.0304 (11) |

*Geometric parameters (Å, º)*

| | | | |
|---|---|---|---|
| Zn1—O3 | 1.9920 (10) | C7—H7 | 0.9500 |
| Zn1—O5 | 1.9063 (10) | C7—C6 | 1.381 (2) |
| Zn1—O7 | 2.0274 (12) | C17—H17 | 0.9500 |
| Zn1—O1 | 1.9298 (11) | C17—C18 | 1.372 (2) |
| Zn2—O6$^{i}$ | 2.0775 (10) | C22—H22 | 0.9500 |
| Zn2—O6 | 2.0775 (10) | C22—C23 | 1.386 (2) |
| Zn2—O4$^{i}$ | 2.1762 (10) | C19—H19 | 0.9500 |
| Zn2—O4 | 2.1762 (10) | C19—C18 | 1.398 (2) |
| Zn2—O2 | 2.0219 (11) | C19—C20 | 1.378 (2) |
| Zn2—O2$^{i}$ | 2.0219 (11) | C18—H18 | 0.9500 |
| O3—C14 | 1.2866 (17) | C20—H20 | 0.9500 |
| O5—C27 | 1.2788 (17) | C20—C15 | 1.4080 (19) |
| O6—C27 | 1.2555 (17) | C15—C14 | 1.4752 (19) |
| O4—C14 | 1.2572 (17) | C25—H25 | 0.9500 |
| O7—H7A | 0.90 (3) | C25—C24 | 1.384 (2) |
| O7—H7B | 0.84 (3) | C34—C35 | 1.394 (3) |
| O2—C1 | 1.2559 (18) | C34—C39 | 1.387 (2) |
| O1—C1 | 1.2742 (19) | C31—H31 | 0.9500 |
| N2—C16 | 1.3674 (18) | C4—H4 | 0.9500 |
| N2—C21 | 1.4151 (18) | C4—C5 | 1.379 (2) |
| N2—H2 | 0.81 (2) | C24—H24 | 0.9500 |
| N3—C33 | 1.3787 (19) | C24—C23 | 1.390 (2) |
| N3—C34 | 1.4166 (19) | C23—H23 | 0.9500 |
| N3—H3 | 0.80 (2) | C5—H5 | 0.9500 |
| N1—C3 | 1.372 (2) | C5—C6 | 1.398 (2) |
| N1—C8 | 1.418 (2) | C35—H35 | 0.9500 |
| N1—H1 | 0.83 (2) | C35—C36 | 1.383 (3) |
| C29—H29 | 0.9500 | C9—H9 | 0.9500 |
| C29—C28 | 1.4024 (19) | C9—C8 | 1.391 (2) |
| C29—C30 | 1.381 (2) | C9—C10 | 1.391 (2) |
| C28—C33 | 1.4126 (19) | C8—C13 | 1.389 (2) |
| C28—C27 | 1.4893 (19) | C6—H6 | 0.9500 |
| C16—C17 | 1.410 (2) | C10—H10 | 0.9500 |

| | | | |
|---|---|---|---|
| C16—C15 | 1.4220 (19) | C10—C11 | 1.383 (3) |
| C33—C32 | 1.414 (2) | C39—H39 | 0.9500 |
| C2—C3 | 1.419 (2) | C39—C38 | 1.393 (3) |
| C2—C7 | 1.397 (2) | C13—H13 | 0.9500 |
| C2—C1 | 1.484 (2) | C13—C12 | 1.386 (2) |
| C26—H26 | 0.9500 | C11—H11 | 0.9500 |
| C26—C21 | 1.393 (2) | C11—C12 | 1.387 (3) |
| C26—C25 | 1.388 (2) | C12—H12 | 0.9500 |
| C3—C4 | 1.410 (2) | C36—H36 | 0.9500 |
| C21—C22 | 1.390 (2) | C36—C37 | 1.387 (4) |
| C30—H30 | 0.9500 | C38—H38 | 0.9500 |
| C30—C31 | 1.395 (2) | C38—C37 | 1.377 (4) |
| C32—H32 | 0.9500 | C37—H37 | 0.9500 |
| C32—C31 | 1.378 (2) | | |

| | | | |
|---|---|---|---|
| O3—Zn1—O7 | 97.20 (5) | C18—C19—H19 | 120.6 |
| O5—Zn1—O3 | 118.92 (5) | C20—C19—H19 | 120.6 |
| O5—Zn1—O7 | 95.94 (5) | C20—C19—C18 | 118.87 (14) |
| O5—Zn1—O1 | 135.15 (5) | C17—C18—C19 | 121.21 (14) |
| O1—Zn1—O3 | 101.15 (5) | C17—C18—H18 | 119.4 |
| O1—Zn1—O7 | 98.30 (5) | C19—C18—H18 | 119.4 |
| O6$^{i}$—Zn2—O6 | 180.0 | C19—C20—H20 | 119.3 |
| O6$^{i}$—Zn2—O4 | 87.99 (4) | C19—C20—C15 | 121.44 (14) |
| O6—Zn2—O4 | 92.00 (4) | C15—C20—H20 | 119.3 |
| O6—Zn2—O4$^{i}$ | 88.00 (4) | C16—C15—C14 | 122.83 (12) |
| O6$^{i}$—Zn2—O4$^{i}$ | 92.00 (4) | C20—C15—C16 | 119.33 (13) |
| O4$^{i}$—Zn2—O4 | 180.00 (4) | C20—C15—C14 | 117.73 (13) |
| O2$^{i}$—Zn2—O6$^{i}$ | 93.86 (4) | C26—C25—H25 | 119.9 |
| O2—Zn2—O6$^{i}$ | 86.14 (4) | C24—C25—C26 | 120.20 (15) |
| O2$^{i}$—Zn2—O6 | 86.14 (4) | C24—C25—H25 | 119.9 |
| O2—Zn2—O6 | 93.85 (4) | C35—C34—N3 | 120.97 (15) |
| O2—Zn2—O4 | 96.22 (4) | C39—C34—N3 | 119.10 (16) |
| O2$^{i}$—Zn2—O4 | 83.78 (4) | C39—C34—C35 | 119.92 (16) |
| O2$^{i}$—Zn2—O4$^{i}$ | 96.22 (4) | O3—C14—C15 | 118.44 (12) |
| O2—Zn2—O4$^{i}$ | 83.78 (4) | O4—C14—O3 | 119.60 (13) |
| O2$^{i}$—Zn2—O2 | 180.0 | O4—C14—C15 | 121.96 (12) |
| C14—O3—Zn1 | 104.17 (9) | C30—C31—H31 | 119.7 |
| C27—O5—Zn1 | 127.60 (9) | C32—C31—C30 | 120.62 (14) |
| C27—O6—Zn2 | 137.10 (9) | C32—C31—H31 | 119.7 |
| C14—O4—Zn2 | 161.37 (10) | C3—C4—H4 | 119.5 |
| Zn1—O7—H7A | 129.0 (18) | C5—C4—C3 | 121.07 (14) |
| Zn1—O7—H7B | 123.9 (19) | C5—C4—H4 | 119.5 |
| H7A—O7—H7B | 106 (3) | O5—C27—C28 | 115.79 (12) |
| C1—O2—Zn2 | 142.24 (10) | O6—C27—O5 | 124.31 (13) |
| C1—O1—Zn1 | 123.40 (10) | O6—C27—C28 | 119.89 (12) |
| C16—N2—C21 | 125.40 (13) | C25—C24—H24 | 120.1 |
| C16—N2—H2 | 118.8 (16) | C25—C24—C23 | 119.74 (15) |
| C21—N2—H2 | 115.4 (16) | C23—C24—H24 | 120.1 |

| | | | |
|---|---|---|---|
| C33—N3—C34 | 122.70 (13) | O2—C1—O1 | 123.47 (14) |
| C33—N3—H3 | 114.7 (15) | O2—C1—C2 | 118.44 (14) |
| C34—N3—H3 | 118.4 (15) | O1—C1—C2 | 118.09 (13) |
| C3—N1—C8 | 125.41 (13) | C22—C23—C24 | 120.36 (16) |
| C3—N1—H1 | 118.4 (16) | C22—C23—H23 | 119.8 |
| C8—N1—H1 | 115.7 (16) | C24—C23—H23 | 119.8 |
| C28—C29—H29 | 118.9 | C4—C5—H5 | 119.4 |
| C30—C29—H29 | 118.9 | C4—C5—C6 | 121.24 (15) |
| C30—C29—C28 | 122.13 (13) | C6—C5—H5 | 119.4 |
| C29—C28—C33 | 119.06 (13) | C34—C35—H35 | 120.1 |
| C29—C28—C27 | 118.00 (12) | C36—C35—C34 | 119.87 (19) |
| C33—C28—C27 | 122.94 (12) | C36—C35—H35 | 120.1 |
| N2—C16—C17 | 120.21 (13) | C8—C9—H9 | 120.0 |
| N2—C16—C15 | 121.75 (13) | C10—C9—H9 | 120.0 |
| C17—C16—C15 | 117.98 (13) | C10—C9—C8 | 120.04 (17) |
| N3—C33—C28 | 122.43 (13) | C9—C8—N1 | 119.28 (15) |
| N3—C33—C32 | 119.45 (13) | C13—C8—N1 | 120.97 (15) |
| C28—C33—C32 | 118.03 (13) | C13—C8—C9 | 119.70 (15) |
| C3—C2—C1 | 123.36 (14) | C7—C6—C5 | 118.31 (15) |
| C7—C2—C3 | 119.75 (14) | C7—C6—H6 | 120.8 |
| C7—C2—C1 | 116.86 (13) | C5—C6—H6 | 120.8 |
| C21—C26—H26 | 120.0 | C9—C10—H10 | 120.0 |
| C25—C26—H26 | 120.0 | C11—C10—C9 | 120.07 (17) |
| C25—C26—C21 | 120.06 (15) | C11—C10—H10 | 120.0 |
| N1—C3—C2 | 121.58 (13) | C34—C39—H39 | 120.2 |
| N1—C3—C4 | 120.70 (14) | C34—C39—C38 | 119.63 (19) |
| C4—C3—C2 | 117.71 (14) | C38—C39—H39 | 120.2 |
| C26—C21—N2 | 118.72 (14) | C8—C13—H13 | 120.0 |
| C22—C21—N2 | 121.48 (13) | C12—C13—C8 | 119.98 (17) |
| C22—C21—C26 | 119.69 (13) | C12—C13—H13 | 120.0 |
| C29—C30—H30 | 120.7 | C10—C11—H11 | 120.1 |
| C29—C30—C31 | 118.65 (14) | C10—C11—C12 | 119.88 (16) |
| C31—C30—H30 | 120.7 | C12—C11—H11 | 120.1 |
| C33—C32—H32 | 119.3 | C13—C12—C11 | 120.29 (18) |
| C31—C32—C33 | 121.37 (14) | C13—C12—H12 | 119.9 |
| C31—C32—H32 | 119.3 | C11—C12—H12 | 119.9 |
| C2—C7—H7 | 119.1 | C35—C36—H36 | 119.9 |
| C6—C7—C2 | 121.88 (15) | C35—C36—C37 | 120.2 (2) |
| C6—C7—H7 | 119.1 | C37—C36—H36 | 119.9 |
| C16—C17—H17 | 119.5 | C39—C38—H38 | 119.8 |
| C18—C17—C16 | 121.07 (14) | C37—C38—C39 | 120.4 (2) |
| C18—C17—H17 | 119.5 | C37—C38—H38 | 119.8 |
| C21—C22—H22 | 120.0 | C36—C37—H37 | 120.0 |
| C23—C22—C21 | 119.94 (15) | C38—C37—C36 | 120.01 (18) |
| C23—C22—H22 | 120.0 | C38—C37—H37 | 120.0 |

| | | | |
|---|---|---|---|
| Zn1—O3—C14—O4 | −0.51 (15) | C3—C4—C5—C6 | −1.7 (3) |
| Zn1—O3—C14—C15 | −179.36 (10) | C21—N2—C16—C17 | 18.7 (2) |

| | | | |
|---|---|---|---|
| Zn1—O5—C27—O6 | 1.2 (2) | C21—N2—C16—C15 | −164.39 (14) |
| Zn1—O5—C27—C28 | −178.84 (9) | C21—C26—C25—C24 | −1.4 (2) |
| Zn1—O1—C1—O2 | −2.4 (2) | C21—C22—C23—C24 | −1.1 (3) |
| Zn1—O1—C1—C2 | 178.08 (10) | C30—C29—C28—C33 | 2.1 (2) |
| Zn2—O6—C27—O5 | −34.5 (2) | C30—C29—C28—C27 | −178.18 (14) |
| Zn2—O6—C27—C28 | 145.52 (11) | C7—C2—C3—N1 | 178.35 (16) |
| Zn2—O4—C14—O3 | −71.0 (3) | C7—C2—C3—C4 | −0.5 (2) |
| Zn2—O4—C14—C15 | 107.8 (3) | C7—C2—C1—O2 | 13.3 (2) |
| Zn2—O2—C1—O1 | 40.1 (3) | C7—C2—C1—O1 | −167.15 (14) |
| Zn2—O2—C1—C2 | −140.43 (14) | C17—C16—C15—C20 | 4.0 (2) |
| N2—C16—C17—C18 | 174.60 (15) | C17—C16—C15—C14 | −172.21 (13) |
| N2—C16—C15—C20 | −172.99 (14) | C19—C20—C15—C16 | −3.0 (2) |
| N2—C16—C15—C14 | 10.8 (2) | C19—C20—C15—C14 | 173.35 (15) |
| N2—C21—C22—C23 | 176.60 (14) | C18—C19—C20—C15 | 0.4 (3) |
| N3—C33—C32—C31 | 179.89 (16) | C20—C19—C18—C17 | 1.3 (3) |
| N3—C34—C35—C36 | 179.26 (16) | C20—C15—C14—O3 | −2.8 (2) |
| N3—C34—C39—C38 | −179.35 (15) | C20—C15—C14—O4 | 178.34 (14) |
| N1—C3—C4—C5 | −177.00 (16) | C15—C16—C17—C18 | −2.4 (2) |
| N1—C8—C13—C12 | −178.26 (16) | C25—C26—C21—N2 | −175.45 (14) |
| C29—C28—C33—N3 | 179.21 (14) | C25—C26—C21—C22 | 0.7 (2) |
| C29—C28—C33—C32 | −4.3 (2) | C25—C24—C23—C22 | 0.4 (3) |
| C29—C28—C27—O5 | 9.52 (19) | C34—N3—C33—C28 | −157.76 (15) |
| C29—C28—C27—O6 | −170.54 (13) | C34—N3—C33—C32 | 25.8 (2) |
| C29—C30—C31—C32 | −2.4 (2) | C34—C35—C36—C37 | 0.0 (3) |
| C28—C29—C30—C31 | 1.3 (2) | C34—C39—C38—C37 | 0.2 (3) |
| C28—C33—C32—C31 | 3.3 (2) | C4—C5—C6—C7 | 0.2 (3) |
| C16—N2—C21—C26 | −132.15 (16) | C27—C28—C33—N3 | −0.5 (2) |
| C16—N2—C21—C22 | 51.8 (2) | C27—C28—C33—C32 | 175.99 (14) |
| C16—C17—C18—C19 | −0.2 (3) | C1—C2—C3—N1 | 0.5 (2) |
| C16—C15—C14—O3 | 173.38 (13) | C1—C2—C3—C4 | −178.34 (14) |
| C16—C15—C14—O4 | −5.4 (2) | C1—C2—C7—C6 | 176.93 (16) |
| C33—N3—C34—C35 | 47.6 (2) | C35—C34—C39—C38 | −0.1 (2) |
| C33—N3—C34—C39 | −133.18 (17) | C35—C36—C37—C38 | 0.1 (3) |
| C33—C28—C27—O5 | −170.79 (13) | C9—C8—C13—C12 | −0.8 (3) |
| C33—C28—C27—O6 | 9.2 (2) | C9—C10—C11—C12 | −1.4 (3) |
| C33—C32—C31—C30 | 0.0 (3) | C8—N1—C3—C2 | 178.42 (16) |
| C2—C3—C4—C5 | 1.9 (2) | C8—N1—C3—C4 | −2.8 (3) |
| C2—C7—C6—C5 | 1.2 (3) | C8—C9—C10—C11 | 1.9 (2) |
| C26—C21—C22—C23 | 0.5 (2) | C8—C13—C12—C11 | 1.4 (3) |
| C26—C25—C24—C23 | 0.8 (3) | C10—C9—C8—N1 | 176.66 (15) |
| C3—N1—C8—C9 | 118.66 (18) | C10—C9—C8—C13 | −0.8 (2) |
| C3—N1—C8—C13 | −63.9 (2) | C10—C11—C12—C13 | −0.3 (3) |
| C3—C2—C7—C6 | −1.0 (3) | C39—C34—C35—C36 | 0.1 (2) |
| C3—C2—C1—O2 | −168.80 (14) | C39—C38—C37—C36 | −0.2 (3) |
| C3—C2—C1—O1 | 10.7 (2) | | |

Symmetry code: (i) −*x*+1, −*y*+1, −*z*+1.

Journal of Molecular Structure 1261 (2022) 132956

Contents lists available at ScienceDirect

Journal of Molecular Structure

journal homepage: www.elsevier.com/locate/molstr

# Synthesis, crystal structure, DFT studies and Hirshfeld surface analysis of Manganese(II) and Cadmium(II) coordination polymers of 2-aminopyridine and dicyanamide

Armel Landry Opepam Mbani[a], Divine Mbom Yufanyi[b,*], Che Dieudonne Tabong[c], Nono Jean Hubert[d], Amah Colette Benedicta Yuoh[e], Awawou Gbambie Paboudam[a], Agwara Moise Ondoh[a,*]

[a] Department of Inorganic Chemistry, Faculty of Science, University of Yaoundé I, P.O. Box 812, Yaoundé, Cameroon
[b] Department of Fundamental Science, Higher Technical Teachers' Training College, The University of Bamenda, Bamenda, Cameroon
[c] Department of Chemistry, Higher Teacher Training College, The University of Bamenda, Bamenda, Cameroon
[d] Department of Chemical and Biological Engineering, National Higher Polytechnic Institute, The University of Bamenda, Bamenda, Cameroon
[e] Department of Chemistry, Faculty of Science, The University of Bamenda, P.O. Box 39 Bambili, Bamenda, Cameroon

ARTICLE INFO

*Article history:*
Received 6 January 2022
Revised 25 March 2022
Accepted 27 March 2022
Available online 29 March 2022

*Keywords:*
2-Aminopyridine
Coordination polymer
Crystal structure
DFT
Dicyanamide
Hirshfeld surface

ABSTRACT

Mn(II) and Cd(II) metal salts reacted with dicyanamide and 2-aminopyridine resulted in the formation of the ligand-rich linear polymeric chain structures $[M(dca)_2(2\text{-Ampy})_2]_n$ (dca = dicyanamide, 2-Ampy = 2-Aminopyridine; *M* = Mn (**1**) or Cd (**2**)), of the same dimensionality, in which the metal centers are $\mu_{1,5}$-bridged by the dca anions. The complexes were characterized by elemental analysis, IR spectroscopy, UV–vis spectroscopy, thermal analysis and single crystal X-ray structure analysis. These coordination polymers crystallize in the Monoclinic space group Cc. The 3D crystal packing structure results from a combination of N—H/H—-N interactions followed by C–H—$\pi$ stacking interactions. Hirshfeld surface (HS) analysis of the polymers was undertaken to investigate further the intermolecular interactions. DFT calculations on **1** and **2** demonstrated a good correlation between the experimental and theoretical data. The in vitro antimicrobial activity of the manganese complex against selected micro-organisms is also reported.



## 1. Introduction

Interest in the design and synthesis of coordination polymers, of varying dimensions (1D, 2D and 3D), has surged due to their interesting physico-chemical properties and potential applications in the domains of catalysis, gas storage, conductivity, superconductivity and magnetism [1–3]. A careful choice of ligand, the metal ion as well as reaction conditions can have a profound influence on the topology of the polymeric network obtained, the coordination geometry and the crystal packing. A combination of strong covalent bonds and weak non-covalent interactions (hydrogen bonding, $\pi-\pi$ stacking, and van der Waals forces) binds the molecular building units together into extended structures with different properties and applications [4–6].

Coordination polymers have been obtained from transition metals and polynitrile ligands such as dicyanamide, dca (dca = $N(CN)_2^-$) [7–10]. Interest in dca is due to its versatile coordination (e.g. monodentate, bidentate) and bridging modes such as, $\mu_{1,3}$ (coordinating through one nitrile nitrogen atom and the other nitrogen atom), $\mu_{1,5}$ (coordinating through the two nitrile nitrogen atoms) and $\mu_{1,3,5}$ (coordinating through all three nitrogen atoms). Also, the negative charge on this ligand indicates that additional anions are not required to balance the charge in the structures formed [8,11–15]. The introduction of co-ligands during synthesis can lead to the modification of structure type and network of the coordination polymers[7].

Several heterocyclic organic ligands, such as pyridine and derivatives, have been used in the construction of coordination polymers with diverse structures and numerous applications [8,16,17]. The rigid pyridine-based ligands are good N-donor ligands to metal ions through the pyridine N-atom, while the substituent groups are most often involved in non-covalent interactions. Aminopyridines (2-, 3-, or 4-Ampy), especially 2-Ampy, exhibit mainly monodentate coordination through the pyridine nitrogen atom though some chelates are also known [18].

* Correspondence author.
*E-mail addresses:* dyufanyi@yahoo.com (D.M. Yufanyi), agwara29@yahoo.com (A.M. Ondoh).

https://doi.org/10.1016/j.molstruc.2022.132956
0022-2860/

Hirshfield Surface analysis has been very useful and effective in the exploration of intermolecular interactions in molecular crystals [19–22]. Information about the intermolecular interactions are encrypted on the surfaces of the molecule and this can be exploited to obtain information on crystal packing. The related fingerprint color plots provide quantitative information on the types of intermolecular contacts in the molecules. The understanding and quantification of intermolecular interactions is crucial to structure prediction and consequently, the design and development of new complexes and materials with desired properties [23–25]. Generally, C-H—N, N-H—N hydrogen bonding with dicyanamide, C-H—$\pi$, C—C and $\pi-\pi$ stacking interactions of the pyridine ring, have been shown to exist in these complexes [7,8].

In continuation of our interest in the synthesis of coordination polymers with diverse structures and physico-chemical properties [26–28], we herein report the synthesis and structural characterization of Mn(II) and Cd(II) coordination polymers. While DFT studies were used to provide insight into the energy and other properties the polymers, the percentage of intermolecular interactions in these complexes were resolved by Hirshfeld surface analysis. In addition, the in vitro antimicrobial activity of the manganese complex against selected micro-organisms is reported.

## 2. Experimental

### 2.1. Materials and method

All chemicals and solvents were obtained from commercial sources and used as received.

### 2.2. Synthesis of $[Mn(2\text{-ampy})_2(\mu_{1,5}\text{-dca})_2]_n$ (1)

To an ethanolic solution (10 mL) of $MnCl_2{\cdot}4H_2O$ (0.1979 g; 1 mmol) at room temperature, was added dropwise, a 10 mL ethanol/water (1:1) solution of sodium dicyanamide, $NaC_2N_3$ (0.16 g; 2 mmol). The colorless mixture was stirred for 30 min after which an ethanolic solution (10 mL) of 2-aminopyridine (0.377 g; 4 mmol) was added drop wise into the stirred solution. The resulting mixture was further stirred for 2 h. The white precipitate formed was filtered, washed with ethanol/distilled water (1:1); air dried and weighed (yield 84%). The filtrate was allowed to evaporate slowly at room temperature from which colorless crystals, suitable for single crystal X-ray diffraction, were obtained within a few days: m.p.: >300 °C. Element Anal. Calc. for $MnC_{14}H_{12}N_{10}$: C, 44.81; H, 3.22; N, 37.33. Found: C, 44.23; H, 3.06; N, 37.54.

### 2.3. Synthesis of the $[Cd(2\text{-ampy})_2(\mu_{1,5}\text{-dca})_2]_n$ (2)

A similar procedure as that for **1** was followed to prepare **2**, except that $MnCl_2{\cdot}4H_2O$ was replaced by $CdCl_2{\cdot}4H_2O$ (0.1834 g; 1 mmol). The white precipitate formed was filtered, washed with ethanol/distilled water (1:1), air dried and weighed (yield 26%). The filtrate was allowed to evaporate slowly at room temperature from which and colorless crystals, suitable for single crystal X-ray diffraction, were obtained within a few days: m.p.: 162 °C. Element Anal. Calc. for $CdC_{14}H_{12}N_{10}$: C, 38.86; H, 2.68; N, 31.92. Found: C, 38.32; H, 2.46; N, 31.27.

### 2.4. Characterization techniques

The melting point temperature was recorded using a Leica VMHB Kofler system. Elemental analysis (C, H, N) was carried out on a Flash 2000 Thermo Scientific analyzer. The infrared spectra were recorded using a Bruker ALPHA-P spectrophotometer directly on a small sample of the complex in the range 400 - 4000 $cm^{-1}$ while the UV-visible spectrum of a DMSO solution of the complex was recorded using an Ocean Insight FX_VS_IRS_ES spectrophotometer at room temperature. The TGA analysis was recorded on a TGA/DSC 1 (STAR System) instrument, between 30 and 600°C under nitrogen atmosphere at a flow rate of 10 $mL^{-1}$ and a temperature ramp of 10°C $min^{-1}$. Powder diffraction pattern for **1** were recorded on a D8 Advance XRD instrument.

### 2.5. Single-crystal X-ray structure determination

X-ray data were collected with a Bruker *APEX*-II CCD diffractometer, $\lambda$(Mo-$K_\alpha$) = 0.71073 Å, $T$ = 100 K for **1**, and a GEMINI CCD diffractometer (Rigaku Inc.), $\lambda$(Mo-$K_\alpha$) = 0.71073 Å, $T$ = 130(2) K, $\omega$-scan rotation for **2**. Data reduction was performed with CrysAlis Pro including the program SCALE3 ABSPACK for empirical absorption correction [29]. All structures were solved by dual space methods with SHELXT-20xy [30]. Structure refinement was done with SHELXL-2018 [31,32] by using full-matrix least-square routines against $F^2$. Hydrogen atoms and NH were located on difference Fourier maps calculated at the final stage of the structure refinement. The remaining hydrogen atoms of **2** were calculated on idealized positions using the riding model. The pictures were generated with the program Mercury [33]. **CCDC 1,055,775** for **1** and **2,132,564** for **2** contains the supplementary crystallographic data for this paper. These data can be obtained free of charge via www.ccdc.cam.ac.uk/data_request/cif (or from the Cambridge Crystallographic Data Centre, 12 Union Road, Cambridge CB2 1EZ, UK; fax: (+44)1223–336–033; or deposit@ccdc.cam.uk).

### 2.6. DFT calculations

Calculations were performed on the complexes to gain further insights into the molecular interactions in the synthesized compounds and to predict some of their electronic properties. Geometry optimization of a fragment each complex was done using Gaussian 09 Revision D.01 [34]. The optimization process was based on X-ray data and a fragment was chosen to obtain a perfect symmetry around the central metal ion with a complete coordination as observed in the polymer. The density functional B3LYP [35–37] associated to LAN2DZ [38,39] was used for these calculations. Furthermore, the dispersion correction for the non-bonding Van der Waal's (vdW) interactions was carried out through the Grimme approach using atom pair-wise additive schemes, the so-called DFT-D3 method [40]. The DFT-B3LYP/LAN2DZ level of theory had been successfully used for the optimization of a Cd polymer [41].

NBO analysis [42,43] was done to identify the nature of the coordination bonds and the orbitals involved in the interactions between the metal ions and the ligands. It was also used to evaluate the importance of these interactions to the stability of these polymers through the stabilization energy ($E^{(2)}$). Electronic properties including molecular electrostatic potential maps, energy of frontier molecular orbitals, energy gap, softness, hardness, chemical potential, and electronegativity [44,45] were calculated to investigate the chemical reactivity and kinetic stability of the studied polymers.

### 2.7. Hirshfeld surface analysis

A full understanding of the crystal structure requires a comparison of the entire molecule and all interactions in the crystalline state [46]. Hirshfeld surface [20,47] and fingerprint [48,49] together constitute a powerful resource for visualizing, exploring, analyzing, and quantifying intermolecular interactions in molecular crystals [50] and therefore they can be used to compare the molecular crystal structures containing similar atoms [50–52]. Hirshfeld surface and fingerprint plots have been used to qualify and quantify similarities and differences between the molecular structures of **1** and **2**.

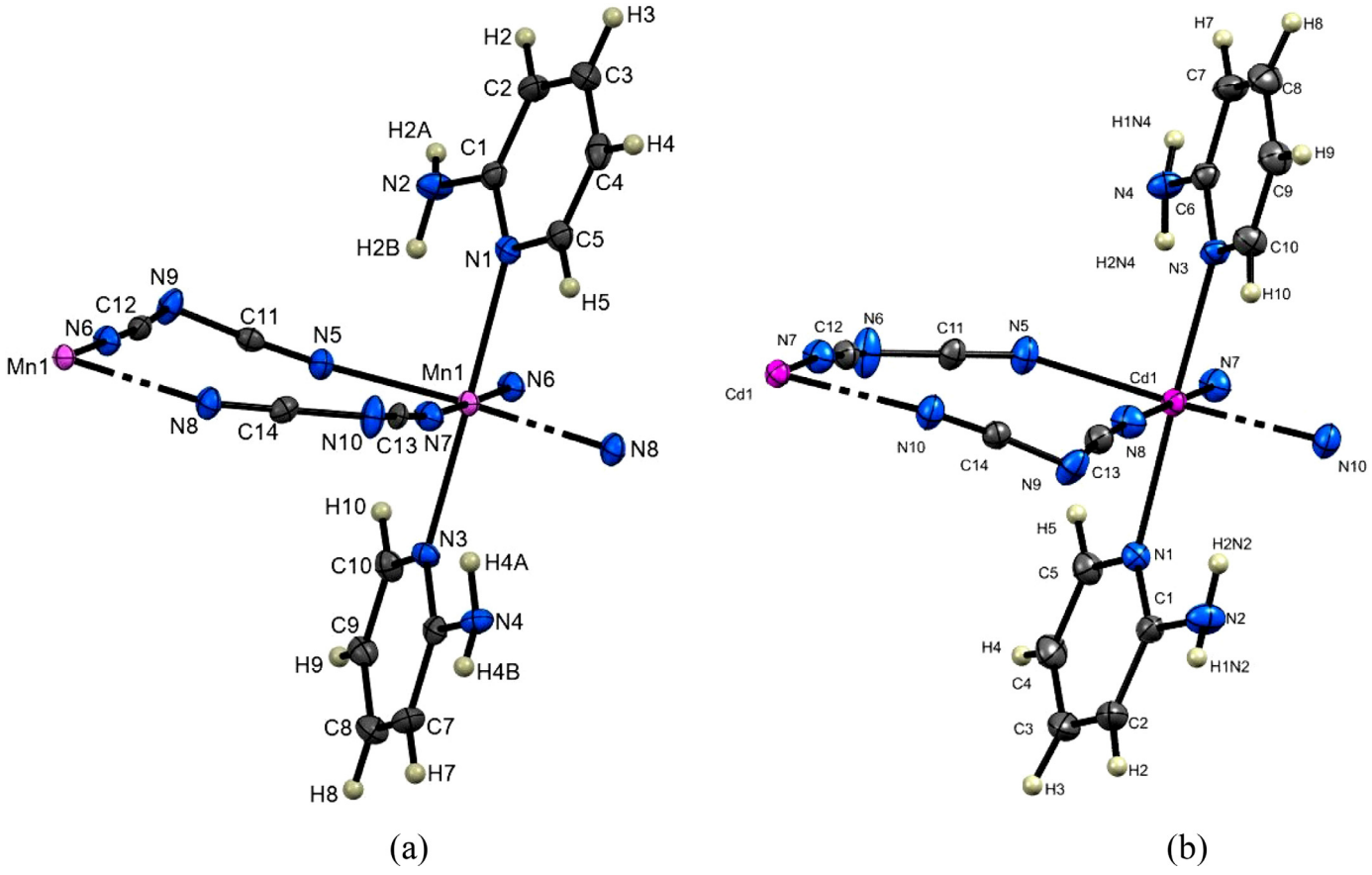


**Fig. 1.** Molecular structure and atom-labeling scheme for (a) **1** and (b) **2** with ellipsoids drawn at 50% probability level.

**Table 1**
Crystal data and structure refinement parameters.

| Crystal data | 1 | 2 |
|---|---|---|
| Chemical formula | $C_{14}H_{12}MnN_{10}$ | $C_{14}H_{12}CdN_{10}$ |
| $M_r$ | 375.28 | 432.74 |
| Crystal system, space group | Monoclinic, *Cc* | Monoclinic, Cc |
| Temperature (K) | 100 | 130(2) |
| *a*, *b*, *c* (Å) | 16.0680(5), 7.5050(3), 14.4658(4) | 16.1412(2), 7.6088(0), 14.5173(2) |
| $\beta$ (°) | 113.087(2) | 113.371(2) |
| $V$ (Å$^3$) | 1604.72(9) | 1636.66(4) |
| $Z$ | 4 | 4 |
| Radiation type | Cu $K\alpha$ | Mo-K$\alpha$ |
| μ (mm$^{-1}$) | 6.88 | 1.355 |
| Crystal size (mm) | 0.29 × 0.15 × 0.03 | 0.30 × 0.20 × 0.10 |
| Data collection | | |
| Diffractometer | Bruker *APEX*-II CCD diffractometer | Xcalibur, Sapphire3, Gemini |
| Absorption correction | Multi-scan *SADABS* | Multi-scan |
| $T_{min}$, $T_{max}$ | 0.541, 0.820 | 0.969, 1.000 |
| No. of measured, independent and observed [$I > 2\sigma(I)$] reflections | 5357, 2593, 2442 | 23,787, 8221, 7995 |
| $R_{int}$ | 0.035 | 0.019 |
| $(\sin\theta/\lambda)_{max}$ (Å$^{-1}$) | 0.617 | 0.861 |
| Refinement | | |
| $R[F^2 > 2\sigma(F^2)]$, $wR(F^2)$, $S$ | 0.030, 0.064, 1.03 | 0.021, 0.048, 1.03 |
| No. of reflections | 2593 | 8221 |
| No. of parameters | 243 | 275 |
| No. of restraints | 2 | 2 |
| H-atom treatment | H atoms treated by a mixture of independent and constrained refinement | All H-atom parameters refined |
| $\Delta\rho_{max}$, $\Delta\rho_{min}$ (e Å$^{-3}$) | 0.31– 0.29 | 2.29 – 0.31 |
| Absolute structure parameter | 0.312 (5) | 0.258 (16) |

**Table 2**
Comparative data on M–$N_{py}$, M-$N_{dca}$ bond lengths and $N_{dca}$–M-$N_{dca}$, $N_{py}$–M-$N_{dca}$ bond angles of some $[M(dca)_2(L)_2]_n$.

| Complex | M-$N_{py}$ (Å) | M-$N_{dca}$ (Å) | | $N_{dca}$–M-$N_{dca}$ (°) | | $N_{py}$–M-$N_{dca}$ (°) | | Ref |
|---|---|---|---|---|---|---|---|---|
| *catena*-[Mn($\mu_{1,5}$-dca)$_2$(py-NH$_2$)$_2$] | 2.2509(11) | 2.2067(11) | 2.2511(11) | 90.26(4) | | 90.77(4) | 91.28(4) | [8] |
| *catena*-[Cd($\mu_{1,5}$-dca)$_2$(py-NH$_2$)$_2$] | 2.2902(16) | 2.3274(17) | 2.3810(17) | 91.40(6) | | 91.13(6) | 91.46(6) | [8] |
| $[Mn(dca)_2(pydz)_2]_n$ | 2.2870(13) | 2.2009(13) | 2.2150(13) | 88.09(5) | 180 | 87.96(5) | 91.14(5) | [9] |
| $[Fe(dca)_2(pydz)_2]_n$ | 2.221(4) | 2.153(3) | 2.153(3) | 87.94(14) | 180 | 88.89(10) | 91.11(10) | [9] |
| $[Co(dca)_2(pydz)_2]_n$ | 2.166(2) | 2.1095(14) | 2.1095(14) | 88.13(8) | 180 | 89.20(5) | 90.80(5) | [9] |
| $[Co(dca)_2(4\text{-OMP})_2]_n$ | 2.126(4) | 2.116(4) | 2.124(5) | 90.34(17) | 180 | 91.16(17) | 90.47(17) | [12] |
| $[Cu(dca)_2(4\text{-OMP})_2]_n$ | 2.013(4) | 1.990(4) | 2.488(5) | 90.50(17) | 180 | 90.37(17) | 91.16(17) | [12] |
| $[Cu(dca)_2(4\text{-MOP})_2]_n$ | 2.0219(10) | 2.0040(10) | 2.4556(10) | 92.10(4) | 180 | 90.33(4) | 90.31(4) | [12] |
| $[Cd(dca)_2(4\text{-MOP})_2]_n$ | 2.302(3) | 2.340(4) | 2.354(3) | 93.24(11) | 180 | 90.66(12) | 91.38(12) | [12] |
| $[Zn(dca)_2(4\text{-MOP})_2]_n$ | 2.1288(15) | 2.1710(19) | 2.1733(19) | 90.89(6) | 180 | 90.28(7) | 90.59(7) | [12] |
| $[Mn(2\text{-ampy})_2(\mu_{1,5}\text{-dca})_2]_n$ | 2.203(3) | 2.211(3) | 2.231(3) | 90.95(10) | 177.96(11) | 88.04(11) | 91.75(10) | This work |
| $[Cd(2\text{-ampy})_2(\mu_{1,5}\text{-dca})_2]_n$ | 2.347(4) | 2.326(19) | 2.343(19) | 88.97(8) | 176.50(8) | 92.28(10) | 93.68(9) | This work |

4-methoxypyridine-N-oxide (4-MOP-NO); 4-hydroxymethylpyridine (4-OMP) and 4-methoxypyridine (4-MOP).

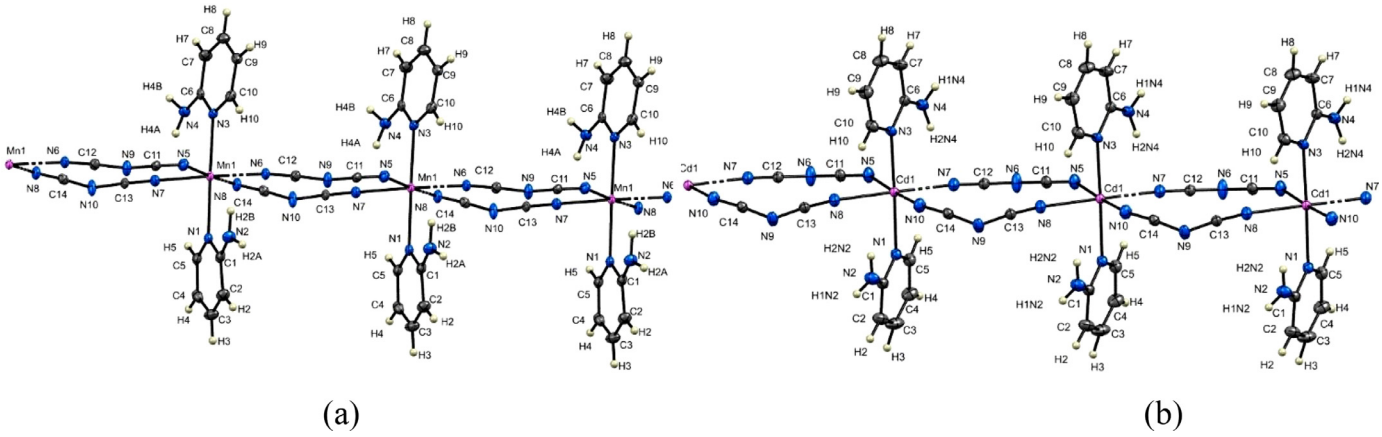


**Fig. 2.** 1D polymeric chains of (a) **1** and (b) **2** along (010).

## 2.8. Antimicrobial tests

The antimicrobial activity of **1**, 2-Ampy and dca together with the reference antibacterial chloramphenicol, and antifungal Gentamicin, were evaluated against one-gram positive bacteria (*Staphylococcus aureus*) one-gram negative bacteria (*Salmonella Typhi*) and one fungus (*Candida albicans*). These tests were carried out in the Applied Microbiology and Molecular Pharmacology Laboratory (LMP) of the University of Yaoundé I, Cameroon according to a previously published protocol [53].

## 3. Results and discussion

### 3.1. Syntheses and crystal structures of 1 and 2

Reaction of the metal salts $MCl_2{\cdot}4H_2O$ ($M$ = Mn, Cd), sodium dicyanamide and 2-Ampy in the molar ratio 1:2:4 in ethanol/water (1:1 v/v) resulted in the formation of colorless polymeric chains $[M(2\text{-ampy})_2(\mu_{1,5}\text{-dca})_2]_n$, $M$ = Mn (**1**), Cd (**2**). The complexes **1** and **2** (Fig. 1) were found to crystallize in the monoclinic space group Cc. The crystal data and structure refinement parameters are presented in Table 1 while the selected bond lengths and bond angles are shown in Table S1 (supplementary section).

The asymmetric units of **1** and **2** contain one metal atom, two bridging bidentate $\mu_{1,5}$-dca anions, coordinating through the nitrile nitrogen, and two monodentate 2-Ampy ligands, through its ring N-atoms ($\kappa^1$N). In both **1** and **2**, the metal atoms are coordinated to four equatorial $\mu_{1,5}$-bridging dca ligands and two monodentate 2-Ampy ligands in axial positions. The coordination environment around each metal center in **1** and **2** represents an $MN_6$-octahedron. The octahedra in **1** and **2** are distorted, with four short M-$N_{dca}$ bonds in the range 2.211(3) – 2.231(3) Å and 2.324(5) - 2.347(4) Å in addition to two long M-$N_{py}$ bonds in the ranges 2.302(3) – 2.303(3) Å and 2.326(2) – 2.351(2) Å, respectively. The N-M-N bond angles in the ranges 86.73(10) - 93.58(10)° and 85.63(11) – 93.68(9)°, respectively for **1** and **2**, are consistent with similar compounds previously reported [18,54]. The N(3)-Mn(1)-N(1) and N(3)-Cd(1)-N(1) bond angles in **1** and **2**, (177.46(14) and 176.98(19)°, respectively) deviate slightly from 180°. The terminal N atoms of four dicyanamide ligands form an approximate square plane in **1** and **2**, with N—M—N bite angles of 88.04(11) and 89.34(12) for **1** and 87.57(9) and 90.74(8) for **2**.

The M–$N_{py}$ distances as well as the M–$N_{dca}$ distances of **1** and **2** (Table 2) are comparable to those of similar $[M(dca)_2(L)_2]_n$ ($M$ = Mn for **1** and Cd for **2**) structures in the literature. These values are however slightly longer than those of their Co(II), Cu(II) and Zn(II) counterparts. The $N_{dca}$-M-$N_{dca}$ as well as the $N_{py}$-M-$N_{dca}$ bond angles for **1** and **2** are smaller in comparison to those of similar structures in the literature, indicating the distortion in the structures.

The metal centers in **1** and **2** are arranged in linear chains along (010) (Fig. 2) with [Mn1 . . .Mn1] and [Cd1…Cd1] intra-chain separations, through the bridging dicyanamido anions, of 7.505 Å and 7.609 Å, whereas the shortest [Mn1…Mn1] and [Cd1…Cd1] inter-chain distances are 7.405 and 7.442 Å, respectively. While the intra-chain separations are similar, the inter-chain distances are slightly longer than those reported (Table 3) for other *catena*–$M(dca)_2L_2$ structures [9,54–57].

The 1D chains (Fig. 2a-b) are stabilized by intra-chain N2—H2A···N4i = 0.80(4) Å and N4—H4A···N7 = 0.89(5) Å H-bonds (Table S1) for **1** and N2—H1N2···N4i = 0.84(5) Å for **2**, between the exocyclic amino group and dca nitrogen atom, while the chains are held together by inter-chain H-bonds N2—H2B···N6ii = 0.96(4) Å, N2—H2B···N5 = 0.96(4) Å and N4—H4B···N9iii = 0.90(4) Å for

**Table 3**
Comparative data on intra-chain and inter-Chain M...M distances of some $[M(dca)_2(L)_2]_n$.

| Complex | M...M Intra-chain (Å) | M...M Inter-chain (Å) | Ref |
|---|---|---|---|
| $Mn(dca)_2(pym)_2$ | 7.58 | 7.573 | [54] |
| $Mn(dca)_2(pym)(H_2O)$ | 7.568 | 6.439 | [54] |
| *catena*-$[Mn(\mu_{1,5}\text{-}dca)_2(4\text{-}MOP\text{-}NO)_2]$ | 7.5065(6) | 6.6283(3) | [55] |
| *catena*-$[Cd(\mu_{1,5}\text{-}dca)_2(4\text{-}MOP\text{-}NO)_2]$ | 7.6311(6) | 6.6699(3) | [55] |
| $[Mn(dca)_2(pydz)2]_n$ | 7.4686(5) | 6.3864(5) | [9] |
| $[Fe(dca)_2(pydz)2]_n$ | 7.4195(9) | 6.378(1) | [9] |
| $[Co(dca)_2(pydz)_2]_n$ | 7.3409(5) | 6.3272(5) | [9] |
| $[Co(dca)_2(4\text{-}OMP)_2]_n$ | 7.213(3) | 7.076(3) | [12] |
| $[Cu(dca)_2(4\text{-}OMP)_2]_n$ | 7.2754(12) | 7.2432(12) | [12] |
| $[Cu(dca)_2(4\text{-}MOP)2]_n$ | 7.3799(4) | 7.0318(4) | [12] |
| $[Cd(dca)_2(4\text{-}MOP)_2]_n$ | 7.5491(9) | 7.1028(8) | [12] |
| $[Zn(dca)_2(4\text{-}MOP)_2]_n$ | 7.3706(4) | 7.0620(4) | [12] |
| $[Mn(2\text{-}ampy)_2(\mu_{1,5}\text{-}dca)_2]_n$ | 7.505 | 7.405 | This work |
| $[Cd(2\text{-}ampy)_2(\mu_{1,5}\text{-}dca)_2]_n$ | 7.609 | 7.442 | This work |

4-methoxypyridine-N-oxide (4-MOP-NO); 4-hydroxymethylpyridine (4-OMP) and 4-methoxypyridine (4-MOP).

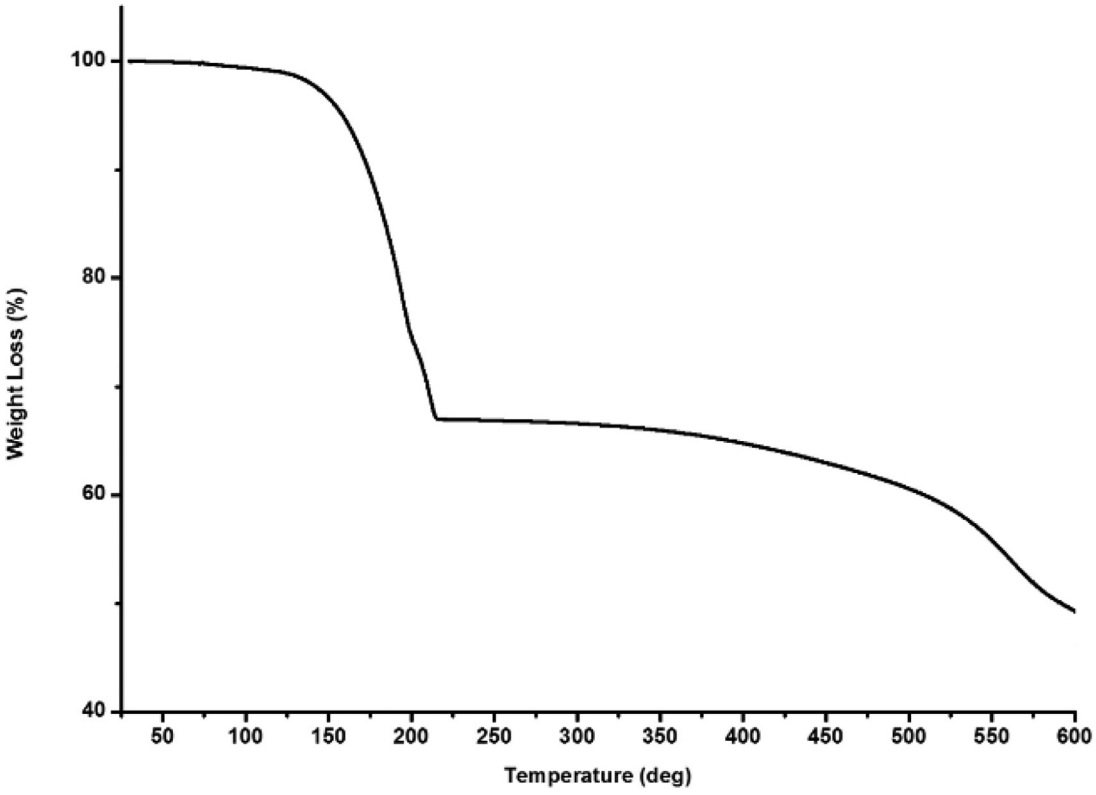


**Fig. 3.** TGA thermogram for **1**.

**1** and N4—H1N4···N9ii = 0.83(4) Å for **2** (Symmetry codes: (i) $x - 1/2, -y + 3/2, z - 1/2$; (ii) x, $y + 1$, z; (iii) $x + 1/2, -y + 1/2, z + 1/2$ for **1**; Symmetry codes: (i) $x + 1/2, -y + 3/2, z + 1/2$; (ii) $x - 1/2, -y + 3/2, z - 1/2$ for **2**), to form a layered structure (Fig. S1 (a)). The layers are interconnected by C—H···N bonds and non-covalent face to face $\pi$–$\pi$ ring stacking interactions to afford a 3-D structure (Fig. S1 (b)).

## 4. Infrared spectroscopy

Characteristic medium to strong IR absorption bands (Fig. S2) for dca include $\upsilon_{as}$(C≡N) + $\upsilon_s$(C≡N) at 2286 $cm^{-1}$, $\upsilon_{as}$(C≡N) at 2228 $cm^{-1}$ and $\upsilon_s$(C≡N) at 2171 $cm^{-1}$. These bands are shifted to higher wavenumbers 2297, 2232 and 2150 $cm^{-1}$in **1** as well as 2293, 2226 and 2162 $cm^{-1}$ in **2**, respectively. These shifts can be attributed to the bridging coordination mode of the ligand and [9,12,14,55,58]. Absorption bands for dca at 1344 $cm^{-1}$ for $\upsilon_{as}$(N–C), 930 $cm^{-1}$ for $\upsilon_s$(N–C), 664 $cm^{-1}$ for $\delta$(CNC), 543 $cm^{-1}$ for $\delta$(NCN), and 529 $cm^{-1}$ for $\delta$(NCN) could not be assigned in the complex because they are masked by vibrational bands of the 2-Ampy ligand as previously reported [9,12,14,55]. The medium to strong absorption bands of 2-Ampy at 3447 and 3353 $cm^{-1}$ for **1** and 3471 and 3372 $cm^{-1}$ for **2**, are attributed to $\upsilon_s(NH_2)$ and $\upsilon_{as}(NH_2)$ vibrations of the $NH_2$ group, respectively. The characteristic $\upsilon_{C=N}$ stretching modes of the pyridine ring shifted from 1595 to 1614 $cm^{-1}$ in the spectra of **1** and **2**, indicating its participation in bonding [18].

### 4.1. UV-Vis Spectroscopy

The UV–vis spectra (Fig. S3) of **1** reveals a strong absorption band at 340 nm which can be attributed to n → $\pi^*$ transitions

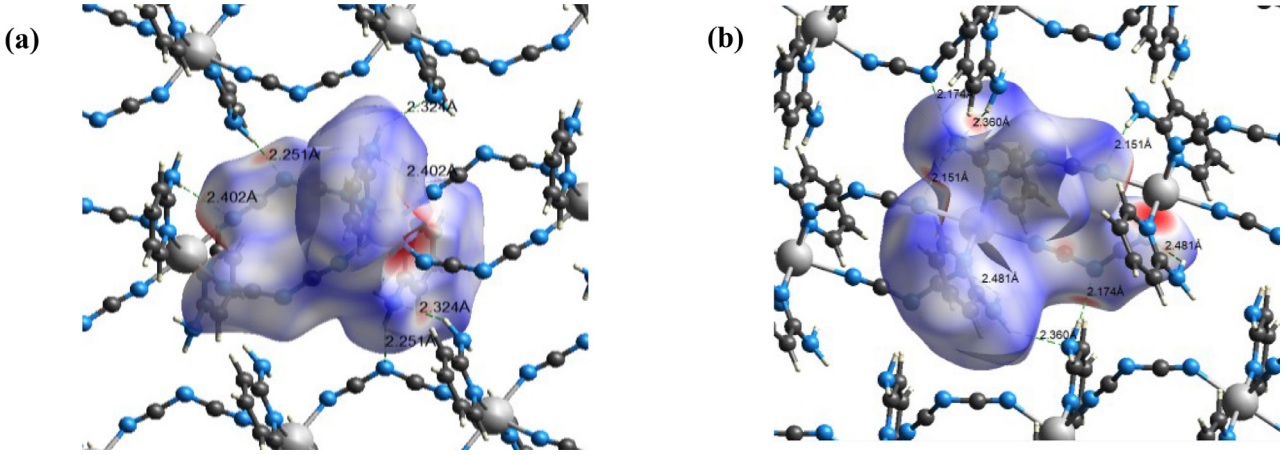


**Fig. 4.** $d_{norm}$ 3D Hirshfeld surface of (a) **1** and (b) **2** with the close contact molecules.

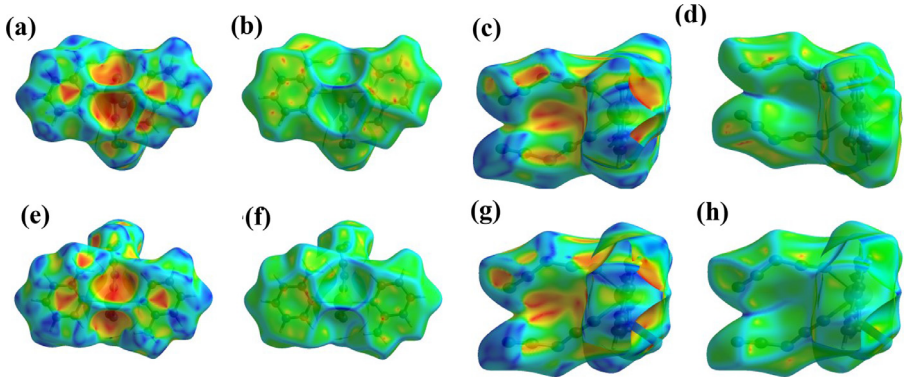


**Fig. 5.** 3D Hirshfeld surface mapped with shape index of **1** ((a) and (c)) and **2** ((e) and (g)) and curvedness of **1** ((b) and (d)) and **2** ((f) and (h)).

**Table 4**
Values (eV) of some chemical reactivity descriptors of **1** and **2**

| | 1 | 2 |
|---|---|---|
| $E_{HOMO}$ | - 5.32 | - 4.34 |
| $E_{LUMO}$ | - 2.19 | - 4.17 |
| *IP* | 5.32 | 4.34 |
| *EA* | 2.19 | 4.17 |
| $\Delta E$ | 3.13 | 0.17 |
| $\chi$ | 3.76 | 4.25 |
| $\mu$ | -3.76 | -4.25 |
| $\eta$ | 1.56 | 0.08 |
| *s* | 0.352 | 5.88 |
| $\omega$ | | 4.51 |

of the azomethine group. In **2**, two intense bands are observed at 350 nm and 385 nm which can be assigned to n → $\pi^*$ transitions of the azomethine group and charge transfer transition from the pyridine N-atom to the metal ion, respectively. Spin-forbidden d-d transitions were not observed in **1** ($Mn^{2+}$; $d^5$) and **2** ($Cd^{2+}$; $d^{10}$) [8,59].

### 4.2. Thermal analysis

To investigate the thermal stability of **1**, thermogravimetric analysis was performed. The thermogram of **1** (Fig. 3) shows two decomposition steps that are accompanied by endothermic events in the DTA curve. The first and major decomposition step takes place with a mass loss of 25.2%, at 180°C corresponds to the loss of one molecule of 2-Ampy (Calc. 25.08%). This is followed by a small mass loss of 7.32% at 200 °C, which can be attributed to the loss of a carbon atom and $NH_3$ (Calc. 7.73%) from the second 2-Ampy molecule. The second major decomposition step which occurs at 550°C ($\Delta m$ = 19.71%) is attributed to loss of the remaining 2-Ampy ligand (calc. 17.59%), leading to the formation of $Mn(dca)_2$. This decomposition pattern is similar to that of the coordination polymer *catena*-[(bis($\mu_2$-dicyanamido-N,N')-bis(pyridazine-N)-manganese(II)] found in the literature[9].

### 4.3. PXRD analysis of 1

The simulated as well as the experimental PXRD patterns of **1** are shown in Fig. S4. The experimentally measured PXRD diffraction peak is consistent with the simulated pattern, indicating the phase purity of the synthesized sample. The difference in intensities between the simulated and experimental patterns is probably due to the preferred orientations of the powder samples.

### 4.4. Hirshfeld surface (HS) analysis

The Hirshfeld surfaces for **1** and **2**, calculated from their X-ray structures using *Crystal Explorer* 17.5[22] software have been mapped over $d_{norm}$ and curvedness (Fig. 4). The intermolecular interactions that dominate in the structure are viewed by the bright red area of $d_{norm}$ surface.

The large and intense red spots around the metallic ion and the terminal nitrogen atoms of dca are indicative of very strong interactions attributed to the coordination bond between metallic ions and nitrogen atom of dca. The medium and intense red spots around the nitrogen and hydrogen atoms indicate hydrogen bonding contacts.

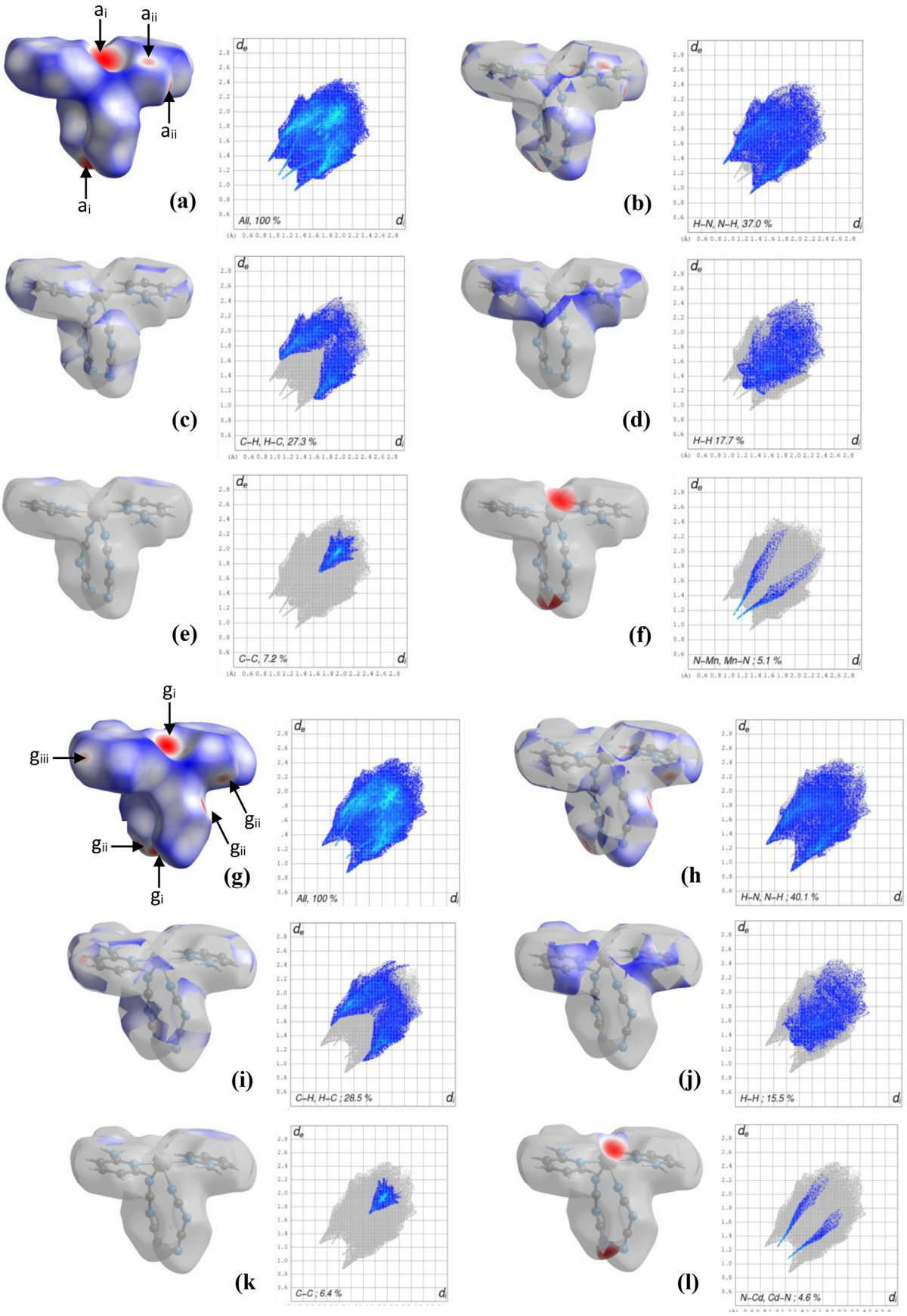


**Fig. 6.** 2D fingerprint plot and delineated fingerprint plot of **1** ((a)-(f)) and **2** ((g)-(l)): $a_i$ and $g_i$ represent N—Mn/Mn—N interactions; $a_{ii}$ and $g_{ii}$ represent N—H/H—N interactions; $g_{iii}$ represents C–H—$\pi$ interactions.

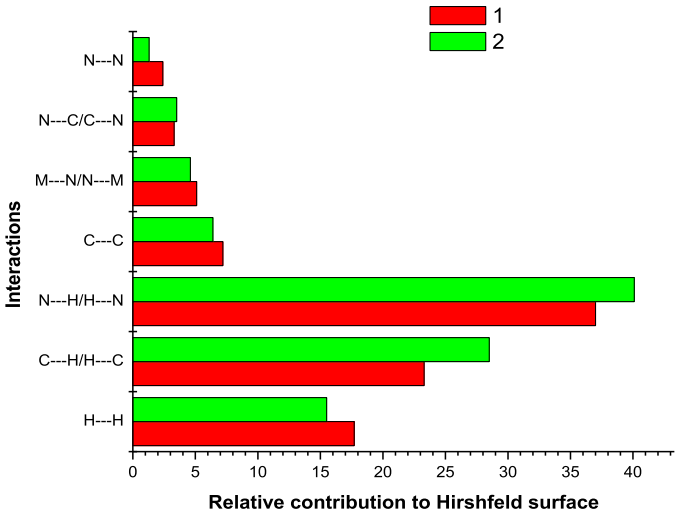


**Fig. 7.** Relative contribution of different interactions to the Hirshfeld surface of **1** and **2**.

The blue and white areas on the Hirshfeld surfaces of **1** and **2** indicate the existence of weak intermolecular interactions in these crystals. The Hirshfeld surfaces mapped over shape-index and curvedness for **1** and **2** (Fig. 5) reveal the presence of C-H—$\pi$ interactions (red spot at the center of the two phenyl rings of each polymer) and $\pi$-$\pi$ interactions between their phenyl rings (appearance of small blue regions surrounding bright-red spots within the phenyls rings).[21,60] The flat region around the phenyl rings confirms the presence of $\pi$-$\pi$ stacking interactions in these polymers (Fig. 5 (a), (b), (e) and (f)). These two interactions may also exist in the circle formed by the central metal and the co-ligands (Fig. 5 (c), (d), (g) and (h)).

The similarity of the 2D fingerprint plots of **1** and **2**, Fig. 6 (a)-(f) for **1** and (g)-(l) for **2**, suggests that they have similar crystal structures and identical space group symmetry.[48] The spikes corresponding to C-H—$\pi$ ($di + de \approx 2.7$ Å), H—H ($di = de = 1.3$ Å) and N—H/H—N ($di + de = 2.2$ Å) interactions are the most prominent features, constituting 82.0 % and 84.1 % of the overall interactions of the crystal packing for **1** and **2**, respectively. Additional spikes due to $\pi$-$\pi$ stacking interactions represented by C—C, C—N/N—C and N—N interactions are minor. The relative contribution of all these interactions to the Hirshfeld surface are presented on Fig. 7.

The optimized geometries of the polymer fragments are presented in Fig. S5 while the values of the bond lengths and bond angles around the central metal ion compared to their X-Rays values are presented in Table S4.

### 4.5. Electronic properties

The calculated values of descriptors, obtained from DFT calculations, used to characterize the global chemical reactivity and kinetic stability of **1** and **2** [41,61,62], are presented in Table 4.

Comparatively, **2**: (i) has high tendency to donate electrons (high value of $E_{HOMO}$) and to accept electrons (high value of $E_{HOMO}$); (ii) is more polarized, more reactive, and therefore kinetically less stable (high value of $\Delta E$ and $s$, but low value of $\eta$) and (iii) is the more nucleophile (high values of $\chi$ and low value of $\mu$ and $\omega$). These results agree with NBO analysis (See Supplementary Section) which show that metal-ligands interactions were more important in **1** compared to **2**.

The distribution of HOMO (nucleophilic regions) and LUMO (electrophilic region) orbitals of **1** and **2** are also presented in Fig. 8. These pictures show that the HOMO and LUMO of the polymeric structures are mainly carried by metal ions. The surface area of **1** covered by the HOMO is greater than that of **2**, indicating its greater stability. The stability of **1** can also be observed through the delocalization of the spin density (Fig. 8) on all the three Mn ions.

### 4.6. IR

Theoretical and experimental values of vibration frequencies of 2-ampy, dca, **1** and **2** are presented in Table 5. The normal mode was assigned using Gausview 6.0.16 software. In comparison with experimental values, the theoretical vibration frequencies of the ligands and complexes calculated at DFT/B3LYP-D3/LANL2DZ level of theory were multiplied by 0.958 scaling factor [41] to eliminate as much as possible, errors associated to different approximations.

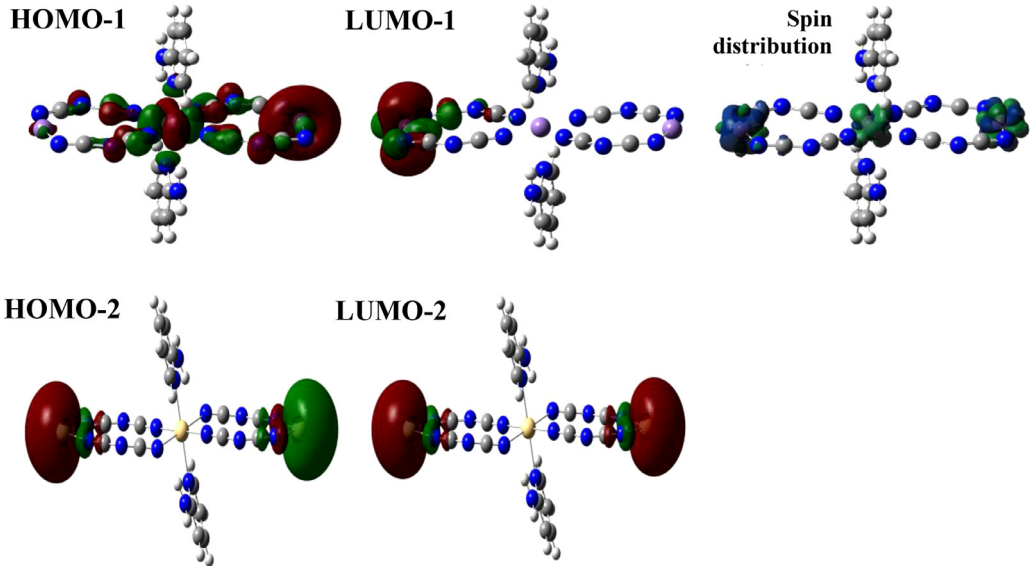


**Fig. 8.** HOMO, LUMO and spin density distribution of **1** and **2**.

**Table 5**
Relevant IR bands for **1** and **2**.

| Compounds | $\upsilon_{(N-H)}$ $cm^{-1}$ | $\upsilon_{(C\equiv N)}$ $cm^{-1}$ | $\upsilon_{(C=N)}$ $cm^{-1}$ | $\upsilon_{(C-N)}$ $cm^{-1}$ | $\upsilon_{(M-N)}$ $cm^{-1}$ | |
|---|---|---|---|---|---|---|
| 2-ampy | Exp | 3444 | / | 1597 | 1039 | / |
| | Calc | 3480 | | | 1307 | |
| Dca | Exp | / | 2228 | / | 1338 | / |
| | Calc | | 2117 | | 1339 | |
| 1 | Exp | 3474 | 2150 | 1614 | 1327 | 412 |
| | Calc | 3616anti 3471sym | 2195 | 1592 | 1338 | 551 |
| 2 | Exp | 3471 | 2162 | 1614 | 1328 | 410 |
| | Calc | 3584 3538sym | 2151 | 1589 | 1330 | 552 |

A good agreement was observed between scaled vibration frequencies and experimental vibration frequencies for most of the normal modes. However, an important deviation between experimental and theoretical values was observed for $NH_2$ and M-N (M = Cd, Mn). These important deviations may be attributed to the level of theory used which overestimates N–H.

## 5. Antimicrobial tests

The potency of the starting materials and the powder of **1** together with the reference antibacterial drug (chloramphenicol) and antifungal drug (Gentamicin) were evaluated for their biological activity against one gram-positive bacteria (*Staphylococcus aureus*) one gram-negative bacteria (*S. Typhi*) and one fungus (*Candida albicans*). The susceptibility of the bacterial and fungal strains towards these compounds were judged by measuring the size of the growth inhibition diameter (IZ). The compound was considered active when it showed an activity zone IZ > 6 mm. The results (Table S3) indicate that **1** showed no activity towards the fungus and very little activity (IZ = 1.25 ± 0.96 mm) against the Gram-negative bacteria species *S. Typhi*. A higher activity was observed against *Staphylococcus aureus* (IZ = 12.5 ± 0.57 mm) as compared to the other microorganisms. However, this activity is lower than that of the reference antibacterial chloramphenicol (IZ = 29.5 ± 1.3 mm).

## 6. Conclusion

Manganese and cadmium coordination polymers have been synthesized and the crystal structures determined using single crystal X-ray diffraction. In the polymeric 1D chains, adjacent metal centers are linked by the doubly $\mu_{1,5}$-bridging dca ligands in the equatorial plane, while two monodentate 2-Ampy ligands are coordinated to the metal ions in the axial positions. Intra-chain N—H···N H-bonds between the exocyclic amino group and dca nitrogen atom stabilizes the polymeric chain, while the chains are held together by inter-chain H-bonds N—H···N. The layers are interconnected by C—H···N bonds and non-covalent face to face $\pi$–$\pi$ ring stacking interactions to afford a 3-D structure. Hirshfeld surface analysis indicates that N–H interactions are the main contacts responsible for the molecular parking in the crystals, with **2** having more N–H interactions compared to **1**. The major interactions found in the crystal packing of the studied polymers are N—H/H—-N interactions followed by C–H—$\pi$ (represented as C—H/H—C) and H—H interactions However, the contribution of N—H/H—N and C–H—$\pi$ interactions are more important in **2** while H—H interactions are more important in **1**. NBO analysis demonstrated that metal-ligand interactions were more important in **1** compared to **2**. DFT calculations at the DFT/B3LYP-D3/LANL2DZ level of theory indicates that there is a difference between the calculated and experimental values of M-N bond lengths (with M = Cd, Mn) in the range 0.20 – 0.176 and 0.020 – 0.078 for **1** and **2**, respectively. Although the DFT-B3LYP-D3/LAN2DZ level of theory gives slight differences in bond lengths for the concerned polymers, it however gives a good geometry.

## Declaration of Competing Interest

The authors declare that they have no known competing financial interests or personal relationships that could have appeared to influence the work reported in this paper.

## CRediT authorship contribution statement

**Armel Landry Opepam Mbani:** Investigation, Methodology, Writing – original draft. **Divine Mbom Yufanyi:** Data curation, Writing – original draft, Writing – review & editing. **Che Dieudonne Tabong:** Writing – review & editing. **Nono Jean Hubert:** Software, Data curation, Writing – review & editing. **Amah Colette Benedicta Yuoh:** Methodology, Writing – original draft. **Awawou Gbambie Paboudam:** Supervision, Resources. **Agwara Moise Ondoh:** Conceptualization, Writing – review & editing, Resources.

## Acknowledgements

The authors are grateful to Rafferty James of the Department of Chemistry, University of Manchester, Manchester M13 9PL, England UK, and Peter Lönnecke of the Institute of Inorganic Chemistry, Universität Leipzig, Johannisallee 29, 04103 Leipzig, Germany, for assistance with single crystal X-ray measurements of the complexes. The support of the National Science Foundation (CHE-1429768) for the purchase of the powder X-ray diffractometer is gratefully acknowledged.

## Supplementary materials

Supplementary material associated with this article can be found, in the online version, at doi:10.1016/j.molstruc.2022.132956.

## References

[1] K.S. Murray, S.R. Batten, B. Moubaraki, D.J. Price, R. Robson, Molecular magnetism in manganese dicyanamide extended network structures, Mol. Cryst. Liquid Cryst. Sci. Technol.. Sec. A 335 (1) (1999) 313–322.
[2] S.R. Batten, K.S. Murray, Structure and magnetism of coordination polymers containing dicyanamide and tricyanomethanide, Coord. Chem. Rev. 246 (1) (2003) 103–130.
[3] J.L. Manson, A.M. Arif, C.D. Incarvito, L.M. Liable-Sands, A.L. Rheingold, J.S. Miller, Structures and magnetic properties of novel 1-D coordination polymers containing both dicyanamide and pyridine-type ligands, J. Solid State Chem. 145 (2) (1999) 369–378.
[4] D. Majumdar, M.S.S. Babu, S. Das, C. Mohapatra, J.K. Biswas, M. Mondal, Syntheses, X-ray crystal structures, photoluminescence properties, antimicrobial activities and hirshfeld surface of two new Cd(II) azide/thiocyanate linked coordination polymers, ChemistrySelect 2 (17) (2017) 4811–4822.
[5] B. Dojer, A. Pevec, M. Jagodič, M. Kristl, M. Drofenik, Three new cobalt(II) carboxylates with 2-, 3- and 4-aminopyridine: syntheses, structures and magnetic properties, Inorg. Chim. Acta 383 (0) (2012) 98–104.
[6] W. Maalej, R. Jaballi, A.B. Rached, P. Guionneau, N. Daro, Z. Elaoud, Supramolecular architectures of mononuclear nickel(II) and homobinuclear copper(II) complexes with the 5,5′-dimethyl-2,2′-bipyridine ligand: syntheses, crystal structures and Hirshfeld surface analyses, J. Mol. Struct. 1250 (2021) 131728.

[7] Z. Setifi, D. Geiger, C. Jelsch, T. Maris, C. Glidewell, M. Mirzaei, M. Arefian, F. Setifi, The first Fe(II) complex bearing end-to-end dicyanamide as a double bridging ligand: crystallography study and Hirshfeld surface analysis; completed with a CSD survey, J. Mol. Struct. 1173 (2018) 697–706.
[8] F.A. Mautner, P. Jantscher, R.C. Fischer, A. Torvisco, R. Vicente, T.N.V. Karsili, S.S. Massoud, Synthesis and characterization of 1D coordination polymers of metal(II)-dicyanamido complexes, Polyhedron 166 (2019) 36–43.
[9] M. Wriedt, C. Nather, Directed synthesis of m-1,3,5 bridged dicyanamides by thermal decomposition of m-1,5 bridged precursor compounds, Dalton Trans. 40 (4) (2011) 886–898.
[10] F.A. Mautner, P.V. Jantscher, R.C. Fischer, A. Torvisco, K. Reichmann, N.M.H. Salem, K.J. Gordon, F.R. Louka, S.S. Massoud, Coordination polymers in dicyanamido-Cadmium(II) with diverse network dimensionalities, Crystals 11 (2) (2021) 181.
[11] A.M. Kutasi, A.R. Harris, S.R. Batten, B. Moubaraki, K.S. Murray, Coordination polymers of dicyanamide and methylpyrazine: syntheses, structures, and magnetic properties, Cryst. Growth Des. 4 (3) (2004) 605–610.
[12] F.A. Mautner, M. Traber, R.C. Fischer, S.S. Massoud, R. Vicente, Synthesis, crystal structures, spectral and magnetic properties of 1-D polymeric dicyanamido-metal(II) complexes, Polyhedron 138 (2017) 13–20.
[13] R. Boča, M. Boča, G. Milan, J. Lothar, C. Wagner, H. Fuess, Versatile coordination mode of dicyanamide in nickel(II) complexes containing polyamines as blocking ligands, Polyhedron 23 (15) (2004) 2337–2348.
[14] F. Mautner, P. Jantscher, R. Fischer, A. Torvisco, K. Reichmann, N. Salem, K. Gordon, F. Louka, S. Massoud, Coordination polymers in Dicyanamido-Cadmium(II) with diverse network dimensionalities, Crystals 11 (2021) 181.
[15] L. Zheng, Crystal Structures Syntheses, Magnetic behaviours, and thermal properties of three hydrogen-bonding networks containing dicyanamide and 4-hydroxypyridine, J. Chem. 2013 (2013) 291703.
[16] S. Suckert, L.S. Germann, R.E. Dinnebier, J. Werner, C. Näther, Synthesis, structures and properties of cobalt thiocyanate coordination compounds with 4-(hydroxymethyl)pyridine as Co-ligand, Crystals 6 (38) (2016) 17 pages.
[17] S. Suckert, H. Terraschke, H. Reinsch, C. Nather, Synthesis, crystal structures, thermal, magnetic and luminescence properties of Mn(II) and Cd(II) thiocyanate coordination compounds with 4-(Boc-amino)pyridine as co-ligand, Inorg. Chim. Acta 461 (2017) 290–297.
[18] A.C.B. Yuoh, M.O. Agwara, D.M. Yufanyi, M.A. Conde, R. Jagan, K.O. Eyong, Synthesis, crystal structure, and antimicrobial properties of a novel 1-d cobalt coordination polymer with dicyanamide and 2-aminopyridine, Inter. J. Inorg. Chem. 2015 (2015) 8 Article ID 106838pages.
[19] G.R. Desiraju, Cryptic crystallography, Nat. Mater. 1 (2) (2002) 77–79.
[20] J.J. McKinnon, A.S. Mitchell, M.A. Spackman, Hirshfeld surfaces: a new tool for visualising and exploring molecular crystals, Chem. Eur. J. 4 (11) (1998) 2136–2141.
[21] R. Anbarasan, P. Eniya, J. Kalyana Sundar, M. Mengesha Woldemariam, Crystal structure and Hirshfeld surface analysis of 4-bromoanilinium nitrate, Acta Crystallogr. E 76 (6) (2020) 973–976.
[22] P.R. Spackman, M.J. Turner, J.J. McKinnon, S.K. Wolff, D.J. Grimwood, D. Jayatilaka, M.A. Spackman, CrystalExplorer: a program for Hirshfeld surface analysis, visualization and quantitative analysis of molecular crystals, J. Appl. Crystallogr. 54 (3) (2021) 1006–1011.
[23] C. Feng, D. Zhang, G.-.Y. Gao, Y. Peng, H. Zhao, Exploration of Intermolecular interaction of one silver(I) polymer with bis(pyrazolyl)methane derivative: experimental observations, Hirshfeld surface analyses and fluorescent properties, J. Inorg. Organomet. Polym. Mater. 26 (2) (2016) 431–438.
[24] C. Feng, Y.-.Q. Zhu, X.Y. Xue, H. Zhao, A triazolate-supported $Fe_3(m_3\text{-}O)$ core: crystal structure, fluorescence, and hirshfeld surface analysis, J.Clust. Sci. 27 (4) (2016) 1181–1190.
[25] N. Dissem, N. Ferhi, T. Maris, A. Duong, Design, structural characterization and Hirshfeld surface analysis of Ni(II) and Zn(II) coordination polymers using mixed linker synthetic strategy based on tetratopic and macrocyclic N-donor ligands, J. Mol. Struct. 1254 (2022) 132317.
[26] C. Amah, A.M. Ondoh, D.M. Yufanyi, D.S.Y. Gaelle, Synthesis, crystal structure and antimicrobial properties of an anhydrous copper(II) complex of pyridine-2-carboxylic acid, Inter. J. Chem. 7 (1) (2015) 10–20.
[27] D. Yufanyi, H. Nono, A. Yuoh, C. Tabong, W. Judith, A. Ondoh, Crystal packing studies, thermal properties and hirshfeld surface analysis in the Zn(II) complex of 3-aminopyridine with thiocyanate as Co-ligand, Open J. Inorg. Chem. 11 (2021) 63–84.
[28] F. Tsague Chimaine, D.M. Yufanyi, A.C. Benedicta Yuoh, D.B. Eni, M.O. Agwara, Synthesis, crystal structure, photoluminescent and antimicrobial properties of a thiocyanato-bridged copper(II) coordination polymer, Cogent Chem. 2 (1) (2016) 1253905.
[29] *CrysAlis Pro*: Empirical absorption Correction, Oxford Diffraction Ltd., 2014.
[30] G.M. Sheldrick, SHELXT-20xy, Acta Crystallogr. A 71 (2015) 3–8.
[31] A. Linden, Chemistry and structure in acta crystallographica section C, Acta Cryst C 71 (Pt 1) (2015) 1–2.
[32] G.M. Sheldrick, Serial crystallography with X-ray free-electron laser pulses, Acta Crystallog. A71 (2015) s1.
[33] C.F. Macrae, P.R. Edgington, P. McCabe, E. Pidcock, G.P. Shields, R. Taylor, M. Towler, J. van de Streek, Mercury: visualization and analysis of crystal structures, J. Appl. Crystallog. 39 (3) (2006) 453–457.
[34] M. Frisch, G. Trucks, H. Schlegel, G. Scuseria, M. Robb, J. Cheeseman, G. Scalmani, V. Barone, B. Mennucci, G. Petersson, H. Nakatsuji, M. Caricato, X. Li, H. Hratchian, A. Izmaylov, J. Bloino, G. Zheng, J. Sonnenberg, M. Hada, D. Fox, Gaussian 09 (Revision D.01), Gaussian Inc., Wallingford CT, 2009.
[35] A.D. Becke, Density-functional exchange-energy approximation with correct asymptotic behavior, Phys. Rev. A 38 (6) (1988) 3098–3100.
[36] C. Lee, W. Yang, R.G. Parr, Development of the Colle-Salvetti correlation-energy formula into a functional of the electron density, Phys.Rev. B 37 (2) (1988) 785–789.
[37] A.D. Becke, A new mixing of Hartree-Fock and local density-functional theories, J. Chem. Phys. 98 (2) (1993) 1372–1377.
[38] P.J. Hay, R.W. Willard, Ab initio effective core potentials for molecular calculations. Potentials for the transition metal atoms *Sc* to Hg, J. Chem. Phys. 82 (1) (1985) 270–283.
[39] P.J. Hay, R.W. Willard, Ab initio effective core potentials for molecular calculations. Potentials for K to Au including the outermost core orbitals, J. Chem. Phys. 82 (1) (1985) 299–310.
[40] E. Marcus, H. Pavel, F. Thomas, S. Sándor, K. Efthimios, Hydrogen bonding and stacking interactions of nucleic acid base pairs: a density-functional-theory based treatment, J. Chem. Phys. 114 (12) (2001) 5149–5155.
[41] Z. Kartal, O. Sahin, Synthesis, X-ray crystallography characterization, and DFT theoretical studies of a new metal compound $[CdCl_2(4\text{-aminopyridine})_2]_n$, J. Mol. Struct. 1243 (2021) 130720.
[42] F. Weinhold, Natural bond orbital analysis: a critical overview of relationships to alternative bonding perspectives, J. Comput. Chem. 33 (30) (2012) 2363–2379.
[43] F. Weinhold, C.R. Landis, E.D. Glendening, What is NBO analysis and how is it useful? Inter. Rev. Phys. Chem. 35 (3) (2016) 399–440.
[44] J.L. Gazquez, A. Cedillo, A. Vela, Electrodonating and electroaccepting powers, J Phys Chem A 111 (10) (2007) 1966–1970.
[45] N. Flores-Holguin, J. Frau, D. Glossman-Mitnik, Chemical reactivity and bioactivity properties of the Phallotoxin family of fungal peptides based on Conceptual Peptidology and DFT study, Heliyon 5 (8) (2019) e02335.
[46] E. Weber, Y. Aoyama, M.R. Caira, G.R. Desiraju, J.P. Glusker, A.D. Hamilton, R.E. Meléndez, A.K. Nangia, Design of organic solids, 1998.
[47] M.A. Spackman, P.G. Byrom, A novel definition of a molecule in a crystal, Chem. Phys. Lett. 267 (3) (1997) 215–220.
[48] M.A. Spackman, J.J. McKinnon, Fingerprinting intermolecular interactions in molecular crystals, CrystEngComm 4 (66) (2002) 378–392.
[49] J.J. McKinnon, M.A. Spackman, A.S. Mitchell, Novel tools for visualizing and exploring intermolecular interactions in molecular crystals, Acta Crystallogr. Sect. B 60 (6) (2004) 627–668.
[50] J.J. McKinnon, D. Jayatilaka, M.A. Spackman, Towards quantitative analysis of intermolecular interactions with Hirshfeld surfaces, Chem. Commun. (37) (2007) 3814–3816.
[51] A. Parkin, G. Barr, W. Dong, C.J. Gilmore, D. Jayatilaka, J.J. McKinnon, M.A. Spackman, C.C. Wilson, Comparing entire crystal structures: structural genetic fingerprinting, Cryst. Eng. Comm. 9 (8) (2007) 648–652.
[52] A. Collins, C.C. Wilson, C.J. Gilmore, Comparing entire crystal structures using cluster analysis and fingerprint plots, Cryst. Eng. Comm. 12 (3) (2010) 801–809.
[53] D.B. Eni, D.M. Yufanyi, J.H. Nono, C.D. Tabong, M.O. Agwara, Synthesis, characterization and thermal properties of 1,10-phenanthroline mixed-ligand complexes of cobalt(II) and copper(II): metal-mediated transformations of the dicyanamide ion, Chem. Pap. 74 (9) (2020) 3003–3016.
[54] J.L. Manson, J.A. Schlueter, C.L. Nygren, $Mn(dca)_2(pym)_2$ and $Mn(dca)_2(pym)(H_2O)$ {dca = dicyanamide; pym = pyrimidine}: new coordination polymers exhibiting 1- and 2-D topologies, Dalton Trans. (6) (2007) 646–652.
[55] F.A. Mautner, P. Jantscher, R.C. Fischer, A. Torvisco, R. Vicente, T.N.V. Karsili, S.S. Massoud, Structure, DFT calculations, and magnetic characterization of coordination polymers of bridged dicyanamido-metal(II) complexes, Magnetochemistry 5 (3) (2019) 41.
[56] A.M. Kutasi, A.R. Harris, S.R. Batten, B. Moubaraki, K.S. Murray, Coordination polymers of dicyanamide and methylpyrazine: syntheses, structures, and magnetic properties, Cryst. Growth Des. 4 (3) (2004) 605–610.
[57] J.L. Manson, J. Gu, J.A. Schlueter, H.H. Wang, Structures and magnetic behavior of 1-, 2-, and 3D coordination polymers in the Cu(II)-dicyanamide-pyrimidine family, Inorg. Chem. 42 (12) (2003) 3950–3955.
[58] J. Carranza, J. Sletten, F. Lloret, M. Julve, Structural analysis and magnetic properties of the copper(II) dicyanamide complexes $[Cu_2(dmphen)_2(dca)_4]$, $[Cu(dmphen)(dca)(NO_3)]n$ and $[Cu(4,4'\text{-}dmbpy)(H_2O)(dca)_2]$ (dca= dicyanamide; Dmphen=2,9-dimethyl-1,10-phenanthroline; 4,4′-dmbpy=4, 4′-dimethyl-2,2′-bipyridine), Inorg. Chim. Acta 357 (2004) 3304–3316.
[59] A. Majumder, G. Pilet, M.a.T. Garland Rodriguez, S. Mitra, Synthesis and structural characterisation of three dicyanamide complexes with Mn(II), Zn(II) and Cd(II): supramolecular architectures stabilised by hydrogen bonding, Polyhedron 25 (13) (2006) 2550–2558.
[60] S.L. Tan, M.M. Jotani, E.R.T. Tiekink, Utilizing Hirshfeld surface calculations, non-covalent interaction (NCI) plots and the calculation of interaction energies in the analysis of molecular packing, Acta Crystallog. Sect. E 75 (3) (2019) 308–318.
[61] S. Babaei, M. Niad, Chemical reactivity descriptors as a tool of prediction in the synthesis of sandwich type polyoxometalate organic inorganic hybrid compounds, Polyhedron 188 (2020) 114710.
[62] S. Babaei, M. Niad, Z. Solati, DFT investigation onto axial ligand effects on the TPP ligand and its manganese complexes [Mn(TPP)(O)(X)] (X=F-, Cl-, Br-), J. Iran. Chem. Soc. (2020) 1–8.